The properties of Dirac materials: Strain, magnetoelectrics and Krein-Hermiticity

by

Geremia Massarelli

A thesis submitted in conformity with the requirements
for the degree of Doctor of Philosophy

Department of Physics
University of Toronto

© Copyright 2023 by Geremia Massarelli

The properties of Dirac materials: Strain, magnetoelectrics and Krein-Hermiticity

Geremia Massarelli
Doctor of Philosophy

Department of Physics
University of Toronto
2023

Abstract

The study of Dirac matter offers a cross section of some of the most dynamic topics in condensed-matter physics. Interest in Dirac-like dispersions in band structures dates back to the early days of solid-state physics; however, in the past decades, emergent Dirac-like behaviour in materials has become a focal point of condensed-matter physics, in no small part because of the new, topological appreciation of these gapless phases of matter. Since then, the field has witnessed an ever-increasing understanding of the exotic properties that emerge in Dirac matter.

The present thesis furthers the exploration of Dirac-like physics in condensed-matter systems and the novel properties that stem from it. After a thorough overview of the physics underpinning these states of matter, we investigate the existence of strain-induced pseudomagnetic fields in nodal superconductors like the cuprates. We provide a realistic proposal to realize strain-induced Landau levels in a cuprate sample, a unique scenario that cannot be achieved with an ordinary magnetic field.

We then turn to a study of the orbital Edelstein effect resulting from spontaneous symmetry breaking within a nodal-line semimetal. In this model, the onset of charge order endows the gapless lines with a mass; they then become sources of orbital magnetic moment. Hence, we exemplify how this magnetoelectric effect can serve as a proxy for symmetry breaking in certain Dirac semimetal phases.

Finally, we develop a formalism of the Schrieffer-Wolff transformation in Krein-Hermitian Hamiltonians, which arise, among other contexts, as the single-particle Hamiltonians of bosonic Bogoliubov–de Gennes systems. These Hamiltonians are Hermitian with respect to an indefinite inner product, and the Krein-unitary transformation we formulate preserves their Krein-Hermiticity. In particular, we explain why an effective Hermitian Hamiltonian

can, under certain conditions, be used to describe subsets of adjacent bands of a larger Krein-Hermitian Hamiltonian, a justification of which seems to have been lacking. We then apply our findings to study the generic codimension of Dirac-like band touchings in such systems, focusing on spin-wave excitations in quantum magnets.

To my *nonno* Gió,
who will forever remain an inspiration.

Acknowledgements

My foremost debt of gratitude is to my supervisor, Professor Arun Paramekanti, whose thoughtful guidance, encouragement, patience and wisdom have, during my years here, been indispensable to my every achievement. It has been a privilege and a pleasure to work with him on several stimulating problems, to learn from him and to benefit from his broad knowledge and insight. Under his watchful eye, I have grown as a researcher and as a person, and I leave with a valuable set of skills that will continue to serve me in my future endeavours.

I am also indebted to the members of my Ph.D. Supervisory Committee, John Y. T. Wei and John E. Sipe, whose comments and guidance over the years helped me chart a research path through the course of my Ph.D., and also helped to give me more confidence in my work. Furthermore, I thank the members of my Departmental Ph.D. Oral Examination Committee, Professors Dvira Segal, John Y. T. Wei, and Arun Paramekanti, and my External Appraiser, Professor Ion Garate, for their invaluable comments and feedback, which allowed me to greatly improve this thesis.

I am hugely grateful to my parents, Clara and Antonio, to my brother, Zachary, and to my grandparents, Loreta, Giuseppe and Antonietta, whose support, encouragement and love have been unlimited. I could never repay my beloved parents, who have too often put my needs before their own, and I thank them for having always supported and never questioned the studies I chose to pursue.

I am ever so thankful to my fellow graduate students, many of whom have become dear friends, for so greatly contributing to my experience at the University of Toronto. Countless stimulating discussions with my peers led to sharing of knowledge, helped overcome obstacles and challenges, and inspired new directions. Moreover, the strong bonds of camaraderie we developed livened up our work days—and work evenings—and were a balm in moments of weariness and difficulty. In no specific order, I thank Sopheak Sorn, Nazim Boudjada, Ciarán Hickey, Adarsh Patri, Panagiotis Stavropoulos, Wonjune Choi, Jyotirmoy Roy, Jacob Gordon, Perry Mahon, Andrei Catuneanu, Li Ern Chern, Arijit Haldar, Finn Lasse Buessen, Sreekar Voleti, Ahmed Rayyan, Austin Lindquist, Daniel Schultz, Emily Zhang, Gideon Wachtel, Aris Spourdalakis, Pranai Vasudev, Christopher Garner and Ben Lau. It leaves me heavy-hearted that many relationships with valued colleagues were abruptly cut short by the COVID-19 pandemic.

I am fortunate to have had a circle of friends, some old and some new, that contributed to making me feel at home in Toronto. Were it not for their company, their warmth and their support, my time here might have felt, especially early on, like something of a lonely exile. In this regard, I thank Fang Xi Lin, Alexander Rachkov, Jeremy Rothschild, Justine Rancy, Christian Farfan Centeno, Rebecca Bartolloni, Claire Launay, Ramy Malak, and Thaddeus.

I should also like to highlight the support staff at the Department of Physics, including Liz

Glover, Teresa Baptista, Sheela Manek, Helen Iyer, Pierre Savaria, Isabela, and Rosemarie Rodney; their friendly faces and helpfulness contributed to making me feel welcome, and brought cheer to the daily routine. A special thanks goes to Krystyna Biel, whose assistance, support and encouragement at various times have been particularly vital.

I would be remiss not to mention some of the teachers who seeded in me a passion for science and for physics, and who gave me the confidence to plunge into an exciting and unconventional path: Alain Desparois, Paul Guertin, Jean-François Malicerte, Michel Duval, Stéphane Lavigne, je vous remercie.

I would like to recognize several years of financial support from *le Fonds de recherche du Québec – Nature et technologies*, and thank the government and legislature of Québec for supporting research in the physical sciences.

Contents

Contents vii

List of Tables xi

List of Figures xiii

List of Publications xxii

Preface xxiii

1 Introduction 1

1.1 Background and historical perspective 2

1.2 Dirac-like systems and topology 6

1.2.1 Topology and classification of gapped states of noninteracting matter 6

1.2.2 Topology and gapless states of noninteracting matter 9

1.3 The Dirac and Weyl Hamiltonians 14

1.4 Common Dirac-like systems: models and experimental evidence 15

1.4.1 Graphene 16

1.4.1.1 Low-energy graphene and effective Dirac electrons 19

1.4.1.2 Magnetic fields in graphene: Minimal coupling from Peierls substitution 22

1.4.1.3 Density of states and Landau levels in graphene 25

1.4.2 Time-reversal invariant topological insulators 30

1.4.2.1 Edge states 31

1.4.3 Cuprate high-temperature superconductors 33

1.4.3.1 Electronic configuration 34

1.4.3.2 High-temperature superconductivity and Gutzwiller approximation 37

1.4.4 Weyl semimetals 42

1.5 Strain, pseudo-magnetic fields and Landau levels in graphene 43

1.5.1 Strain, crystals and tight binding 44

1.5.2 Tight-binding graphene Hamiltonian with inhomogeneous hopping . 48

1.5.3 Experimental detection of strain-induced Landau levels in graphene 50
1.6 The Edelstein effects . . . 51
1.6.1 The (spin) Edelstein effect . . . 53
1.6.2 The orbital Edelstein effect . . . 55
1.6.3 Other variants of the Edelstein effect . . . 60
1.7 A primer on Krein spaces . . . 61
1.7.1 Hermiticity and changes of basis . . . 61
1.7.2 Elements of the theory of Krein spaces . . . 63
1.7.2.1 Eigenvalues of Krein-Hermitian matrices . . . 63
1.7.2.2 Eigenvectors of Krein-Hermitian matrices and diagonalizability 64
1.7.2.3 The diagonalizing transformation . . . 66

2 Pseudo-Landau levels of Bogoliubov quasiparticles in strained nodal superconductors 70
2.1 Introduction . . . 70
2.2 Effective low-energy theory . . . 71
2.3 Pseudo-Landau levels . . . 73
2.3.1 Pseudo-LLs from gap variations . . . 73
2.3.2 Pseudo-LLs from hopping variations . . . 74
2.4 Lattice model results . . . 74
2.5 Experimental signature of pseudo-LLs . . . 75
2.6 Experimental realizations . . . 77
2.6.1 Strained nanowires or films . . . 77
2.6.2 Proximity to nematic order . . . 78
2.7 Summary . . . 78
Appendix 2.A Absence of "scalar gauge potential" in BdG equation . . . 79
Appendix 2.B Dirac BdG solution - gap variations . . . 80
Appendix 2.C Dirac BdG solution - hopping variations . . . 81
Appendix 2.D Tunneling density of states (TDOS) . . . 83
2.D.1 Uniform case . . . 83
2.D.2 Pseudo-Landau Level case: Gap variations . . . 83
Appendix 2.E d-wave SC in a narrow strip . . . 84
Appendix 2.F Pseudo-Landau levels of strained d-wave SC in the (1,0)-edged strip geometry . . . 86
Appendix 2.G Mean field equations for correlated d-wave SC with strain . . . 87

3 Orbital Edelstein effect from density-wave order 89
3.1 Introduction . . . 89
3.2 Orbital Edelstein effect . . . 90
3.3 Model . . . 91

3.3.1 Non-interacting band structure . . . 93
3.3.2 Repulsive interactions . . . 94
3.4 Results . . . 95
3.4.1 Mean-field theory of charge-density-wave order . . . 95
3.4.2 Magnetoelectric response in Phase I . . . 96
3.4.3 Role of line nodes . . . 97
3.5 Discussion and conclusion . . . 102
Appendix 3.A Classical phase diagram . . . 104
Appendix 3.B Details of the mean-field calculation . . . 105
Appendix 3.C Nonsymmorphic symmetries and protection of the gapless lines in the high-symmetry phase . . . 106
Appendix 3.D Crystal class $\bar{4}2m$ . . . 107

4 Krein-unitary Schrieffer-Wolff transformation and band touchings in bosonic Bogoliubov-de Gennes and other Krein-Hermitian Hamiltonians 109
4.1 Introduction . . . 109
4.2 Bosonic BdG Hamiltonians . . . 111
4.2.1 Diagonalization . . . 112
4.2.2 Unitary transformations . . . 113
4.3 Krein-Hermitian Hamiltonians and perturbation theory . . . 114
4.3.1 Krein spaces . . . 114
4.3.2 Schrieffer-Wolff transformation for Krein-Hermitian Hamiltonians . . . 116
4.4 Band touchings and codimension in magnon systems . . . 120
4.4.1 Two-band effective Hamiltonian for magnon systems . . . 121
4.4.2 Constraint of magnetic inversion symmetry and examples . . . 121
4.4.2.1 Magnetic inversion and spin-rotation symmetries . . . 122
4.4.2.2 Effective magnetic inversion and Heisenberg ferromagnets . . . 123
4.4.2.3 Nodal lines in a stacked honeycomb quantum magnet . . . 124
4.4.2.4 XXZ model of a stacked honeycomb quantum magnet . . . 125
4.5 Conclusion . . . 129
Appendix 4.A Details of perturbative SW transformation . . . 130
Appendix 4.B Details and parameter values for XXZ model . . . 132
Appendix 4.C Implementation of symmetries in magnon Hamiltonians . . . 134
4.C.1 Overview . . . 134
4.C.2 Spin Hamiltonian . . . 135
4.C.3 Unitary symmetries . . . 137
4.C.4 Antiunitary symmetries . . . 139
4.C.4.1 When is V_h symmetric? . . . 141
4.C.5 Examples . . . 142
4.C.5.1 Magnetic inversion symmetry . . . 142

4.C.5.2 Time reversal with spin rotation 143
4.C.5.3 Effective magnetic inversion symmetry 143
4.C.5.4 Translation with spin rotation 144
4.C.5.5 Axial spin-rotation symmetry 144
4.C.6 Magnetic inversion and reality condition 144

5 Conclusion **146**
5.1 Pseudo-magnetic fields of quasiparticles in nodal superconductors 147
5.2 Slightly gapped nodal lines as sources in the orbital Edelstein effect 149
5.3 Krein-unitary Schrieffer-Wolff transformation and band touchings in bosonic Bogoliubov–de Gennes Hamiltonians 151

Bibliography **156**

List of Tables

1.1 Periodic table of topological insulators and superconductors in the ten AZ classes. The columns $\mathcal{T}$, $\mathcal{C}$, and $\mathcal{S}$ show which of the three basic symmetries are present in each class and, in the case of $\mathcal{T}$ and $\mathcal{C}$, whether they square to $+1$ or -1. The entries show the type of topological invariant (if any) in dimensions $d \in \{0, \ldots, 7\}$. The first two classes, A and AIII, are the "complex classes" and have periodicity 2. The remaining eight classes are the "real classes" and have periodicity 8. (Figure reproduced, with permission, from Ref. 50, i.e., Ching-Kai Chiu, Jeffrey C. Y. Teo, Andreas P. Schnyder, and Shinsei Ryu, *Reviews of Modern Physics*, 88:035005 (2016). Copyright 2016 by the American Physical Society.) 7

1.2 Determining δ_{CL}, the generic codimension of band touchings, in each of the AZ+$\mathcal{P}$ symmetry classes, listed in the first column. The second, third and fourth columns show minimal representations of the AZ+$\mathcal{P}$ symmetries. The fourth and fifth columns show the minimal basis (shown in bold) for an effective Hamiltonian locally describing adjacent bands. The last column shows the resulting band touchings in 3D. (Table reproduced, with permission, from Ref. 76, i.e., Tomáš Bzdušek and Manfred Sigrist, *Physical Review B*, 96:155105 (2017). Copyright 2017 by the American Physical Society.) . . . 12

1.3 Topological invariants protecting band touchings in the AZ+$\mathcal{P}$ classification. The behaviour of the AZ-like symmetries $\mathfrak{T}$, $\mathfrak{C}$ and $\mathcal{S}$ is shown; "CL" stands for "Cartan label". The topological classification applicable to a p-sphere is shown for each class, with the ones relevant to 3D in bold. (Table adapted, with permission, from Ref. 76, i.e., Tomáš Bzdušek and Manfred Sigrist, *Physical Review B*, 96:155105 (2017). Copyright 2017 by the American Physical Society.) 13

1.4 The 18 gyrotropic crystal classes, divided into chiral (11 crystal classes) and non-chiral (7 crystal classes) [150, 152]. 52

4.1 The effects of the symmetries h_{MI} and h_{EMI} on the band touchings in the easy-axis stacked honeycomb XXZ model, which has spin-rotation symmetry about the $\hat{z}$ axis. See Sec. 4.4.2.4 for details and Appendix 4.B for parameter values. 128

List of Figures

1.1 Schematic showing examples of gapless manifolds (shown in red) enclosed by p-spheres of appropriate dimensions. (a): An isolated gapless point in 3D *cannot* be adequately enclosed by a 1-sphere (i.e., a circle), since the circle can be smoothly deformed into a point without encountering the band touching. (a), (b), (c), (d), and (e): Gapless lines and surfaces that can be enclosed by one or multiple p-spheres. A 0-sphere is understood to be two points, as shown in (d). (Figure reproduced, with permission, from Ref. 76, i.e., Tomáš Bzdušek and Manfred Sigrist, *Physical Review B*, 96:155105 (2017). Copyright 2017 by the American Physical Society.) 10

1.2 (a): Crystal structure of graphene—the honeycomb is made up of two interpenetrating triangular lattices. The two crystallographically distinct (but chemically identical) sites are labelled "A" and "B" and are shown in green and orange. The NN and NNN bonds are shown in solid black and dashed red, respectively. (b) Band structure of graphene. The first Brillouin zone for the triangular lattice is shown as an inset. The p_z bands, which intersect the Fermi energy, are blue; the sp^2 bands are dotted and red. The Dirac crossings are located at the (inequivalent) K and K' points. (Figures reproduced from Ref. 90, i.e., Andrey K. Geim and Allan H. MacDonald, "Graphene: Exporing carbon flatland", *Physics Today*, 60(8):35 (2007), with the permission of AIP Publishing.) 17

1.3 ARPES data showing the band structure of graphene for energies near the Fermi energy. (a) Valence band dispersion along a selected path in the first Brillouin zone. The black curve shows the predicted band structure. Note that the Dirac energy E_{D} is just below the Fermi Energy E_{F}. (b) Close-up view of the Dirac point at the K point, showing the linear dispersion. The electron density of $1.1 \times 10^{13}\,\mathrm{cm}^{-2}$ is shown. (Reproduced with the permission of Springer Nature from Ref. 94, i.e., Aaron Bostwick et al., "Quasiparticle dynamics in graphene", *Nature Physics*, 3:36 (2007).) 20

1.4 Landau levels in graphene, as seen with STS at $T = 4.4\,\mathrm{K}$. (a) Differential conductance, proportional to the real-space spectral function $A(\omega, \mathbf{r})$, as a function of bias voltage for different magnetic field strengths. The zero-field trace shows the linear density of states characteristic of Dirac spectra. Peaks in the nonzero-field traces correspond to Landau levels, and the Landau-level indices are shown on the $B = 10\,\mathrm{T}$ trace. (b) The Landau-level energies are shown to be linear in $\mathrm{sgn}(n)\sqrt{|nB|}$, as expected from Eq. (1.56). (Figure reproduced from Ref. 98, i.e., Eva Y. Andrei, Guohong Li, and Xu Du, "Electronic properties of graphene: a perspective from scanning tunneling microscopy and magnetotransport", *Reports on Progress in Physics* 75(5):056501 (2012). © IOP Publishing. Reproduced with permission. All rights reserved. Permission conveyed through Copyright Clearance Center, Inc.) 29

1.5 Spin-resolved ARPES data showing helical Dirac surface states in Bi_2Te_3. (a): The linearly dispersing surface bands are seen within the bulk gap. Gold-colored shading shows the continuum of bulk bands. The red arrows indicate spin directions. (b): Data shows the Fermi surface, and red arrows depict spin-momentum locking. (c) and (d): Evidence for spin-momentum locking. Data is taken along the k_x direction in the surface momentum space, as shown in the inset of (c). The y spin polarization (c) is nonzero and changes at the Dirac point ($k_x =$), while the x and z spin polarizations (d) are scattered around zero. (Reproduced with the permission of Springer Nature from Ref. 100, i.e., D. Hsieh et al., "A tunable topological insulator in the spin helical Dirac transport regime", *Nature*, 460:1101 (2009).) 33

1.6 Schematic phase diagram of the hole-doped cuprates, as a function of hole doping p and temperature T. Near zero doping lies an antiferromagnetic correlated insulator phase (AF). At high doping, the material is an ordinary Fermi liquid (FL), with low-temperature resistivity proportional to T^2. At lower doping, the system is a "strange metal" non-Fermi liquid (SM), characterized by resistivity proportional to T. At intermediate dopings lies the superconducting dome, delimited by the superconducting critical temperature T_c. Purportedly, hidden within the dome is a quantum critical point, which occurs at doping p^*. The pseudogap (PG) regime is characterized by a partially developed superconducting gap; its onset is at T^*. There is also a charge-density wave (CDW) phase. (Used with the permission of Annual Reviews, Inc., from Ref. 112, i.e., Cyril Proust and Louis Taillefer, "The Remarkable Underlying Ground States of Cuprate Superconductors", *Annual Review of Condensed Matter Physics* 10:409 (2019); permission conveyed through Copyright Clearance Center, Inc.) 34

1.7 CuO_2 planes (separated by charge-reservoir spacer layers) in the cuprate family of materials. The Cu^{2+} ions are shown in pink and the O^{2-} ions are shown in light green. The wavefunctions of the highest occupied orbitals are shown in the bottom-left. (Reproduced with the permission of Springer Nature from Ref. 110, i.e., B. Keimer et al., "From quantum matter to high-temperature superconductivity in copper oxides", *Nature*, 518:179 (2015).) 35

1.8 (a): The sole band that crosses the Fermi energy in the cuprate family of materials, shown along high-symmetry paths in momentum space. (b): Schematic Fermi surface. Also shown is the momentum-space path travelled in (a). (Reproduced with the permission of Springer Nature from Ref. 86, i.e., Makoto Hashimoto et al., "Energy gaps in high-transition-temperature cuprate superconductors", *Nature Physics*, 10:483 (2014).) 36

1.9 Hopping process from $j\uparrow$ to $i\uparrow$, used to determine the factor g_t. (a) In the state $|\mathrm{BCS}\rangle$, there may or may not be down spins at sites i and j. (b) In the state $|\mathrm{GS}\rangle$, in which double occupancy is forbidden, there can be no down spins present at sites i and j. (Figure reproduced from Ref. 125, i.e., F. C. Zhang, C. Gros, T. M. Rice, and H. Shiba, "A renormalised Hamiltonian approach to a resonant valence bond wavefunction", *Superconductor Science and Technology* 1(1):36–46 (1988). © IOP Publishing. Reproduced with permission. All rights reserved. Permission conveyed through Copyright Clearance Center, Inc.) 38

1.10 Spin exchange process between i and j, used to determine the factor g_J. (Figure reproduced from Ref. 125, i.e., F. C. Zhang, C. Gros, T. M. Rice, and H. Shiba, "A renormalised Hamiltonian approach to a resonant valence bond wavefunction", *Superconductor Science and Technology* 1(1):36–46 (1988). © IOP Publishing. Reproduced with permission. All rights reserved. Permission conveyed through Copyright Clearance Center, Inc.) 38

1.11 ARPES data showing the Dirac-like dispersion of quasiparticle excitations in the superconducting phase of the cuprate $Bi_2Sr_2CaCu_2O_{8+\delta}$, with hole-doping $\delta = 0.14$ at $T = 10\,\mathrm{K}$. (a): Cutout at the node showing the anisotropic dispersion of excitations, with velocity v_F perpendicular to the Fermi surface and v_Δ parallel to the Fermi surface. The (holelike) Fermi surface is shown as a red dotted curve. (b): Data from panel (a) along cuts perpendicular and parallel to the Fermi surface, clearly showing the difference in the slopes v_F and v_Δ. (c): Magnitude of the gap $\Delta_\mathbf{k}$ along the Fermi surface, showing that it vanishes along the line $k_x = k_y$. (Figure reproduced, with permission, from Ref. 129, i.e., I. M. Vishik et al., *Physical Review Letters*, 104:207002 (2010). Copyright 2010 by the American Physical Society.) 41

1.12 Experimental discovery of Weyl semimetals in the 3D compound NbAs. (a) Predicted location of a subset of Weyl nodes in a fixed-k_z plane; Weyl nodes are labeled with "1", and trivial Fermi pockets are shown in red. (b) ARPES-measured Fermi surface in the same plane as in panel (a). "Cut 3" is taken along aline at which Weyl nodes are expected. (c) Band structure along Cut 3, showing a linear dispersion. (Reproduced with the permission of Springer Nature from Ref. 88, i.e., Su-Yang Xu et al., "Discovery of a Weyl fermion state with Fermi arcs in niobium arsenide", *Nature Physics*, 11:748 (2015).) 43

1.13 Effects of different types of stain on the reciprocal lattice vectors (black arrows) and first Brillouin zone (shaded areas) of the graphene sheet shown in Fig. 1.2a. Panel (a) shows the case of unstrained graphene, whereas panels (b), (c), and (d) show, respectively, uniaxial tensile strain in the x direction, uniaxial tensile strain in the y direction, and shear strain. Specific values are given in the main text. (Figure reproduced from Ref. 96, i.e., Gerardo G. Naumis, Salvador Barraza-Lopez, Maurice Oliva-Leyva, and Humberto Terrones, "Electronic and optical properties of strained graphene and other strained 2D materials: a review", *Reports on Progress in Physics* 80(9):096501 (2017). © IOP Publishing. Reproduced with permission. All rights reserved. Permission conveyed through Copyright Clearance Center, Inc.) 46

1.14 STS data revealing strain-induced Landau levels along a pronounced ridge in a graphene sample. (a): Intensity curves at 13 points along the ridge, offset for clarity. The peaks correspond to strain-induced Landau levels. (b): Energy of the peaks as a function of $\mathrm{sgn}(n)\sqrt{|n|}$, where in the Landau-level index. The linear behaviour agrees with the dependence given in Eq. (1.56), and the solid line is the best-fit line to experimental data. (c): Residuals from panel (b), calculated with respect to the best-fit theoretical prediction. (Figure reproduced, with permission, from Ref. 143, i.e., Hui Yan et al., *Physical Review B*, 85:035422 (2012). Copyright 2012 by the American Physical Society.) 51

1.15 Generation of a net magnetic moment under the effect of a current in a system with Bychkov–Rashba–type SOC ($H = (p_x^2 + p_y^2)/(2m) + r(p_x\sigma_y - p_y\sigma_x)$). For the sake of illustrative simplicity, the second, smaller Fermi surface, which produces an opposite but lesser contribution, is not shown. LEFT PANEL: In equilibrium, each spin dipole moment has an equal and opposite pair, yielding no net magnetization. RIGHT PANEL: The current-driving electric field modifies the electron distribution function, increasing the occupation at one end of the Fermi surface and decreasing it at the other, giving rise to a net magnetization. (Figure reproduced, with permission, from Ref. 156, i.e., Jairo Sinova et al., *Reviews of Modern Physics*, 87:1213 (2015). Copyright 2015 by the American Physical Society.) 54

1.16 Kerr-rotation microscopy data revealing the (spin) Edelstein effect in 2D electron gases confined to (110) AlGaAs quantum wells. The Kerr rotation angle—a proxy for the out-of-plane spin magnetization—is given by A_0 and the voltage is given by V_p. Data is shown for electric fields along crystal directions $[1\bar{1}1]$, $[1\bar{1}2]$ and $[1\bar{1}0]$ (all in plane). (Reproduced with the permission of Springer Nature from Ref. 158, i.e., Vanessa Sih et al., "Spatial imaging of the spin Hall effect and current-induced polarization in two-dimensional electron gases", *Nature Physics*, 1:31 (2005).) 55

1.17 In general, the motion of a wave packet (shown in position space with center of mass $\mathbf{r}_\mathrm{c}$) can have both a translational and a rotational part. The rotational part leads to nonzero $\mathbf{m}_{\mathbf{k}n}$. (Figure reproduced, with permission, from Ref. 166, i.e., Di Xiao, Yugui Yao, Zhong Fang, and Qian Niu, *Physical Review Letters*, 97:026603 (2006). Copyright 2006 by the American Physical Society.) 56

1.18 Crystal structure for the chiral tight-binding model used in Ref. 151 and described in the text. The winding, solenoid-like hopping paths give the crystal a handedness, which is a sufficient—but not necessary—criterion for the orbital Edelstein effect. (Figure reproduced, with permission, from Ref. 151, i.e., Taiki Yoda, Takehito Yokoyama, and Shuichi Murakami, *Nano Letters*, 18:916 (2018). Copyright 2018 American Chemical Society.) 57

1.19 Comparison of $\alpha_{zz}^{\mathrm{orb}}$ calculated numerically from the tight-binding model (colored lines) and calculated from the low-energy formula of Eq. (1.123) (black dashed lines), for various parameter values. In the small-ε_0 limit, the response depends only on $\varepsilon_0 = 3t_2 - 2t_3$ as required by Eq. (1.123), but beyond that, the behaviour deviates from the low-energy prediction. (Figure adapted, with permission, from Ref. 151, i.e., Taiki Yoda, Takehito Yokoyama, and Shuichi Murakami, *Nano Letters*, 18:916 (2018). Copyright 2018 American Chemical Society.) 59

2.1 (Color online) (a) Rotated Brillouin zone for the square lattice showing schematic Fermi surface (solid, black) for optimal hole-doped cuprate SCs. Quasiparticle Dirac nodes are located at $\pm\mathbf{K}_1$ and $\pm\mathbf{K}_2$, and we show local coordinate axes used in our low-energy theory. (b) Strip geometry (not to scale) used in the numerics with width W and length $L \gg W$. Shading gradient illustrates spatial variation in the pairing or hopping amplitude across the strip. 72

2.2 (Color online) (a) Spectrum of uniform d-wave SC on a $(1,1)$-edged strip versus momentum k_L along the L-direction, showing Dirac nodes and zero energy ABSs. Circles indicate regions shown in the next two panels. (b) Formation of flat pseudo-Landau levels near the outer Dirac nodes due to uniform hopping-amplitude gradient in the [1,1] direction; shown here is the near-node region indicated in (a). (c) Similar to (b) but with extended s-wave pairing gradient, which induces pseudo-LLs near the central Dirac node indicated in panel (a). 75

2.3 (Color online) Low energy TDOS versus energy Ω/Δ_d (scaled to the d-wave gap), from diagonalization of BdG Hamiltonian in the strip geometry, plotted across scaled strip width $0 < w/W < 1$. (a) Uniform d-wave SC, showing ABSs near zero energy localized near $w/W = 0, 1$, and QP bound state TDOS exhibiting rapid spatial oscillations. (b) Hopping gradient case showing extra pseudo-LL peaks. 76

2.4 (Color online) Trilayer heterostructure with cuprate SC thin film epitaxially sandwiched between two piezoelectric perovskite films along the (110) surface. An inhomogeneous strain can be induced in the cuprate layer by asymmetrically polarizing the two piezo layers. Metallic outer gates (yellow regions) are used to apply the piezo voltages, with the cuprate layer serving as the common inner gate. For typical values of piezo constant ($d_{31} \sim$ 50-275pm/V) and dielectric breakdown field ($\sim$ 25MV/m) for piezoelectric perovskites [225, 226] such as $Pb(Zr_xTi_{1-x})O_3$, we estimate that lattice strains $\sim$ 0.1-1% can be induced in the cuprate layer. 77

2.5 (Color online) (a) Spectrum of uniform d-wave SC on a $(1,0)$-edged strip versus momentum k_L along the L-direction showing Dirac nodes. Note that there are no zero energy ABSs in this geometry. Circle indicates region shown in the next two panels. (b) Formation of flat pseudo-Landau levels in the low-energy regime due to uniform hopping-amplitude gradient in the $[1,0]$ direction; shown here is the near-node region indicated in (a). (c) Similar to (b) but with extended s-wave pairing gradient. 87

3.1 (Color online) Tetragonal crystal structure showing identical atoms (large gray spheres) on the A and B sublattices, with a legend for hopping amplitudes and repulsion strengths. Primitive translations $\mathbf{a}$, $\mathbf{b}$, and $\mathbf{c}$ are defined in the main text. The volume shown corresponds to two unit cells as defined in Sec. 3.3, and the projection of the unit cell onto the x-y plane is shaded in blue. The secondary atoms (small dark-blue spheres) are *not* considered in the tight-binding model, as discussed in the main text. 92

3.2 (Color online) Location of the line nodes (solid lines, shown in color) present in the symmetric phase within the first Brillouin zone as defined in Sec. 3.3. High-symmetry points are labeled. 94

3.3 (Color online) CDW phases arising in the MF study as a function of the electronic filling ρ and g (which parametrizes the repulsion strength). Continuous and discontinuous transitions are respectively shown as thin and thick solid lines, while insulating lines, which occur at fillings 1/4, 1/2, and 3/4, are dashed. The nature of Phases I and II is described in the text. 96

3.4 (Color online) CDW phases arising in the MF study at half filling ($\rho = 0.5$) as a function of temperature and g (which parametrizes the repulsion strength). The transition into Phase I from the symmetric phase is continuous. The nature of Phase I is described in the text. 97

3.5 (Color online) Evolution of the magnetoelectric response through a phase transition with $g = 1.5t_1$ and $\rho = 0.5$. TOP PANEL Order parameter $\left(\rho^{\mathrm{a}}_{\mathbf{Q}_0}\right)$ as a function of temperature. BOTTOM PANEL Components of the OEE response tensor α^{orb} as a function of temperature. Components that are not shown are identically zero. 98

3.6 (Color online) Mean-field band structure at half filling (with parameters as specified in the main text) at three different temperatures: $k_{\mathrm{B}}T/t_1 = 2.00$ (top), 1.20 (middle), and 0.05 (bottom). The black dotted lines show the location of the chemical potential μ at each temperature, and the shaded areas centered at μ show the width $k_{\mathrm{B}}T$. 99

3.7 (Color online) Magnetic moment $m_{\mathbf{k}n,\kappa}$ and product $-m_{\mathbf{k}n,\kappa}v_{\mathbf{k}n,\kappa}$ for bands $n \in \{1, 2\}$ and components $\kappa \in \{a, b\}$ at $k_{\mathrm{B}}T = 1.20\,t_1$. (Note that $\mathbf{m}_{\mathbf{k}n}$ is the same for both bands.) For clarity, the first Brillouin zone is not drawn to scale. The largest contributions to these two quantities are attributable to the line nodes depicted in Fig. 3.2. The solid lines in middle and right panels depict $\varepsilon_{\mathbf{k}n} = \mu$ surfaces. The dashed lines show $\varepsilon_{\mathbf{k}n} = \mu \pm k_{\mathrm{B}}T$ surfaces, which delimit the region most heavily weighted in the integral of Eq. 3.13. The slices shown are $k_c = -\pi$, $-\pi/2$, 0, $\pi/2$, and π. 100

3.8 (Color online) For a current $\mathbf{j}$ oriented in the $\hat{\mathbf{b}}$ direction, solenoid-like paths due to the t_{2A} hoppings (green) and the t_{2B} hoppings (red) have opposite helicity. If $t_{2A} = t_{2B}$, the magnetizations from the two solenoids cancel. Crystal is not drawn to scale. 103
3.9 (Color online) For a current $\mathbf{j}$ oriented in the $\hat{\mathbf{b}}$ direction, solenoid-like paths with their axis along A atoms (solid lines) have opposite helicity to those with their axis along B atoms (dashed lines). If the atoms are indistinguishable, the magnetizations from the two solenoids cancel on average. Crystal is not drawn to scale. 103
3.10 (Color online) Phase diagram showing the lowest-energy charge ordered states resulting from a model of electrostatic charges subject to the interaction of Eq. 3.10; the colors correspond to the indicated charge ordering patterns. The white star shows the relative parameter values used in the MF calculation. . 105

4.1 Schematic depiction of the SW transformation for Krein-Hermitian matrices, shown in the eigenbasis of the unperturbed Hamiltonian K^0. The Krein-unitary transformation T block-diagonalizes the perturbed Hamiltonian with respect to the subspace $\mathcal{P}_0$, and the effective Hamiltonian in the subspace $\mathcal{P}_0$ is $P_0\tilde{K}P_0$. The signs above the columns of K^0 show the Krein signatures of its eigenvectors; in the case shown here, $m_+ = 2$ and $m_- = 1$. This implies that the eigenstates of $P_0\tilde{K}P_0$ will have the same signatures, as illustrated schematically by the signs above the columns of $\tilde{K}$. 116
4.2 (a) Schematic depiction of spins left invariant by a magnetic inversion symmetry $h_{\mathrm{MI}} = \{P|2\mathbf{x}_0\}T$ whose inversion center, shown in orange, is located at $\mathbf{x}_0$. (b) Spins left invariant by an effective magnetic inversion symmetry $h_{\mathrm{EMI}} = \{P; Q^{\mathrm{s}}|2\mathbf{x}_0\}T$ whose inversion center, shown in red, is located at $\mathbf{x}_0$. The spin rotation Q^{s}, which is only allowed if the spin Hamiltonian lacks certain SOCs, effectively "undoes" the effect of time reversal and returns the spins to their initial configuration, as detailed in Sec. 4.4.2.2. 122
4.3 Crystal structure of the magnetic Co^{2+} ions in $CoTiO_3$. Two layers are shown, both as a 3D illustration in panel (a) and as a projection along the stacking direction $\hat{z}$ in panel (b). The crystal's primitive lattice vectors $\mathbf{a}_1$, $\mathbf{a}_2$, and $\mathbf{a}_3$ are shown; the magnetic order (depicted in Fig. 4.4) doubles the third one to $2\mathbf{a}_3$. Sublattice indices 1, 2, 3, and 4 of the magnetic unit cell are shown in panel (a). 124
4.4 Magnetic orders in the stacked-honeycomb systems of Secs. 4.4.2.3 and 4.4.2.4. (a) When easy-plane interactions dominate, the order is in plane; the specific case of x-direction order, used in our numerical calculations, is shown. (b) When easy-axis interactions dominate, the order is parallel to the stacking direction $\hat{z}$. 126

4.5 Magnonic gap closings in a stacked honeycomb magnet modeled with an XXZ interaction together with a weak DM interaction, with parameter values given in Appendix 4.B. As argued in the text, the gap closings in the presence of magnetic inversion should generically be gapless lines, and indeed a plethora of gapless lines (shown in blue) are found. If magnetic inversion symmetry is broken (see main text and Appendix 4.B), the gap closings are Weyl points and are shown in red. Note that some of the gapless lines in (a) and (c) and all the lines in (b) reach the first-Brillouin-zone boundary and re-emerge at the opposite face. 127

List of Publications

[1] **Geremia Massarelli**, Gideon Wachtel, John Y. T. Wei, and Arun Paramekanti. "Pseudo-Landau levels of Bogoliubov quasiparticles in strained nodal superconductors". *Phys. Rev. B*, 96:224516 (2017).

[2] **Geremia Massarelli**, Bryce Wu, and Arun Paramekanti. "Orbital Edelstein effect from density-wave order". *Phys. Rev. B*, 100:075136 (2019).

[3] Arijit Haldar, **Geremia Massarelli**, and Arun Paramekanti. "Higher-order topology and corner triplon excitations in two-dimensional quantum spin-dimer models". *Phys. Rev. B*, 104:184403 (2021).

[4] **Geremia Massarelli**, Ilia Khait, and Arun Paramekanti. "Krein-unitary Schrieffer-Wolff transformation and band touchings in bosonic Bogoliubov–de Gennes and other Krein-Hermitian Hamiltonians". *Phys. Rev. B*, 106:144434 (2022).

Preface

The present thesis is written in the format referred to as a *publication-based thesis* (PBT) by the University of Toronto School of Graduate Studies, "a coherent work consisting of a number of scholarly publications focusing on the same research problem". It is based on three of the four published journal articles listed above, which constitute its middle chapters and are reproduced verbatim, except for certain changes made at the copyediting stage and to adapt them to the thesis's page layout. In each of these three journal articles, the thesis writer is the first author or coauthor and made a substantial contribution.

The article *Pseudo-Landau levels of Bogoliubov quasiparticles in strained nodal superconductors* [1], which constitutes Chapter 2, was authored by the thesis writer (some conceptualization, much of the calculations, some manuscript preparation), Gideon Wachtel (some conceptualization, some calculations), John Y. T. Wei (some conceptualization, some manuscript preparation), and Arun Paramekanti (much of the conceptualization, much of the calculations, much of the manuscript preparation).

The article *Orbital Edelstein effect from density-wave order* [2], which constitutes Chapter 3, was authored by the thesis writer (much of the conceptualization, much of the calculations, much of the manuscript preparation), Bryce Wu (some calculations), and Arun Paramekanti (guidance, much of the conceptualization, some manuscript preparation).

The article *Krein-unitary Schrieffer-Wolff transformation and band touchings in bosonic Bogoliubov-de Gennes and other Krein-Hermitian Hamiltonians* [4], which constitutes Chapter 4, was authored by the thesis writer (much of the conceptualization, much of the calculations, much of the manuscript preparation), Ilia Khait (much of the conceptualization, much of the calculations, much of the manuscript preparation), and Arun Paramekanti (guidance, some of the conceptualization, some of the manuscript preparation).

The introductory and concluding chapters are entirely the work of the thesis writer. None of these projects appear or will appear in another graduate thesis or dissertation, as the thesis writer was the only graduate student in each of the collaborations: Arun Paramekanti is the thesis writer's supervisor; John Y. T. Wei is a faculty member; Gideon Wachtel, Arijit Haldar, and Ilia Khait were postdoctoral fellows; and Bryce Wu was an undergraduate research assistant.

This document strives to be consistent in its use of Gaussian electromagnetic units, except in Sec. 1.6 and Chapter 3, which use SI units for consistency with references.

Chapter 1

Introduction

Dirac-like systems, whose quasiparticles are governed by effectively massless and relativistic wave equations or field theories and obey linear dispersion relations ($E \propto |\mathbf{p}|$), permeate much of modern condensed-matter physics [5–7]. Materials whose low-energy fermionic excitations are dictated by Dirac-like Hamiltonians include superfluid phases of ^{3}He, graphene, surface states of topological insulators, nodal superconductors (like the cuprate high-temperature superconductors), and Weyl semimetals. In regards to fermionic systems, the designation of "Dirac-like" is typically used in specific reference to the low-energy excitations. Hence, such systems share several characteristics of Dirac physics in their low-energy regimes, even though the underlying microscopic physics leading to Dirac-like behaviour is different in each of the examples given above. In bosonic systems, the low-energy, long-wavelength physics—i.e., the Goldstone mode—is often Dirac like [8]; in recent years, however, Dirac-like character of bands at higher energies in boson systems has attracted significant interest [9], though it does not influence systems' low-energy properties and can sometimes be challenging to detect.

Arguably, the interest in Dirac-like physics within condensed-matter systems is, to some extent, attributable to the window into high-energy physics it can provide. In some cases, a condensed-matter system can serve as a tabletop implementation, whose high-energy counterpart would be much harder to achieve [10]. In other cases, condensed-matter systems provide the only known implementation of certain high-energy phenomena: for a long time, neutrinos were believed to be Weyl fermions, but the discovery of nonzero neutrino mass precluded that possibility, leaving condensed-matter systems as the only known embodiment of Weyl physics [11]. In yet other instances, Dirac-like condensed-matter systems may even provide fundamental insights into the standard model of particle physics, gravity, and the quantum vacuum [10, 12, 13].

However, the recent surge in interest for Dirac-like physics stems primarily from the onset of the topological age in condensed-matter physics, during which topology, global and robust properties of quantum systems encoded in their wave functions and described by discrete topological numbers, emerged as another fundamental organizing principle of

matter, alongside and in conjunction with symmetry [14–16]. A pillar of the topological understanding of condensed-matter systems has been the study of symmetry-protected topological (SPT) phases in solid-state systems. Early on, the focus was on topological invariants that distinguish gapped states of fermionic matter, first with the Chern number that characterizes Chern insulators [17–20], and then with the $\mathbb{Z}_2$ Fu-Kane-Mele invariant [21] that characterises time-reversal-invariant topological insulators [22–24]. Later, though, similar concepts of topological protection and topological invariants were found to apply to gapless states of matter: the stability, robustness or protection of massless Dirac-like spectra were understood as a consequence of a topological charge they carry. Moreover, it was also found that many topological gapless materials, like their gapped cousins, obey some sort of bulk-boundary correspondence [15], a cornerstone feature of topological states of matter.

Evidently, Dirac matter is a ubiquitous theme in present-day condensed-matter physics [5–7], and its study offers a cross section of some of the most dynamic topics in the field. Better understanding its properties and characteristics is a pertinent endeavor that can provide fresh insight on these topics.

1.1 Background and historical perspective

Interest in Dirac-like physics within condensed-matter systems can be traced back to the study of degeneracies in early solid-state physics. The present section provides some physical background while retracing, with no pretensions of historical rigor, some relevant developments and notable physicists of the past century.

Naturally, interest in energy level degeneracy arose concomitantly with quantum mechanics itself [25–30]: degeneracies are often robust qualitative features of a Hamiltonian that can offer significant insight and do not depend on the system's quantitative details. The mechanics of group representation theory was applied to quantum systems to understand how the symmetry group of a Hamiltonian affects and determines the energy level degeneracy [26, 27]. Broadly, degeneracies can be classified as either *essential* or *accidental*. Essential degeneracies stem from higher-dimensional irreducible representations (irreps) of the Hamiltonian's symmetry group[1], as the states in the corresponding irreducible subspace are necessarily degenerate [31, Sec. 25]. Accidental degeneracies[2] are those not enforced by symmetries of the Hamiltonian, and occur between states from different (either equivalent or inequivalent) irreps [31, Sec. 25]. The occurence of accidental degeneracies was studied as

[1]Time-reversal symmetry can sometimes enforce additional degeneracy *between* representations; such additional degeneracies can also be considered "essential" [31].

[2]This definition of "accidental degeneracy" appears to be most common in the literature [30–35]. In this sense, an accidental degeneracy may or may not be robust to small perturbations, and in a band structure, an accidental degeneracy may occur within or away from a high-symmetry region of the first Brillouin zone [31, Sec. 25]. Unfortunately, at least one other usage for the phrase "accidental degeneracy" appears in the literature; namely, it sometimes refers to a degeneracy that can be gapped out by small perturbations that preserve the symmetry of the Hamiltonian [36] and can only ever be approached by fine-tuning of parameters. These are what Herring referred to as "vanishingly improbable" degeneracies [32].

early as 1929 by John von Neumann and Eugene Wigner [25, 35, 37]. To understand the stability of gapless points (or, more generally, gapless regions) in a parameter space, they compared the space of Hamiltonians without degeneracies to the space of Hamiltonians with a degeneracy; the difference in dimensionality between these spaces gives the generic codimension of the degenerate regions in the Hamiltonian's parameter space. In other words, they established the dimensionality of parameter space that must be explored in order to overcome "level repulsion", the propensity of eigenvalues to avoid crossing when not required by symmetry [33].

Before reviewing their argument, we dwell on accidental degeneracies, of which there are two types. Given a Hamiltonian H with a unitary symmetry U, i.e., $U^\dagger H U = H$, the Hamiltonian can be block-diagonalized into blocks corresponding to the different eigenvalues of U, and the resulting blocks are no longer constrained by U [16]. If *all* the Hamiltonian's unitary symmetries are used to "maximally" block-diagonalize H, then the resulting blocks are "symmetryless", meaning they are not constrained by any unitary symmetries and have little structure[3]. As it turns out, each block corresponds to a distinct (i.e., inequivalent) irrep present in the state space [16]. Schematically, letting $\{\lambda_1, \ldots, \lambda_m\}$ represent the inequivalent irreps, with respective dimensions $\{d_1, \ldots, d_m\}$, the result of the decomposition is

$$H = \left[\begin{array}{c|c|c} H^{(\lambda_1)} \otimes \mathbb{1}_{d_1} & & \\ \hline & \ddots & \\ \hline & & H^{(\lambda_m)} \otimes \mathbb{1}_{d_m} \end{array}\right]; \tag{1.1}$$

here, the matrices $\{H^{(\lambda_1)}, \ldots H^{(\lambda_m)}\}$ are the resulting symmetryless blocks, whose sizes are given by the multiplicity of the corresponding irreps within the state space. (The essential degeneracies are reflected in the tensor products with $\mathbb{1}_d$, which cause the eigenvalues in a given block to be repeated d times, where d is the dimension of the corresponding irrep.) Accidental degeneracies can either arise (i) from states belonging to different blocks, in which case they are part of inequivalent representations, or (ii) from states belonging to the same block, in which case they are part of equivalent representations [16, 32]. Whereas those of type (ii) are subject to level repulsion, those of type (i) are not, and can generically be encountered by varying a single parameter of the Hamiltonian [29, 32].

We now briefly lay out the argument of von Neumann and Wigner, which concerns accidental degeneracies of type (ii), following Ref. 37. Consider a parameter-dependent symmetryless $N \times N$ Hermitian Hamiltonian $H(\vec{w})$, where $\vec{w}$ is the set of (real-valued) parameters. Since $H(\vec{w})$ has no unitary symmetries, it has generic dependence on $\vec{w}$. Suppose $H(\vec{w})$ has f distinct eigenvalues $\varepsilon_1(\vec{w})$, ..., $\varepsilon_f(\vec{w})$, whose respective degeneracies are n_1, ..., n_f. Using eigendecomposition, we can count the degrees of freedom of $H(\vec{w})$

[3]The method for decomposing H into symmetryless blocks is formalized in Ref. 16; in essence, it involves an application of Schur's lemma [31, Appendix D] to H. See also Ref. 32 and Ref. 31, Sec. 25.

subject to this constraint on its eigenvalues: a priori, the N eigenvectors contribute N^2 degrees of freedom, since they make up a $\mathrm{U}(N)$ matrix, and $\dim \mathrm{U}(N) = N^2$; however, the basis of each eigenspace $\varepsilon_\alpha(\vec{w})$ is only unique up to a unitary transformation $\mathrm{U}(n_\alpha)$, so we subtract $\sum_{\alpha=1}^{f} {n_\alpha}^2$. Finally, the f real eigenvalues also add to the degrees of freedom. Hence, the dimensionality of the space of Hamiltonians yielding the specified degeneracy is

$$d = N^2 + f - \sum_{\alpha=1}^{f} {n_\alpha}^2. \tag{1.2}$$

In particular, in the nondegenerate case, $f = N$ and $n_\alpha = 1$ for all α, so

$$d_{\text{nondegen.}} = N^2. \tag{1.3}$$

On the other hand, with a single double degeneracy, $f = N - 1$ and

$$\begin{aligned} d_{\text{2-degen.}} &= N^2 + (N-1) - \left(2^2 + (N-2)\right) \\ &= N^2 - 3. \end{aligned} \tag{1.4}$$

Since $\delta_{\text{2-degen.}} := d_{\text{nondegen.}} - d_{\text{2-degen.}} = 3$ parameters must (generically) be varied in order to encounter such a degeneracy, $\delta_{\text{2-degen.}}$ gives the (generic) codimension in parameter space of the region with those degeneracies. This implies, for instance, that regions in parameter space with a twofold degeneracy are curves in a 4D parameter space, are isolated points in a 3D parameter space, and do not occur in 2D or 1D parameter spaces. Other accidental degeneracies are vanishingly improbable [32], and are gapped out by arbitrarily small perturbations. The present analysis can also be carried out for a real symmetric (rather than complex Hermitian) Hamiltonian $H(\vec{w})$, in which case one finds $\delta_{\text{2-degen.}} = 2$ [37]. In contrast, accidental degeneracies of type (i) generically have codimension 1 under all circumstances [29, 32].

In the following years, the theory of electronic band structures, and particularly its study in terms of space groups and their irreducible representations [28, 38, 39], was developed [30], exploiting representation theory to give symmetry-based explanations for essential degeneracies, which can occur in high-symmetry regions of momentum space. Notably, linear dispersions often arise in the neighborhood of such degeneracies [31, 40]—a tight-binding model with symmetry-enforced band touchings along high-symmetry lines in momentum space, and with linear dispersion in directions orthogonal to those lines, is studied in detail in Chapter 3.

The occurence of accidental degeneracies in band structures of three-dimensional crystals was investigated soon after, by the physicist Conyers Herring [32, 35, 41, 42]. Many decades before they would become a focal point for condensed-matter physicists, he predicted that they should be common [30] and stable against symmetry-preserving perturbations, and classified them according to whether they occur between inequivalent irreducible subspaces

(type (i), above) or between equivalent irreducible subspaces (type (ii), above) [31, 32]. Accidental degeneracies of type (i) can occur only in high-symmetry regions of the first Brillouin zone, since away from high-symmetry regions, there is but one type of irreducible representation [31, 32][4]. Away from high-symmetry regions of momentum space, accidental degeneracies of type (ii) can occur, and, indeed, these are the only possible degeneracies there. Their particular form depends on certain symmetries and on the presence (or absence) of spin-orbit coupling. In systems lacking space-time inversion symmetry, he found that isolated twofold-degenerate band touchings are stable, and that the dispersion in their neighborhoods are generally linear, effectively predicting Weyl points [29, 32, 41, 43]. In systems with space-time inversion symmetry and in which spin-orbit coupling is negligible, he found that twofold-degenerate curves are expected to be stable, with linear dispersion perpendicular to the curves, effectively predicting nodal-line semimetals [30, 35, 44].

Alternately, the results on accidental degeneracies of type (ii) in band structures can be arrived at using the arguments of von Neumann and Wigner, letting the Bloch Hamiltonian $H(\mathbf{k})$ play the role of the (symmetryless) Hamiltonian parametrized by the crystal momentum $\mathbf{k}$. In the absence of space-time inversion symmetry and away from high-symmetry momenta, $H(\mathbf{k})$ is a generic complex Hermitian matrix with $\delta_{\text{2-degen.}} = 3$, implying that in 3D, twofold degenerate isolated points can occur and are stable against small perturbations. On the other hand, if space-time inversion symmetry is present and spin-orbit coupling is negligible, then $H(\mathbf{k})$ is purely real[5] and $\delta_{\text{2-degen.}} = 2$; in this case, twofold-degenerate curves are generically stable in 3D. These are the same results arrived at by other means by Herring.

After three quarters of a century, this pioneering work would return to the forefront of condensed-matter physics with the realization that the stability or robustness of many essential and accidental degeneracies could be understood as a result of topological "charges" they carry.

We note that the themes in this section, like the decomposition into symmetryless blocks, the types of accidental degeneracies that may occur, and the codimension of generic band touchings, are explored in the context of bosonic Bogoliubov–de Gennes Hamiltonians in Chapter 4. As detailed there, some care must be taken in adapting the arguments, as the single-particle Hamiltonian in such problems is non-Hermitian, and is diagonalized via a non-unitary transformation.

[4]Note that this restriction can be relaxed in other systems. For example, in magnon models—which admit richer symmetries, as discussed in Sec. 4.4 and Appendix 4.C—accidental degeneracies of type (i) do occur away from high-symmetry regions. Such a model is discussed in Sec. 4.4.2.4, and the band touchings are explained in Table 4.1 and the surrounding text.

[5]If spin-orbit coupling is absent and spin plays no role in the dynamics, the electrons can be considered spinless, and it is known from basic quantum mechanics that, for integer-spin particles, time reversal is represented by complex conjugation in the appropriate basis [45, Sec. 4.4]. The same goes for the composite operation of space-time inversion acting on the Bloch Hamiltonian.

1.2 Dirac-like systems and topology

In this section, we explain the topological nature of the linear, or Dirac-like, band touchings described so far, and touch upon some of the properties that stem from it. We first review the tenfold classification of symmetry-protected topological (SPT) phases of *gapped* matter, and introduce the three basic symmetries that play a central role in that classification scheme and in numerous others. From there, it becomes natural to consider SPT phases of *gapless* matter, the description of which involves many of the same notions and concepts.

1.2.1 Topology and classification of gapped states of noninteracting matter

After the discovery of Chern insulators, characterized by a nontrivial Chern number (also known as the Thouless–Kohmoto–Nightingale–den Nijs invariant), and of 2D and 3D time-reversal invariant topological insulators, characterized by the Fu-Kane-Mele invariant, research efforts led to a full topological classification of gapped states of noninteracting fermionic matter—like insulators and gapped superconductors—based on symmetry [46–49]. In this context, a gapped state of fermionic matter, meaning one that is the ground state of a Hamiltonian with a bulk energy gap, is said to be topologically nontrivial if its wave function is topologically distinct from that of a trivial state of matter, like an atomic insulator (a collection of independent atoms). More specifically, two gapped-state wave functions are topologically equivalent if they can be continuously deformed into each other without closing the bulk energy gap [16, 50].

We mention that the states in this classification, called SPT states, are but one type of topological phase, part of a broader understanding of the phases of matter in terms of symmetry, topology and entanglement [14, 16, 51].

Given a many-body Hamiltonian

$$\hat{H} = \sum_{\nu,\nu'} c_\nu^\dagger H_{\nu\nu'} c_{\nu'}, \tag{1.5}$$

the *single-particle Hamiltonian* H, a matrix with elements $H_{\nu\nu'}$, is first block-diagonalized into symmetryless blocks $H^{(\lambda)}$, as described in Sec. 1.1; this way, the resulting blocks are not constrained by any *unitary* symmetries and are very generic. Once this is done, there are exactly three remaining symmetry constraints that can be placed on a symmetryless block H (where we have dropped the superscript for simplicity): they are time-reversal symmetry $\mathcal{T}$, particle-hole symmetry $\mathcal{C}$, and the product of these two, called chiral symmetry ($\mathcal{S}$). None of these three constraints can be treated together with the unitary symmetries, either because their action on the single-particle Hamiltonian H is antiunitary ($\mathcal{T}$ and $\mathcal{C}$), or because they

				d							
Class	$\mathcal{T}$	$\mathcal{C}$	$\mathcal{S}$	0	1	2	3	4	5	6	7
A	0	0	0	$\mathbb{Z}$	0	$\mathbb{Z}$	0	$\mathbb{Z}$	0	$\mathbb{Z}$	0
AIII	0	0	1	0	$\mathbb{Z}$	0	$\mathbb{Z}$	0	$\mathbb{Z}$	0	$\mathbb{Z}$
AI	$+$	0	0	$\mathbb{Z}$	0	0	0	$2\mathbb{Z}$	0	$\mathbb{Z}_2$	$\mathbb{Z}_2$
BDI	$+$	$+$	1	$\mathbb{Z}_2$	$\mathbb{Z}$	0	0	0	$2\mathbb{Z}$	0	$\mathbb{Z}_2$
D	0	$+$	0	$\mathbb{Z}_2$	$\mathbb{Z}_2$	$\mathbb{Z}$	0	0	0	$2\mathbb{Z}$	0
DIII	$-$	$+$	1	0	$\mathbb{Z}_2$	$\mathbb{Z}_2$	$\mathbb{Z}$	0	0	0	$2\mathbb{Z}$
AII	$-$	0	0	$2\mathbb{Z}$	0	$\mathbb{Z}_2$	$\mathbb{Z}_2$	$\mathbb{Z}$	0	0	0
CII	$-$	$-$	1	0	$2\mathbb{Z}$	0	$\mathbb{Z}_2$	$\mathbb{Z}_2$	$\mathbb{Z}$	0	0
C	0	$-$	0	0	0	$2\mathbb{Z}$	0	$\mathbb{Z}_2$	$\mathbb{Z}_2$	$\mathbb{Z}$	0
CI	$+$	$-$	1	0	0	0	$2\mathbb{Z}$	0	$\mathbb{Z}_2$	$\mathbb{Z}_2$	$\mathbb{Z}$

Table 1.1: Periodic table of topological insulators and superconductors in the ten AZ classes. The columns $\mathcal{T}$, $\mathcal{C}$, and $\mathcal{S}$ show which of the three basic symmetries are present in each class and, in the case of $\mathcal{T}$ and $\mathcal{C}$, whether they square to $+1$ or -1. The entries show the type of topological invariant (if any) in dimensions $d \in \{0, \ldots, 7\}$. The first two classes, A and AIII, are the "complex classes" and have periodicity 2. The remaining eight classes are the "real classes" and have periodicity 8. (Figure reproduced, with permission, from Ref. 50, i.e., Ching-Kai Chiu, Jeffrey C. Y. Teo, Andreas P. Schnyder, and Shinsei Ryu, *Reviews of Modern Physics*, 88:035005 (2016). Copyright 2016 by the American Physical Society.)

anticommute with H rather than commuting with it ($\mathcal{C}$ and $\mathcal{S}$):

$$\mathcal{T}^{-1} H \mathcal{T} = +H, \tag{1.6a}$$

$$\mathcal{C}^{-1} H \mathcal{C} = -H, \tag{1.6b}$$

$$\mathcal{S}^{-1} H \mathcal{S} = -H. \tag{1.6c}$$

It is on these basic, general constraints, which tend to be robust because of their nonspatial nature, that this topological classification is based, and the resulting topological phases do not require any unitary symmetries to protect them. [16, 50].

The different possible combinations of the symmetries $\mathcal{T}$, $\mathcal{C}$ and $\mathcal{S}$, listed in Table 1.1, give rise to the 10 Altland-Zirnbauer classes[6], hence the name "tenfold way" designating the classification. Each of $\mathcal{T}$ and $\mathcal{C}$ may or may not be a symmetry (the latter denoted by "0" in Table 1.1); if either one is a symmetry, it can either square to $+1$ or -1, as shown in Table 1.1. As for $\mathcal{S}$, its presence as a symmetry is determined by that of $\mathcal{T}$ and $\mathcal{C}$ (present if $\mathcal{T}$ and $\mathcal{C}$ are present, absent if precisely one of $\mathcal{T}$ and $\mathcal{C}$ are absent), except if both $\mathcal{T}$ and $\mathcal{C}$ are absent [16, 50].

Of course, for fermions, i.e., half-integer-spin particles, time reversal necessarily squares to -1 [45]. However, there are situations in which an effective time-reversal symmetry, which is distinct from physical time reversal but otherwise has the same mathematical form [16],

[6]The Altland-Zirnbauer classes of generic Hamiltonians arose years before this work on SPT phases, in the context of random matrix theory [16, 50].

can be defined, and such an operator may square to $+1$. Such a scenario arises, for instance, in an electron system with spin-rotation symmetry.

The entries in the table show the type of topological index, if any, that distinguishes different topological phases in systems of a certain symmetry class and dimensionality; this result can be obtained using the apparatus of homotopy groups, among other methods [16]. Homotopy groups formalize the intuitive notion of whether objects can (or cannot) be smoothly deformed into each other, and can be used to obtain the families of topologically distinct gapped states subject to the appropriate symmetry constraints. Take, for example, systems in symmetry class A—with none of the three basic symmetries—and with $d = 2$, which are characterized by an integer topological invariant: this is the Chern number, which can be nonzero in systems with broken time-reversal symmetry, like the integer quantum Hall state and the Haldane model [18]. Furthermore, the $\mathbb{Z}_2$ time-reversal invariant topological insulators in 2D and 3D, characterized by the Fu-Kane-Mele invariant, appear in symmetry class AII, in which $\mathcal{T}$ squares to -1. This reflects the importance of strong spin-orbit couplings in these systems, for if spin-orbit coupling were negligible, the electrons would have approximate spin-rotation symmetry, meaning an effective time reversal symmetry with $\mathcal{T}^2 = +1$ could be defined. We emphasize that while two states of a given symmetry class with different topological invariants cannot be deformed into each other without a bulk-gap closing, they *can* be connected *by symmetry-breaking perturbations*, i.e., via a path in parameter space that is permitted to exit the symmetry class; this, of course, is no surprise, since the topology is different from one symmetry class to another.

Although unitary symmetries are not needed to protect the topological phases of Table 1.1, their presence can give rise to additional topological phases not captured in the tenfold way. Examples include "weak topological insulators", which, unlike the "strong" topological insulators discussed thus far, rely on translational symmetry to protect the topology [16, 50], as well as new topological phases that are protected by point-group symmetries [50], like mirror symmetries or rotation symmetries [52–54]. Systems whose topology is protected by unitary symmetries of the crystal space group are called *topological crystalline insulators*, and their classification is starkly more involved than that of Table 1.1 [55–57].

An important feature of gapped SPT phases is the presence of gapless boundary modes; hence the careful reference to the "*bulk* gap" of the insulating states made so far. The boundary modes can be understood physically: the same way the gap must close between topological and trivial phases of a parameter space, a gap closing must occur in position space between the topological insulator and the (trivial) vaccum, giving rise to gapless boundary states protected by the bulk topology. Indeed, these gapless surface states can be taken as an alternate definition of SPT phases, and can be used as an equivalent means of deriving the above classification—this principle is known as the *bulk-boundary correspondence* [16]. The gapless surface states of 3D time-reversal invariant topological insulators are discussed in Sec. 1.4.2.

Finally, we mention that in quadratic many-boson systems, the classification in terms of internal symmetries simplifies considerably: for such systems, the particle-hole and chiral symmetries do not exist at the many-body level, and the tenfold way reduces to a threefold way [58]. In addition, although the notion of a "gapped state" as one with an energy gap between valence and conduction bands does not carry over for a boson system, the central idea of topologically equivalent systems being deformable into each other without closing a bulk gap continues to hold; furthermore, the topology manifests itself with the presence of protected in-gap boundary states.

1.2.2 Topology and gapless states of noninteracting matter

As we have seen, the occurence of various types of band touchings in solid-state systems and their stability against perturbation was recognized from the early days of quantum theory. However, the understanding that this robustness stems from topological charges carried by the band touchings [15, 59], and the properties stemming therefrom, like exotic surface states [50] and narrow constraints on annihilation of band touchings [60], had not been appreciated until fairly recently[7].

In their study of the topological protection of Fermi surfaces, Volovik [12, 61] and Hořava [62] seemingly first identified that isolated-point band touchings like those identified long ago by Herring—which we now call Weyl points—are stable because of the topological charge they carry, and can annihilate if two oppositely-charged ones meet [15, 50, 63, 64]. In addition, Hořava's results showed that the typical Dirac-like theory that describes the neighborhoods of these band touchings emerges naturally from the machinery of K theory. Soon after, topological semimetals and nodal superconductors, which harbor topologically protected band touchings and, in some cases, topological boundary states, came under intense study [50]. These include Weyl semimetals, with their exotic Fermi arc surface states [41, 65–71]; Dirac semimetals, which occur at high-symmetry momenta, require crystal symmetries and can have Fermi-arc surface states [72–75]; and nodal-line semimetals[8], which in some instances are accompanied with topological surface states [15, 60].

Many of the same concepts from Sec. 1.2.1 carry over to gapless band structures. Whereas in the gapped case, topological tools are used to characterize global characteristics of the wave function over the entire Brillouin zone, in the gapless case, they are applied to a p-sphere S^p that encloses the manifold on which the valence and conduction bands touch (see the examples in Fig. 1.1), capturing the global characteristics of the wave function on S^p. Everywhere on S^p, there is a gap between occupied and unoccupied states, and if

[7] Although it is the band touchings that topologically protected, it is common to read about "topologically protected Fermi surfaces"; while the location of the Fermi surface influences a system's properties, the topological protection does not require the Fermi energy to intersect the band touching, either in whole or in part [50].

[8] Unfortunately, the oxymoronic phrase "nodal line" has become standard in the community to refer to gapless lines in a band structure.

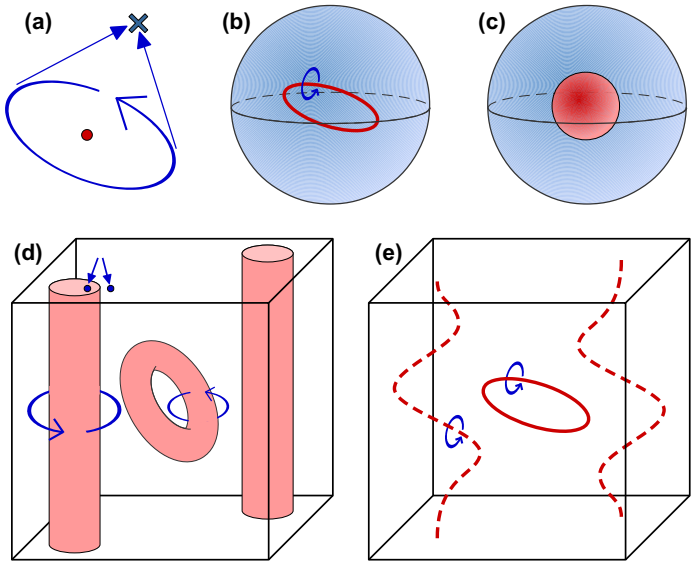

Figure 1.1: Schematic showing examples of gapless manifolds (shown in red) enclosed by p-spheres of appropriate dimensions. (a): An isolated gapless point in 3D *cannot* be adequately enclosed by a 1-sphere (i.e., a circle), since the circle can be smoothly deformed into a point without encountering the band touching. (a), (b), (c), (d), and (e): Gapless lines and surfaces that can be enclosed by one or multiple p-spheres. A 0-sphere is understood to be two points, as shown in (d). (Figure reproduced, with permission, from Ref. 76, i.e., Tomáš Bzdušek and Manfred Sigrist, *Physical Review B*, 96:155105 (2017). Copyright 2017 by the American Physical Society.)

there turns out to be a nontrivial topological invariant calculated on S^p, then there is a topological obstruction to shrinking S^p to a single point without encountering a gap closing; this signals that a gapless manifold is enclosed in S^p. If two gap closings are each individually characterized by a nontrivial invariant, but a sphere S^p enclosing both is not, this signals that the two can annihilate and gap out if they come together [50, 76].

Several classification schemes for topological gapless systems mirror those of gapped ones, with some based only on the AZ symmetries $\mathcal{T}$, $\mathcal{C}$ and $\mathcal{S}$, and others requiring additional unitary symmetries for protection [50]. Band touchings protected solely by the AZ symmetries can be characterized by, among others, winding numbers and Chern numbers, and their classification gives rise to a table in close analogy with Table 1.1 [50, Sec. V A]. The set of possibilities is enriched when considering topological gapless phases protected by (unitary) spatial symmetries like mirrors and rotations [50, Sec. V B and V C], with a richness that reflects the great multitude of space groups that exist in nature [55–57]. In those situations, the protected band touchings typically occur in specific high-symmetry regions of the Brillouin zone, and are often essential degeneracies or accidental degeneracies of type (i). Counterintuitively, in some cases, the *absence* of certain symmetries make band touchings topological: the Kramers-theorem–enforced twofold band touchings that occur at time-reversal–invariant momenta are Weyl nodes provided there is no Weyl-node-charge–switching symmetry, like inversion or a reflection, that maps the point to itself [77, Sec. SI G].

We note that topological phases of gapless matter can also be protected by non-symmorphic space-group symmetries [40, 78–82]. Band touchings protected by such symmetries, at times in combination with time reversal, have special status [31, 40, 78, 83]: they are sometimes referred to as symmetry *enforced* [40], because their occurence is model independent. This characteristic of theirs is, of course, at variance with accidental degeneracies, but also with symmorphic-symmetry-protected essential degeneracies, which depend on the choice of states included in the state space of a given model. Non-symmorphic symmetries are those symmetries of a space group that cannot be expressed as a point group operation composed with a primitive translation, no matter the choice of origin; rather, they are expressed as a point group operation composed with a fractional, sub-primitive translation [31, 83]. A nodal-line semimetal state in which the gapless lines are enforced by non-symmorphic space-group symmetries is discussed in detail in Chapter 3.

A pleasingly simple classification [76] of topological band touchings applies to general momenta, i.e., momenta away from high-symmetry points, where all states are from the same irrep. It is based on a set of modified AZ symmetries that constrain the Bloch Hamiltonian locally in momentum space, and, in a way, it completes the work of Herring by further categorizing type-(ii) accidental degeneracies. The modified AZ symmetries give rise to 10 AZ-like symmetry classes, and for each one, the topological invariants that can potentially protect band touchings are identified. We dwell on this result a bit.

In the Bloch basis, the three basic AZ symmetries constrain the Bloch Hamiltonian as follows:

$$\mathcal{T}^{-1} H_{\mathbf{k}} \mathcal{T} = +H_{-\mathbf{k}}, \tag{1.7a}$$

$$\mathcal{C}^{-1} H_{\mathbf{k}} \mathcal{C} = -H_{-\mathbf{k}}, \tag{1.7b}$$

$$\mathcal{S}^{-1} H_{\mathbf{k}} \mathcal{S} = -H_{\mathbf{k}}. \tag{1.7c}$$

Notably, $\mathcal{T}$ and $\mathcal{C}$ relate the Hamiltonian at different momenta, and do not place any local constraints on $H_{\mathbf{k}}$ (except at the discrete time-reversal-invariant momenta). It is clear that *local* constraints on $H_{\mathbf{k}}$ lead most straightforwardly to band touchings and accidental degeneracies of type (ii). Drawing inspiration from the importance of space-time inversion symmetry in Herring's results, one can foresee that the modified operators

$$\mathfrak{T} := \mathcal{T}\mathcal{P}, \tag{1.8a}$$

$$\mathfrak{C} := \mathcal{C}\mathcal{P}, \tag{1.8b}$$

where $\mathcal{P}$ is spatial inversion symmetry, *do* place local constraints on $H_{\mathbf{k}}$, since inversion

CL	$\mathfrak{T}$	$\mathfrak{C}$	$\mathcal{S}$	basis of $\mathcal{H}_{2\times 2}$	basis of $\mathcal{H}_{4\times 4}$	δ_{CL}	nodes in $D=3$
A	$\times$	$\times$	$\times$	$\boldsymbol{\{\mathbb{1},\sigma_x,\sigma_y,\sigma_z\}}$	$\{\mathbb{1},\sigma_x,\sigma_y,\sigma_z\}\otimes\{\mathbb{1},\tau_x,\tau_y,\tau_z\}$	3	point
AIII	$\times$	$\times$	σ_z	$\boldsymbol{\{\sigma_x,\sigma_y\}}$	$\{\sigma_x,\sigma_y\}\otimes\{\mathbb{1},\tau_x,\tau_y,\tau_z\}$	2	line
AI	$\mathcal{K}$	$\times$	$\times$	$\boldsymbol{\{\mathbb{1},\sigma_x,\sigma_z\}}$	$\{\mathbb{1},\sigma_x,\sigma_z\}\otimes\{\mathbb{1},\tau_x,\tau_z\}\cup\{\sigma_y\otimes\tau_y\}$	2	line
BDI	$\mathcal{K}$	$\sigma_z\mathcal{K}$	σ_z	$\boldsymbol{\{\sigma_x\}}$	$\sigma_x\otimes\{\mathbb{1},\tau_x,\tau_z\}\cup\{\sigma_y\otimes\tau_y\}$	1	surface
D	$\times$	$\mathcal{K}$	$\times$	$\boldsymbol{\{\sigma_y\}}$	$\sigma_y\otimes\{\mathbb{1},\tau_x,\tau_z\}\cup\{\mathbb{1},\sigma_x,\sigma_z\}\otimes\tau_y$	1	surface
DIII	$\mathrm{i}\sigma_y\mathcal{K}$	$\sigma_x\mathcal{K}$	σ_z	$\varnothing$	$\boldsymbol{\{\sigma_x,\sigma_y\}\otimes\tau_y}$	2	line
AII	$\mathrm{i}\sigma_y\mathcal{K}$	$\times$	$\times$	$\{\mathbb{1}\}$	$\boldsymbol{\mathbb{1}\otimes\{\mathbb{1},\tau_x,\tau_z\}\cup\{\sigma_x,\sigma_y,\sigma_z\}\otimes\tau_y}$	5	(none)
CII	$\mathrm{i}\tau_y\mathcal{K}$	$-\mathrm{i}\sigma_z\otimes\tau_y\mathcal{K}$	σ_z	$\varnothing$	$\boldsymbol{\{\sigma_x\otimes\mathbb{1}\}\cup\sigma_y\otimes\{\tau_x,\tau_y,\tau_z\}}$	4	(none)
C	$\times$	$\mathrm{i}\sigma_y\mathcal{K}$	$\times$	$\boldsymbol{\{\sigma_x,\sigma_y,\sigma_z\}}$	$\{\sigma_x,\sigma_y,\sigma_z\}\otimes\{\mathbb{1},\tau_x,\tau_z\}\cup\{\mathbb{1}\otimes\tau_y\}$	3	point
CI	$\mathcal{K}$	$\mathrm{i}\sigma_y\mathcal{K}$	$\mathrm{i}\sigma_y$	$\boldsymbol{\{\sigma_x,\sigma_z\}}$	$\{\sigma_x,\sigma_z\}\otimes\{\mathbb{1},\tau_x,\tau_z\}$	2	line

Table 1.2: Determining δ_{CL}, the generic codimension of band touchings, in each of the AZ+$\mathcal{P}$ symmetry classes, listed in the first column. The second, third and fourth columns show minimal representations of the AZ+$\mathcal{P}$ symmetries. The fourth and fifth columns show the minimal basis (shown in bold) for an effective Hamiltonian locally describing adjacent bands. The last column shows the resulting band touchings in 3D. (Table reproduced, with permission, from Ref. 76, i.e., Tomáš Bzdušek and Manfred Sigrist, *Physical Review B*, 96:155105 (2017). Copyright 2017 by the American Physical Society.)

"undoes" the $\mathbf{k}\to-\mathbf{k}$ transformation:

$$\mathfrak{T}^{-1}H_{\mathbf{k}}\,\mathfrak{T}=+H_{\mathbf{k}}, \tag{1.9a}$$

$$\mathfrak{C}^{-1}H_{\mathbf{k}}\,\mathfrak{C}=-H_{\mathbf{k}}, \tag{1.9b}$$

$$\mathcal{S}^{-1}H_{\mathbf{k}}\,\mathcal{S}=-H_{\mathbf{k}}. \tag{1.9c}$$

Like $\mathcal{T}$ and $\mathcal{C}$, $\mathfrak{T}$ and $\mathfrak{C}$ act antiunitarily on the single-particle Hamiltonian, and can square to $+1$ or -1; hence, they give rise to 10 symmetry classes called the "AZ+$\mathcal{P}$" classes[9], defined analogously to the original AZ classes (see Table 1.3) [76]. In addition, since inversion symmetry $\mathcal{P}$ is typically not broken by material strains, the classification based on $\mathfrak{T}$ and $\mathfrak{C}$ is thought to be fairly robust, like the ones based on solely internal symmetries [76].

The generic codimension of gapless manifolds depends on a system's AZ+$\mathcal{P}$ class; see the column δ_{CL} of Table 1.2, where CL, short for "Cartan class", is another name for the AZ classes. In Ref. 76, the codimensions are derived using a method different from those of von Neumann and Wigner and of Herring: first, one chooses adequate minimal representations for the operators $\mathfrak{T}$, $\mathfrak{C}$ and $\mathcal{S}$ (shown in the second, third and fourth columns of Table 1.2, respectively). Then, based on symmetry-allowed matrix terms, one can write down the minimal basis for the effective Hamiltonian that locally describes adjacent bands; the size of the minimal Hamiltonian is 2×2, or 4×4 if Kramers's theorem enforces global double degeneracy. These bases are shown in the fifth and sixth columns of Table 1.2, with the minimal basis for each class indicated in bold. The generic codimension of band touchings,

[9] In the notation of the original article [76], they are called "AZ+$\mathcal{I}$" classes.

	$\mathfrak{T}$	$\mathfrak{C}$	$\mathcal{S}$	$p = \ldots$								
CL	($\mathcal{T}$	$\mathcal{C}$	$\mathcal{S}$)	0	1	2	3	4	5	6	7	8
A	$\times$	$\times$	$\times$	$\mathbb{0}$	$\mathbb{0}$	$\mathbf{\mathbb{Z}}$	$\mathbb{0}$	$\mathbb{Z}$	$\mathbb{0}$	$\mathbb{Z}$	$\mathbb{0}$	$\mathbb{Z}$
AIII	$\times$	$\times$	1	$\mathbb{0}$	$\mathbf{\mathbb{Z}}$	$\mathbf{\mathbb{0}}$	$\mathbb{Z}$	$\mathbb{0}$	$\mathbb{Z}$	$\mathbb{0}$	$\mathbb{Z}$	$\mathbb{0}$
AI	$+1$	$\times$	$\times$	$\mathbb{0}$	$\mathbf{\mathbb{Z}_2}$	$\mathbf{\mathbb{Z}_2}$	$\mathbb{0}$	$2\mathbb{Z}$	$\mathbb{0}$	$\mathbb{0}$	$\mathbb{0}$	$\mathbb{Z}$
BDI	$+1$	$+1$	1	$\mathbf{\mathbb{Z}_2}$	$\mathbf{\mathbb{Z}_2}$	$\mathbf{\mathbb{0}}$	$2\mathbb{Z}$	$\mathbb{0}$	$\mathbb{0}$	$\mathbb{0}$	$\mathbb{Z}$	$\mathbb{Z}_2$
D	$\times$	$+1$	$\times$	$\mathbf{\mathbb{Z}_2}$	$\mathbf{\mathbb{0}}$	$\mathbf{2\mathbb{Z}}$	$\mathbb{0}$	$\mathbb{0}$	$\mathbb{0}$	$\mathbb{Z}$	$\mathbb{Z}_2$	$\mathbb{Z}_2$
DIII	-1	$+1$	1	$\mathbb{0}$	$\mathbf{2\mathbb{Z}}$	$\mathbf{\mathbb{0}}$	$\mathbb{0}$	$\mathbb{0}$	$\mathbb{Z}$	$\mathbb{Z}_2$	$\mathbb{Z}_2$	$\mathbb{0}$
AII	-1	$\times$	$\times$	$\mathbb{0}$	$\mathbb{0}$	$\mathbb{0}$	$\mathbb{0}$	$\mathbb{Z}$	$\mathbb{Z}_2$	$\mathbb{Z}_2$	$\mathbb{0}$	$2\mathbb{Z}$
CII	-1	-1	1	$\mathbb{0}$	$\mathbb{0}$	$\mathbb{0}$	$\mathbb{Z}$	$\mathbb{Z}_2$	$\mathbb{Z}_2$	$\mathbb{0}$	$2\mathbb{Z}$	$\mathbb{0}$
C	$\times$	-1	$\times$	$\mathbb{0}$	$\mathbb{0}$	$\mathbf{\mathbb{Z}}$	$\mathbb{Z}_2$	$\mathbb{Z}_2$	$\mathbb{0}$	$2\mathbb{Z}$	$\mathbb{0}$	$\mathbb{0}$
CI	$+1$	-1	1	$\mathbb{0}$	$\mathbf{\mathbb{Z}}$	$\mathbf{\mathbb{Z}_2}$	$\mathbb{Z}_2$	$\mathbb{0}$	$2\mathbb{Z}$	$\mathbb{0}$	$\mathbb{0}$	$\mathbb{0}$

Table 1.3: Topological invariants protecting band touchings in the AZ+$\mathcal{P}$ classification. The behaviour of the AZ-like symmetries $\mathfrak{T}$, $\mathfrak{C}$ and $\mathcal{S}$ is shown; "CL" stands for "Cartan label". The topological classification applicable to a p-sphere is shown for each class, with the ones relevant to 3D in bold. (Table adapted, with permission, from Ref. 76, i.e., Tomáš Bzdušek and Manfred Sigrist, *Physical Review B*, 96:155105 (2017). Copyright 2017 by the American Physical Society.)

δ_{CL}, is then determined by counting how many coefficients of the minimal basis must simultaneously vanish to give rise to a band touching between the adjacent bands [76]. (The method of effective Hamiltonians describing subsets of bands is discussed and justified in Sec. 4.4, in which it is also extended to a type of non-Hermitian matrix that arises in bosonic Bogoliubov–de Gennes systems. There, we use it to show that the generic codimension of accidental degeneracies of type (ii) in these systems is the same as in fermion systems for AZ+$\mathcal{P}$ classes A and AI.)

Each generically stable gapless manifold thus arising is protected by one or two topological invariants defined on p-spheres that enclose it, as shown in Table 1.3 [76]. For example, Weyl nodes in 3D, which can occur in the absence of space-time inversion symmetry $\mathfrak{T}$ (AZ+$\mathcal{P}$ class A), are characterized by a nontrivial $\mathbb{Z}$ invariant; this is just the Chern number calculated on a 2-sphere containing the Weyl point inside it. On the other hand, the gapless lines that occur in systems with space-time inversion symmetry and negligible spin-orbit coupling (AZ+$\mathcal{P}$ class AI) are protected by up to two different $\mathbb{Z}_2$ invariants: one (the Berry phase) is defined on loops (1-spheres) that thread the gapless line, and the other, when applicable, is defined on 2-spheres that completely enclose the gapless line.

1.3 The Dirac and Weyl Hamiltonians

The Dirac equation was formulated as a wave equation for electrons in an effort to wed quantum mechanics with Lorentz invariance, the basic symmetry of special relativity [5,6,84]. In order to write a time-evolution equation of first order in spatial and temporal derivatives, Dirac formulated a matrix-valued Hamiltonian,

$$H_{\text{Dirac}} = c\sum_{i=1}^{3} \alpha_i p_i + mc^2\beta, \tag{1.10}$$

where $p_i = -\mathrm{i}\frac{\partial}{\partial x_i}$ is the momentum operator in position space and α_i and β are adequate Hermitian matrices. In terms of H_{Dirac}, the famed Dirac equation is

$$\mathrm{i}\frac{\partial}{\partial t}\psi(t,\mathbf{x}) = H_{\text{Dirac}}\psi(t,\mathbf{x}), \tag{1.11}$$

where $\psi(t,\mathbf{x})$ is a multi-component wavefunction. In order to obey Lorentz invariance, the matrices must satisfy $\{\alpha_i,\alpha_j\} = 2\delta_{ij}\mathbb{1}$, $\beta^2 = \mathbb{1}$, and $\{\alpha_i,\beta\} = 0$ [6]. In that case, by simply squaring the Hamiltonian, i.e.,

$$(H_{\text{Dirac}})^2 = c^2\mathbf{p}^2 + m^2c^4, \tag{1.12}$$

it is clear that its plane-wave eigenstates satisfy the relativistic dispersion relation, $E^2 = c^2\mathbf{p}^2 + m^2c^4$. It turns out that the Hamiltonian gives both positive-energy and negative-energy solutions. Dirac's initial interpretation of these negative-energy solutions was to posit a full "sea" of electrons occupying the negative-energy states, and enabling his prediction of the positron as a hole left in the Dirac sea when an electron is excited from a negative-energy state to a positive-energy one [45]. Though this view was abandoned in elementary particle physics, it does hold for fermionic condensed-matter systems, in which the Fermi sea is a reality.

In $3+1$ spacetime dimensions, the matrices β and α_i must be at least of size 4×4 to fulfill the mutual anticommutation conditions, and the four-component spinor ψ governed by the Hamiltonian is called a Dirac fermion. The form of the matrices β and α_i is not unique; in one common representation, they take the form

$$\alpha_i = \begin{bmatrix} \sigma_i & \\ & -\sigma_i \end{bmatrix}, \qquad \beta = \begin{bmatrix} & -\sigma_0 \\ -\sigma_0 & \end{bmatrix}, \tag{1.13}$$

where $\{\sigma_1,\sigma_2,\sigma_3\}$ are the Pauli matrices and σ_0 is the 2×2 identity matrix [5,84]. The energy eigenvalues, both twofold degenerate, are $E = \sqrt{c^2\mathbf{p}^2 + m^2c^4}$ and $E = -\sqrt{c^2\mathbf{p}^2 + m^2c^4}$. The four degrees of freedom correspond to spin-one-half and to particle-antiparticle degrees of freedom [5,84].

With a massless particle, the dispersion becomes linear and gapless, with a fourfold degeneracy at $\mathbf{p} = 0$. The special case of $m = 0$ in the Hamiltonian of Eq. (1.10) is noteworthy: in this case, H_{Dirac} becomes block diagonal and the system decouples into two two-component spinors [5, 84]. These two-component spinors describe Weyl fermions, and the Hamiltonian that governs them,

$$H_{\text{Weyl}} = \pm c \sum_{i=1}^{3} \sigma_i p_i, \tag{1.14}$$

is the Weyl Hamiltonian [5, 84]. There are no known Weyl fermions in nature; neutrinos were once believed to be Weyl fermions, until they were found to have a small, but nonzero, mass [84].

In $2+1$ and $1+1$ dimensions, the matrices β and α_i can be of size 2×2 [6, 85]. In particular, in $2+1$ dimensions, we can take $\alpha_1 = \sigma_1$, $\alpha_2 = \sigma_2$, and $\beta = \sigma_3$, giving

$$H_{\text{Dirac}} = c \sum_{i=1}^{2} \sigma_i p_i + mc^2 \sigma_3. \tag{1.15}$$

The dispersion remains the same as in the $(3+1)$-dimensional case, but now without the twofold degeneracy.

In the following section, we will describe some well-known examples of (massless) Dirac-like physics that occurs in condensed-matter systems. In these systems, Dirac or Weyl Hamiltonians accurately describe a region of momentum modes, and depending on the filling and on the rest of the dispersion, they may govern the low-energy properties of the systems. In electron systems, the Fermi velocity v_{F} plays the role of the speed of light c [6], and if the Fermi energy is aligned with the Dirac or Weyl node, the system is a Dirac or Weyl semimetal, respectively. The degrees of freedom giving rise to the matrix structure of such Hamiltonians depend on the microscopic physics at play—from sublattice degrees of freedom in graphene, from the electron spin in the surface states of 3D topological insulators, from a combined spin and particle-hole degree of freedom in the cuprate superconductors—yet in each case, the effective Dirac-like physics gives rise to many of the same universal features in these materials [6].

1.4 Common Dirac-like systems: models and experimental evidence

In the present section, we discuss some important examples of Dirac-like matter, including experimental evidence of their realization. This serves both to review certain characteristic properties of Dirac matter, and to introduce some of the concepts that appear in this thesis. More attention is devoted to those systems that come up in the subsequent chapters.

Much of the experimental evidence presented is in the form of angle-resolved photoemission spectroscopy (ARPES) data. ARPES measures the occupied part of the single-particle electronic spectral function [86]. The spectral function $A(\omega, \mathbf{k})$ of a many-body electron system gives the probability that an electron can be added to (removed from) state $\mathbf{k}$ with an energy cost ω ($-\omega$), provided the occupancy of state $\mathbf{k}$ allows it [87].

The underpinning physical principle is the photoelectric effect: the incoming photons, of known frequency and momentum, are absorbed by electrons in the system. Then, by measuring the energy and momentum of the outgoing electrons, their initial energy and momentum can be deduced. ARPES is primarily a surface probe, but depending on certain factors (e.g., the penetration depth of the light), it can used to some extent to probe the bulk [88].

Some scanning tunneling spectroscopy (STS) data is also presented; STS measures the local density of states, i.e., the position-space spectral function $A(\omega, \mathbf{x})$ [87].

1.4.1 Graphene

Graphene is a 2D sheet of carbon atoms arranged in a honeycomb lattice, as depicted in Fig. 1.2a. In isolation, carbon's electronic configuration is [He]$2s^2 2p^2$ [89]. In the graphene geometry, the $2s$ orbital and the two in-plane $2p$ orbitals ($2p_x$ and $2p_y$) hybridize into so-called sp^2 molecular orbitals involving three electrons—a type of σ bond. The remaining electron resides in the out-of-plane $2p_z$ orbital. At charge neutrality, the Fermi energy E_F lies between the two bands that result from the two $2p_z$ orbitals per unit cell; the strongly bound sp^2 states are energetically far from the Fermi energy (see Fig. 1.2b) [5, 90, 91].

The p_z orbitals have different symmetry from the sp^2 states: the former is odd under the mirror symmetry operation m_z, the reflection through the graphene plane, while the latter is even (like s, p_x, and p_y). Therefore, since m_z is a symmetry of the graphene sheet, there are no Hamiltonian matrix elements connecting the p_z and sp^2 states, and the p_z states can be treated independently [90]—see Eq. (1.1) and the surrounding discussion about equivalent and inequivalent representations. The resulting Hamiltonian for the $2p_z$ states should accurately describe the band structure in the energy range between the highest occupied and lowest unoccupied sp^2 states, wherein lies E_F (see Fig. 1.2b); the hybridization of the $2p_z$ states gives rise to a so-called π bond.

Hence, letting $c_{i\sigma}$ be the electron annihilation operators for the $2p_z$ orbital with spin σ at site i, the tight-binding Hamiltonian takes the form [91]

$$H = -t \sum_{\langle i,j \rangle, \sigma} \left(c_{i\sigma}^\dagger c_{j\sigma} + \mathrm{H.c.} \right) - t' \sum_{\langle\langle i,j \rangle\rangle, \sigma} \left(c_{i\sigma}^\dagger c_{j\sigma} + \mathrm{H.c.} \right), \tag{1.16}$$

where $-t \approx -2.8\,\mathrm{eV}$ is the hopping amplitude between nearest neighbours (NNs), denoted by $\langle i, j \rangle$, and $-t'$ (thought to be between $0.02\,t$ and $0.2\,t$) is the hopping amplitude between next-nearest neighbours (NNNs), denoted by $\langle\langle i, j \rangle\rangle$ [91]. In a honeycomb crystal like

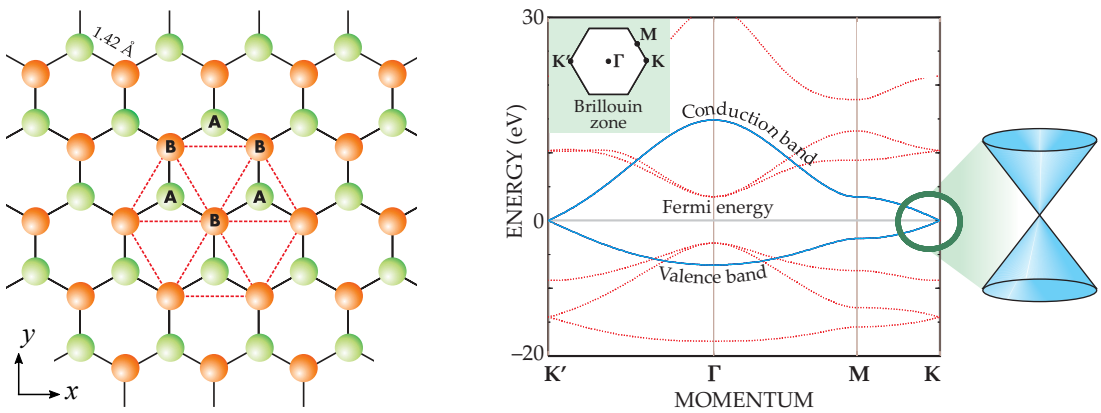

(a) (b)

Figure 1.2: (a): Crystal structure of graphene—the honeycomb is made up of two interpenetrating triangular lattices. The two crystallographically distinct (but chemically identical) sites are labelled "A" and "B" and are shown in green and orange. The NN and NNN bonds are shown in solid black and dashed red, respectively. (b) Band structure of graphene. The first Brillouin zone for the triangular lattice is shown as an inset. The p_z bands, which intersect the Fermi energy, are blue; the sp^2 bands are dotted and red. The Dirac crossings are located at the (inequivalent) K and K' points. (Figures reproduced from Ref. 90, i.e., Andrey K. Geim and Allan H. MacDonald, "Graphene: Exporing carbon flatland", *Physics Today*, 60(8):35 (2007), with the permission of AIP Publishing.)

graphene, the NN bonds connect different sublattices (called A and B), and NNN bonds connect like sublattices—see Fig. 1.2a. Decomposing the site index i into a Bravais lattice site $\mathbf{R}$ and a sublattice index $\alpha \in \{A, B\}$, we can define Fourier-transformed operators,

$$c_{\mathbf{k}\alpha\sigma} = \frac{1}{\sqrt{N}} \sum_{\mathbf{R}} \mathrm{e}^{-\mathrm{i}\mathbf{k}\cdot\mathbf{r}_{\mathbf{R}\alpha}} c_{\mathbf{R}\alpha\sigma}, \tag{1.17}$$

where N is the number of unit cells and $\mathbf{r}_{\mathbf{R}\alpha}$ is the position of the atom at site $i = (\mathbf{R}, \alpha)$. In terms of these, the Hamiltonian becomes

$$H = \sum_{\mathbf{k},\sigma} \psi^\dagger_{\mathbf{k}\sigma} H_{\mathbf{k}} \psi_{\mathbf{k}\sigma}, \quad \psi^\dagger_{\mathbf{k}\sigma} = \begin{bmatrix} c^\dagger_{\mathbf{k}A\sigma} & c^\dagger_{\mathbf{k}B\sigma} \end{bmatrix}, \tag{1.18a}$$

$$H_{\mathbf{k}} = \begin{bmatrix} -t' f(\mathbf{k}) & -t g(\mathbf{k}) \\ -t g(\mathbf{k})^* & -t' f(\mathbf{k}) \end{bmatrix}, \tag{1.18b}$$

where $\psi_{\mathbf{k}\sigma}$ is a "spinor" in the space of sublattices, $g(\mathbf{k}) = \sum_{l=1}^{3} \mathrm{e}^{\mathrm{i}\mathbf{k}\cdot\mathbf{w}_l}$ in terms of the NN vectors

$$\mathbf{w}_1 = a\hat{y}, \qquad \mathbf{w}_2 = a\left(-\frac{\sqrt{3}}{2}\hat{x} - \frac{1}{2}\hat{y}\right), \qquad \mathbf{w}_3 = a\left(\frac{\sqrt{3}}{2}\hat{x} - \frac{1}{2}\hat{y}\right), \tag{1.19}$$

$f(\mathbf{k}) = \sum_{l=1}^{3} \mathrm{e}^{\mathrm{i}\mathbf{k}\cdot\mathbf{w}'_l}$ in terms of the NNN vectors

$$\mathbf{w}'_1 = \sqrt{3}a\hat{x}, \qquad \mathbf{w}'_2 = \sqrt{3}a\left(-\frac{1}{2}\hat{x} + \frac{\sqrt{3}}{2}\hat{y}\right), \qquad \mathbf{w}'_3 = \sqrt{3}a\left(-\frac{1}{2}\hat{x} - \frac{\sqrt{3}}{2}\hat{y}\right), \tag{1.20}$$

and a is the carbon-carbon distance. After diagonalization, we arrive at

$$H = \sum_{\mathbf{k},\sigma}\left(\varepsilon_{\mathbf{k}+}c^{\dagger}_{\mathbf{k},+,\sigma}c_{\mathbf{k},+,\sigma} + \varepsilon_{\mathbf{k}-}c^{\dagger}_{\mathbf{k},-,\sigma}c_{\mathbf{k},-,\sigma}\right), \tag{1.21a}$$

$$\varepsilon_{\mathbf{k}\pm} = -t'f(\mathbf{k}) \pm t|g(\mathbf{k})| = -t'f(\mathbf{k}) \pm t\sqrt{3 + f(\mathbf{k})}, \tag{1.21b}$$

where the momentum is summed over the first Brillouin zone, the two bands are denoted by "+" and "−", and in the second line, we used the fact that $|g(\mathbf{k})|^2 = 3 + f(\mathbf{k})$.

Band touchings in graphene Note that band touchings occur at (and only at) the $\mathrm{K} = 4\pi/(3\sqrt{3}a)\hat{x}$ and $\mathrm{K}' = -\mathrm{K}$ points of the first Brillouin zone (see Fig. 1.2b), where $\varepsilon_{\mathrm{K}\pm} = \varepsilon_{\mathrm{K}'\pm} = 3t'$. Indeed, when neglecting spin-orbit coupling (SOC) as we have, the electrons are effectively spinless [31], and the single-particle states $|\mathrm{K}, A\rangle = c^{\dagger}_{\mathrm{K}A}|0\rangle$ and $|\mathrm{K}, B\rangle = c^{\dagger}_{\mathrm{K}B}|0\rangle$ can be shown to transform as a two-dimensional irrep of G_{K}, the little group at K, giving rise to a degeneracy at that wavevector [92, 93]. This implies that the addition of longer-range hoppings that preserve the crystal symmetry cannot open a gap at that momentum. (The same goes for the inequivalent wavevector K′, which is related by inversion symmetry.) On the other hand, when SOC is accounted for, the picture changes and the bands are split. However, because of the graphene geometry and because carbon is a light atom, the SOC is weak, and the gap in graphene is known to be small—on the order of 10^{-3} meV [5, 6, 84, 91]. Hence, the small SOC present in graphene, and the small gap it gives rise to, are usually neglected.

It turns out that the band touchings at K and K′ in the absence of SOC are also protected by the space-time inversion ($\mathcal{PT}$) symmetry: even if the crystal symmetry is reduced (for instance, by homogeneous strain—see Sec. 1.5), the band touchings are displaced away from the BZ corners, but do not gap out under small perturbations as long as $\mathcal{PT}$ symmetry remains [84]. This can be readily understood from Table 1.2, applicable at general momenta: our model of graphene, for which $\mathcal{PT} = \mathfrak{T}$ squares to +1 because SOC is negligible, is in AZ+$\mathcal{P}$ class AI (any particle-hole symmetry is ruled out by t', which makes the band structure asymmetric about zero energy), indicating that isolated-point band touchings are generically stable. Furthermore, Table 1.3 indicates that they are protected by a $\mathbb{Z}_2$ invariant, which turns out be the Berry phase quantized to 0 or π [76].

The effect of inversion symmetry—which we take to be 2D inversion, i.e., a rotation about the $\hat{z}$ axis—on the spinors of Eq. (1.18) is

$$\mathcal{P}^{\dagger}\psi_{\mathbf{k}\sigma}\mathcal{P} = \tau_1\psi_{-\mathbf{k}\sigma}. \tag{1.22}$$

As for time reversal, its effect is

$$\mathcal{T}^{-1}\psi_{\mathbf{k}\sigma}\mathcal{T} = \psi_{-\mathbf{k}\sigma}, \qquad \mathcal{T}^{-1}\psi^\dagger_{\mathbf{k}\sigma}\mathcal{T} = \psi^\dagger_{-\mathbf{k}\sigma}. \tag{1.23a}$$

Note that both $\mathcal{P}$ and $\mathcal{T}$ are assumed to act only on spatial coordinates and not on spin, which is possible because the Hamiltonian of Eq. (1.18) is diagonal in spin since there is no spin-orbit coupling[10]. The composite symmetry $\mathcal{PT}$ has the effect

$$(\mathcal{PT})^{-1}\psi_{\mathbf{k}\sigma}(\mathcal{PT}) = \tau_1\psi_{-\mathbf{k}\sigma} \tag{1.24a}$$

$$(\mathcal{PT})^{-1}\psi^\dagger_{\mathbf{k}\sigma}(\mathcal{PT}) = \psi^\dagger_{-\mathbf{k}\sigma}\tau_1. \tag{1.24b}$$

Momentarily expressing the Bloch Hamiltonian as $H_{\mathbf{k}} = d^0_{\mathbf{k}} + \mathbf{d}_{\mathbf{k}} \cdot \boldsymbol{\tau}$, the constraint due to space-time inversion takes the form

$$[\mathcal{PT}, H] = 0 \qquad \Leftrightarrow \qquad H_{\mathbf{k}} = \tau_1 H^*_{\mathbf{k}} \tau_1 \qquad \Leftrightarrow \qquad d^3_{\mathbf{k}} = 0. \tag{1.25}$$

This is the form of the Hamiltonian of Eq. (1.18), but now we see that any additional hoppings cannot introduce a τ_3 term, as long as they obey $\mathcal{PT}$ symmetry.

In Sec. 1.2, we claimed that for integer-spin (in our case, effectively spinless) problems, $\mathcal{PT}$ symmetry forces $H_{\mathbf{k}} = H^*_{\mathbf{k}}$ in an adequate basis. In the case at hand, such a basis can be reached by a rotation $\mathrm{e}^{-\mathrm{i}\tau_1\pi/4}$ in sublattice space. In either basis, the result is the same: in order for the bands to touch, two functions (either $d^1_{\mathbf{k}}$ and $d^2_{\mathbf{k}}$, or $d^1_{\mathbf{k}}$ and $d^3_{\mathbf{k}}$) of two variables must vanish simultaneously, which generically happens at isolated points—a rephrasing of the AZ+$\mathcal{P}$ argument above.

For larger Hamiltonians, the same argument holds, provided the two adjacent bands of interest are separated from the rest of the spectrum by a gap (and belong to equivalent representations). In that case, at least locally in momentum space, an effective 2×2 Hamiltonian can be derived for the two bands using the Schrieffer–Wolff transformation, making it analogous to the one discussed above. This type of argument is discussed in detail in Sec. 4.4.

1.4.1.1 Low-energy graphene and effective Dirac electrons

In neutral graphene, the Fermi energy is exactly at the energy at which the conduction and valence bands meet, at K and $\mathrm{K}' = -\mathrm{K}$. Expanding the dispersion relation about these two points, using the fact that $f(\pm\mathrm{K} + \mathbf{q}) = -3 + 9a^2|\mathbf{q}|^2/4 + \mathcal{O}(q^2)$, gives

$$\varepsilon_{\mathrm{K}+\mathbf{q},\pm} = \varepsilon_{\mathrm{K}'+\mathbf{q},\pm} = 3t' \pm v_{\mathrm{F}}|\mathbf{q}| + \mathcal{O}(q^2), \tag{1.26}$$

[10] We can also view $\mathcal{P}$ and $\mathcal{T}$ in a system without SOC as follows: letting $\tilde{\mathcal{P}}$ and $\tilde{\mathcal{T}}$ denote the "physical" operations, which act both on spin and space, define $\mathcal{P} := \mathrm{e}^{\mathrm{i}\sigma_3\pi/2}\tilde{\mathcal{P}} = \mathrm{i}\sigma_3\tilde{\mathcal{P}}$ and $\mathcal{T} := \mathrm{e}^{\mathrm{i}\sigma_2\pi/2}\tilde{\mathcal{T}} = \mathrm{i}\sigma_2\tilde{\mathcal{T}}$. In particular, whereas $\tilde{\mathcal{T}}^2 = -1$, $\mathcal{T}^2 = +1$, and so the electron is effectively spinless.

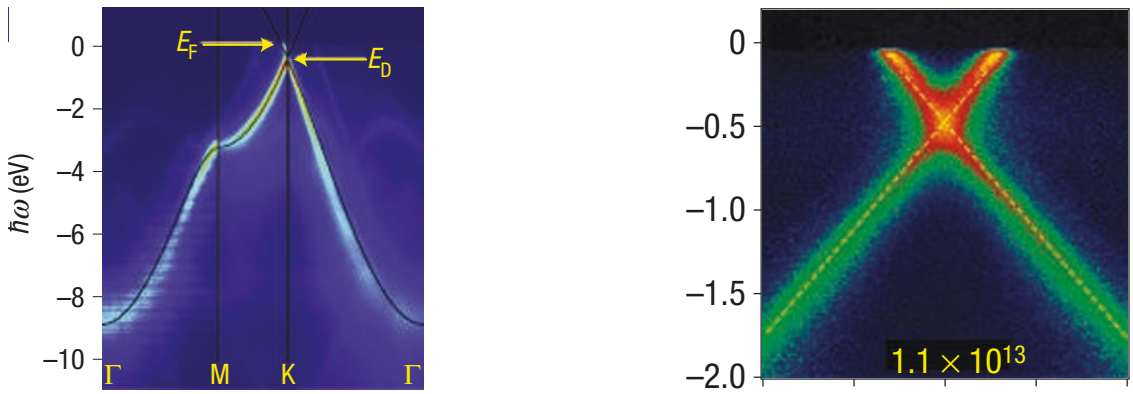

(a) (b)

Figure 1.3: ARPES data showing the band structure of graphene for energies near the Fermi energy. (a) Valence band dispersion along a selected path in the first Brillouin zone. The black curve shows the predicted band structure. Note that the Dirac energy E_{D} is just below the Fermi Energy E_{F}. (b) Close-up view of the Dirac point at the K point, showing the linear dispersion. The electron density of $1.1 \times 10^{13}\,\mathrm{cm}^{-2}$ is shown. (Reproduced with the permission of Springer Nature from Ref. 94, i.e., Aaron Bostwick et al., "Quasiparticle dynamics in graphene", *Nature Physics*, 3:36 (2007).)

where $v_{\mathrm{F}} = 3at/2 \approx 10^6\,\mathrm{m/s}$, roughly 300 times slower than the speed of light [90]. These linear band touchings are clearly seen with ARPES: the data of Fig. 1.3 show the linear dispersion at the K point. In the experimental data, states below and just above the Dirac point energy (E_{D}) are visible because the Fermi energy E_{F} is slightly higher than E_{D}.

In the low-energy limit, only states near the K and $\mathrm{K}' = -\mathrm{K}$ points are relevant, and the Bloch Hamiltonian $H_{\mathbf{k}}$ can be expanded to leading order around those points:

$$H_{\pm\mathrm{K}+\mathbf{q}} = \begin{bmatrix} 3t' & v_{\mathrm{F}}(\pm q_x - \mathrm{i}q_y) \\ v_{\mathrm{F}}(\pm q_x + \mathrm{i}q_y) & 3t' \end{bmatrix} = 3t'\tau_0 + v_{\mathrm{F}}\left(\pm q_x \tau_1 + q_y \tau_2\right). \tag{1.27}$$

Here, the τ_μ are Pauli matrices in the sublattice space. The subleading-order terms ($\mathcal{O}(q^2)$) are negligible as long as $a|\mathbf{q}| \ll 1$, or in terms of energy, $|E| \ll t$. Hence, the following Hamiltonian captures the low-energy modes of the Hamiltonian of Eq. (1.18):

$$H_{\mathrm{LE}} = v_{\mathrm{F}} \sum_{\mathbf{q},\sigma} \left(\psi^\dagger_{\mathrm{K}+\mathbf{q},\sigma} \left(\mathbf{q}\cdot\boldsymbol{\tau}\right) \psi_{\mathrm{K}+\mathbf{q},\sigma} - \psi^\dagger_{\mathrm{K}'+\mathbf{q},\sigma} \left(\mathbf{q}\cdot\boldsymbol{\tau}^*\right) \psi_{\mathrm{K}'+\mathbf{q},\sigma} \right) \tag{1.28a}$$

$$= v_{\mathrm{F}} \sum_{\mathbf{q},\sigma} \left(\psi^\dagger_{\mathbf{q},1,\sigma} \left(\mathbf{q}\cdot\boldsymbol{\tau}\right) \psi_{\mathbf{q},1,\sigma} - \psi^\dagger_{\mathbf{q},2,\sigma} \left(\mathbf{q}\cdot\boldsymbol{\tau}^*\right) \psi_{\mathbf{q},2,\sigma} \right). \tag{1.28b}$$

Note that we have set $t' = 0$, since in the low-energy limit, t' merely shifts the eigenstate energies. In the second line, we have introduced spinors labelled by the valley index, where 1 and 2 respectively correspond to K and K'. The momentum sum can now be considered unrestricted, since the high-energy states are not relevant.

The Hamiltonian above exhibits sublattice-momentum locking, an analogue of spin-

momentum locking, but with the sublattices $\{A, B\}$ serving as a pseudospin degree of freedom. In other words, the particles have a well-defined *helicity*, the projection of the (pseudo)spin onto the direction of the momentum, given by

$$h_{(\mathrm{K})} = \frac{1}{2}\,\boldsymbol{\tau}\cdot\frac{\mathbf{p}}{|\mathbf{p}|} \tag{1.29a}$$

in the K valley and by

$$h_{(\mathrm{K}')} = \frac{1}{2}\,\boldsymbol{\tau}^*\cdot\frac{\mathbf{p}}{|\mathbf{p}|} \tag{1.29b}$$

in the K′ valley. Massless relativistic particles can have well-defined helicity because—unlike for massless particles—no boost can reverse the particle's direction of motion, and the electrons are effectively massless and relativistic with speed of light v_{F} [90].

By writing $\psi_{\mathbf{q},1,\sigma}$ in terms of position space operators,

$$\begin{aligned}\psi_{\mathbf{q},1,\sigma} &= \psi_{\mathrm{K}+\mathbf{q},\sigma}\\ &= \frac{1}{\sqrt{N}}\sum_{\mathbf{R}} \mathrm{e}^{-\mathrm{i}(\mathrm{K}+\mathbf{q})\cdot\mathbf{R}}\psi_{\mathbf{R},\sigma}\\ &= \frac{1}{\sqrt{N}}\sum_{\mathbf{R}} \mathrm{e}^{-\mathrm{i}\mathbf{q}\cdot\mathbf{R}}\left(\mathrm{e}^{-\mathrm{i}\mathrm{K}\cdot\mathbf{R}}\psi_{\mathbf{R},\sigma}\right),\end{aligned} \tag{1.30}$$

we see that its Fourier transform is $\mathrm{e}^{-\mathrm{i}\mathrm{K}\cdot\mathbf{R}}\psi_{\mathbf{R},\sigma}$; likewise, the Fourier transform of $\psi_{\mathbf{q},2,\sigma}$ is $\mathrm{e}^{-\mathrm{i}\mathrm{K}'\cdot\mathbf{R}}\psi_{\mathbf{R},\sigma}$. Now, the fields $\mathrm{e}^{-\mathrm{i}\mathrm{K}\cdot\mathbf{R}}\psi_{\mathbf{R},\sigma}$ and $\mathrm{e}^{-\mathrm{i}\mathrm{K}\cdot\mathbf{R}}\psi_{\mathbf{R},\sigma}$ are "slowly varying" relative to a in the low-energy regime (i.e., for small $\mathbf{q}$). Hence, we can treat them as continuous functions of $\mathbf{R}$ and define

$$\psi_{1\sigma}(\mathbf{R}) \coloneqq \frac{1}{\sqrt{\mathcal{A}_{\mathrm{uc}}}}\mathrm{e}^{-\mathrm{i}\mathrm{K}\cdot\mathbf{R}}\psi_{\mathbf{R},\sigma}, \tag{1.31a}$$

$$\psi_{2\sigma}(\mathbf{R}) \coloneqq \frac{1}{\sqrt{\mathcal{A}_{\mathrm{uc}}}}\mathrm{e}^{-\mathrm{i}\mathrm{K}'\cdot\mathbf{R}}\psi_{\mathbf{R},\sigma}, \tag{1.31b}$$

where $\mathcal{A}_{\mathrm{uc}}$ is the area of a unit cell. This way, letting $b \in \{\mathrm{K}, \mathrm{K}'\}$ denote the valley index, the operators $\psi_{\mathbf{q},b,\sigma}$ and $\mathbf{q}\psi_{\mathbf{q},b,\sigma}$ can be expressed in terms of the position-space fields,

$$\psi_{\mathbf{q},b,\sigma} = \frac{1}{\sqrt{N\mathcal{A}_{\mathrm{uc}}}}\int \mathrm{d}^2R\; \mathrm{e}^{-\mathrm{i}\mathbf{q}\cdot\mathbf{R}}\psi_{b\sigma}(\mathbf{R}), \tag{1.32a}$$

$$\mathbf{q}\psi_{\mathbf{q},b,\sigma} = \frac{1}{\sqrt{N\mathcal{A}_{\mathrm{uc}}}}\int \mathrm{d}^2R\; \mathrm{e}^{-\mathrm{i}\mathbf{q}\cdot\mathbf{R}}\left(-\mathrm{i}\nabla_{\mathbf{R}}\right)\psi_{b\sigma}(\mathbf{R}), \tag{1.32b}$$

and the low-energy Hamiltonian of Eq. (1.28) becomes

$$H_{\mathrm{LE}} = \frac{v_{\mathrm{F}}}{N\mathcal{A}_{\mathrm{uc}}} \sum_{\sigma} \int \mathrm{d}^2R\, \mathrm{d}^2R' \left(\psi^{\dagger}_{\mathbf{R},1,\sigma} \left(-\mathrm{i}\nabla_{\mathbf{R}'} \cdot \boldsymbol{\tau}\right) \psi_{\mathbf{R}',1,\sigma} - \psi^{\dagger}_{\mathbf{R},2,\sigma} \left(-\mathrm{i}\nabla_{\mathbf{R}'} \cdot \boldsymbol{\tau}^*\right) \psi_{\mathbf{R}',2,\sigma} \right) \underbrace{\sum_{\mathbf{q}} \mathrm{e}^{\mathrm{i}\mathbf{q}\cdot(\mathbf{R}-\mathbf{R}')}}_{N\mathcal{A}_{\mathrm{uc}}\delta^2(\mathbf{R}-\mathbf{R}')} \tag{1.33a}$$

$$= v_{\mathrm{F}} \sum_{\sigma} \int \mathrm{d}^2R \left(\psi^{\dagger}_{\mathbf{R},1,\sigma} \left(-\mathrm{i}\nabla \cdot \boldsymbol{\tau}\right) \psi_{\mathbf{R},1,\sigma} - \psi^{\dagger}_{\mathbf{R},2,\sigma} \left(-\mathrm{i}\nabla \cdot \boldsymbol{\tau}^*\right) \psi_{\mathbf{R},2,\sigma} \right). \tag{1.33b}$$

This shows that the low-energy dynamics of electrons in neutral graphene is dictated by a (massless) field-theory equivalent of the (2+1)-dimensional Dirac Hamiltonian of Eq. (1.15)—in fact, one per spin and valley quantum number—with the Fermi velocity v_{F} playing the role of the speed of light.

The effectively relativistic motion of electrons in graphene gives rise to several peculiar electronic properties [91], like Klein tunneling and the resulting enhanced conductivity and low degree of localization [6, 90, 95], an anomalous Hall effect [96], and Zitterbewegung [96], among others.

1.4.1.2 Magnetic fields in graphene: Minimal coupling from Peierls substitution

In the continuum low energy model of graphene, a magnetic field $\mathbf{B} = \nabla \times \mathbf{A}$ enters through minimal coupling [91], that is, through the substitution

$$\begin{bmatrix} -\mathrm{i}\partial_x \\ -\mathrm{i}\partial_y \end{bmatrix} \to \begin{bmatrix} -\mathrm{i}\partial_x + (e/c)A_x \\ -\mathrm{i}\partial_y + (e/c)A_y \end{bmatrix}; \tag{1.34}$$

it also gives rise to a Zeeman term, which we neglect for simplicity. It will later be useful to see how the minimal coupling substitution arises from the tight-binding Hamiltonian of Eq. (1.16).

An orbital magnetic field can be included in a tight-binding Hamiltonian via the Peierls substitution [97]: the tunneling amplitudes acquires an additional phase due to the magnetic field [89, Chapter 14], so hopping terms in the Hamiltonian are modified in the following way:

$$t_{ij}\, c_i^{\dagger} c_j \to \mathrm{e}^{\mathrm{i}\theta_{ij}}\, t_{ij}\, c_i^{\dagger} c_j, \tag{1.35a}$$

$$\theta_{ij} := -\frac{e}{c} \int_j^i \mathrm{d}\mathbf{x} \cdot \mathbf{A}(\mathbf{x}) \approx -\frac{e}{c} \left(\mathbf{x}_i - \mathbf{x}_j\right) \cdot \mathbf{A}\left(\frac{\mathbf{x}_i + \mathbf{x}_j}{2}\right). \tag{1.35b}$$

Here, $e > 0$ is the elementary charge, the integral is taken on the straight line from $\mathbf{x}_j$ to $\mathbf{x}_i$, and we have assumed that $\mathbf{A}(\mathbf{x})$ is slowly varying on the scale of the lattice, enabling us to approximate the integral as a product. We examine the tight-binding Hamiltonian

of graphene, Eq. (1.16), subject to this change. Anticipating that the NNN terms do not contribute, we focus on the NN terms:

$$H^{\text{mag}} = -t \sum_{\langle i,j \rangle, \sigma} \mathrm{e}^{\mathrm{i}\theta_{ij}} c^{\dagger}_{i\sigma} c_{j\sigma} + \text{H.c.} \tag{1.36a}$$

$$= -t \sum_{\sigma} \sum_{i \in A} \sum_{l=1}^{3} \mathrm{e}^{\mathrm{i}\theta_{\mathbf{x}_i + \mathbf{w}_l,\, \mathbf{x}_i}} \; c^{\dagger}_{\mathbf{x}_i + \mathbf{w}_l, B, \sigma} \; c_{\mathbf{x}_i, A, \sigma} + \text{H.c.} \tag{1.36b}$$

$$= -t \sum_{\sigma} \sum_{\mathbf{k}, \mathbf{k}'} c^{\dagger}_{\mathbf{k} B \sigma} \, c_{\mathbf{k}' A \sigma} \left(\frac{1}{N} \sum_{i \in A} \mathrm{e}^{-\mathrm{i}(\mathbf{k} - \mathbf{k}') \cdot \mathbf{x}_i} \sum_{l=1}^{3} \mathrm{e}^{-\mathrm{i}\mathbf{k} \cdot \mathbf{w}_l} \mathrm{e}^{\mathrm{i}\theta_{\mathbf{x}_i + \mathbf{w}_l,\, \mathbf{x}_i}} \right) + \text{H.c.} \tag{1.36c}$$

Since $\theta_{\mathbf{x}_i + \mathbf{w}_l,\, \mathbf{x}_i}$ is slowly varying in space, its Fourier transform, placed in parentheses in Eq. (1.36c), is appreciable only for small $\mathbf{k} - \mathbf{k}'$. Hence, the two valleys, K and K$'$, can still be treated independently, and we can split the sums into terms proximate to each valley. In terms of the spinors $\psi^{\dagger}_{\mathbf{q}1\sigma} = \begin{pmatrix} c^{\dagger}_{\mathbf{q}1A\sigma} & c^{\dagger}_{\mathbf{q}1B\sigma} \end{pmatrix}$ and $\psi^{\dagger}_{\mathbf{q}2\sigma} = \begin{pmatrix} c^{\dagger}_{\mathbf{q}2A\sigma} & c^{\dagger}_{\mathbf{q}2B\sigma} \end{pmatrix}$, introduced in Eq. (1.28) and respectively defined at valleys K and K$'$,

$$\begin{aligned} H^{\text{mag}}_{\text{LE}} = & -t \sum_{\mathbf{q}, \mathbf{q}', \sigma} c^{\dagger}_{\mathbf{q}1B\sigma} \, c_{\mathbf{q}'1A\sigma} \frac{1}{N} \sum_{i \in A} \mathrm{e}^{-\mathrm{i}(\mathbf{q} - \mathbf{q}') \cdot \mathbf{x}_i} \left(\sum_{l=1}^{3} \mathrm{e}^{-\mathrm{i}\mathrm{K} \cdot \mathbf{w}_l} \mathrm{e}^{-\mathrm{i}\mathbf{q} \cdot \mathbf{w}_l} \mathrm{e}^{\mathrm{i}\theta_{\mathbf{x}_i + \mathbf{w}_l,\, \mathbf{x}_i}} \right) + \text{H.c.} \\ & - t \sum_{\mathbf{q}, \mathbf{q}', \sigma} c^{\dagger}_{\mathbf{q}2B\sigma} \, c_{\mathbf{q}'2A\sigma} \frac{1}{N} \sum_{i \in A} \mathrm{e}^{-\mathrm{i}(\mathbf{q} - \mathbf{q}') \cdot \mathbf{x}_i} \left(\sum_{l=1}^{3} \mathrm{e}^{-\mathrm{i}\mathrm{K}' \cdot \mathbf{w}_l} \mathrm{e}^{-\mathrm{i}\mathbf{q} \cdot \mathbf{w}_l} \mathrm{e}^{\mathrm{i}\theta_{\mathbf{x}_i + \mathbf{w}_l,\, \mathbf{x}_i}} \right) + \text{H.c.} \end{aligned} \tag{1.37}$$

Consider the factors placed in parentheses in Eq. (1.37). We consider the momentum $\mathbf{q}$ to be small because we are interested in the low-energy regime. Furthermore, we assume the phases $\theta_{\mathbf{x}_i + \mathbf{w}_l,\, \mathbf{x}_i}$ are small in the appropriate sense, because of the shortness of the bonds $\mathbf{w}_l$ [97]. Hence, we can expand the exponentials involving $\mathbf{q}$ and $\theta_{\mathbf{x}_i + \mathbf{w}_l,\, \mathbf{x}_i}$ to leading order in these small quantities:

$$\begin{aligned} & \sum_{l=1}^{3} \mathrm{e}^{-\mathrm{i}\mathrm{K} \cdot \mathbf{w}_l} \mathrm{e}^{-\mathrm{i}\mathbf{q} \cdot \mathbf{w}_l} \mathrm{e}^{\mathrm{i}\theta_{\mathbf{x}_i + \mathbf{w}_l,\, \mathbf{x}_i}} \\ & \qquad = \underbrace{\sum_{l=1}^{3} \mathrm{e}^{-\mathrm{i}\mathrm{K} \cdot \mathbf{w}_l}}_{0} + \sum_{l=1}^{3} \mathrm{e}^{-\mathrm{i}\mathrm{K} \cdot \mathbf{w}_l} \left(-\mathrm{i}\, \mathbf{q} \cdot \mathbf{w}_l \right) + \sum_{l=1}^{3} \mathrm{e}^{-\mathrm{i}\mathrm{K} \cdot \mathbf{w}_l} \mathrm{i}\, \theta_{\mathbf{x}_i + \mathbf{w}_l,\, \mathbf{x}_i} + \dots \end{aligned} \tag{1.38}$$

The expression for the other valley, K$'$, is analogous. The first term on the right-hand side in Eq. (1.38) vanishes—it must, as we know the NN terms do not contribute to zeroth order to the zero-field low-energy graphene Hamiltonian. The second term gives precisely the zero-field Hamiltonian H_{LE} of Eq. (1.28). The third term constitutes the leading-order

contribution from the magnetic field—the ingredient of interest. For shorthand, we define

$$\mathcal{A}_{\mathrm{K}}(\mathbf{x}_i) := -\frac{2\mathrm{i}}{3a}\sum_{l=1}^{3}\mathrm{e}^{-\mathrm{i}\mathrm{K}\cdot\mathbf{w}}\theta_{\mathbf{x}_i+\mathbf{w}_l,\,\mathbf{x}_i} \approx \frac{e}{c}\big(+A_x(\mathbf{x}_i)+\mathrm{i}A_y(\mathbf{x}_i)\big), \tag{1.39a}$$

$$\mathcal{A}_{\mathrm{K}'}(\mathbf{x}_i) := -\frac{2\mathrm{i}}{3a}\sum_{l=1}^{3}\mathrm{e}^{-\mathrm{i}\mathrm{K}'\cdot\mathbf{w}}\theta_{\mathbf{x}_i+\mathbf{w}_l,\,\mathbf{x}_i} \approx \frac{e}{c}\big(-A_x(\mathbf{x}_i)+\mathrm{i}A_y(\mathbf{x}_i)\big), \tag{1.39b}$$

where the expressions on the right were obtained by letting $\mathbf{A}(\mathbf{x}_i+\mathbf{w}_l/2)\approx\mathbf{A}(\mathbf{x}_i)$. In terms of the definition of Eq. (1.39), the Hamiltonian of Eq. (1.37) becomes

$$H_{\mathrm{LE}}^{\mathrm{mag}} = H_{\mathrm{LE}} + v_{\mathrm{F}}\sum_{\mathbf{q},\mathbf{q}',\sigma} c^{\dagger}_{\mathbf{q}1B\sigma}\,c_{\mathbf{q}'1A\sigma}\frac{1}{N}\sum_{i\in A}\mathrm{e}^{-\mathrm{i}(\mathbf{q}-\mathbf{q}')\cdot\mathbf{x}_i}\mathcal{A}_{\mathrm{K}}(\mathbf{x}_i) + \mathrm{H.c.} + (\text{valley 2}) \tag{1.40}$$

Approximating the position sum as $N^{-1}\sum_{i\in A}\approx(N\mathcal{A}_{\mathrm{uc}})^{-1}\int\mathrm{d}x_i^2$ and expressing the fermion operators in terms of the Fourier transform of Eq. (1.32a), the Hamiltonian becomes

$$H_{\mathrm{LE}}^{\mathrm{mag}} = H_{\mathrm{LE}} + v_{\mathrm{F}}\sum_{\sigma}\int\mathrm{d}^2x\left(\psi^{\dagger}_{1\sigma}(\mathbf{x})\begin{bmatrix} & \mathcal{A}_{\mathrm{K}}(\mathbf{x})^* \\ \mathcal{A}_{\mathrm{K}}(\mathbf{x}) & \end{bmatrix}\psi_{1\sigma}(\mathbf{x}) + (\text{valley 2})\right) \tag{1.41a}$$

$$= v_{\mathrm{F}}\sum_{\sigma}\int\mathrm{d}^2x\left(\psi^{\dagger}_{1\sigma}(\mathbf{x})\left(-\mathrm{i}\nabla+\frac{e}{c}\mathbf{A}\right)\cdot\boldsymbol{\tau}\,\psi_{1\sigma}(\mathbf{x}) - \psi^{\dagger}_{2\sigma}(\mathbf{x})\left(-\mathrm{i}\nabla+\frac{e}{c}\mathbf{A}\right)\cdot\boldsymbol{\tau}^*\,\psi_{2\sigma}(\mathbf{x})\right), \tag{1.41b}$$

where the dot products in the last lines are understood to be over the in-plane (x and y) components. In the case of the NNN hoppings, both the terms linear in $\mathbf{q}$ and those linear in θ_{ij} in the expansion of Eq. (1.38) vanish, and so NNN hoppings do not contribute to linear order.

Hence, we have reviewed how the minimal-coupling substitution, Eq. (1.34), arises in the low-energy continuum model of graphene. Later, we will discuss mechanical strain, which enters the Hamiltonian in a very much analogous way, and which can give rise to effective magnetic fields in graphene.

Note that the Hamiltonian of Eq. (1.41b) is, as expected, not time-reversal invariant unless $\mathbf{A}=0$[11]: starting from Eq. (1.23) and from the definition of $\psi_{b\sigma}(\mathbf{x})$, it is easy to see that

$$\mathcal{T}^{-1}\psi_{1\sigma}(\mathbf{x})\mathcal{T} = \psi_{2\sigma}(\mathbf{x}), \qquad \mathcal{T}^{-1}\psi^{\dagger}_{1\sigma}(\mathbf{x})\mathcal{T} = \psi^{\dagger}_{2\sigma}(\mathbf{x}), \tag{1.42a}$$

$$\mathcal{T}^{-1}\psi_{2\sigma}(\mathbf{x})\mathcal{T} = \psi_{1\sigma}(\mathbf{x}), \qquad \mathcal{T}^{-1}\psi^{\dagger}_{2\sigma}(\mathbf{x})\mathcal{T} = \psi^{\dagger}_{1\sigma}(\mathbf{x}). \tag{1.42b}$$

Applying time reversal to the Hamiltonian of Eq. (1.41b) gives

$$\mathcal{T}^{-1}H_{\mathrm{LE}}^{\mathrm{mag}}\mathcal{T} = H_{\mathrm{LE}}^{\mathrm{mag}}\Big|_{\mathbf{A}\to-\mathbf{A}}, \tag{1.43}$$

[11] Strictly speaking, it is time-reversal invariant as long as $\mathbf{B}=\nabla\times\mathbf{A}=0$.

as it should.

1.4.1.3 Density of states and Landau levels in graphene

The Landau levels in graphene have a dependence on the field magnitude B and on the level index n that is characteristic of Dirac electrons [5, 91]. For comparison, we first recall the Landau-level spectrum and density of states for quadratically dispersing electrons in 2D.

The Hamiltonian for an electron in the presence of a magnetic field $\mathbf{B}(\mathbf{x}) = \nabla \times \mathbf{A}(\mathbf{x})$ is

$$H = \frac{\left(\mathbf{p} + \frac{e}{c}\mathbf{A}(\mathbf{x})\right)^2}{2m}, \tag{1.44}$$

where we have neglected the Zeeman term for simplicity. In the Landau gauge, an out-of-plane magnetic field $\mathbf{B} = B\hat{z}$ can be accomplished by choosing $\mathbf{A} = -By\hat{x}$, yielding

$$H = \frac{p_y^2}{2m} + \frac{\left(p_x - \frac{eB}{c}y\right)^2}{2m} \tag{1.45a}$$

$$H = \frac{p_y^2}{2m} + \frac{1}{2}m\omega_{\mathrm{c,\,quad}}^2\left(y - \ell_B^2 p_x\right)^2, \tag{1.45b}$$

where $\omega_{\mathrm{c,\,quad}} := \frac{eB}{mc}$ is the cyclotron frequency in a quadratic dispersion and $\ell_B = \sqrt{\frac{c}{eB}}$ is the magnetic length. Since $[H, p_x] = 0$, the energy eigenstates have definite x-direction momentum k_x; they and their energies are given by

$$|\psi_n(k_x)\rangle = |k_x\rangle_x \otimes T\left(\ell_B^2 k_x \hat{y}\right)|n\rangle_y, \quad \varepsilon_n = \omega_{\mathrm{c,\,quad}}\left(n + \frac{1}{2}\right), \quad n \in \{0, 1, 2, \dots\}, \tag{1.46}$$

where $T(\mathbf{x})$ is the spatial translation operator and $|n\rangle$ are the harmonic-oscillator eigenstates.

To calculate the density of states, we must make the sensible assumption that physically meaningful states have their harmonic-oscillator origins located within the sample, which we take to have dimensions $L_x \times L_y$. To achieve this, we restrict $\ell_B^2 k_x \in [0, L_y]$ or, equivalently, $k_x \in [0, L_y/\ell_B^2]$. Assuming periodic boundary conditions, the spacing of k_x values is $2\pi/L_x$, meaning there are $\frac{L_x L_y}{2\pi\ell_B^2}$ allowed k_x values. In light of this, the density of states is given by

$$g(E) = \frac{1}{L_x L_y}\sum_{\sigma\in\{\uparrow,\downarrow\}}\sum_{k_x}\sum_{n=0}^{+\infty}\delta(E - \varepsilon_n) \tag{1.47a}$$

$$= \frac{1}{L_x L_y}(2)\left(\frac{L_x L_y}{2\pi\ell_B^2}\right)\sum_{n=0}^{+\infty}\delta(E - \varepsilon_n) \tag{1.47b}$$

$$= \frac{1}{\pi\ell_B^2}\sum_{n=0}^{+\infty}\delta(E - \varepsilon_n). \tag{1.47c}$$

Explicitly showing the field dependence,

$$g(E) = \frac{eB}{\pi c} \sum_{n=0}^{+\infty} \delta\left(E - \frac{eB}{mc}\left(n + \frac{1}{2}\right)\right). \tag{1.47d}$$

Hence, in 2D, the magnetic field reorganizes the spectrum into equally-spaced, positive-energy Landau levels, and the spacing is proportional to B.

Landau levels in graphene The eigenstates of the Hamiltonian of Eq. (1.41b) can be found by diagonalizing the corresponding first-quantized Hamiltonian [87], i.e.,

$$H_{\mathrm{LE}}^{\mathrm{mag}}(\mathbf{x}) = \left[\begin{array}{c|c} H_{\mathrm{K}}(\mathbf{x}) & \\ \hline & H_{\mathrm{K}'}(\mathbf{x}) \end{array}\right], \tag{1.48a}$$

$$H_{\mathrm{K}}(\mathbf{x}) = \quad v_{\mathrm{F}}\left(-\mathrm{i}\nabla + \frac{e}{c}\mathbf{A}(\mathbf{x})\right) \cdot \boldsymbol{\tau}, \tag{1.48b}$$

$$H_{\mathrm{K}'}(\mathbf{x}) = -v_{\mathrm{F}}\left(-\mathrm{i}\nabla + \frac{e}{c}\mathbf{A}(\mathbf{x})\right) \cdot \boldsymbol{\tau}^*. \tag{1.48c}$$

We have suppressed spin indices, since there is no spin dependence in the Hamiltonian.

A magnetic field $\mathbf{B} = B\hat{z}$ perpendicular to the graphene plane can be accomplished in the Landau gauge by choosing $\mathbf{A} = -By\hat{x}$. With this choice, it turns out that the square of the first-quantized Hamiltonian of Eq. (1.48) has a familiar form. Letting $\mathbf{q} = -\mathrm{i}\nabla$,

$$H_{\mathrm{K}}(\mathbf{x})^2 = v_{\mathrm{F}}^2\left(q_y^2 + \ell_B^{-4}(y - \ell_B^2 q_x)^2 + \ell_B^{-2}\tau_3\right), \tag{1.49a}$$

$$H_{\mathrm{K}'}(\mathbf{x})^2 = v_{\mathrm{F}}^2\left(q_y^2 + \ell_B^{-4}(y - \ell_B^2 q_x)^2 - \ell_B^{-2}\tau_3\right), \tag{1.49b}$$

where $\ell_B \coloneqq \sqrt{c/(e|B|)}$ is the magnetic length. These are just the Hamiltonians of harmonic oscillators in the y direction, with a minimum at the position $y = \ell_B^2 q_x$ and with an additional Zeeman-like term. Since $[H_b(\mathbf{x})^2, q_x] = 0$ and $[H_b(\mathbf{x})^2, \tau_3] = 0$, where $b \in \{\mathrm{K}, \mathrm{K}'\}$ is the valley index, the eigenstates of the operators of Eq. (1.49) are of the form $|q_x\rangle_x \otimes |\zeta\rangle_y \otimes |\tau\rangle_\tau$, where ζ is yet to be determined and $\tau = \pm 1$. Expressing the position and momentum in terms of canonical ladder operators,

$$y - \ell_B^2 q_x =: \frac{\ell_B}{\sqrt{2}}\left(a^\dagger + a\right), \tag{1.50a}$$

$$q_y =: \frac{\mathrm{i}}{\sqrt{2}\ell_B}\left(a^\dagger - a\right), \tag{1.50b}$$

the squared Hamiltonians become

$$H_{\mathrm{K}}(\mathbf{x})^2 = \omega_{\mathrm{c}}^2\left(a^\dagger a + \frac{1+\tau_3}{2}\right), \tag{1.51a}$$

$$H_{\mathrm{K}'}(\mathbf{x})^2 = \omega_{\mathrm{c}}^2\left(a^\dagger a + \frac{1-\tau_3}{2}\right), \tag{1.51b}$$

where $\omega_{\mathrm{c}} = \sqrt{2}v_{\mathrm{F}}/\ell_B$. It is now easy to write the eigenstates of the squared Hamiltonians in terms of harmonic oscillator states $|n\rangle$. Letting $|k_x, n, \tau\rangle := |q_x\rangle_x \otimes T(\ell_B^2 q_x \hat{y})\,|n\rangle_y \otimes |\tau\rangle_\tau$, where T is the translation operator, the ground state of $H_{\mathrm{K}}(\mathbf{x})^2$ is

$$|k_x, 0, -\rangle\,, \tag{1.52a}$$

and the excited state spaces are

$$\mathrm{span}(|k_x, n-1, +\rangle\,, |k_x, n, -\rangle), \quad n \in \{1, 2, 3, \dots\}; \tag{1.52b}$$

on the other hand, the ground state of $H_{\mathrm{K}'}(\mathbf{x})^2$ is

$$|k_x, 0, +\rangle\,, \tag{1.53a}$$

and the excited state spaces are

$$\mathrm{span}(|k_x, n-1, -\rangle\,, |k_x, n, +\rangle), \quad n \in \{1, 2, 3, \dots\}. \tag{1.53b}$$

The eigenvalues of $H_b(\mathbf{x})$ can be found by diagonalizing said Hamiltonian in each eigenspace of $H_b(\mathbf{x})^2$—this way, squaring the Hamiltonians simplifies the problem into a set of 2×2 eigenproblems. The eigenstates of $H_{\mathrm{K}}(\mathbf{x})$ and $H_{\mathrm{K}'}(\mathbf{x})$ are indexed by an integer $n \in \mathbb{Z}$, and are respectively

$$|q_x, n\rangle_{\mathrm{K}} = \begin{cases} |q_x, 0, -\rangle & n = 0 \\ \Big(|q_x, |n|-1, +\rangle - \mathrm{sgn}(n)\,|q_x, |n|, -\rangle\Big)/\sqrt{2} & n \neq 0 \end{cases} \tag{1.54a}$$

and

$$|q_x, n\rangle_{\mathrm{K}'} = \begin{cases} |q_x, 0, +\rangle & n = 0 \\ \Big(|q_x, |n|-1, -\rangle + \mathrm{sgn}(n)\,|q_x, |n|, +\rangle\Big)/\sqrt{2} & n \neq 0. \end{cases} \tag{1.54b}$$

In position space,

$$|q_x, n\rangle_{\mathrm{K}} \to \begin{cases} L_x^{-1} \mathrm{e}^{\mathrm{i}xq_x} \begin{bmatrix} 0 \\ \phi_0(y - \ell_B^2 q_x) \end{bmatrix} & n = 0 \\ L_x^{-1} \mathrm{e}^{\mathrm{i}xq_x} \begin{bmatrix} \phi_{|n|-1}(y - \ell_B^2 q_x) \\ -\mathrm{sgn}(n)\phi_{|n|}(y - \ell_B^2 q_x) \end{bmatrix} / \sqrt{2} & n \neq 0 \end{cases} \tag{1.55a}$$

and

$$|q_x, n\rangle_{\mathrm{K}'} \to \begin{cases} L_x^{-1} \mathrm{e}^{\mathrm{i}xq_x} \begin{bmatrix} \phi_0(y - \ell_B^2 q_x) \\ 0 \end{bmatrix} & n = 0 \\ L_x^{-1} \mathrm{e}^{\mathrm{i}xq_x} \begin{bmatrix} \mathrm{sgn}(n)\phi_{|n|}(y - \ell_B^2 q_x) \\ \phi_{|n|-1}(y - \ell_B^2 q_x) \end{bmatrix} / \sqrt{2} & n \neq 0, \end{cases} \tag{1.55b}$$

where L_x is the length of the system in the x direction and ϕ_n are the harmonic oscillator eigenstates. In both cases, they eigenvalues are

$$H_b(\mathbf{x}) \, |q_x, n\rangle_b = \omega_{\mathrm{c}} \, \mathrm{sgn}(n) \sqrt{|n|} \, |q_x, n\rangle_b \, . \tag{1.56}$$

Unlike with a parabolic dispersion, the Landau levels here scale with $\sqrt{|nB|}$: they are not equally spaced, and they scale with $\sqrt{|B|}$ rather than $|B|$. This behaviour, which is characteristic of a Dirac-like Hamiltonian, is clearly seen in the STS data shown in Fig. 1.4 for different values of magnetic field B.

Density of states Within the low-energy range in which the continuum model is applicable, the density of states is given by

$$g(E) = \frac{1}{L_x L_y} \sum_{\sigma \in \{\uparrow,\downarrow\}} \sum_{b \in \{\mathrm{K},\mathrm{K}'\}} \sum_{q_x} \sum_{n \in \mathbb{Z}} \delta\Big(E - \omega_{\mathrm{c}} \, \mathrm{sgn}(n) \sqrt{|n|}\Big). \tag{1.57}$$

The sums over σ and b each give factors of 2. The sum over q_x must be restricted, much like the the case of quadratically dispersing electrons: since the origins of the harmonic oscillator wavefunctions should remain within 0 and L_y, q_x can only range from 0 to L_y/ℓ_B^2 (see Eq. (1.55)). Assuming periodic boundary conditions, the spacing of q_x is $2\pi/L_x$, and so there are $L_x L_y/(2\pi\ell_B^2)$ allowed values of q_x. Therefore,

$$g(E) = \frac{1}{L_x L_y}(2)(2)\left(\frac{L_x L_y}{2\pi\ell_B^2}\right) \sum_{n \in \mathbb{Z}} \delta\Big(E - \omega_{\mathrm{c}} \, \mathrm{sgn}(n) \sqrt{|n|}\Big) \tag{1.58a}$$

$$= \frac{2}{\pi\ell_B^2} \sum_{n \in \mathbb{Z}} \delta\Big(E - \omega_{\mathrm{c}} \, \mathrm{sgn}(n) \sqrt{|n|}\Big). \tag{1.58b}$$

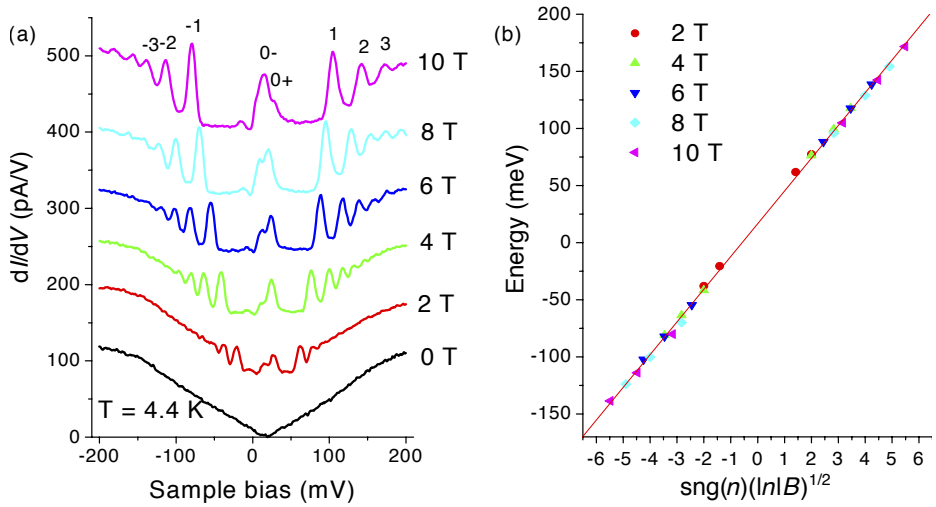

Figure 1.4: Landau levels in graphene, as seen with STS at $T = 4.4\,\mathrm{K}$. (a) Differential conductance, proportional to the real-space spectral function $A(\omega, \mathbf{r})$, as a function of bias voltage for different magnetic field strengths. The zero-field trace shows the linear density of states characteristic of Dirac spectra. Peaks in the nonzero-field traces correspond to Landau levels, and the Landau-level indices are shown on the $B = 10\,\mathrm{T}$ trace. (b) The Landau-level energies are shown to be linear in $\mathrm{sgn}(n)\sqrt{|nB|}$, as expected from Eq. (1.56). (Figure reproduced from Ref. 98, i.e., Eva Y. Andrei, Guohong Li, and Xu Du, "Electronic properties of graphene: a perspective from scanning tunneling microscopy and magnetotransport", *Reports on Progress in Physics* 75(5):056501 (2012). © IOP Publishing. Reproduced with permission. All rights reserved. Permission conveyed through Copyright Clearance Center, Inc.)

1.4.2 Time-reversal invariant topological insulators

As discussed in Sec. 1.2.1, topologically distinct insulating states of a given symmetry class cannot be continuously deformed into each other without closing the energy gap, giving rise to topologically protected gapless states at the boundary between a topological system and the "trivial" vacuum. Hence, the presence of these boundary states are signaled by a nontrivial topological invariant, a property of the bulk Hamiltonian—this is the bulk-boundary correspondence.

In three-dimensional electronic systems in which spin plays an important role, such as those with non-negligible SOC, time-reversal symmetry necessarily squares to -1. In the absence of particle-hole and chiral symmetries, these systems fall into class AII, meaning insulating phases can be classified according to a $\mathbb{Z}_2$ topological invariant [23, 24, 50], the Fu-Kane-Mele (FKM) invariant [21][12]. In inversion-symmetric crystals, the FKM invariant can be calculated from the product of the inversion eigenvalues of the occupied Bloch states at the time-reversal invariant momenta (TRIM) (including only one state in each Kramers pair) [24]; more generally, the invariant is defined in terms of the Pfaffian of the so-called gluing matrix [50].

It turns out several materials realize minimal examples of 3D topological insulators with nontrivial FKM invariant, with each surface harbouring a single massless 2D Dirac Hamiltonian centered at zero momentum. They are Bi_2Se_3, Bi_2Te_3, and Sb_2Te_3 [5, 6, 99], which all share the same (inversion-symmetric) space group and rhombohedral crystal structure [99].

At neutrality, $X \in \{\mathrm{Sb}, \mathrm{Bi}\}$ has three valence electrons in its outer p shell, while $Y \in \{\mathrm{Se}, \mathrm{Te}\}$ has four valence electrons in its outer p shell, with the latter lying energetically below the former [5, 99]. Naïvely, one expects that in X_2Y_3, two X atoms donate six valence electrons to three Y atoms, leaving the X atoms with full p shells and the Y atoms with empty ones, giving rise to a topologically trivial insulator [5]. While this picture is correct for Sb_2Se_3 (which also shares the same crystal structure as the other three), it is incorrect for Bi_2Se_3, Bi_2Te_3, and Sb_2Te_3, in which SOC is strong enough to cause a band inversion in the neighborhood of the Γ point [5, 99]. There, the states derived from X lie *below* those from Y, leading to a change in the inversion eigenvalues of the occupied Bloch states at the Γ point and a nontrivial FKM invariant in the three compounds.

In all four compounds, this physics, and the low-energy behaviour more generally, is captured by a continuum model in the neighborhood of the Γ point. In the basis $\big(|P1_z^+, \uparrow\rangle, |P2_z^-, \uparrow\rangle, |P1_z^+, \downarrow\rangle, |P2_z^-, \downarrow\rangle\big)$, where the $P1$ states are derived primarily from X and the $P2$

[12] There are also three "weak" topological $\mathbb{Z}_2$ invariants, which depend sensitively on translational symmetry, making for a four-index topological classification in translation-invariant systems [23, 24].

states, from Y, the Bloch Hamiltonian is given by [5, 99]

$$H_{\mathbf{k}} = \varepsilon^0_{\mathbf{k}} + \mathcal{M}_{\mathbf{k}}\sigma_0\tau_3 + A_1 k_z \sigma_3\tau_1 + A_2(k_x\sigma_1 + k_y\sigma_2)\tau_1, \tag{1.59a}$$

$$\varepsilon^0_{\mathbf{k}} := C + D_1 k_z^2 + D_2 k_\perp^2, \quad \mathcal{M}_{\mathbf{k}} := M - B_1 k_z^2 - B_2 k_\perp^2, \tag{1.59b}$$

where $k_\perp := \sqrt{k_x^2 + k_y^2}$, and tensor products are implied, i.e., $\sigma_\mu\tau_\nu = \sigma_\mu \otimes \tau_\nu$. The four bands have energies $\varepsilon_{\mathbf{k}-}, \varepsilon_{\mathbf{k}-}, \varepsilon_{\mathbf{k}+}, \varepsilon_{\mathbf{k}+}$, where

$$\varepsilon_{\mathbf{k}\pm} = \varepsilon^0_{\mathbf{k}} \pm \sqrt{A_1^2 k_z^2 + A_2^2 k_\perp^2 + \mathcal{M}_{\mathbf{k}}^2}, \tag{1.60}$$

so the model is gapped as long as $M \neq 0$. The parameter M increases with SOC, and the band inversion in the neighborhood of Γ—a signature of the topologically nontrivial phase—occurs for $M > 0$. Indeed, since $H_{\mathbf{k}} = C + M\sigma_0\tau_3$ and inversion symmetry $\mathcal{I} = \sigma_0\tau_3$, it is easy to explicitly see that the inversion eigenvalues of the lower-energy states are opposite between negative and positive M.

1.4.2.1 Edge states

We can use the low-energy Hamiltonian to derive the gapless edge theory of the material, using a Jackiw-Rebbi-type ansatz: let $M(z)$ be position dependent and cross from negative for $z < 0$ to positive for $z > 0$, with $M(0) = 0$. Since a gap closing must separate the topologically trivial ($M < 0$) and nontrivial ($M > 0$) phases, we expect gapless states localized at the $z = 0$ place, which separates trivial and nontrivial regions in space. With the understanding that the trivial phase is equivalent to the vacuum, this procedure gives us the edge states [6]. The ansatz takes the form

$$\psi_{k_x,k_y}(x,y,z) = c\,\mathrm{e}^{\mathrm{i}k_x x}\mathrm{e}^{\mathrm{i}k_y y}\mathrm{e}^{-\gamma\int_0^z \mathrm{d}\tilde{z}\, M(\tilde{z})}\phi_{k_x,k_y}, \tag{1.61}$$

where c is a normalization constant, γ is a yet-undetermined positive number, and ϕ_{k_x,k_y} is a yet-undetermined four-component spinor. In position space, the linearized Hamiltonian takes the form

$$H_{\text{lin}} = C + M(z)\sigma_0\tau_3 + A_1(-\mathrm{i}\partial_z)\sigma_3\tau_1 + A_2\Big((-\mathrm{i}\partial_x)\sigma_1 + (-\mathrm{i}\partial_y)\sigma_2\Big)\tau_1, \tag{1.62}$$

and the eigenvalue equation for the ansatz of Eq. (1.61) becomes

$$E\psi_{k_x,k_y}(x,y,z) = H_{\text{lin}}\psi_{k_x,k_y}(x,y,z) \tag{1.63a}$$

$$= \Big((\sigma_0\tau_3 + \mathrm{i}\gamma A_1\sigma_3\tau_1)M(z) + (k_x\sigma_1 + k_y\sigma_2)\tau_1\Big)\psi_{k_x,k_y}(x,y,z) \tag{1.63b}$$

$$\Leftrightarrow E\phi_{k_x,k_y} = \Big((\sigma_0\tau_3 + \mathrm{i}\gamma A_1\sigma_3\tau_1)M(z) + (k_x\sigma_1 + k_y\sigma_2)\tau_1\Big)\phi_{k_x,k_y}. \tag{1.63c}$$

Since the edge states should not be sensitive to the details of $M(z)$, the solutions ϕ_{k_x,k_y} should be part of $\ker(\sigma_0\tau_3 + \mathrm{i}\gamma A_1\sigma_3\tau_1)$. The kernel is nontrivial only for $|\gamma A_1| = 1$, and since $A_1 > 0$ [99], we must choose $\gamma = 1/A_1$. Specifically,

$$\ker(\sigma_0\tau_3 + \mathrm{i}\sigma_3\tau_1) = \mathrm{span}(u_1, u_2), \tag{1.64a}$$

$$u_1 \coloneqq \frac{1}{\sqrt{2}}\begin{bmatrix}0\\0\\\mathrm{i}\\1\end{bmatrix}, \quad u_2 \coloneqq \frac{1}{\sqrt{2}}\begin{bmatrix}1\\\mathrm{i}\\0\\0\end{bmatrix}. \tag{1.64b}$$

Note that u_1 and u_2 are states of definite spin: u_1 has spin down and u_2 has spin up. Since the Hamiltonian H_{lin} is closed in this subspace, we get an effective Hamiltonian for the surface states. In terms of Pauli matrices η_μ corresponding to the basis (u_1, u_2), it is

$$H_{\mathrm{surf}} = A_2(k_x\eta_1 + k_y\eta_2), \tag{1.65}$$

a 2D massless Dirac Hamiltonian[13]. From its eigenstates, we find

$$E_+ = k_\perp, \qquad \phi_{k_x,k_y,+} = \frac{1}{\sqrt{2}}\begin{bmatrix}u_1 & u_2\end{bmatrix}\begin{bmatrix}1\\ \frac{k_x+\mathrm{i}k_y}{k_\perp}\end{bmatrix}, \tag{1.66a}$$

$$E_- = -k_\perp, \qquad \phi_{k_x,k_y,+} = \frac{1}{\sqrt{2}}\begin{bmatrix}u_1 & u_2\end{bmatrix}\begin{bmatrix}-1\\ \frac{k_x+\mathrm{i}k_y}{k_\perp}\end{bmatrix}. \tag{1.66b}$$

The eigenstates have definite pseudohelicity in the pseudospin of the η_μ matrices. The surface state dispersion and the spin-momentum locking in Bi_2Te_3 is depicted in Fig. 1.5.

The topological protection of the gapless surfaces state can also be seen directly from the surface Hamiltonian of Eq. (1.65) [50]. The Hamiltonian H_{surf} is invariant under time-reversal symmetry, which takes the form $\mathcal{T} = \mathrm{i}\eta_2 K$, where K is the operation of complex conjugation [99]. However, the only possible mass term—that proportional to η_3—breaks time-reversal symmetry, and hence is forbidden in a time-reversal-symmetric theory.

The surface Hamiltonian can even be used to show that the system's topological invariant is of type $\mathbb{Z}_2$, rather than $\mathbb{Z}$. Consider two copies of H_{surf} "added" together via a direct product, i.e., $\mathbb{1}_2 \otimes H_{\mathrm{surf}}$ [50]. Since the topological invariant of the system gives the number of surface states[14], $\mathbb{1}_2 \otimes H_{\mathrm{surf}}$ is the surface Hamiltonian for a system with a doubled topological invariant. However, doubling a $\mathbb{Z}_2$ invariant just makes it trivial again. In the case at hand, the Hamiltonian $\mathbb{1}_2 \otimes H_{\mathrm{surf}}$ *does* have a mass term allowed by the time-reversal symmetry $\mathbb{1}_2 \otimes \mathrm{i}\eta_2 K$, namely, $\eta_2 \otimes \eta_3$, meaning the surface states described by $\mathbb{1}_2 \otimes H_{\mathrm{surf}}$

[13] In a real material, another Dirac theory describes states at the opposite surface, ensuring compliance with the Nielsen-Ninomiya theorem.

[14] More specifically, $N_{\mathrm{s}} \bmod 2 = \Delta\nu \bmod 2$, where N_{s} is the number of surface states and $\Delta\nu$ is the change in the topological invariant ν across the boundary [6].

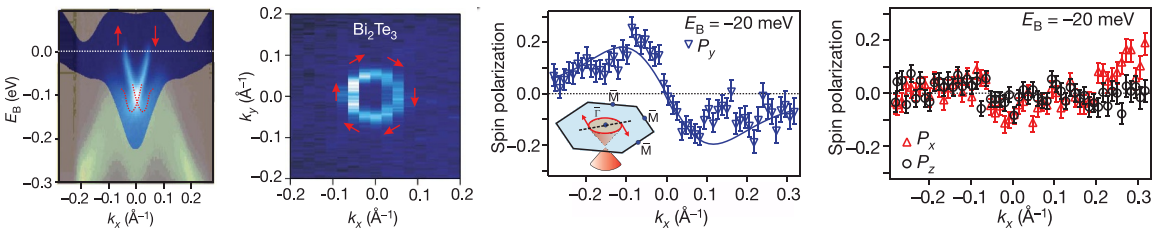

(a) (b) (c) (d)

Figure 1.5: Spin-resolved ARPES data showing helical Dirac surface states in Bi_2Te_3. (a): The linearly dispersing surface bands are seen within the bulk gap. Gold-colored shading shows the continuum of bulk bands. The red arrows indicate spin directions. (b): Data shows the Fermi surface, and red arrows depict spin-momentum locking. (c) and (d): Evidence for spin-momentum locking. Data is taken along the k_x direction in the surface momentum space, as shown in the inset of (c). The y spin polarization (c) is nonzero and changes at the Dirac point ($k_x =$), while the x and z spin polarizations (d) are scattered around zero. (Reproduced with the permission of Springer Nature from Ref. 100, i.e., D. Hsieh et al., "A tunable topological insulator in the spin helical Dirac transport regime", *Nature*, 460:1101 (2009).)

are not topologically protected and can become gapped. Therefore, the topological index characterizing the Hamiltonian of Eq. (1.59) must be of type $\mathbb{Z}_2$.

Note also that 2D materials in class AII are characterized by a $\mathbb{Z}_2$ topological index, and harbor 1D Dirac Hamiltonians on their surfaces. This topological state, called the quantum spin Hall state [22], has been realized in HgTe/CdTe quantum well structures [6, 99].

1.4.3 Cuprate high-temperature superconductors

The copper-oxide, or cuprate, superconductors were the first class of high-temperature superconductors to be discovered, and have been a fixture [86, 101–115] and at times an object of controversy [116, 117] in condensed-matter physics since their discovery in 1986 [118]. Even after three and a half decades, the mechanism for the high-temperature superconductivity, as well as the nature of the "normal" state leading to it, is still debated [115].

The cuprates' phase diagram hosts a large number of phases [110], some of which are shown in the simplified phase diagram of Fig. 1.6. In particular, we see the dome-shaped superconducting phase with transition temperature T_c that occurs at intermediate hole doping p, as well as the antiferromagnetic correlated insulator phase (AF) that occurs around zero doping, the pseudogap (PG) region beside it, the "strange metal" non-Fermi liquid (SM) phase above the purported quantum critical point [119, 120] at doping p^*, and the ordinary Fermi liquid (FL) phase a high doping. The electron-doped side of the phase diagram (not shown) also has a superconducting dome, but with lower critical temperatures [113].

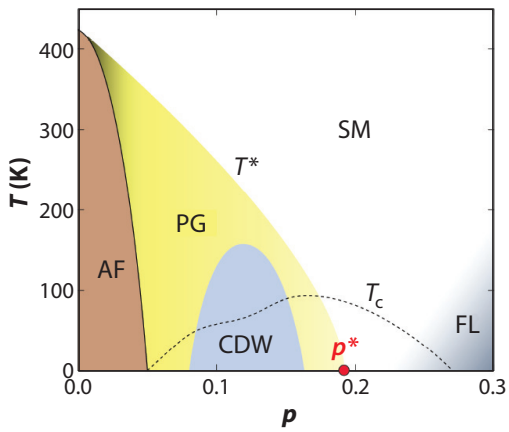

Figure 1.6: Schematic phase diagram of the hole-doped cuprates, as a function of hole doping p and temperature T. Near zero doping lies an antiferromagnetic correlated insulator phase (AF). At high doping, the material is an ordinary Fermi liquid (FL), with low-temperature resistivity proportional to T^2. At lower doping, the system is a "strange metal" non-Fermi liquid (SM), characterized by resistivity proportional to T. At intermediate dopings lies the superconducting dome, delimited by the superconducting critical temperature T_c. Purportedly, hidden within the dome is a quantum critical point, which occurs at doping p^*. The pseudogap (PG) regime is characterized by a partially developed superconducting gap; its onset is at T^*. There is also a charge-density wave (CDW) phase. (Used with the permission of Annual Reviews, Inc., from Ref. 112, i.e., Cyril Proust and Louis Taillefer, "The Remarkable Underlying Ground States of Cuprate Superconductors", *Annual Review of Condensed Matter Physics* 10:409 (2019); permission conveyed through Copyright Clearance Center, Inc.)

1.4.3.1 Electronic configuration

The cuprates' crystal structures are either tetragonal or orthorhombic, depending on the specific material [104]. The key feature they all share are weakly coupled CuO_2 planes made up of Cu^{2+} and O^{2-} ions (Fig. 1.7) [104]. This quasi-two-dimensional structure suggests that the materials' electronic properties are essentially determined by the CuO_2 planes [86] and, indeed, "the results of band-structure calculations for various cuprates [...] all show energy bands predominantly derived from the CuO_2 planes, with no significant dispersion in the c-axis direction" [104]. Furthermore, there is strong experimental evidence for charge confinement in CuO_2 layers [104]. Their quasi-two-dimensional electronic structure makes the cuprates particularly good candidates for ARPES [86].

At zero doping, the Cu^{2+} ions have $3d^9$ configuration, leaving one empty state, while the O^{2-} ions have configuration $2p^6$, leaving no empty states [121,122]. On both Cu^{2+} and O^{2-}, tetragonal crystal fields split the hydrogenic wavefunctions: in Cu^{2+}, all the split levels are filled except the uppermost one, a $3d_{x^2-y^2}$ state, which is half filled with a single electron; in O^{2-}, all the split levels are filled *including* the highest one—either $2p_x$ or $2p_y$, depending on the environment (see Fig. 1.7)—which is filled with two electrons [121]. The orientation of these states within the crystal, as well as the wavefunction overlaps, are depicted in Fig. 1.7.

The hybridization between these uppermost Cu^{2+} and O^{2-} states splits their energy,

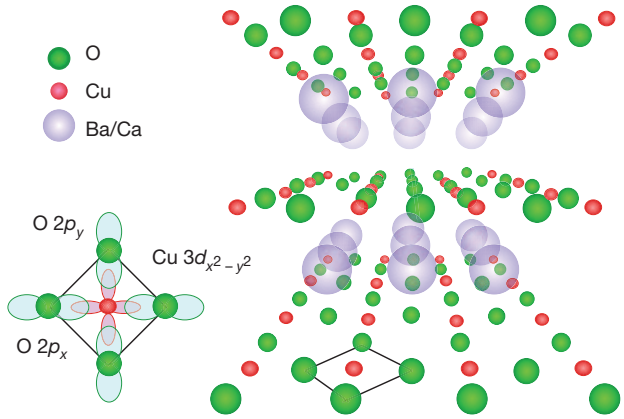

Figure 1.7: CuO_2 planes (separated by charge-reservoir spacer layers) in the cuprate family of materials. The Cu^{2+} ions are shown in pink and the O^{2-} ions are shown in light green. The wavefunctions of the highest occupied orbitals are shown in the bottom-left. (Reproduced with the permission of Springer Nature from Ref. 110, i.e., B. Keimer et al., "From quantum matter to high-temperature superconductivity in copper oxides", *Nature*, 518:179 (2015).)

leaving a single band that crosses the Fermi level, as shown in Fig. 1.8. (The insulating phase around zero doping arises from interaction effects rather than band theory.) It turns out this band can be described by a simple Hubbard model involving the Cu^{2+} sites alone: the model involves hole-like objects called *Zhang-Rice singlets*, which are in fact delocalized holes residing on the O^{2-} ions and centered at a Cu^{2+} ion [123, 124]. Such a simple model describes many—though not all—electronic properties of the CuO_2 layers [121].

The model Hamiltonian is the Hubbard model on a square lattice [119]:

$$H_{\text{Hub}} = -t \sum_{\langle ij \rangle \sigma} \left(c_{i\sigma}^{\dagger} c_{j\sigma} + \text{H.c.} \right) + U \sum_{i} n_{i\uparrow} n_{i\downarrow}, \tag{1.67}$$

where $n_{i\sigma} = c_{i\sigma}^{\dagger} c_{i\sigma}$ with $\sigma \in \{\uparrow, \downarrow\}$. In the cuprates, U is large compared to t; therefore, double occupancy is heavily penalized, and at half filling ($n = 1$, where n is the number of electrons per site), Mott insulator physics arises ("AF" phase in Fig. 1.6). At zero and positive hole doping δ, where $\delta = 1 - n$, the Hamiltonian of Eq. (1.67) in the large-U limit can be transformed via a Schrieffer-Wolff transformation to the low-energy subspace (up to

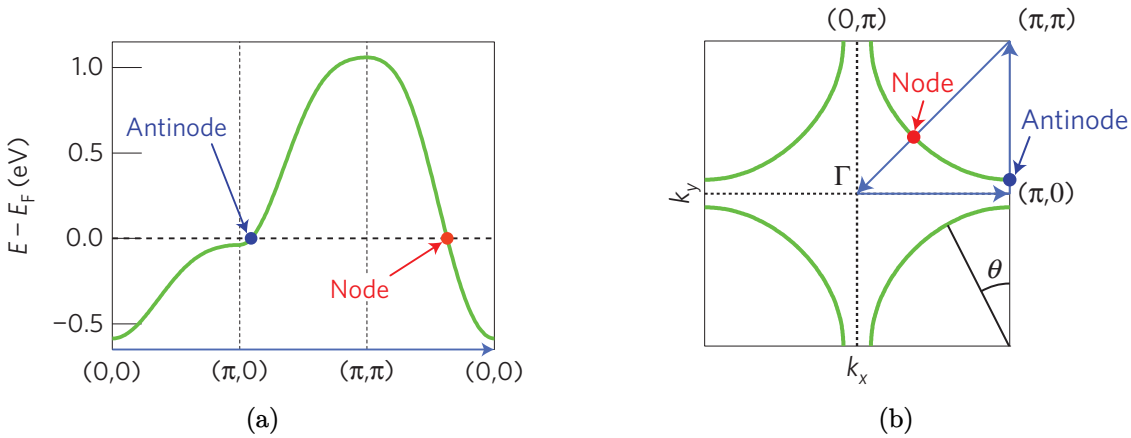

Figure 1.8: (a): The sole band that crosses the Fermi energy in the cuprate family of materials, shown along high-symmetry paths in momentum space. (b): Schematic Fermi surface. Also shown is the momentum-space path travelled in (a). (Reproduced with the permission of Springer Nature from Ref. 86, i.e., Makoto Hashimoto et al., "Energy gaps in high-transition-temperature cuprate superconductors", *Nature Physics*, 10:483 (2014).)

order t/U), in which no sites are doubly occupied [119]. The result is[15]

$$H = H_t + H_J, \tag{1.68a}$$

$$H_t = -t\,\mathcal{P}_{\mathrm{G}} \left(\sum_{\langle ij\rangle\sigma} c_{i\sigma}^{\dagger} c_{j\sigma} + \mathrm{H.c.} \right) \mathcal{P}_{\mathrm{G}}, \tag{1.68b}$$

$$H_J = J \sum_{\langle ij\rangle} \mathbf{S}_i \cdot \mathbf{S}_j, \tag{1.68c}$$

where $J \coloneqq 4t^2/U$, and $\mathcal{P}_{\mathrm{G}} \coloneqq \prod_i (1 - n_{i\uparrow} n_{i\downarrow})$ is the *Gutzwiller projection operator*, which projects onto the subspace of non-doubly-occupied sites. The Hamiltonian of Eq. (1.68) should be thought of as an operator in the projected Hilbert space, in which the allowed states at each lattice site are $|0\rangle$, $|\uparrow\rangle$, and $|\downarrow\rangle$—this excludes the state $|\uparrow\downarrow\rangle$ allowed in the original Hilbert space. In this transformed form, the antiferromagnetic interactions leading to antiferromagnetism at small doping are explicit. (Zhang and Rice showed [123] that the Hamiltonian of Eq. (1.68), an effective Hamiltonian involving only the Cu d holes, can also be derived from the realistic three-orbital model involving the uppermost Cu^{2+} and O^{2-} orbitals, justifying previous work that asserted the adequacy of the single-band Hubbard model of Eq. (1.67).)

A common ansatz for the ground state of a strong-U Hubbard model is $\mathcal{P}_{\mathrm{G}} |\mathrm{FS}\rangle$, that is, a Fermi sea wavefunction with site double occupancy projected away. To capture superconductivity, the ground-state ansatz instead becomes $\mathcal{P}_{\mathrm{G}} |\mathrm{BCS}\rangle$, where $|\mathrm{BCS}\rangle$ is a

[15] An additional, so-called "three-site hopping" term is often neglected for simplicity [119]; this term is higher-order in δ, and so can safely be neglected for small hole doping [125]. Furthermore, no projection is needed on the spin term because they yield zero when acting on doubly-occupied sites; specifically, $\mathbf{S}\,|\uparrow\downarrow\rangle = \frac{1}{2}\boldsymbol{\sigma}_{ss'} c_s^{\dagger} c_{s'}\,|\uparrow\downarrow\rangle = \frac{1}{2}\boldsymbol{\sigma}_{ss'}\delta_{ss'}\,|\uparrow\downarrow\rangle = 0$.

BCS-like superconducting ground state[16] [119, 123]. However, the ground-state ansatz $\mathcal{P}_{\mathrm{G}} |\mathrm{BCS}\rangle$ (like $\mathcal{P}_{\mathrm{G}} |\mathrm{FS}\rangle$) is a complicated correlated quantum state not amenable to an exact analytical treatment. One must either resort to numerics [126, 127], or to an approximation like the one we now review.

1.4.3.2 High-temperature superconductivity and Gutzwiller approximation

The Gutzwiller approximation is a rough approximation allowing for analytical evaluations of correlation functions in the correlated ground state

$$|\mathrm{GS}\rangle \coloneqq \mathcal{P}_{\mathrm{G}} |\mathrm{BCS}\rangle \tag{1.69}$$

in terms of those of the analytically tractable state $|\mathrm{BCS}\rangle$, assuming complete statistical independence of the electron populations on the lattice sites [119]. In order to determine the state $|\mathrm{BCS}\rangle$ that gives the lowest-energy ansatz $|\mathrm{GS}\rangle$, an additional Hartree-Fock-Bogoliubov mean-field theory approximation is necessary [125]. This approach has been shown to give a decent semi-quantitative account of observables in cuprate superconductors [119, 125].

Gutzwiller approximation The idea of the Gutzwiller approximation is to relate correlation functions in $|\mathrm{GS}\rangle$ and $|\mathrm{BCS}\rangle$ via statistical occupation factors. First, consider hopping processes: letting $\langle\cdot\rangle$ denote expectation values with respect to $|\mathrm{GS}\rangle$ and $\langle\cdot\rangle_0$ denote those with respect to $|\mathrm{BCS}\rangle$, one asserts that $\langle c^\dagger_{i\sigma} c_{j\sigma}\rangle = g_t \langle c^\dagger_{i\sigma} c_{j\sigma}\rangle_0$, where the factor g_t depends on average occupancy of the states $i\sigma$ and $j\sigma$. Figures 1.9a and 1.9b depict the process $c^\dagger_{i\uparrow} c_{j\uparrow}$ in the states $|\mathrm{BCS}\rangle$ and $|\mathrm{GS}\rangle$, respectively. It illustrates that spin-down electrons may or may not be present at sites i and j in the former case, but cannot be present in the latter case because of the non-double-occupancy constraint. The relative probability of this process in the two states gives the value of g_t [125]:

$$g_t = \frac{\sqrt{n_{j\uparrow}(1-n_i)n_{i\uparrow}(1-n_j)}}{\sqrt{n_{j\uparrow}(1-n_{i\uparrow})n_{i\uparrow}(1-n_{j\uparrow})}}, \tag{1.70a}$$

where $n_i = n_{i\uparrow} + n_{i\downarrow}$. Assuming a translation- and spin-rotation-invariant state, the occupations $n_{i\sigma} = n/2$ for all i and σ, and one finds

$$g_t = \frac{2\delta}{1+\delta}. \tag{1.70b}$$

By spin-rotation symmetry, the same g_t applies to spin-down hopping. The behaviour of g_t at small hole doping ($\delta \to 0$) shows how the Gutzwiller approximation captures the strong suppression of hopping in the correlated state $|\mathrm{GS}\rangle$ that arises from the projection $\mathcal{P}_{\mathrm{G}}$.

[16] Though we call it "BCS", the superconducting symmetry and even the parity are a priori undetermined.

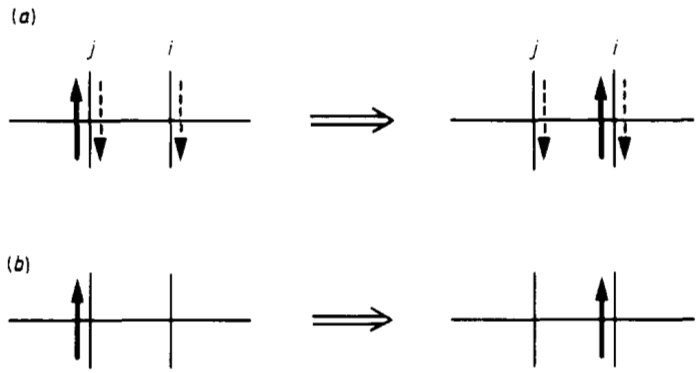

Figure 1.9: Hopping process from $j \uparrow$ to $i \uparrow$, used to determine the factor g_t. (a) In the state $|\mathrm{BCS}\rangle$, there may or may not be down spins at sites i and j. (b) In the state $|\mathrm{GS}\rangle$, in which double occupancy is forbidden, there can be no down spins present at sites i and j. (Figure reproduced from Ref. 125, i.e., F. C. Zhang, C. Gros, T. M. Rice, and H. Shiba, "A renormalised Hamiltonian approach to a resonant valence bond wavefunction", *Superconductor Science and Technology* 1(1):36–46 (1988). © IOP Publishing. Reproduced with permission. All rights reserved. Permission conveyed through Copyright Clearance Center, Inc.)

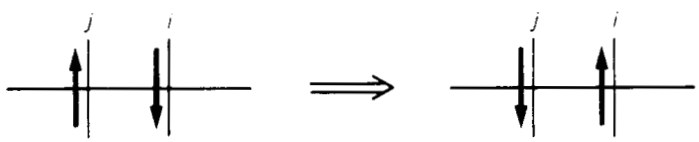

Figure 1.10: Spin exchange process between i and j, used to determine the factor g_J. (Figure reproduced from Ref. 125, i.e., F. C. Zhang, C. Gros, T. M. Rice, and H. Shiba, "A renormalised Hamiltonian approach to a resonant valence bond wavefunction", *Superconductor Science and Technology* 1(1):36–46 (1988). © IOP Publishing. Reproduced with permission. All rights reserved. Permission conveyed through Copyright Clearance Center, Inc.)

Next, consider spin exchange processes: in this case, one asserts that $\langle \mathbf{S}_i \cdot \mathbf{S}_j \rangle = g_J \langle \mathbf{S}_i \cdot \mathbf{S}_j \rangle_0$. The processes that yield nonzero spin interaction $\mathbf{S}_i \cdot \mathbf{S}_j = S_i^z S_j^z + (S_i^+ S_j^- + S_i^- S_j^+)/2$ have a single electron on each site i and j [125]. To compute the factor g_J, one can consider, for example, the spin exchange depicted in Fig. 1.10: from the relative probabilities of the process $S_i^+ S_j^-$ in the states $|\mathrm{GS}\rangle$ and $|\mathrm{BCS}\rangle$, one finds

$$g_J = \frac{\sqrt{n_{j\uparrow} n_{i\downarrow} n_{j\downarrow} n_{i\uparrow}}}{\sqrt{n_{j\uparrow}(1-n_{j\downarrow}) n_{i\downarrow}(1-n_{i\uparrow}) n_{j\downarrow}(1-n_{j\uparrow}) n_{i\uparrow}(1-n_{i\downarrow})}} \tag{1.71a}$$

$$= \frac{4}{(1+\delta)^2}, \tag{1.71b}$$

where in the second line we have again assumed a translation- and spin-rotation-invariant state. Other processes resulting from the spin interaction give the same factor. Hence, Eq. (1.71) shows that at low hole doping, spin correlation is enhanced in the correlated state.

The ground-state ansatz $|\mathrm{GS}\rangle = \mathcal{P}_\mathrm{G} |\mathrm{BCS}\rangle$ must still be determined by minimizing the

energy $W \coloneqq \langle H \rangle$. Noting that within the Gutzwiller approximation,

$$\langle H_t \rangle = g_t \langle H_t \rangle_0 \,, \tag{1.72a}$$

$$\langle H_J \rangle = g_J \langle H_J \rangle_0 \,, \tag{1.72b}$$

where the first equation stems from the fact that $\langle \mathcal{P}_\mathrm{G}\, c^\dagger_{i\sigma} c_{j\sigma} \mathcal{P}_\mathrm{G} \rangle = \langle c^\dagger_{i\sigma} c_{j\sigma} \rangle = g_t \langle c^\dagger_{i\sigma} c_{j\sigma} \rangle_0$, we may write $W = \langle H_t + H_J \rangle = \langle \tilde{H} \rangle_0$, where

$$\tilde{H} \coloneqq g_t H_t + g_J H_J. \tag{1.73}$$

Hence, by finding the ground state $|\mathrm{BCS}\rangle$ of the effective, or "renormalized", Hamiltonian $\tilde{H}$, one also finds (within the Gutzwiller approximation) the highly correlated ground state $|\mathrm{GS}\rangle$ of H via Eq. (1.69).

Mean-field theory of the effective Hamiltonian The effective Hamiltonian $\tilde{H}$ is still an interacting Hamiltonian, but it is amenable to a mean-field treatment. To find its ground state $|\mathrm{BCS}\rangle$ and the energy W, a Hartree-Fock-Bogoliubov mean-field theory is performed on the effective Hamiltonian $\tilde{H}$ [119,124,125,128]. The interaction $\mathbf{S}_i \cdot \mathbf{S}_j = c^\dagger_{i\sigma} \frac{1}{2} \boldsymbol{\sigma}_{\sigma\sigma'} c_{i\sigma'} \cdot c^\dagger_{js} \frac{1}{2} \boldsymbol{\sigma}_{ss'} c_{js'}$ is decoupled into the Hartree, Fock, and pairing channels, and the ansatz is assumed to be translationally and fully spin-rotationally invariant (implying spin-singlet pairing [76]). The resulting superconducting state turns out to be energetically competitive with other proximate ground states over a wide range of hole doping, both within mean-field theory and when compared with more sophisticated methods, and corresponds well to experimental observations [119]. The remaining fields resulting from the decoupling are $\langle c^\dagger_{i\sigma} c_{i+\hat{\mu},\sigma} \rangle =: \chi_\mu$ and $\langle c_{i\uparrow} c_{i+\hat{\mu},\downarrow} \rangle = \langle c_{i\uparrow} c_{i-\hat{\mu},\downarrow} \rangle =: \Delta_\mu$, where $\mu \in \{x, y\}$. However, the lower-energy state turns out to have $\chi_x = \chi_y =: \chi$, and $\Delta_x = -\Delta_y =: \Delta$ [125], so with the benefit of hindsight, one can choose a mean-field Hamiltonian with only two variational parameters χ and Δ, together with the electron density constraint $\langle c^\dagger_{i\sigma} c_{i\sigma} \rangle = n/2$. After Fourier-transforming to momentum space, it is given by

$$\tilde{H}_\mathrm{MFT} = \sum_{\mathbf{k}\sigma} \xi_\mathbf{k} c^\dagger_{\mathbf{k}\sigma} c_{\mathbf{k}\sigma} - \sum_\mathbf{k} \Delta_\mathbf{k} \left(c^\dagger_{\mathbf{k}\uparrow} c^\dagger_{-\mathbf{k}\downarrow} + \mathrm{H.c.} \right), \tag{1.74}$$

where

$$\xi_\mathbf{k} = -2\tilde{t}(\cos k_x + \cos k_y) - \mu, \qquad \tilde{t} \coloneqq g_t t + \frac{3}{4} g_J J \chi, \tag{1.75a}$$

$$\Delta_\mathbf{k} = \tilde{\Delta}(\cos k_x - \cos k_y), \qquad \tilde{\Delta} \coloneqq \frac{3}{2} g_J J \Delta. \tag{1.75b}$$

Note that the d-wave symmetry of $\Delta_\mathbf{k}$ emerges naturally as the lower-energy state in this approach, a prediction that predated the experimental detection of d-wave superconductivity in the cuprates [119].

As derived in Sec. 2.G (though with an additional, next-nearest-neighbor hopping t'), the self-consistency equations, together with the hole-number constraint, are

$$\Delta \stackrel{!}{=} \frac{1}{2N} \sum_{\mathbf{k}} \frac{\Delta_{\mathbf{k}}}{2E_{\mathbf{k}}} (\cos k_x - \cos k_y), \tag{1.76a}$$

$$\chi \stackrel{!}{=} \frac{1}{4N} \sum_{\mathbf{k}} \left(1 - \frac{\xi_{\mathbf{k}}}{E_{\mathbf{k}}}\right) (\cos k_x + \cos k_y), \tag{1.76b}$$

$$n = 1 - \delta \stackrel{!}{=} \frac{1}{N} \sum_{\mathbf{k}} \left(1 - \frac{\xi_{\mathbf{k}}}{E_{\mathbf{k}}}\right), \tag{1.76c}$$

where N is the number of lattice sites and $E_{\mathbf{k}} \coloneqq \sqrt{\xi_{\mathbf{k}}^2 + |\Delta_{\mathbf{k}}|^2}$; these must be solved keeping in mind the explicit dependence of g_t and g_J on δ. The excited states of the Hamiltonian H are given by [125]

$$|\Psi_{\mathbf{k}\sigma}\rangle = \mathcal{P}_{\mathrm{G}} \gamma_{\mathbf{k}\sigma}^{\dagger} |\mathrm{BCS}\rangle, \tag{1.77}$$

where $\gamma_{\mathbf{k}\sigma}^{\dagger}$ is a creation operator for the Bogoliubov eigenstates of $\tilde{H}_{\mathrm{MFT}}$, and it can be shown what their energy is $E_{\mathbf{k}}$.

Because of the d-wave symmetry of $\Delta_{\mathbf{k}}$, The quasiparticle dispersion $E_{\mathbf{k}}^{\mathrm{QP}}$ has four nodes, located at the intersections of the lines $k_x = \pm k_y$ with the effective Fermi surface, where $\xi_{\mathbf{k}} = 0$. Specifically, they are at

$$\mathbf{k}_0 = (k_{0x}, k_{0y}) \coloneqq \arccos\left(\frac{-\mu}{4\tilde{t}}\right)(1, 1) \tag{1.78}$$

and at symmetry-related momenta. The dispersions in the neighborhoods of these nodes is Dirac-like, though anisotropic: for near the node in the first quadrant of momentum space,

$$\varepsilon_{\mathbf{k}\pm} = \pm\sqrt{v_F^2 \left(\frac{\delta k_x + \delta k_y}{\sqrt{2}}\right)^2 + v_\Delta^2 \left(\frac{\delta k_x - \delta k_y}{\sqrt{2}}\right)^2}, \tag{1.79}$$

where $\delta\mathbf{k} \coloneqq \mathbf{k} - \mathbf{k}_0$ and

$$v_{\mathrm{F}} = 2\,|\tilde{t}|\sqrt{1 - \frac{\mu^2}{16\tilde{t}^2}}, \tag{1.80a}$$

$$v_\Delta = \left|\tilde{\Delta}\right|\sqrt{1 - \frac{\mu^2}{16\tilde{t}^2}}. \tag{1.80b}$$

In Chapter 2, the Hamiltonians describing the neighborhoods of the four nodal points are derived by linearizing about those points, and are shown to be 2D Dirac Hamiltonians. Note that in a nodal superconductor such as this one, Dirac-like low-energy physics arises without the need to tune the chemical potential μ [5].

Figure 1.11 shows ARPES data clearly showing the anisotropic Dirac dispersion of the nodal quasiparticle excitations in the superconducting phase of the hole-doped cuprate

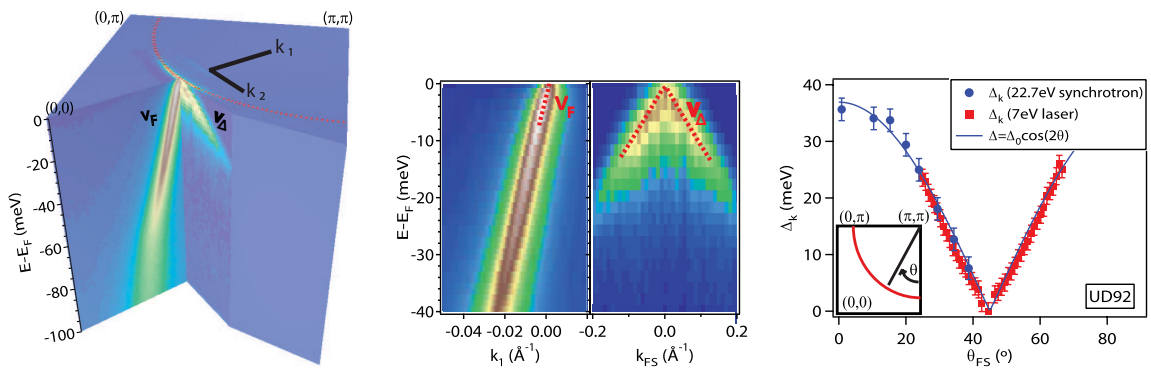

(a) (b) (c)

Figure 1.11: ARPES data showing the Dirac-like dispersion of quasiparticle excitations in the superconducting phase of the cuprate $Bi_2Sr_2CaCu_2O_{8+\delta}$, with hole-doping $\delta = 0.14$ at $T = 10\,\mathrm{K}$. (a): Cutout at the node showing the anisotropic dispersion of excitations, with velocity v_F perpendicular to the Fermi surface and v_Δ parallel to the Fermi surface. The (holelike) Fermi surface is shown as a red dotted curve. (b): Data from panel (a) along cuts perpendicular and parallel to the Fermi surface, clearly showing the difference in the slopes v_F and v_Δ. (c): Magnitude of the gap $\Delta_\mathbf{k}$ along the Fermi surface, showing that it vanishes along the line $k_x = k_y$. (Figure reproduced, with permission, from Ref. 129, i.e., I. M. Vishik et al., *Physical Review Letters*, 104:207002 (2010). Copyright 2010 by the American Physical Society.)

$Bi_2Sr_2CaCu_2O_{8+\delta}$ [129].

Symmetry protection of the gapless nodes The AZ+$\mathcal{P}$ classification is directly applicable to the gapless nodes of the Hamiltonian of Eq. (1.74), because they are not at high-symmetry momenta—indeed, there are *no* mirror symmetries along the lines $k_y = \pm k_x$ because of the symmetry of $\Delta_\mathbf{k}$. With a BdG system such as this one, the determination of the AZ+$\mathcal{P}$ symmetry class (much like that of the AZ symmetry class) is delicate because of the Nambu spinors $[c_{\mathbf{k}\uparrow}, c^\dagger_{-\mathbf{k}\downarrow}]^\top$ that form the basis of the single-particle Hamiltonian, and the result depends on the level of spin-rotation symmetry [46, 50, 76]. Although we spare ourselves the details, it turns out that because of

- inversion symmetry with even gap parity ($\Delta_\mathbf{k} = \Delta_{-\mathbf{k}}$),
- time-reversal symmetry,
- and full SU(2) spin-rotation symmetry,

cuprate models such as that of Eq. (1.74) belong to AZ+$\mathcal{P}$ class CI [76, Fig. 3], in which isolated nodal points are stable in 2D (Table 1.2); furthermore, these nodal points are protected by a nontrivial winding number [76, Table 1].

In Chapter 2, we will see how a perturbation like an extended s-wave pairing, $\Delta^s_\mathbf{k} = \Delta^s(\cos k_x + \cos k_y)$, displaces the nodes in momentum space, but does not gap them out.

This is no surprise, as the perturbations considered there preserve the symmetries in the itemized list above, leaving the AZ+$\mathcal{P}$ class unchanged.

Effect of a magnetic field Finally, we emphasize that a magnetic field couples to the quasiparticle excitations of a nodal superconductor very differently from the electrons in semimetallic systems like graphene (Sec. 1.4.1.2), owing to the fact that the components of a Nambu spinor like $\left[c_{\mathbf{k}\uparrow}, c^{\dagger}_{-\mathbf{k}\downarrow}\right]^{\top}$ transform differently under gauge transformations [5]. For a large range of magnetic field strengths, "the field penetrates in the form of flux tubes and the order parameter phase winds by 2π near the core of each vortex." [5]

1.4.4 Weyl semimetals

Allowing for a less isotropic situtation than that of Eq. (1.14), a Bloch Hamiltonian describing adjacent bands in the neighborhood of a Weyl node takes the form

$$H_{\mathbf{k}} = \sum_{i=1}^{3}\sum_{j=1}^{3} v_{ij} k_i \sigma_j, \tag{1.81}$$

where the σ_j are the Pauli matrices in the space of the two bands and v_{ij} is a symmetric, nonsingular matrix of real numbers with dimension of velocity. As mentioned in Sec. 1.2.2, Weyl nodes are protected by a nontrivial Chern number calculated on a 2-sphere enclosing the node. The Chern number is calculated from the Berry connection $\mathbf{A}^n_{\mathbf{k}} \coloneqq \mathrm{i}\,\langle n(\mathbf{k})|\,\nabla_{\mathbf{k}}\,|n(\mathbf{k})\rangle$, where $|n(\mathbf{k})\rangle$ are the Bloch states:

$$C = \frac{1}{2\pi}\int\limits_{\text{2-sphere}} \mathbf{F}^n_{\mathbf{k}} \cdot \mathrm{d}\mathbf{S}. \tag{1.82}$$

Here, $\mathbf{F}^n_{\mathbf{k}} \coloneqq \nabla \times \mathbf{A}^n_{\mathbf{k}}$ is the Berry curvature [130]. Calculation reveals that, for a Weyl point like that of Eq. (1.81), the Chern number is simply given by $C = \operatorname{sgn}\det(v_{ij})$; this is called the *chirality* of the Weyl point [131]. Because of their chirality, Weyl points give rise to several unusual transport phenomena, like the chiral anomaly, an apparent violation of charge conservation [131, 132].

Experimental evidence The occurence of Weyl nodes has already been discussed in Secs. 1.1 and 1.2.2: they naturally arise at general momenta in the band structures of 3D systems lacking $\mathcal{PT}$ symmetry, because the three momentum parameters are just enough to overcome level repulsion in $H_{\mathbf{k}}$. A Weyl semimetal phase occurs when the Fermi energy crosses one or more Weyl nodes, with no other electron states present at that energy.

The data of Fig. 1.12 show the experimental detection of Weyl nodes in NbAs, an inversion-symmetry-breaking (and $\mathcal{PT}$-breaking) 3D crystal [88]. By adjusting the wavelength of the incident light, the experimentalists probe a specific k_z value at which Weyl nodes are

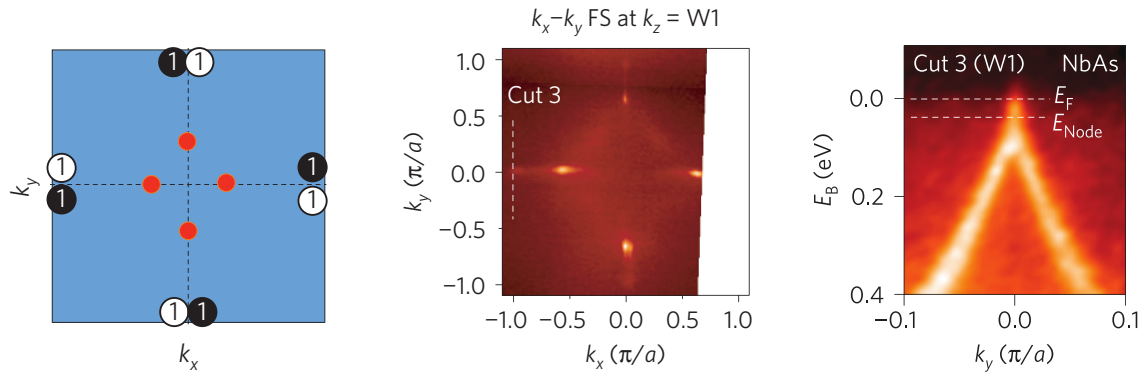

(a) (b) (c)

Figure 1.12: Experimental discovery of Weyl semimetals in the 3D compound NbAs. (a) Predicted location of a subset of Weyl nodes in a fixed-k_z plane; Weyl nodes are labeled with "1", and trivial Fermi pockets are shown in red. (b) ARPES-measured Fermi surface in the same plane as in panel (a). "Cut 3" is taken along aline at which Weyl nodes are expected. (c) Band structure along Cut 3, showing a linear dispersion. (Reproduced with the permission of Springer Nature from Ref. 88, i.e., Su-Yang Xu et al., "Discovery of a Weyl fermion state with Fermi arcs in niobium arsenide", *Nature Physics*, 11:748 (2015).)

expected from band strutcure calculations (the points labeled with "1" in Fig. 1.12(a)); the ARPES-measured Fermi surface at this k_z is shown in Fig. 1.12(b). The ARPES-measured band structure along "Cut 3", taken at fixed k_x and shown in Fig. 1.12(b), is displayed in Fig. 1.12(c), conclusively showing a Dirac-like dispersion. (Evidence of linear dispersion in other directions is provided in Ref. 88.) Though two nodes are expected along Cut 3, (see Fig. 1.12(a)), the two are extremely close together in momentum space, and are difficult to distinguish in the ARPES data.

Together with the detection of surface Fermi-arc surface states [88], these data provide strong evidence for the realization of a Weyl semimetal state in NbAs.

1.5 Strain, pseudo-magnetic fields and Landau levels in graphene

In graphene and other Dirac semimetallic states of matter, material strain, the deformation of matter away from its equilibrium configuration, has been shown to alter the low-energy electronic properties in a way analogous to electric and (orbital) magnetic fields. These *pseudo-magnetic fields* can give rise to Landau levels, which have been detected in experiments [96, see references therein]. In extreme situations, the effective field strengths may far surpass those which can be achieved with a true magnetic field [133]. These findings have opened up a new field of study called "straintronics", the control of electronic properties by means of material strain [96].

The effective Dirac Hamiltonian that describes graphene at low energies is the key ingredi-

ent allowing for strain to mimic electric and magnetic fields; in short, with a Hamiltonian that is linear in momentum, an additive perturbation can end up looking like minimally-coupled electric and magnetic fields [132]. Indeed, the same physics has been predicted in other Dirac materials, like transition-metal dichalcogenides [134, 135], Dirac semimetals [136–138], and Weyl semimetals [137–140]. More generally, such "pseudo-fields" (or "axial fields") that arise in inhomogeneous Dirac-like systems are characterized by the fact that, unlike true electric and magnetic fields, they couple to the Dirac or Weyl Hamiltonian with a sign determined by the chirality of the band touching point [132]; in strained graphene, this reflects the preservation of time-reversal symmetry. Interestingly, these systems provide a condensed-matter realization of the pseudo-fields that arise in particle physics, except with a simpler, Abelian (or "$U(1)$") gauge field instead of non-Abelian ones [132].

In Chapter 2, we show that similar physics of strain-induced pseudo-magnetic fields arises in nodal superconductors, providing a unique way to realize Landau levels for Bogoliubov quasiparticles. The present section provides context by describing strain effects in graphene, in which pseudomagnetic and pseudoelectric fields were first predicted and discovered.

1.5.1 Strain, crystals and tight binding

Deformations of a material can be described by a *displacement field* $\mathbf{u}(\mathbf{r})$, which relates the position $\mathbf{x}$ of a patch of material to its new location $\mathbf{x}'$ under the influence of the displacement [96]:

$$\mathbf{x}'(\mathbf{x}) = \mathbf{x} + \mathbf{u}(\mathbf{x}). \tag{1.83}$$

A sensible displacement field must satisfy restrictions such that the map from $\mathbf{x}$ to $\mathbf{x}'$ is one to one (i.e., injective).

General deformations of a body can include rigid-body transformations, namely, translations and rotations. The strain tensor discards rigid-body transformations, encoding only the (local) changes in length in different directions [96]. Indeed, the tensor can be derived in this way: take two nearby points $\mathbf{x}$ and $\mathbf{x}+\mathbf{h}$ of the original body, with separation $s = \sqrt{h_\mu h_\mu}$ (summation implied over repeated indices in a term). In the transformed body, the length s' between them is given by

$$\begin{aligned}
(s')^2 &= \Big(x'_\mu(\mathbf{x}+\mathbf{h}) - x'_\mu(\mathbf{x})\Big)\Big(x'_\mu(\mathbf{x}+\mathbf{h}) - x'_\mu(\mathbf{x})\Big) && \text{(1.84a)}\\
&= \Big(h_\mu + u_\mu(\mathbf{x}+\mathbf{h}) - u_\mu(\mathbf{x})\Big)\Big(h_\mu + u_\mu(\mathbf{x}+\mathbf{h}) - u_\mu(\mathbf{x})\Big) && \text{(1.84b)}\\
&= \left(\delta_{\mu\alpha} + \left.\frac{\partial u_\mu}{\partial x_\alpha}\right|_{\mathbf{x}}\right) h_\alpha \left(\delta_{\mu\beta} + \left.\frac{\partial u_\mu}{\partial x_\beta}\right|_{\mathbf{x}}\right) h_\beta && \text{(1.84c)}\\
&= s^2 + \left.\left(\frac{\partial u_\alpha}{\partial x_\beta} + \frac{\partial u_\beta}{\partial x_\alpha} + \frac{\partial u_\mu}{\partial x_\alpha}\frac{\partial u_\mu}{\partial x_\beta}\right)\right|_{\mathbf{x}} h_\alpha h_\beta. && \text{(1.84d)}
\end{aligned}$$

In the limit of small $\partial u_\alpha/\partial x_\beta + \partial u_\beta/\partial x_\alpha$ (corresponding to the limit of small deformations),

one can apply the expansion $\sqrt{1+a} = 1 + \frac{1}{2}a + \mathcal{O}(a^2)$ and arrive at the leading-order change in length,

$$s' = s + u_{\alpha\beta}\frac{h_\alpha}{s}\frac{h_\beta}{s}s, \tag{1.85}$$

where the *strain tensor* is [96]

$$u_{\alpha\beta} \coloneqq \frac{1}{2}\left(\frac{\partial u_\alpha}{\partial x_\beta} + \frac{\partial u_\beta}{\partial x_\alpha}\right). \tag{1.86}$$

Rigid-body transformations, on the other hand, are given by the skew-symmetric part of the displacement field [96]:

$$\omega_{\alpha\beta} \coloneqq \frac{1}{2}\left(\frac{\partial u_\alpha}{\partial x_\beta} - \frac{\partial u_\beta}{\partial x_\alpha}\right). \tag{1.87}$$

Hence, the strain tensor $u_{\alpha\beta}$ describes changes in lengths due to the deformation. If we further assume that the rigid-body component of the displacement can be neglected (which should be true at least locally in space), then we can use the strain tensor to express the change in a vector separating nearby points on the material [96]. Specifically, consider $\mathbf{h}'$, separating $\mathbf{x}'(\mathbf{x})$ and $\mathbf{x}'(\mathbf{x}+\mathbf{h})$:

$$\begin{aligned} h'_\mu &= x'_\mu(\mathbf{x}+\mathbf{h}) - x'_\mu(\mathbf{x}) && (1.88a)\\ &= h_\mu + u_\mu(\mathbf{x}+\mathbf{h}) - u_\mu(\mathbf{x}) && (1.88b)\\ &= \left(\delta_{\mu\nu} + \frac{\partial u_\mu}{\partial x_\nu}(\mathbf{x})\right) h_\nu && (1.88c)\\ &= \left(\delta_{\mu\nu} + u_{\mu\nu}(\mathbf{x})\right) h_\nu. && (1.88d) \end{aligned}$$

In the last step, we have assumed $\partial u_\mu / \partial x_\nu = u_{\mu\nu}$, as explained above. In vector notaion [96],

$$\mathbf{h}' = (\mathbb{1} + u(\mathbf{x}))\,\mathbf{h}. \tag{1.89}$$

This formulation of deformation and strain is based on a continuum picture of materials, and $u_{\mu\nu}$ is sometimes called the *macroscopic* strain, emphasizing the fact that the relative displacements of atoms within a multi-atom unit cell may not directly reflect $u_{\mu\nu}$. The assumption that the positions $\{\boldsymbol{\delta}_n\}$ of the atoms within the unit cell *do* directly reflect $u_{\mu\nu}$, in the sense that they simply transform according to Eq. (1.89), is called the *Cauchy-Born rule* and is sometimes, but not always, justified [96].

Changes in the primitive lattice translations $\{\mathbf{a}_i\}$, though, *necessarily* reflect $u_{\mu\nu}$, at least locally in space; specifically, they transform as Eq. (1.89) [96]:

$$\mathbf{a}'_i = (\mathbb{1} + u)\mathbf{a}_i. \tag{1.90}$$

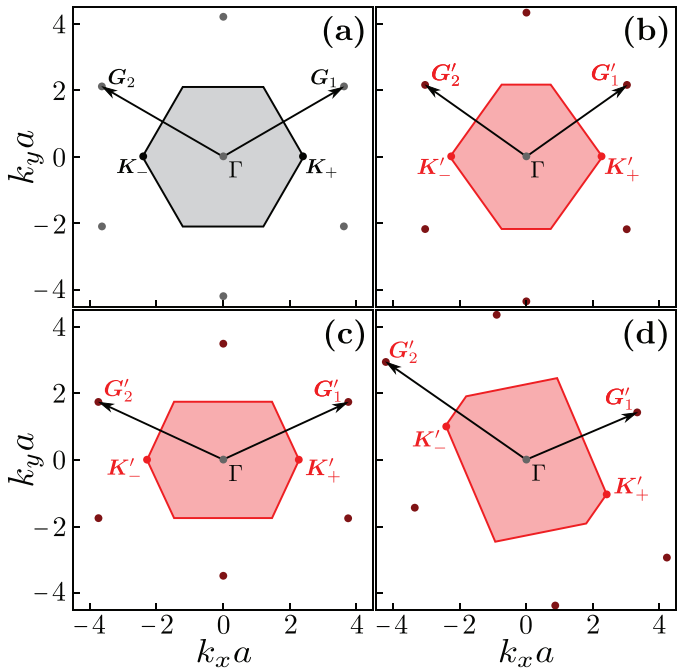

Figure 1.13: Effects of different types of stain on the reciprocal lattice vectors (black arrows) and first Brillouin zone (shaded areas) of the graphene sheet shown in Fig. 1.2a. Panel (a) shows the case of unstrained graphene, whereas panels (b), (c), and (d) show, respectively, uniaxial tensile strain in the x direction, uniaxial tensile strain in the y direction, and shear strain. Specific values are given in the main text. (Figure reproduced from Ref. 96, i.e., Gerardo G. Naumis, Salvador Barraza-Lopez, Maurice Oliva-Leyva, and Humberto Terrones, "Electronic and optical properties of strained graphene and other strained 2D materials: a review", *Reports on Progress in Physics* 80(9):096501 (2017). © IOP Publishing. Reproduced with permission. All rights reserved. Permission conveyed through Copyright Clearance Center, Inc.)

The reciprocal lattice vectors, on the other hand, undergo the inverse transformation [96]:

$$\mathbf{b}_i' = (\mathbb{1} + u)^{-1}\mathbf{b}_i. \tag{1.91}$$

Figure 1.13 shows the transformation of graphene's reciprocal lattice vectors and first Brillouin zone under different types of *uniform* strain, compared to the unstrained case in panel (a). (The pristine graphene sheet in real space is shown in Fig. 1.2a.) Panels (b) and (c) show, respectively, tensile uniaxial strain in the x direction,

$$u = \begin{bmatrix} 0.2 & \\ & -0.2\nu \end{bmatrix}, \tag{1.92}$$

and in the y direction,

$$u = \begin{bmatrix} -0.2\nu & \\ & 0.2 \end{bmatrix}. \tag{1.93}$$

Here, the *Poisson ratio* ν, which describes how much the material "recoils" in other directions when subjected to uniaxial strain, is set to $\nu = 0.165$ [96]. In each of these two cases, the change in the first Brillouin zone simply reflects the fact that a dilation of the lattice in the x direction causes a contraction of the reciprocal lattice in the x direction; the same is true for the y direction. Panel (d) shows the (somewhat less straightforward) effect of a shear strain

$$u = \begin{bmatrix} & 0.2 \\ 0.2 & \end{bmatrix}. \tag{1.94}$$

A change in the bond length a between two atoms leads to a change in the hopping amplitude t between them. This dependence is described by the electron Grüneisen parameter β, given by

$$\beta = -\frac{\partial \ln t}{\partial \ln a}, \tag{1.95}$$

and in terms of which the change in t is approximately given by

$$\delta t = \frac{\partial t}{\partial a}\delta a + \mathcal{O}(\delta a^2) \tag{1.96a}$$

$$= -\frac{\beta t}{a}\delta a + \mathcal{O}(\delta a^2) \tag{1.96b}$$

More specifically, consider a hopping amplitude between atoms at $\mathbf{x}$ and $\mathbf{x} + \mathbf{h}$. Combining Eqs. (1.85) and (1.96), and assuming the Cauchy-Born rule holds[17], the change in this

[17] Again, this assumption is only necessary between atoms belonging to different sublattices. In general, the Cauchy-Born rule does not hold between the A and B sublattices in graphene, but it is commonly used as an assumption [96].

amplitude owing to a strain is

$$\delta t_{\mathbf{x}+\mathbf{h},\mathbf{x}} = -\beta t \; u_{\mu\nu}(\mathbf{x}) \frac{h_\mu h_\nu}{|\mathbf{h}|^2} \tag{1.97}$$

One may want to evaluate the strain at the center of the bond, $u_{\mu\nu}(\mathbf{x}+\mathbf{h}/2)$, for greater accuracy; however, this correction is of higher order in $\mathbf{h}$, and we have already neglected higher-order terms in $\mathbf{h}$ both in the change in length (Eq. (1.85)) and the change in the hopping amplitude (Eq. (1.96)).

Uniform strain, i.e., strain for which the tensor u is position independent, preserves translational invariance in the crystal [96]; this is why the reciprocal lattice vectors and Brillouin zones shown in Fig. 1.13 were meaningful. Non-uniform strain breaks translational invariance and spoils the Bloch picture; however, in the low-energy continuum limit that describes the Dirac nodes in graphene (Sec. 1.4.1.1), it is possible to obtain an effective Hamiltonian describing the effects of smoothly varying strain on the electrons. We now review this.

1.5.2 Tight-binding graphene Hamiltonian with inhomogeneous hopping

Nonuniform strain causes the hopping amplitudes to become dependent on position and direction: $t \to t + \delta t_{ij}$ and $t' \to t' + \delta t'_{ij}$, where δt_{ij} and $\delta t'_{ij}$ are, respectively, small compared to t and t', and vary smoothly with respect to the lattice scale a. In general, the real-space tight-binding Hamiltonian takes the form

$$H^{\text{strain}} = -\sum_{\langle i,j\rangle,\sigma} \left((t+\delta t_{ij})\, c^\dagger_{i\sigma} c_{j\sigma} + \text{H.c.} \right) - \sum_{\langle\langle i,j\rangle\rangle,\sigma} \left(\left(t' + \delta t'_{ij}\right) c^\dagger_{i\sigma} c_{j\sigma} + \text{H.c.} \right) \tag{1.98a}$$

$$= -\sum_\sigma \sum_{i\in A} \sum_{l=1}^{3} (t + \delta t_{\mathbf{x}_i+\mathbf{w}_l,\mathbf{x}_i}) \; c^\dagger_{\mathbf{x}_i+\mathbf{w}_l,B,\sigma} \; c_{\mathbf{x}_i,A,\sigma} + \text{H.c.} \tag{1.98b}$$

$$-\sum_\sigma \sum_{\alpha\in\{A,B\}} \sum_{i\in\alpha} \sum_{l=1}^{3} \left(t' + \delta t'_{\mathbf{x}_i+\mathbf{v}_l,\mathbf{x}_i}\right) \; c^\dagger_{\mathbf{x}_i+\mathbf{w}_l,\alpha,\sigma} \; c_{\mathbf{x}_i,\alpha,\sigma} + \text{H.c.}$$

$$= -\sum_\sigma \sum_{\mathbf{k},\mathbf{k}'} c^\dagger_{\mathbf{k}B\sigma} \, c_{\mathbf{k}'A\sigma} \left(\frac{1}{N} \sum_{i\in A} \mathrm{e}^{-\mathrm{i}(\mathbf{k}-\mathbf{k}')\cdot\mathbf{x}_i} \sum_{l=1}^{3} \mathrm{e}^{-\mathrm{i}\mathbf{k}\cdot\mathbf{w}_l} \left(t + \delta t_{\mathbf{x}_i+\mathbf{w}_l,\mathbf{x}_i}\right) \right) + \text{H.c.}$$

$$-\sum_\sigma \sum_{\alpha\in\{A,B\}} \sum_{\mathbf{k},\mathbf{k}'} c^\dagger_{\mathbf{k}\alpha\sigma} \, c_{\mathbf{k}'\alpha\sigma} \left(\frac{1}{N} \sum_{i\in\alpha} \mathrm{e}^{-\mathrm{i}(\mathbf{k}-\mathbf{k}')\cdot\mathbf{x}_i} \sum_{l=1}^{3} \mathrm{e}^{-\mathrm{i}\mathbf{k}\cdot\mathbf{v}_l} \left(t' + \delta t'_{\mathbf{x}_i+\mathbf{v}_l,\mathbf{x}_i}\right) \right) + \text{H.c.} \tag{1.98c}$$

These equations are completely analogous to those in Eq. (1.36), in which it was the Peierls phase, rather than material deformations, that made the hopping amplitudes inhomogeneous. We briefly explain the procedure for arriving at the low-energy Hamiltonian, which is analogous to the one presented in detail following Eq. (1.36): because the strain is smoothly varying on the scale of a, the Fourier transforms of the hopping amplitudes, placed in

large parentheses in the last step above, are only non-negligible for small $\mathbf{k}-\mathbf{k}'$; hence, they do not couple the two valleys, and each momentum sum can be split into two sums centered at each of the two valleys. (The assumptions $|\delta t_{ij}| \ll |t|$ and $|\delta t'_{ij}| \ll |t'|$ ensure that the momenta relevant to low energies are still near the original valleys.) The resulting Hamiltonians are then expanded to first order in the two small quantities $\mathbf{q}$ (the deviation from the valley center) and either δt_{ij} or $\delta t'_{ij}$. The terms linear in $\mathbf{q}$ give the unstrained low-energy Hamiltonian of Eq. (1.33b), and the terms linear in δt_{ij} and in $\delta t'_{ij}$ give the corrections due to strain.

After re-expressing the field operators in position space, the resulting low-energy Hamiltonian is given by [91]

$$H_{\mathrm{LE}}^{\mathrm{strain}} = v_{\mathrm{F}} \sum_{\sigma} \int \mathrm{d}^2 x \Bigg[\psi_{1\sigma}^{\dagger}(\mathbf{x}) \Big(\big(-\mathrm{i}\nabla + v_{\mathrm{F}}^{-1} \mathbf{A}^{\mathrm{s}}(\mathbf{x})\big) \cdot \boldsymbol{\tau} + v_{\mathrm{F}}^{-1} \phi^{\mathrm{s}}(\mathbf{x}) \tau_0 \Big) \psi_{1\sigma}(\mathbf{x}) \\ - \psi_{2\sigma}^{\dagger}(\mathbf{x}) \Big(\big(-\mathrm{i}\nabla - v_{\mathrm{F}}^{-1} \mathbf{A}^{\mathrm{s}}(\mathbf{x})\big) \cdot \boldsymbol{\tau}^* - v_{\mathrm{F}}^{-1} \phi^{\mathrm{s}}(\mathbf{x}) \tau_0 \Big) \psi_{2\sigma}(\mathbf{x}) \Bigg]. \quad (1.99)$$

As one can see, the hopping-amplitude modulations have given rise to a *pseudo-magnetic vector potential* $\mathbf{A}^{\mathrm{s}}(\mathbf{x})$, which is minimally coupled to the (low-energy) electron fields, much like an ordinary vector potential. It arises from the nearest-neighbor hopping perturbation δt_{ij} and is given by [91]

$$\mathbf{A}^{\mathrm{s}}(\mathbf{x}) := \Big(\mathrm{Re}\left(\mathcal{A}^{\mathrm{s}}(\mathbf{x})\right), \mathrm{Im}\left(\mathcal{A}^{\mathrm{s}}(\mathbf{x})\right) \Big), \quad (1.100a)$$

$$\mathcal{A}^{\mathrm{s}}(\mathbf{x}_i) := -\sum_{l=1}^{3} \mathrm{e}^{-\mathrm{i}\mathrm{K}\cdot\mathbf{w}_l} \; \delta t_{\mathbf{x}_i+\mathbf{w}_l,\mathbf{x}_i}. \quad (1.100b)$$

However, unlike an ordinary magnetic vector potential, it couples with opposite signs at valleys K and K′ (c.f. Eq. (1.41b)). This difference makes the above Hamiltonian time-reversal invariant, which it must be, since strain—unlike a magnetic field—does not break time-reversal symmetry [91]. Indeed, using the transformations of Eq. (1.42), it is easy to see that

$$\mathcal{T}^{-1} H_{\mathrm{LE}}^{\mathrm{strain}} \mathcal{T} = H_{\mathrm{LE}}^{\mathrm{strain}} \quad (1.101)$$

(c.f. Eq. (1.43)). The hopping-amplitude modulations have also given rise to a *pseudo-electric potential* $\phi^{\mathrm{s}}(\mathbf{x})$ in $H_{\mathrm{LE}}^{\mathrm{strain}}$, which is diagonal in the sublattice degree of freedom, and originates from the next-nearest-nearest-neighbor perturbation $\delta t'_{ij}$ [91]:

$$\phi^{\mathrm{s}}(\mathbf{x}_i) := -2 \sum_{l=1}^{3} \cos(\mathrm{K}\cdot\mathbf{v}_l) \delta t'_{\mathbf{x}_i+\mathbf{v}_l,\mathbf{x}_i} = \sum_{l=1}^{3} \delta t'_{\mathbf{x}_i+\mathbf{v}_l,\mathbf{x}_i}, \quad (1.102)$$

where the second equality stems from the fact that $\cos(\mathrm{K}\cdot\mathbf{v}_l) = -1/2$ for all l. (We note

that $\phi^{\mathrm{s}}(\mathbf{x}_i)$ is the same for both sublattices because the strain is assumed to be smooth on the scale of a.) The potential $\phi^{\mathrm{s}}(\mathbf{x}_i)$ is an example of what is called a "deformation potential" [96].

Using Eq. (1.97), it is a straightforward matter to find the pseudo-potentials in terms of the strain tensor:

$$\mathbf{A}^{\mathrm{s}}(\mathbf{x}) = \left(-\frac{3}{4}\beta t(u_{xx}(\mathbf{x}) - u_{yy}(\mathbf{x})), \frac{3}{2}\beta t u_{xy}(\mathbf{x})\right), \tag{1.103}$$

$$\phi^{\mathrm{s}}(\mathbf{x}) = -\frac{3}{2}\beta' t'(u_{xx}(\mathbf{x}) + u_{yy}(\mathbf{x})). \tag{1.104}$$

Here, $u_{xy} = u_{yx}$ is the shear strain. The above expression for $\mathbf{A}^{\mathrm{s}}(\mathbf{x})$ assumes that the Cauchy-Born rule holds; however, no such assumption is needed for $\phi^{\mathrm{s}}(\mathbf{x})$, since t' relates like sublattices.

We end with a few notes. First, while a uniform magnetic vector potential cannot affect the band structure because it is gauge-equivalent to zero, a uniform pseudo-magnetic vector potential will truly displace the Dirac nodes in momentum space (illustrated in Ref. 96). Second, the hopping amplitudes in a graphene sheet are affected not only by strain, but also by, e.g., ripples in the out-of-plane direction [91, 96]; we have neglected this because the goal was to demonstrate how pseudo-magnetic fields arise. Third, Ref. 96 indicates that a more careful derivation in which one keeps track of the displacement of the Dirac point from the start yields an additional term in the pseudo-magnetic vector potential and an anisotropic, strain-dependent Fermi velocity; the extra term, however, does not give rise to pseudomagnetism. More generally, a number of schemes have been devised to improve upon the approximations used above (see Refs. 141, 142, among others); nonetheless, little seems to change in the limit of small deformations. Fourth, the electromagnetic analogy even carries to time-dependent situations, as "a time-dependent deformation [gives] rise to a pseudo-electric field given by $\mathbf{E}_s = -\partial_t \mathbf{A}_s$" [96]; however, since the resulting pseudo-electric field has opposite signs in the two valleys, it does not generate current and has not yet been observed [96].

1.5.3 Experimental detection of strain-induced Landau levels in graphene

In the presence of a uniform pseudo-magnetic field $\mathbf{B}^{\mathrm{s}} = \nabla \times \mathbf{A}^{\mathrm{s}}(\mathbf{x})$, the spectrum and density of states from the above Hamiltonian are the same as those of a uniform magnetic field, discussed in Sec. 1.4.1.3; however, the states will differ slightly (even with the same choice of gauge) because $\mathbf{A}^{\mathrm{s}}$ has opposite signs at the two valleys, whereas $\mathbf{A}$ has the same sign.

The STS data in Fig. 1.14 reveal strain-induced Landau levels in a graphene sample [143]. Part of the sample was under strong strain because of the presence of a ridge measuring 10 nm in height, 15 nm in width and 60 nm in length. The many traces in Fig. 1.14(a) correspond to spectra measured at different points along the ridge. The Landau-level energies are taken

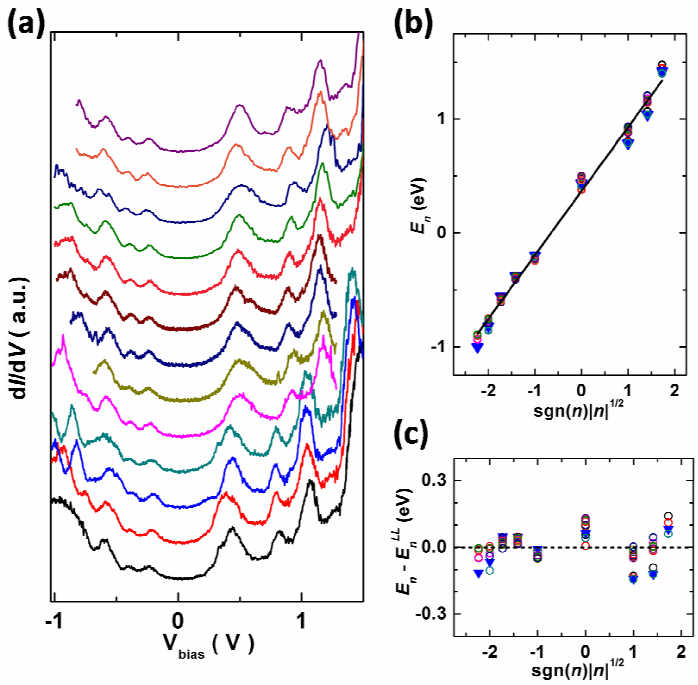

Figure 1.14: STS data revealing strain-induced Landau levels along a pronounced ridge in a graphene sample. (a): Intensity curves at 13 points along the ridge, offset for clarity. The peaks correspond to strain-induced Landau levels. (b): Energy of the peaks as a function of $\mathrm{sgn}(n)\sqrt{|n|}$, where in the Landau-level index. The linear behaviour agrees with the dependence given in Eq. (1.56), and the solid line is the best-fit line to experimental data. (c): Residuals from panel (b), calculated with respect to the best-fit theoretical prediction. (Figure reproduced, with permission, from Ref. 143, i.e., Hui Yan et al., *Physical Review B*, 85:035422 (2012). Copyright 2012 by the American Physical Society.)

to be the peaks in the spectrum, and as shown in Fig. 1.14(b) and Fig. 1.14(c), they agree well with the predicted behaviour.

1.6 The Edelstein effects

The purpose of this section is to introduce the Edelstein effects, which are a central focus of Chapter 3. The Edelstein effects, which collectively also go by the name "kinetic magnetoelectric effect" (KME) [144], are magnetoelectric effects wherein an electric-field-driven dissipative current generates a net magnetization in a metal. In general, there is an "intrinsic" contribution to the KME, which arises from the properties of the Bloch states themselves, and an "extrinsic" contribution, which stems from impurity-scattering processes [144]. We focus on the intrinsic contribution, paying special attention to the role played by Dirac physics.

In general, magnetoelectric effects are a family of effects whose defining property is the coupling between electric and magnetic degrees of freedom in a material [145]. Though the field is not new, it has seen a significant revival in the past two decades [146], in no

small part because of the considerable progress in multiferroics—materials in which multiple ferroic orders, like ferromagnetism and ferroelectricity, coexist—and the potential for device applications [145, 147–149].

The simplest magnetoelectric effect is the so-called linear magnetoelectric effect. Most commonly, in linear media, an electric field $\mathbf{E}$ gives rise to a polarization $\mathbf{P} = \chi_{\mathrm{e}}\mathbf{E}$, and an auxiliary magnetic field $\mathbf{H}$ gives rise to a magnetization $\mathbf{M} = \chi_{\mathrm{m}}\mathbf{H}$. In the linear magnetic effect, characterized by the tensor α, electric fields can give rise to magnetization and magnetic fields, to polarization [146]:

$$\mathbf{P} = \chi_{\mathrm{e}}\mathbf{E} + \alpha\mathbf{H}, \tag{1.105a}$$

$$\mathbf{M} = \chi_{\mathrm{m}}\mathbf{H} + \alpha\mathbf{E}. \tag{1.105b}$$

These effects can be further divided into equilibrium ones and non-equilibrium ones. In the latter case, for example, a current may be needed to achieve the effect.

Symmetries of the macroscopic point group place constraints on the form of α. Since the tensor α relates a polar vector, $\mathbf{E}$, to an axial vector, $\mathbf{M}$, it is a rank-2 axial tensor, which transforms as [150]

$$\alpha_{\nu\kappa} \to \alpha'_{\nu\kappa} = \det(R) \sum_{\nu',\kappa'} R_{\nu\nu'} R_{\kappa\kappa'} \alpha_{\nu'\kappa'} \tag{1.106}$$

under an (active) rigid-body transformation R. (Here and below, ν and κ are spatial indices and summation is implied over repeated indices in a term.) For any transformation R that is part of a crystal's macroscopic point group, the tensor α must be left invariant by the transformation of Eq. (1.106), i.e., $\alpha' = \alpha$. Hence, in each of the 32 3D crystal classes, one can find the symmetry allowed-form of α. In particular, when inversion symmetry $R = -\mathbb{1}_3$ is present, $\alpha \to -\alpha$, forcing $\alpha = 0$. The crystal classes for which a nonzero α is symmetry allowed are called *gyrotropic* [151, 152]; the form of α in each of these classes is shown in Table I of Ref. 153. Of the 21 non-centrosymmetric crystal classes, 18 of them, listed in Table 1.4, are gyrotropic [150, 152]. The gyrotropic crystal classes include all 11 chiral crystal classes, (those with neither inversions, nor mirrors, nor rotoreflections), but also certain non-chiral classes [152]. One non-chiral gyrotropic class will be the focus of Chapter 3.

Chiral (and, hence, gyrotropic)	*1*, *2*, *222*, *4*, *422*, *3*, *32*, *6*, *622*, *23*, *432*
Gyrotropic, but not chiral	*m*, *mm2*, $\bar{4}$, *4mm*, $\bar{4}$*2m*, *3m*, *6mm*

Table 1.4: The 18 gyrotropic crystal classes, divided into chiral (11 crystal classes) and non-chiral (7 crystal classes) [150, 152].

1.6.1 The (spin) Edelstein effect

Originally, the Edelstein effect referred to the induction of a net spin magnetization in a conductor under the effect of an electric-field-driven current [154, 155]; this is now often called the "spin Edelstein effect" for clarity [151]. It has also been referred to as the "inverse spin-galvanic effect" [156, 157].

Crystals with broken inversion symmetry can exhibit crystalline SOC, which enters the Bloch Hamiltonian like a momentum-dependent Zeeman term [157–159] and gives rise to "spin-momentum locking" of the Bloch states; the most familiar examples of crystalline SOC are the Rashba (or Bychkov–Rashba) and Dresselhaus effects [157], but more generally, the form of the interaction depends on the crystal symmetry. The Bloch states $|u_{\mathbf{k}n}\rangle$ can then carry a spin magnetic moment [160]

$$\mathbf{s}_{\mathbf{k}n} \coloneqq -\frac{ge}{2m_{\mathrm{e}}} \langle u_{\mathbf{k}n}| \frac{1}{2}\boldsymbol{\sigma} |u_{\mathbf{k}n}\rangle \,, \tag{1.107}$$

in terms of the electron mass m_{e} and the electron g factor. A necessary condition for $\mathbf{s}_{\mathbf{k}n}$ to be non-zero is space-time-inversion symmetry breaking [160]. In equilibrium, the total magnetization arising from spin is then

$$\mathbf{M}^{\mathrm{spin,\,eq}} = \frac{1}{\mathcal{V}} \sum_{\mathbf{k},n} f^0_{\mathbf{k}n} \mathbf{s}_{\mathbf{k}n}, \tag{1.108}$$

where $\mathcal{V}$ is the system's volume and $f^0_{\mathbf{k}n} \coloneqq f(\varepsilon_{\mathbf{k}n} - \mu)$ is the Fermi-Dirac distribution function at temperature β^{-1}, i.e., $f(\xi) \coloneqq (1+\mathrm{e}^{\beta\xi})^{-1}$. Let us assume time-reversal symmetry in the unperturbed system; for this reason, for every state $|u_{\mathbf{k}n}\rangle$, there is an orthogonal time-reversed state $\mathcal{T}|u_{\mathbf{k}n}\rangle$[18] with the same occupation and with opposite spin magnetic moment [160], so $\mathbf{M}^{\mathrm{spin,\,eq}} = 0$.

This conclusion changes when the system is driven out of equilibrium [155]. The simplest way to understand this is to use semiclassical electron dynamics and the steady-state, non-equilibrium distribution function resulting from an applied electric field $\mathbf{E}$. Adopting the relaxation-time approximation, the distribution function to lowest order in $\mathbf{E}$ is [161]

$$f_{\mathbf{k}n} = f^0_{\mathbf{k}n} + e\tau \left(\mathbf{E}\cdot\mathbf{v}_{\mathbf{k}n}\right) \left.\frac{\mathrm{d}f}{\mathrm{d}\xi}\right|_{\xi=\varepsilon_{\mathbf{k}n}-\mu} ; \tag{1.109}$$

here, $\mathbf{v}_{\mathbf{k}n} \coloneqq \nabla_{\mathbf{k}}\varepsilon_{\mathbf{k}n}$ is the electron group velocity and τ is the impurity-scattering relaxation

[18] Kramers's theorem ensures that $|u_{\mathbf{k}n}\rangle$ and $\mathcal{T}|u_{\mathbf{k}n}\rangle$ are distinct and orthogonal.

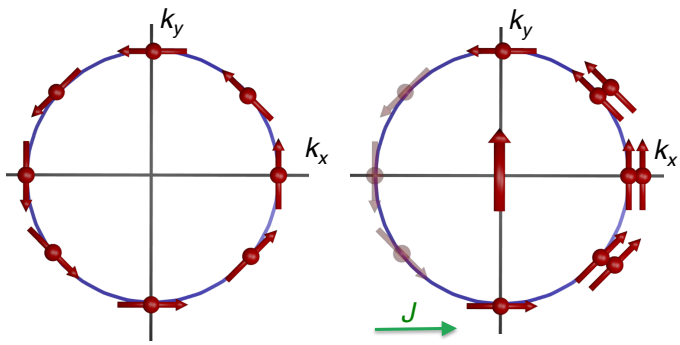

Figure 1.15: Generation of a net magnetic moment under the effect of a current in a system with Bychkov–Rashba–type SOC ($H = (p_x^2 + p_y^2)/(2m) + r(p_x\sigma_y - p_y\sigma_x)$). For the sake of illustrative simplicity, the second, smaller Fermi surface, which produces an opposite but lesser contribution, is not shown. LEFT PANEL: In equilibrium, each spin dipole moment has an equal and opposite pair, yielding no net magnetization. RIGHT PANEL: The current-driving electric field modifies the electron distribution function, increasing the occupation at one end of the Fermi surface and decreasing it at the other, giving rise to a net magnetization. (Figure reproduced, with permission, from Ref. 156, i.e., Jairo Sinova et al., *Reviews of Modern Physics*, 87:1213 (2015). Copyright 2015 by the American Physical Society.)

time. Under the influence of the electric field, the net magnetization due to spin becomes

$$\mathbf{M}^{\text{spin}} = \frac{1}{\mathcal{V}} \sum_{\mathbf{k},n} f_{\mathbf{k}n} \mathbf{s}_{\mathbf{k}n} \tag{1.110a}$$

$$= \frac{1}{\mathcal{V}} \sum_{\mathbf{k},n} e\tau \left(\mathbf{E} \cdot \mathbf{v}_{\mathbf{k}n}\right) \left.\frac{\mathrm{d}f}{\mathrm{d}\xi}\right|_{\xi=\varepsilon_{\mathbf{k}n}-\mu} \mathbf{s}_{\mathbf{k}n}, \tag{1.110b}$$

and the (spin contribution to the) magnetoelectric tensor α appearing in

$$\mathbf{M} = \alpha \mathbf{E} \tag{1.111}$$

is given by

$$\alpha_{\nu\kappa}^{\text{spin}} = \frac{e\tau}{\mathcal{V}} \sum_{\mathbf{k},n} s_{\mathbf{k}n,\nu} v_{\mathbf{k}n,\kappa} \left.\frac{\mathrm{d}f}{\mathrm{d}\xi}\right|_{\xi=\varepsilon_{\mathbf{k}n}-\mu}. \tag{1.112}$$

The generation of a net magnetic moment is schematically depicted in Fig. 1.15; note that the function $\mathrm{d}f/\mathrm{d}\xi|_{\xi=\varepsilon_{\mathbf{k}n}-\mu}$ is a nascent Dirac delta function in zero-temperature limit, meaning that only states in the vicinity of the Fermi surface play an important role in α^{spin} at low temperatures. From the form of α^{spin} in Eq. (1.112), we can check that it vanishes in the presence of inversion symmetry, as argued above from general symmetry considerations. Indeed, inversion constrains $\mathbf{s}_{-\mathbf{k}n} = \mathbf{s}_{\mathbf{k}n}$ and $\mathbf{v}_{-\mathbf{k}n} = -\mathbf{v}_{-\mathbf{k}n}$ [160], leading to $\alpha^{GME} = 0$.

The Edelstein effect was observed in numerous 2D systems during the 2000s decade; see references within Ref. 144 and Ref. 156, Sec. II D. For example, V. Sih et al. measure current-induced magnetization (alongside the spin Hall effect, another magnetoelectric effect) in a 2D electron gas confined in (110) AlGaAs quantum wells, in which both Bychkov–Rashba and Dresselhaus SOC fields are present [158]. In the experiment, the out-of-plane spin

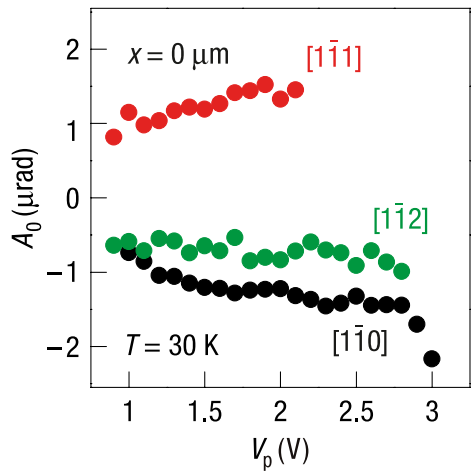

Figure 1.16: Kerr-rotation microscopy data revealing the (spin) Edelstein effect in 2D electron gases confined to (110) AlGaAs quantum wells. The Kerr rotation angle—a proxy for the out-of-plane spin magnetization—is given by A_0 and the voltage is given by V_p. Data is shown for electric fields along crystal directions $[1\bar{1}1]$, $[1\bar{1}2]$ and $[1\bar{1}0]$ (all in plane). (Reproduced with the permission of Springer Nature from Ref. 158, i.e., Vanessa Sih et al., "Spatial imaging of the spin Hall effect and current-induced polarization in two-dimensional electron gases", *Nature Physics*, 1:31 (2005).)

magnetization is measured in the 2D electron gas using scanning Kerr rotation microscopy. With this technique, the component of the spin magnetization parallel to the light beam can be found from the Kerr rotation angle.

Figure 1.16 shows the (zero-magnetic-field) Kerr rotation angle A_0 as a function of the applied voltage, for three different electric field directions, $[1\bar{1}1]$, $[1\bar{1}2]$ and $[1\bar{1}0]$. The data are compatible with the linear relation of Eq. (1.111), and the anisotropic behaviour is attributed [158] to the direction-dependence of the Dresselhaus field.

1.6.2 The orbital Edelstein effect

In 2D systems such as that discussed above, only the electrons' *spin* magnetic dipole moment was available to contribute to the net magnetization, as the (in-plane) current cannot drive any orbital motion around the current direction [144]. In 3D systems, the extra spatial dimension allows for an additional, *orbital* magnetic dipole moment to contribute to the net magnetization $\mathbf{M}$ [144, 151, 152, 160, 162]. In other words, the current can induce a rotational motion of the wave packet around its center of mass, provided the crystal symmetry and current direction allow it. Unlike its spin counterpart, the orbital Edelstein effect is not limited by the strength of SOC; rather, the magnitude of the orbital Edelstein effect is determined by crystal structure and hopping amplitudes [162].

The magnetic moment of a Bloch state is given by

$$\mathbf{m}_{\mathbf{k}n} = \frac{e}{2}\mathrm{Im}\,\langle \nabla_{\mathbf{k}} u_{\mathbf{k}n} | \times (H_{\mathbf{k}} - \varepsilon_{\mathbf{k}n}) \, | \nabla_{\mathbf{k}} u_{\mathbf{k}n} \rangle \,, \tag{1.113}$$

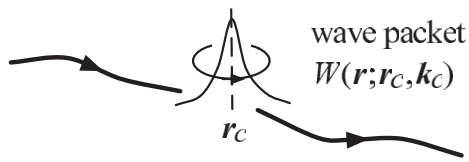

Figure 1.17: In general, the motion of a wave packet (shown in position space with center of mass $\mathbf{r}_\mathrm{c}$) can have both a translational and a rotational part. The rotational part leads to nonzero $\mathbf{m}_{\mathbf{k}n}$. (Figure reproduced, with permission, from Ref. 166, i.e., Di Xiao, Yugui Yao, Zhong Fang, and Qian Niu, *Physical Review Letters*, 97:026603 (2006). Copyright 2006 by the American Physical Society.)

where $H_\mathbf{k}\left|u_{\mathbf{k}n}\right\rangle = \varepsilon_{\mathbf{k}n}\left|u_{\mathbf{k}n}\right\rangle$. This formula can be arrived at in multiple ways. In semiclassical electron dynamics, it arises as an energy correction $-\mathbf{m}_{\mathbf{k}n}\cdot\mathbf{B}$ to the energy $\varepsilon_{\mathbf{k}n}$ of a wave packet $|W\rangle$ constructed from band n and centered at $\mathbf{k}$ in momentum space [163,164], and it physically corresponds to the magnetic dipole moment of the wave packet rotating about its center of mass [165,166]. Indeed, it can be calculated as $\mathbf{m}_{\mathbf{k}n} = -(e/2)\left\langle W\right|(\hat{\mathbf{x}}-\mathbf{x}_\mathrm{c})\times\hat{\mathbf{v}}\left|W\right\rangle$, where $\hat{\mathbf{x}}$ is the position operator, $\hat{\mathbf{v}}$ is the velocity operator, and $\mathbf{x}_\mathrm{c}$ is the wave packet's center of mass in position space [166].

The total orbital magnetization $\mathbf{M}$ has been calculated from semiclassics [165,166], using perturbation theory [167], and in linear-response theory [160]. According to some references, it contains two terms: one is the occupation-weighted sum of $\mathbf{m}_{\mathbf{k}n}$ (analogous to $\mathbf{M}^\mathrm{spin}$ in Eq. (1.110a)), and the other is of topological nature, involving the Berry curvature and reflecting the existence of boundary currents [166,168]. However, the validity of the second term has been called into question based on physical arguments [144, footnote 21], and we ignore it here for simplicity. Hence, we consider the net orbital magnetization to be given by

$$\mathbf{M}^\mathrm{orb} = \frac{1}{\mathcal{V}}\sum_{\mathbf{k},n}\mathbf{m}_{\mathbf{k}n}f_{\mathbf{k}n}, \tag{1.114}$$

where $f_{\mathbf{k}n}$ is the electron distribution function.

The symmetry properties of $\mathbf{m}_{\mathbf{k}n}$ are the same as those of $\mathbf{s}_{\mathbf{k}n}$ (in particular, under time reversal and inversion [162]), so it, too, does not yield a net magnetization in equilibrium, but may do so in the presence of an electric-field driven current. Therefore, the combine magnetization is given by

$$\mathbf{M} = \mathbf{M}^\mathrm{spin} + \mathbf{M}^\mathrm{orb} \tag{1.115a}$$

$$= \frac{1}{\mathcal{V}}\sum_{\mathbf{k},n} e\tau\left(\mathbf{E}\cdot\mathbf{v}_{\mathbf{k}n}\right)\left.\frac{\mathrm{d}f}{\mathrm{d}\xi}\right|_{\xi=\varepsilon_{\mathbf{k}n}-\mu}\left(\mathbf{s}_{\mathbf{k}n}+\mathbf{m}_{\mathbf{k}n}\right), \tag{1.115b}$$

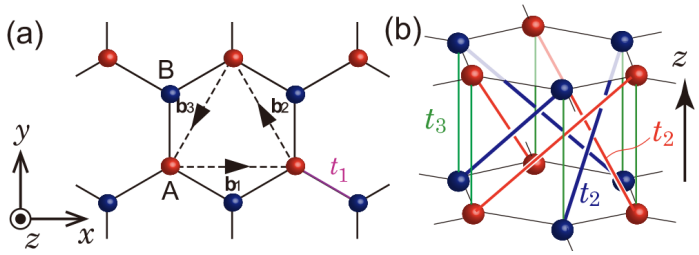

Figure 1.18: Crystal structure for the chiral tight-binding model used in Ref. 151 and described in the text. The winding, solenoid-like hopping paths give the crystal a handedness, which is a sufficient—but not necessary—criterion for the orbital Edelstein effect. (Figure reproduced, with permission, from Ref. 151, i.e., Taiki Yoda, Takehito Yokoyama, and Shuichi Murakami, *Nano Letters*, 18:916 (2018). Copyright 2018 American Chemical Society.)

and so the combined response tensor is

$$\alpha_{\nu\kappa} = \alpha^{\text{spin}}_{\nu\kappa} + \alpha^{\text{orb}}_{\nu\kappa} \tag{1.116a}$$

$$= \frac{e\tau}{\mathcal{V}} \sum_{\mathbf{k},n} \left(s_{\mathbf{k}n,\nu} + m_{\mathbf{k}n,\nu}\right) v_{\mathbf{k}n,\kappa} \left.\frac{\mathrm{d}f}{\mathrm{d}\xi}\right|_{\xi=\varepsilon_{\mathbf{k}n}-\mu}. \tag{1.116b}$$

In fact, current-induced magnetization has been observed in elemental tellurium, a 3D material [169], but it is not clear if the spin and orbital contributions can possibly be distinguished, since, from symmetry considerations, both can be expected to arise together [151, 169].

The orbital Edelstein effect in Weyl semimetals The Weyl nodes occuring in Weyl semimetals have been found to act as sources of $\mathbf{m}_{\mathbf{k}n}$, and influence the form of the response tensor $\alpha^{\text{orb}}_{\nu\kappa}$ [151]. Ahead of Chapter 3, in which we investigate how gapless lines in a model of a nodal-line semimetal act as strong sources of orbital magnetic moment, we now review the case of Weyl nodes.

In their study of the orbital Edelstein effect in chiral crystals as a condensed-matter analog of solenoids [151], T. Yoda et al. introduce a tight-binding model of stacked honeycomb layers featuring a peculiar interlayer hopping, shown in Fig. 1.18. This interlayer hopping is chiral (its crystal class, 622, is chiral and, hence, also gyrotropic), i.e., it gives the crystal a handedness, and it allows for solenoid-like, winding pathways for electrons travelling in the stacking direction.

After Fourier-ransforming, the Bloch Hamiltonian for this model takes the form

$$H = \sum_{\mathbf{k}} \begin{bmatrix} c^\dagger_{\mathbf{k}A} & c^\dagger_{\mathbf{k}B} \end{bmatrix} H_{\mathbf{k}} \begin{bmatrix} c_{\mathbf{k}A} \\ c_{\mathbf{k}B} \end{bmatrix}, \tag{1.117a}$$

$$H_{\mathbf{k}} = d^0_{\mathbf{k}} \tau_0 + \mathbf{d}_{\mathbf{k}} \cdot \boldsymbol{\tau}, \tag{1.117b}$$

where the Pauli matrices $\{\tau_\nu\}$ act in the the space of sublattices A and B shown in Fig. 1.18, and where spin has been suppressed, as no spin-orbit coupling is present in the model (and

it is not needed to give rise the the orbital Edelstein effect). In terms of the same in-plane NN and NNN vectors defined for graphene in Sec. 1.4.1, the functions $\{d_\nu\}$ are given by

$$d^0_{\mathbf{k}} = 2t_2 \cos(ck_z) \sum_{l=1}^{3} \cos(\mathbf{v}_l \cdot \mathbf{k}) + 2t_3 \cos(ck_z), \tag{1.118a}$$

$$d^1_{\mathbf{k}} = t_1 \sum_{l=1}^{3} \cos(\mathbf{w}_l \cdot \mathbf{k}), \tag{1.118b}$$

$$d^2_{\mathbf{k}} = t_1 \sum_{l=1}^{3} \sin(\mathbf{w}_l \cdot \mathbf{k}), \tag{1.118c}$$

$$d^3_{\mathbf{k}} = -2t_2 \sin(ck_z) \sum_{l=1}^{3} \sin(\mathbf{v}_l \cdot \mathbf{k}), \tag{1.118d}$$

where a is the NN length within the honeycomb layers, c is the stacking distance in the $\hat{z}$ direction, and the (real-valued) hopping amplitudes are defined in Fig. 1.18.

This tight-binding model gives rise to four Weyl points at high-symmetry momenta. In the neighborhood of these points, the linearized Bloch Hamiltonian is given by

$$H_{\mathbf{q},\mu\nu} = -\nu\varepsilon_0\tau_0 - (\mu v_1 q_x \tau_1 + v_2 q_y \tau_2) + \mu\nu v_3 q_z \tau_3, \tag{1.119}$$

where $\varepsilon_0 \coloneqq 3t_2 - 2t_3$, $v_1 \coloneqq v_2 \coloneqq \sqrt{3}t_1 a/2$, $v_3 \coloneqq 3\sqrt{3}t_2 c$, $\mathbf{q}$ is the deviation from the Weyl node, and the indices $\mu, \nu \in \{+1, -1\}$ denote the four distinct Weyl nodes. The nodes are not all at the same energy; rather, two are at energy ε_0 and two are at energy $-\varepsilon_0$. When ε_0 is small compared to the bandwidth, though, and the Fermi energy ε_{F} is nearby, the model is a Weyl semimetal, as all the Fermi surface components are approximately spheres centered at the Weyl points. Hence, in this phase, the electronic properties, including the response tensor α, are determined by the Weyl Hamiltonians of Eq. (1.119).

From the expression of Eq. (1.113), a simple expression can be derived for the orbital magnetic moment $\mathbf{m}_{\mathbf{k}n}$ in a two-band model expressed as in Eq. (1.117b) [151, 160]:

$$m_{\mathbf{k}n,\kappa} = -e\varepsilon_{\kappa\gamma\lambda} \frac{\mathbf{d}_{\mathbf{k}}}{2|\mathbf{d}_{\mathbf{k}}|^2} \cdot \left(\frac{\partial \mathbf{d}_{\mathbf{k}}}{\partial k_\gamma} \times \frac{\partial \mathbf{d}_{\mathbf{k}}}{\partial k_\lambda} \right). \tag{1.120}$$

Notably, this expression shows that in a two-band model, the orbital magnetization is the same in both bands. Using Eq. (1.120), $\mathbf{m}_{\mathbf{k}n}$ can be calculated for the Weyl Hamiltonian of Eq. (1.119):

$$\mathbf{m}_{\mathbf{k}n} = -\nu \frac{e}{2} \frac{v_1 v_2 v_3}{v_1^2 q_x^2 + v_2^2 q_y^2 + v_3^2 q_z^2} \mathbf{q}. \tag{1.121}$$

We see that the orbital magnetic moment becomes arbitrarily large in the neighborhood of the Weyl point, as $\mathbf{m}_{\mathbf{k}n} \propto 1/|\mathbf{q}|$. However, since the area of the fermi surface scales as q_{F}^2, where is the Fermi wave vector measured from a Weyl point, the contribution of a Weyl node to α^{orb} scales with q_{F}, and depends linearly on the energy separation from the Weyl

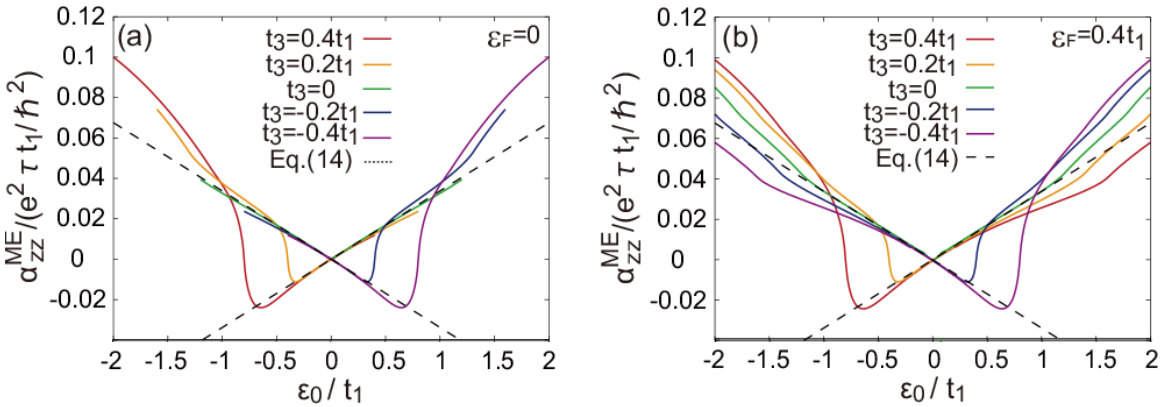

Figure 1.19: Comparison of α_{zz}^{orb} calculated numerically from the tight-binding model (colored lines) and calculated from the low-energy formula of Eq. (1.123) (black dashed lines), for various parameter values. In the small-ε_0 limit, the response depends only on $\varepsilon_0 = 3t_2 - 2t_3$ as required by Eq. (1.123), but beyond that, the behaviour deviates from the low-energy prediction. (Figure adapted, with permission, from Ref. 151, i.e., Taiki Yoda, Takehito Yokoyama, and Shuichi Murakami, *Nano Letters*, 18:916 (2018). Copyright 2018 American Chemical Society.)

node. Specifically, for each of the four Weyl nodes indexed by μ and ν,

$$\alpha_{\kappa\kappa}^{\text{orb}}(\mu,\nu) = \text{sgn}(v_1 v_2 v_3)\frac{e^2\tau}{12\pi^2}(\varepsilon_0 + \nu\varepsilon_{\text{F}}), \tag{1.122}$$

and the net magnetoelectric tensor α^{orb} is given by

$$\alpha_{\kappa\kappa}^{\text{orb}} = \text{sgn}(v_1 v_2 v_3)\frac{e^2\tau}{3\pi^2}\varepsilon_0. \tag{1.123}$$

Figure 1.19 shows the agreement in the small-ε_0 regime between α_{zz}^{orb} calculated with this formula and calculated numerically from the lattice model.

In Chapter 3, we investigate a model in which slightly gapped nodal lines, rather than Weyl nodes, act as a source of orbital magnetic moment $\mathbf{m}_{\mathbf{k}n}$. However, because these (gapped) nodal lines are not at fixed energy, the Fermi surface does not remain in their neighborhood, but instead extends far away from it, where the Bloch Hamiltonian is no longer Dirac like. This precludes a simple analytical picture of the effect of the nodal lines on α^{orb}, such as that expressen in Eq. (1.123); instead, we must resort to numerics.

Finally, we note that the authors T. Yoda et al. develop a careful comparison between the magnetization arising from their model, and that of a classical solenoid with an equivalent number of loops of "wire" per unit length. They find that the magnetization in their model can, for certain parameter values, be much higher than the classical analog would suggest, meaning that a chiral crystal can be considerably more efficient at generating magnetization than a classical solenoid of the same size.

Their chiral model has a preferred axis for its solenoids, the stacking axis $\hat{z}$. In Chapter 3, the charge-ordered phase of the model we consider has non-chiral, but gyrotropic, structure.

It does not have a preferred direction for a solenoidal picture; rather, the solenoidal paths followed by the electrons are determined by the direction of the electric current.

1.6.3 Other variants of the Edelstein effect

For completeness, we comment on other variants of the Edelstein effect.

In the *inverse (spin) Edelstein effect* (also known as the "spin galvanic effect"), a nonequilibrium spin magnetization gives rise to an electrical current [156]. Like the Edelstein effect, it requires the system to be driven out of equilibrium by an external field: circularly polarized light gives rise to a steady state with different populations in the spin-up and spin-down bands [170]. Furthermore, presuming broken inversion symmetry, the bands are split by crystalline spin-orbit coupling, and an asymmetric spin-flip scattering can give rise to an electrical current [156, 170].

Furthermore, the Edelstein effect and inverse Edelstein effect have been reported in a number of topological insulator materials, in which the conducting boundary states can carry a current [171–177].

An analogue the spin Edelstein effect has been studied in superconductors, in which case the flow of a supercurrent gives rise to a net spin magnetization in non-centrosymmetric superconductors [153, 159, 178–181]. Much like in the case of metals, the crystalline SOC arising from the broken inversion symmetry plays a key role; however, unlike the case of metals, it is not a dissipative process, but is rather a property of the thermodynamic equilibrium state [178].

The inverse Edelstein effect in superconductors also differs from that in normal metals: in the former case, a equilibrium spin magnetization can give rise to to a flow of supercurrent, without the need for the system to be driven by radiation [179, 182–184]. As in the previous cases, crystalline SOC arising from broken inversion symmetry plays a crucial role.

Very recently, an orbital Edelstein effect in superconductors has been predicted [185]. In that work, the authors employ a framework that describes the KME—that is, the combined spin and orbital Edelstein effects—on the same footing in both the normal and superconducting states. In particular, their formalism enables them to understand how the KME evolves from the normal metal phase, in which the effect is due to current-carrying excitations, to the superconducting phase, in which it is due to current-carrying excitations *as well as* the paired electrons that constitute the supercurrent. For instance, they predict that the linear magnetoelectric response tensor may or may not undergo an abrupt change across the transition temperature T_{c}, depending on whether the pairing is or is not uniform on the Fermi surfaces, respectively; this property might serve as an additional diagnostic for momentum-dependent pairing.

1.7 A primer on Krein spaces

Chapter 4 of this thesis considers, inter alia, quadratic bosonic Bogoliubov–de Gennes Hamiltonians and their band touchings. As is explained there, the appropriate single-particle Hamiltonian in these systems has the form

$$\tau^3 H. \tag{1.124}$$

Here, H is the Hermitian $2N \times 2N$ coefficient matrix that appears in the Hamiltonian $\hat{H} = \frac{1}{2}\Phi^\dagger H \Phi$, where $\Phi = [b_1, \dots b_N, b_1^\dagger, \dots, b_N^\dagger]$ is the Nambu vector of bosonic annihilation and creation operators. The Pauli matrices in the annihilation-creation space, or "particle-hole" space[19], are given by τ^ν, where $\nu \in \{0, \dots, 3\}$. Often, as in Eq. (1.124), τ^ν is short for $\tau^\nu \otimes \mathbb{1}_N$; generally, this should be clear from context.

The single-particle Hamiltonian $\tau^3 H$ is not Hermitian; however, it is *Krein-Hermitian*, i.e., Hermitian with respect to an indefinite inner product [58, 186, 187]. The present section serves as an introduction to certain notions of Krein spaces that are used in Chapter 4. The discussion is from a physicist's perspective: many simplifications are made to keep the discussion free of complications, and no effort is made to convey the elegance of the formalism. Most notably, we restrict ourselves to finite-dimensional spaces.

1.7.1 Hermiticity and changes of basis

First, we informally motivate the notion of Krein Hermiticity. Consider a Hermitian matrix A in some basis S. As is well known, any orthogonal change of basis preserves the Hermiticity of A. However, under a general transformation P to a basis S',

$$A^\dagger = A \tag{1.125a}$$

$$\left(P^{-1}[A]_{S'}P\right)^\dagger = P^{-1}[A]_{S'}P \tag{1.125b}$$

$$(P^\dagger P)[A]_{S'}^\dagger (P^\dagger P)^{-1} = [A]_{S'} \tag{1.125c}$$

$$\eta^{-1}[A]_{S'}^\dagger \eta = [A]_{S'}, \tag{1.125d}$$

where, in the last line, we have let $\eta := (P^\dagger P)^{-1}$; note that η is Hermitian, invertible and positive definite. The matrix $[A]_{S'}$ is not Hermitian, but it has a real-valued spectrum because it is related to a Hermitian matrix by a similarity transformation. This observation invites the definition of a generalized Hermiticity, sometimes called *pseudo-Hermiticity*,

$$[A]_{S'}^\sharp = [A]_{S'}, \tag{1.126}$$

[19] Though the notion of particles and holes does not make sense for bosons, this nomenclature is often employed in analogy with the fermionic case.

where $M^\sharp = \eta^{-1} M^\dagger \eta$. Such matrices arise as effective Hamiltonians, for example, when using the variational approximation with a linear combination of atomic orbitals, in situations in which the orbitals are not orthogonal. The Hermitian matrix η can be thought of as a metric, which was unity in the original basis, but has changed form due to the coordinate transformation.

Now, let us consider the converse situation: we let η be a Hermitian, nondegenerate (i.e., invertible) matrix, and ask whether there is a basis in which η becomes the identity. If so, then any matrix that is pseudo-Hermitian with respect to η is simply Hermitian in some other basis. If η is positive definite (or negative definite), then we can answer in the affirmative, for Cholesky decomposition allows us to write $\eta = P^\dagger P$, where P is invertible, and we can simply retrace the steps of Eq. (1.125). On the other hand, if η is indefinite (neither positive nor negative definite), then the answer is *no*. We can, however, transform η to a canonical form that is "most analogous" to the identity: first, use the eigendecomposition $\eta = U_\eta \eta_\mathrm{d} U_\eta^\dagger$, and find

$$\begin{aligned}
\eta &= U_\eta \eta_\mathrm{d} U_\eta^\dagger && (1.127\mathrm{a})\\
&= U_\eta \sqrt{\operatorname{abs} \eta_\mathrm{d}} \operatorname{sgn} \eta_\mathrm{d} \sqrt{\operatorname{abs} \eta_\mathrm{d}} U_\eta^\dagger && (1.127\mathrm{b})\\
&= V_\eta^\dagger \eta_\mathrm{s} V_\eta, && (1.127\mathrm{c})
\end{aligned}$$

where $V_\eta \coloneqq \sqrt{\operatorname{abs} \eta_\mathrm{d}} U_\eta^\dagger$, $\eta_\mathrm{s} \coloneqq \operatorname{sgn} \eta_\mathrm{d}$, and the functions abs and sgn are understood to act element-wise. The matrix V_η defines a transformation to a new basis S_0, and in that basis, the metric takes the form of the matrix η_s, which is diagonal with elements $+1$ (with multiplicity given by the number of positive eigenvalues of η) and -1 (with multiplicity given by the number of negative eigenvalues of η). We can verify this by taking a matrix that is pseudo-Hermitian with respect to η and checking that in the basis S_0, it is instead pseudo-Hermitian with respect to η_s: suppose $B = \eta^{-1} B^\dagger \eta$; then,

$$\begin{aligned}
V_\eta^{-1} [B]_0 V_\eta &= \underbrace{\eta^{-1}}_{V_\eta^{-1} \eta_\mathrm{s} \left(V_\eta^\dagger\right)^{-1}} V_\eta^\dagger [B]_0^\dagger \left(V_\eta^{-1}\right)^\dagger \underbrace{\eta}_{V_\eta^\dagger \eta_\mathrm{s} V_\eta} && (1.128\mathrm{a})\\
V_\eta^{-1} [B]_0 V_\eta &= V_\eta^{-1} \eta_\mathrm{s} [B]_0^\dagger \eta_\mathrm{s} V_\eta && (1.128\mathrm{b})\\
[B]_0 &= \eta_\mathrm{s} [B]_0^\dagger \eta_\mathrm{s}. && (1.128\mathrm{c})
\end{aligned}$$

Since η_s is its own inverse, this shows that $[B]_0$ is indeed pseudo-Hermitian with respect to η_s.

There is a clear connection with special relativity and its indefinite Minkowski metric: unlike a positive definite metric, which can be "ignored" by choosing the right coordinates, we conclude that an indefinite metric cannot be ignored even the simplest coordinates.

1.7.2 Elements of the theory of Krein spaces

A *Krein space* is a Hilbert space that, in addition to the ordinary inner product, is endowed with an indefinite, nondegenerate inner product [186]. For two vectors $\phi, \psi \in \mathbb{C}^{n_\mathrm{K}}$, where n_K is the dimension of the space, the Krein inner product can be written as

$$\langle \phi, \psi \rangle_\eta \coloneqq \phi^\dagger \eta \psi, \tag{1.129}$$

where the *Krein metric* η is Hermitian, indefinite and nondegenerate. As is familiar from special relativity, in which case η is the Minkowski metric, a vector ϕ can have positive signature ($\langle \phi, \phi \rangle_\eta > 0$), negative signature ($\langle \phi, \phi \rangle_\eta < 0$), or zero signature ($\langle \phi, \phi \rangle_\eta = 0$).

The *Krein adjoint* $A^\sharp = \eta^{-1} A^\dagger \eta$ of a matrix A satisfies $\langle A\phi, \psi \rangle_\eta = \langle \phi, A^\sharp \psi \rangle_\eta$, much like the Hermitian adjoint with the ordinary inner product. A matrix K is said to be *Krein Hermitian* if it is self Krein adjoint, i.e., $K^\sharp = K$. (Note that while Hamiltonians of the form of Eq. (1.124) come with a particle-hole constraint, such a constraint is not in general present in Krein-Hermitian matrices.) A matrix T is said to be *Krein unitary* if $T^\sharp T = T T^\sharp = \mathbb{1}$; Krein unitary transformations preserve the Krein inner product, since $\langle T\phi, T\psi \rangle_\eta = \langle \phi, T^\sharp T \psi \rangle_\eta = \langle \phi, \psi \rangle_\eta$.

1.7.2.1 Eigenvalues of Krein-Hermitian matrices

A Krein-Hermitian matrix may have non-real eigenvalues, but this possibility is rather constrained. To see this, consider the characteristic polynomial $\chi_K(\lambda) \coloneqq \det(\lambda \mathbb{1} - K)$ of a Krein-Hermitian matrix K, and take its complex conjugate:

$$\begin{aligned}
\chi_K(\lambda)^* &= \det\left((\lambda \mathbb{1} - K)^*\right) && (1.130\mathrm{a})\\
&= \det\left((\lambda \mathbb{1} - K)^\dagger\right) && (1.130\mathrm{b})\\
&= \det\left(\lambda^* \mathbb{1} - K^\dagger\right) && (1.130\mathrm{c})\\
&= \det\left(\lambda^* \eta \eta^{-1} - \eta K \eta^{-1}\right) && (1.130\mathrm{d})\\
&= \det\left(\eta(\lambda^* \mathbb{1} - K)\eta^{-1}\right) && (1.130\mathrm{e})\\
&= \det \eta \ \det(\lambda^* \mathbb{1} - K) \underbrace{\det(\eta^{-1})}_{(\det \eta)^{-1}} && (1.130\mathrm{f})\\
&= \chi_K(\lambda^*). && (1.130\mathrm{g})
\end{aligned}$$

Since the $\chi_K(\lambda)^* = \chi_K(\lambda^*)$, the characteristic polynomial has real-valued coefficients, which implies that its roots—the eigenvalues of K—*are either real, or come in complex-conjugate pairs* [188]. From this fact, we can already see that, as K is perturbed, the only way a nondegenerate (specifically, with algebraic multiplicity 1) real eigenvalue can become complex is if it meets with another real eigenvalue, and the two split away from the real axis in

opposite directions. Later, we will see that two such real eigenvalues may or may not be allowed to become complex in this way, depending on the nature of their eigenvectors.

1.7.2.2 Eigenvectors of Krein-Hermitian matrices and diagonalizability

Consider two eigenvectors ϕ and ϕ' of a Krein-Hermitian matrix K, such that [189, Sec. 5.5]

$$K\phi = \lambda\phi, \tag{1.131a}$$
$$K\phi' = \lambda'\phi'. \tag{1.131b}$$

On one hand, taking the Hermitian adjoint of Eq. (1.131a) and right-multiplying by ϕ', we get

$$\phi^\dagger \eta K \eta^{-1} = \lambda^* \phi^\dagger \tag{1.132a}$$
$$\Leftrightarrow \quad \phi^\dagger \eta K = \lambda^* \phi^\dagger \eta \tag{1.132b}$$
$$\Rightarrow \quad \phi^\dagger \eta K \phi' = \lambda^* \phi^\dagger \eta \phi' \tag{1.132c}$$
$$\Leftrightarrow \quad \langle \phi, K\phi' \rangle_\eta = \lambda^* \langle \phi, \phi' \rangle_\eta. \tag{1.132d}$$

On the other hand, left-multiplying Eq. (1.131b) by $\phi^\dagger \eta$, we get

$$K\phi' = \lambda'\phi' \tag{1.133a}$$
$$\Rightarrow \quad \phi^\dagger \eta K \phi' = \lambda' \phi^\dagger \eta \phi' \tag{1.133b}$$
$$\Leftrightarrow \quad \langle \phi, K\phi' \rangle_\eta = \lambda' \langle \phi, \phi' \rangle_\eta. \tag{1.133c}$$

Taking the difference between Eqs. (1.132d) and (1.133c) gives the following constraint on the Krein inner product of ϕ and ϕ':

$$0 = (\lambda^* - \lambda')\langle \phi, \phi' \rangle_\eta. \tag{1.134}$$

This equation implies that two eigenvectors of K are *Krein orthogonal* (orthogonal with respect to the Krein metric) if their eigenvalues are not complex-conjugate pairs.

If we take $\phi' = \phi$, then Eq. (1.134) becomes $0 = (\operatorname{Im}\lambda)\langle \phi, \phi \rangle_\eta$, which implies that any eigenvector with a non-real eigenvalue has signature zero. It also *suggests* that an eigenvector with real eigenvalue has non-zero signature and can be normalized such that $\langle \phi, \phi \rangle_\eta = \pm 1$, and we will shortly discuss under what circumstances this turns out to be true. As for two eigenvectors ϕ and ϕ' corresponding to complex-conjugated nondegenerate (specifically, algebraic multiplicity 1) eigenvalues, they can be normalized such that $\langle \phi, \phi' \rangle_\eta = 1$, as Eq. (1.134) suggests.

One must also realize that in general, a Krein-Hermitian matrix can fail to be diagonalizable, and have nontrivial Jordan blocks in its Jordan canonical form.

Some basic results from *Krein stability theory* shed more light on the diagonalizability of Krein-Hermitian matrices, as well as on the effect of perturbations [58, 187]. Before stating them, we define the *signature of an eigenspace*: if all vectors in an eigenspace have the same nonzero signature, then that eigenspace is said to have *definite signature*; otherwise, it has *indefinite signature*. Quoting from Chapter 4,

- "[a]ccording to Krein stability theory, if each eigenspace of K has definite signature, a perturbed Hamiltonian $K + \epsilon K'$ for sufficiently small ϵ [including K itself] is diagonalizable with real eigenvalues [...]. Furthermore, its eigenvectors can be chosen to be orthonormal with respect to the Krein inner product." In other words, this is a sufficient condition for K to be diagonalizable with real eigenvalues and Krein-orthonormal eigenvectors.

- "Conversely, if K has an indefinite eigenspace, either with or without nontrivial Jordan blocks, then K either has non-real eigenvalues or there are arbitrarily small perturbations that make them non-real". We already knew that eigenspaces of non-real eigenvalues have indefinite signature, since their eigenvectors automatically have signature zero. However, this result reveals what happens upon the collision of two real eigenvalues whose eigenspaces have definite signature: if the two eigenspaces have the same (nonzero) signature, any small perturbation will leave them real. If, on the contrary, the two eigenspaces have opposite signatures, then at the meeting point they will form a larger eigenspace with signature zero, and further perturbations may split the eigenvalues off the real axis; this has been called a "Krein collision" [187]. It also reveals that an eigenvalue corresponding to a nontrivial Jordan block—whose eigenspace cannot have definite signature by virtue of the previous point—is also vulnerable to being split off the real axis by small perturbations; such a point is called an "exceptional point" [187]. For more details on these matters, see, for instance, Ref. 187.

A considerable simplification occurs if K is positive definite with respect to the Krein inner product[20], or *Krein positive definite*, i.e., that the real-valued quantity $\langle \psi, K\psi \rangle_\eta > 0$ for any $\psi \in \mathbb{C}^{n_K} \backslash \{\mathbf{0}\}$. (An equivalent condition is that the Hermitian matrix ηK be positive-definite in the ordinary sense. In the specific case of the Hamiltonian of Eq. (1.124), i.e., $K = \tau^3 H$ and $\eta = \tau^3$, the condition is simply that H be positive definite.) In this case, from Eq. (1.133c) with $\phi' = \phi$,

$$\langle \phi, K\phi \rangle_\eta = \lambda \langle \phi, \phi \rangle_\eta, \tag{1.135}$$

one can conclude that K has no zero eigenvalues and no signature-zero eigenstates, that all eigenvalues are purely real, and that the signature of each eigenvector matches the sign

[20] Recall that a definition of positive definiteness for an $n \times n$ Hermitian matrix A (with respect to the ordinary inner product) is that $\mathbf{v}^\dagger M \mathbf{v} = \langle \mathbf{v}, M\mathbf{v} \rangle > 0$ for any $\mathbf{v} \in \mathbb{C}^n \backslash \{\mathbf{0}\}$. The analogy with the Krein-Hermitian case should be clear.

of its eigenvalue. Hence, each of its eigenspaces have definite signature, so Krein stability theory implies that K (as well as small perturbations $K + \epsilon K'$) is necessarily diagonalizable with real eigenvalues and Krein-orthonormal eigenvectors.

In this same situation, i.e., assuming K is Krein positive definite, one can formulate a bound on perturbations $\epsilon K'$ that guarantees that $K + \epsilon K'$ is also Krein positive definite [58, Sec. IV C]. In terms of the operator norm $\|\cdot\|$ (equal to the largest singular value), this bound turns out to be $\|\epsilon K'\| < \|K^{-1}\|^{-1}$; here, $\|K^{-1}\|^{-1}$, the smallest singular value of K, is a lower bound on the smallest eigenvalue (in absolute value) of K[21]. We emphasize that the effect of perturbations on eigenvalues is not a simple matter for non-normal matrices [190,191]. For a normal (including Hermitian) matrix M, a perturbation M' displaces each eigenvalue by at most $\|M'\|$ in the complex plane. Instead, for a non-normal matrix like K, the effect of a perturbation on the eigenvalues depends on the details of K; indeed, this very question gives rise to the notion of *pseudospectra* in mathematics [190,191].

Returning to the case of a Krein-positive-definite K, the bound given above can be derived as follows [58, Sec. IV C]. A sufficient condition for $K + \epsilon K'$ to remain Krein positive definite is that none of its eigenvalues reach zero, since in that case no eigenvalues with opposite-signature eigenspaces can collide. Now, since K is invertible, one can write

$$\det(K + \epsilon K') = (\det K)\det(\mathbb{1} + K^{-1}\epsilon K'). \tag{1.136}$$

To ensure that no eigenvalue of $K + \epsilon K'$ can reach zero, we bound ϵ such that $\det(K + \epsilon K')$, or, equivalently, $\det(\mathbb{1} + K^{-1}\epsilon K')$ cannot become zero. Since the operator norm of a matrix bounds its spectrum, the spectrum of $\mathbb{1} + K^{-1}\epsilon K'$ is located within a disk of radius $\|K^{-1}\epsilon K'\|$ centered at 1 in the complex plane. Hence, requiring $\|K^{-1}\epsilon K'\| < 1$ ensures that $\mathbb{1} + K^{-1}\epsilon K'$ cannot have a zero eigenvalue and, hence, that $\det(\mathbb{1} + K^{-1}\epsilon K') \neq 0$. One can simply choose, as claimed above, $\|\epsilon K'\| < \|K^{-1}\|^{-1}$, in which case

$$\|K^{-1}\epsilon K'\| \leq \|K^{-1}\|\|\epsilon K'\| < \|K^{-1}\|\|K^{-1}\|^{-1} = 1, \tag{1.137}$$

implying $\|K^{-1}\epsilon K'\| < 1$, as required.

1.7.2.3 The diagonalizing transformation

Naïvely, one may expect that a Krein-Hermitian matrix whose eigenspaces all have definite signature—which is diagonalizable with real eigenvalues and Krein-orthonormal eigenvectors—is diagonalized by a Krein-unitary transformation. However, this guess turns out to be too simplistic. As a simple counterexample, suppose K is such a Krein-Hermitian matrix (specifically, with respect to some metric η), and call the diagonalization transformation S:

[21] In general, the spectrum of a matrix A is located within an annulus centered at 0 in the complex plane with inner radius $\|A^{-1}\|^{-1}$ (the smallest singular value of A) and outer radius $\|A\|$ (the largest singular value of A), with the understanding that $\|A^{-1}\|^{-1} = 0$ if the smallest singular value vanishes.

$D = S^{-1}KS$. The transformation

$$S = \left[\begin{array}{c|c|c} s_1 & \dots & s_{n_\mathrm{K}} \end{array}\right], \tag{1.138}$$

whose columns s_i are the (Krein-normalized) eigenvectors of K, is Krein unitary if, and only if, $S^\dagger \eta S = \eta$. However, as mentioned above, we know from Sec. 1.7.2.2 that the eigenvectors of K are Krein-orthonormal, meaning that

$$S^\dagger \eta S = \begin{bmatrix} \langle s_1, s_1\rangle_\eta & \cdots & \langle s_1, s_{n_\mathrm{K}}\rangle_\eta \\ \vdots & \ddots & \vdots \\ \langle s_{n_\mathrm{K}}, s_1\rangle_\eta & \cdots & \langle s_{n_\mathrm{K}}, s_{n_\mathrm{K}}\rangle_\eta \end{bmatrix} = \begin{bmatrix} 1 & & & & & \\ & \ddots & & & & \\ & & 1 & & & \\ & & & -1 & & \\ & & & & \ddots & \\ & & & & & -1 \end{bmatrix} \neq \eta \tag{1.139}$$

Hence, $S^\dagger \eta S$ is generally not equal to η, which disproves the naïve expectation stated above.

Instead, what is generally true about an η-Krein-Hermitian matrix K with definite-signature eigenspaces is that it can be transformed via a Krein-unitary transformation T to a matrix [186, Sec. III A 1]

$$\tilde{K} := TKT^\sharp = TKT^{-1} \tag{1.140}$$

that is both Hermitian and Krein Hermitian with respect to η [186, Sec. III A 1]:

$$\tilde{K} = \tilde{K}^\sharp = \tilde{K}^\dagger. \tag{1.141}$$

Let us take a pedestrian approach to understand this and some of its implications. This last equation implies that $\tilde{K}$ and η commute,

$$\tilde{K} = \eta^{-1}\tilde{K}\eta \quad \Leftrightarrow \quad [\tilde{K}, \eta] = 0, \tag{1.142}$$

meaning that they can be diagonalized simultaneously. Let U be the unitary transformation that simultaneously diagonalizes $\tilde{K}$ and η:

$$\eta_\mathrm{d} = U^\dagger \eta U, \qquad\qquad D = U^\dagger \tilde{K} U. \tag{1.143}$$

(It is easy to check that the induced decomposition of $\tilde{K}$, i.e., $\tilde{K} = UDU^\dagger$, is indeed both Hermitian and Krein-Hermitian with respect to η.) Now, as we know from the discussion of Sec. 1.7.1, η is nearly in its "canonical" form (in which it is diagonal with elements $+1$ and -1). The canonical form is given by $\eta_\mathrm{s} = (V^{-1})^\dagger \eta V^{-1}$, where $V = \sqrt{\operatorname{abs}\eta_\mathrm{d}}\, U^\dagger$. In the basis

defined by the transformation V, the matrix $\tilde{K}$ takes the form

$$[\tilde{K}]_0 = V\tilde{K}V^{-1} \tag{1.144a}$$

$$= \sqrt{\operatorname{abs}\eta_{\mathrm{d}}}\,\underbrace{U^\dagger\tilde{K}U}_{D}\,\sqrt{\operatorname{abs}\eta_{\mathrm{d}}}^{\,-1} \tag{1.144b}$$

$$= D, \tag{1.144c}$$

where in the last step we have used the fact that both D and $\sqrt{\operatorname{abs}\eta_{\mathrm{d}}}$ are diagonal (in essence, a rescaling of axes leaves a diagonal matrix unchanged). Hence, the matrix $\tilde{K}$ is *also* diagonal in the canonical basis of η.

To summarize, we have seen that the diagonalization of K can be written as

$$D = VT\ K\ T^{-1}V^{-1} = S^{-1}KS, \tag{1.145}$$

where $S = T^{-1}V^{-1}$. Here, T is the η-Krein-unitary transformation that appears in Eq. (1.140), and V is a composition of the matrix U (that simultaneously diagonalizes $\tilde{K}$ and η) and the coordinate rescaling $\sqrt{\operatorname{abs}\eta_{\mathrm{d}}}$. We draw two main conclusions from these observations.

First, *for an η-Krein-Hermitian matrix K whose eigenspaces all have definite signature (which implies that K is diagonal with real eigenvalues and η-orthonormal eigenvectors), the number of positive-signature and negative-signature eigenvectors is determined by the signature of η (i.e., the number of positive and negative eigenvalues of η).* To show this, we evaluate

$$\begin{bmatrix} \langle s_1, s_1\rangle_\eta & & \\ & \ddots & \\ & & \langle s_{n_{\mathrm{K}}}, s_{n_{\mathrm{K}}}\rangle_\eta \end{bmatrix} = S^\dagger\eta S \tag{1.146a}$$

$$= (V^{-1})^\dagger (T^{-1})^\dagger \eta T^{-1}V^{-1} \tag{1.146b}$$

$$= (V^{-1})^\dagger \underbrace{(T^\sharp)^\dagger}_{\eta T\eta^{-1}} \eta T^\sharp V^{-1} \tag{1.146c}$$

$$= (V^{-1})^\dagger \eta \underbrace{TT^\sharp}_{\mathbb{1}} V^{-1} \tag{1.146d}$$

$$= (V^{-1})^\dagger \eta V^{-1} \tag{1.146e}$$

$$= \eta_{\mathrm{s}}. \tag{1.146f}$$

Yet, the diagonal of η_{s} is precisely given by the signs of the eigenvalues of η, so the claim holds.

Second, *for an η-Krein-Hermitian matrix K whose eigenspaces all have definite signature (which implies that K is diagonal with real eigenvalues and η-orthonormal eigenvectors), if one works in the canonical basis of η, then K (expressed in said basis) is simply diagonalized via*

a η_s-Krein-unitary transformation. To see this, we rewrite the transformation of Eq. (1.145) in terms of $[T]_0$, where $[T]_0 = VTV^{-1}$:

$$D = VT\ K\ T^{-1}V^{-1} \tag{1.147a}$$
$$= V(V^{-1}[T]_0V)K(V^{-1}[T]_0V)^{-1}V^{-1} \tag{1.147b}$$
$$= [T]_0V\ K\ V^{-1}[T]_0^{-1} \tag{1.147c}$$
$$= [T]_0[K]_0[T]_0^{-1} \tag{1.147d}$$

In the last step, we have recognized that $VKV^{-1} = [K]_0$. Furthermore, we note that $[T]_0$ is Krein unitary with respect to η_s:

$$\eta_s^{-1}[T]_0^\dagger\eta_s = \eta_s^{-1}(VTV^{-1})^\dagger\eta_s \tag{1.148a}$$
$$= \eta_s^{-1}(V^{-1})^\dagger T^\dagger V^\dagger\eta_s \tag{1.148b}$$
$$= \underbrace{(V^\dagger\eta_s)^{-1}}_{V\eta^{-1}}\eta T\eta^{-1}\underbrace{V^\dagger\eta_s}_{\eta V^{-1}} \tag{1.148c}$$
$$= VTV^{-1} \tag{1.148d}$$
$$= [T]_0. \tag{1.148e}$$

Hence, we see that using $[T]_0$ instead of T is, in a sense, akin to switching the order of the two transformations that make up the diagonalization (constrast Eq. (1.147a) with Eq. (1.147c)). There are practical advantages to changing basis to bring the metric to its canonical form *before* diagonalizing $[K]_0$ via $[T]_0$: first, Krein Hermiticity with respect to a canonical η_s is conceptually and computationally simpler, and second, one can obtain $[T]_0$ from the eigendecomposition of $[K]_0$ via standard means. Indeed, the derivation and results of Chapter 4 all assume a Krein metric in its canonical form.

Chapter 2

Pseudo-Landau levels of Bogoliubov quasiparticles in strained nodal superconductors[1]

2.1 Introduction

The ability to tune electronic properties with strain in a wide range of quantum materials has led to the emerging area of 'straintronics' [192]. Strain has been shown to be an important knob in graphene, topological materials, and oxide electronics, allowing one to tune band dispersion and topology [91, 133, 193–199], and to control magnetism [200, 201] and ferroelectricity [202] in thin films. Uniaxial strain has also been used to shed light on fundamental questions in correlated materials, from searching for chiral $p_x \pm ip_y$ pairing in Sr_2RuO_4 [203], to understanding nematicity in pnictide superconductors [204] and in the 'hidden order' state of URu_2Si_2 [205].

In graphene, a two-dimensional (2D) electronic membrane [206], strain modifies the wavefunction overlap between neighboring orbitals and causes a momentum space displacement of the massless Dirac point in the dispersion, thus simulating the effect of a vector potential [91, 96, 194]. A spatial variation of the strain in graphene nanobubbles and 'artificial graphene' leads to colossal pseudo-magnetic fields of up to $\sim$300T, and a pseudo-Landau level (pseudo-LL) spectrum [133, 193, 195]. Strain also induces a deformation potential which acts as a 'scalar gauge potential'; the corresponding in-plane electric fields can lead to a breakdown of the pseudo-LLs [96, 207–209]. There have been theoretical studies of Josephson coupling through pseudo-LLs [210, 211], and interaction effects which can lead to exotic correlated states [212, 213]. Strain effects have also been generalized to 3D Dirac and Weyl semimetals [139, 214–216], Kitaev spin liquids [217], and atoms in optical lattices [218, 219].

In light of these developments, we address in this paper the important question of how

[1]Chapter adapted from Ref. 1, i.e., Geremia Massarelli, Gideon Wachtel, John Y. T. Wei, and Arun Paramekanti, *Phys. Rev. B*, 96:224516 (2017). Copyright 2017 by the American Physical Society.

these phenomena manifest themselves in superconducting phases of matter. Specifically, we consider the possibility of engineering time-reversal invariant pseudo-gauge fields for Bogoliubov quasiparticle (QP) excitations of nodal superconductors (SCs). Our key observation is that the QP Dirac nodes of the SC will shift in momentum space under the modification of the single-particle dispersion or the form of the pairing gap. Thus, spatial variations of the dispersion or the pairing term can mimic a spatially varying gauge field. Using an effective low energy theory for 2D d-wave SCs as well as a numerical lattice model study, we show that this induces pseudo-LLs of Bogoliubov QPs and discuss its signatures in the spatially resolved tunneling density of states (TDOS).

Our work highlights two key differences between strained nodal SCs and materials such as graphene or Dirac-Weyl semimetals. (i) Unlike electrons, Bogoliubov QPs do not have a well-defined electrical charge and do not couple directly to external orbital magnetic fields. Thus, strain engineering provides a unique window to explore LL physics of Bogoliubov QPs. (ii) We show that strain variations in a d-wave SC with time-reversal symmetry cannot induce a pseudo-'scalar potential' for Bogoliubov QPs. This is unlike the impact of the deformation potential for graphene. In this regard, pseudo-LLs of Bogoliubov QPs are more robust and are 'symmetry protected'.

We suggest two routes to realizing this physics in the cuprate SCs: via strain engineering in thin films and nanowires, or via edge effects or s-wave proximity coupling in the vicinity of an isotropic to nematic SC quantum phase transition (QPT) [220]. Our study sheds light on how inhomogeneous strain can reorganize the low energy spectrum of nodal SCs.

2.2 Effective low-energy theory

The low energy excitations of a uniform 2D d-wave SC on a square lattice reside near the two pairs of gap nodes $\mathbf{K}_{\pm 1} \equiv \pm(K, K)$ and $\mathbf{K}_{\pm 2} \equiv \pm(K, -K)$ as in Fig. 2.1(a). We combine the slowly varying fermion fields near the node pairs into Nambu spinors $\Psi^\dagger_{\ell\alpha}(\mathbf{r}) \equiv (\psi^\dagger_{\ell\alpha}(\mathbf{r}), \epsilon_{\alpha\nu}\psi_{-\ell\nu}(\mathbf{r}))$, where α, ν are spin labels ($\uparrow$ or $\downarrow$), and $\ell = 1, 2$ labels the nodes $\mathbf{K}_{1,2}$. The low energy excitations of a nodal SC are described by the effective Dirac Hamiltonian $H_0 = \sum_{\ell,\alpha} \int d^2\mathbf{r} \Psi^\dagger_{\ell\alpha}(\mathbf{r}) \mathfrak{h}_0^{(\ell)} \Psi_{\ell\alpha}(\mathbf{r})$, with

$$\mathfrak{h}_0^{(\ell)} = -i\sigma^z \vec{v}_{\mathrm{f}}^{(\ell)} \cdot \vec{\nabla} - i\sigma^x \vec{v}_{\Delta}^{(\ell)} \cdot \vec{\nabla} \tag{2.1}$$

where $\vec{v}_{\mathrm{f}}^{(\ell)}, \vec{v}_{\Delta}^{(\ell)}$ denote the Fermi velocity and the gap velocity (respectively, normal and tangential to the Fermi surface), and $\sigma^{x,z}$ are Pauli matrices. Diagonalizing H_0 in momentum space leads to the massless Dirac dispersion $E_\ell(\mathbf{k}) = (v_{\mathrm{f}}^2 k_x^2 + v_\Delta^2 k_y^2)^{1/2}$ where (k_x, k_y) denotes the deviation in momentum from $\mathbf{K}_\ell$ (with local coordinate axes as shown in Fig. 2.1(a)), and the Dirac cone anisotropy is set by v_{f}/v_Δ.

We next turn to the effect of time-reversal invariant slow spatial variations in the hopping and pairing amplitudes of this nodal SC, which adds to the microscopic lattice Hamiltonian

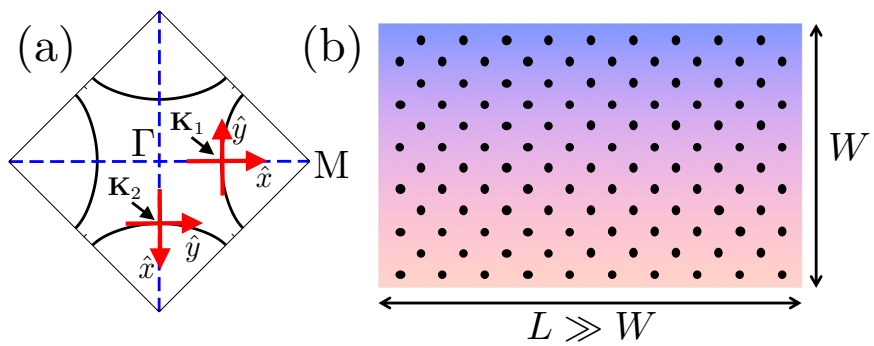

Figure 2.1: (Color online) (a) Rotated Brillouin zone for the square lattice showing schematic Fermi surface (solid, black) for optimal hole-doped cuprate SCs. Quasiparticle Dirac nodes are located at $\pm\mathbf{K}_1$ and $\pm\mathbf{K}_2$, and we show local coordinate axes used in our low-energy theory. (b) Strip geometry (not to scale) used in the numerics with width W and length $L \gg W$. Shading gradient illustrates spatial variation in the pairing or hopping amplitude across the strip.

terms of the form

$$\delta H_1 = -\frac{1}{2}\sum_{\mathbf{R},\eta,\alpha} \delta t_\eta(\mathbf{R})(c^\dagger_{\mathbf{R},\alpha} c_{\mathbf{R}+\eta,\alpha} + \text{h.c.}) \tag{2.2}$$

$$\delta H_2 = \frac{1}{8}\sum_{\mathbf{R},\eta} \delta\Delta_\eta(\mathbf{R})(c^\dagger_{\mathbf{R}\uparrow} c^\dagger_{\mathbf{R}+\eta,\downarrow} - c^\dagger_{\mathbf{R}\downarrow} c^\dagger_{\mathbf{R}+\eta,\uparrow} + \text{h.c.}) \tag{2.3}$$

where η denotes the set of neighbors of site $\mathbf{R}$ and 'h.c.' stands for Hermitian conjugate. A low energy expansion of the fermion fields leads to the modified Hamiltonian

$$\mathfrak{h}^{(\ell)} = \begin{pmatrix} -iv_{\text{f}}\partial_x + f_\ell(\mathbf{r}) & -is_\ell v_\Delta \partial_y + g_\ell(\mathbf{r}) \\ -is_\ell v_\Delta \partial_y + g_\ell(\mathbf{r}) & iv_{\text{f}}\partial_x - f_\ell(\mathbf{r}) \end{pmatrix} \tag{2.4}$$

where $s_\ell = (-1)^\ell$, with

$$f_\ell(\mathbf{r}) = -\sum_\eta \delta t_\eta(\mathbf{r}) \cos(\mathbf{K}_\ell \cdot \eta) \tag{2.5}$$

$$g_\ell(\mathbf{r}) = \frac{1}{4}\sum_\eta \delta\Delta_\eta(\mathbf{r}) \cos(\mathbf{K}_\ell \cdot \eta), \tag{2.6}$$

and we have implicitly assumed that we have rotated $\mathbf{r}$ into the local coordinate axes for node ℓ. Note that a conventional deformation potential or spatially varying chemical potential may also be included in $f_\ell(\mathbf{r})$ in Eq. 4. We can recast this Hamiltonian as

$$\mathfrak{h}^{(\ell)} = v_{\text{f}}\sigma^z(-i\partial_x + \mathcal{A}^{(\ell)}_x(\mathbf{r})) + s_\ell v_\Delta \sigma^x(-i\partial_y + \mathcal{A}^{(\ell)}_y(\mathbf{r})) \tag{2.7}$$

where we have defined the 'vector potential' $\vec{\mathcal{A}}^{(\ell)}$ via $v_{\text{f}}\mathcal{A}^{(\ell)}_x(\mathbf{r}) \equiv f_\ell(\mathbf{r})$ and $v_\Delta \mathcal{A}^{(\ell)}_y(\mathbf{r}) \equiv s_\ell g_\ell(\mathbf{r})$. Thus slow spatial modulations of parameters in a nodal superconductor will lead to

an effective low energy theory of Dirac quasiparticles coupled to a spatially varying 'vector potential'.

The issue of whether additional gauge potentials (e.g. a 'scalar gauge potential' which minimally couples to time-derivatives rather than space derivatives) can arise in a strained SC amounts to asking if any other Pauli matrix components are permitted in $\mathfrak{h}^{(\ell)}$. To address this, we note that terms proportional to the identity matrix will act as a valley-odd chemical potential, while a component proportional to σ^y will correspond to complex pairing. Both terms are forbidden by time-reversal and spin-rotation symmetries in a d-wave SC, and thus cannot destabilize the pseudo-LLs; in this sense, the pseudo-LLs may be regarded as 'symmetry protected' (see Appendix A for details). The key point is that slow modulations of the parameters of a nodal superconductor will leave the nodal quasiparticle excitations pinned to zero energy but can displace it in momentum space. Thus, d-wave Bogoliubov QPs, unlike electrons in graphene, do not experience an inhomogeneous 'scalar' gauge potential [96, 209]. However, breaking time-reversal symmetry, for instance with a supercurrent, will lead to a Doppler shift for the QPs [221, Section 5-1], shifting the energy of the nodal excitations, which thus provides an analog of a 'scalar potential'.

2.3 Pseudo-Landau levels

We next turn to the spectrum of $\mathfrak{h}^{(\ell)}(\mathbf{r})$ for two illustrative cases, with $\vec{\mathcal{A}}$ induced by variations in the pairing gap or hopping amplitude, to show the emergence of pseudo-LLs. We then supplement the continuum theory with numerical results on a lattice realization.

2.3.1 Pseudo-LLs from gap variations

Let us impose an additional extended s-wave pairing with a uniform gradient along the $[1,1]$ direction, which translates to $\delta\Delta_{+x}(\mathbf{r}) = \delta\Delta_{+y}(\mathbf{r}) = (x_a/a_0 + x_b/a_0 + 1/2)\Delta_s$. Here, (x_a, x_b) refer to (global) coordinates corresponding to the a and b crystal axes, and a_0 is the lattice constant. Using this, we find $f_\ell(\mathbf{r}) = 0$, while, in the local coordinates at $\ell = 1, 2$, we have $g_1(\mathbf{r}) = \beta v_\Delta x$ and $g_2(\mathbf{r}) = \beta v_\Delta y$, with $\beta \equiv \sqrt{2}\frac{\Delta_s}{v_\Delta a_0}\cos K$.

For node pair $\ell = 2$, this leads to $\vec{\mathcal{A}}^{(2)} = (0, \beta y)$, which yields $\vec{\mathcal{B}}^{(2)} = 0$. In this case, the energy spectrum is unaffected by the modulation, while the wavefunctions are obtained by a gauge rotation as $\mathrm{e}^{-\frac{i}{2}\beta y^2}\Psi^{(2)}(\mathbf{r})$, where $\Psi^{(2)}(\mathbf{r})$ is the Nambu spinor wavefunction of the uniform d-wave SC for node pair $\ell = 2$.

For node pair $\ell = 1$, we arrive at $\vec{\mathcal{A}}^{(1)} = (0, -\beta x)$, i.e., the Landau gauge for a pseudo-magnetic field $\vec{\mathcal{B}}^{(1)} = -\beta\hat{z}$. Setting the Nambu wavefunction $\Psi^{(1)}(\mathbf{r}) = \mathrm{e}^{iky}\Phi^{(1)}(x)$, we get (see Appendix B)

$$\left[-iv_{\mathrm{f}}\sigma^z\partial_x + \beta v_\Delta \sigma^x (x - \frac{k}{\beta})\right]\Phi^{(1)}(x) = E\Phi^{(1)}(x). \tag{2.8}$$

Defining $|\uparrow\rangle = \frac{1}{\sqrt{2}}(1, i\ \mathrm{sgn}\beta)^T$ and $|\downarrow\rangle = \frac{1}{\sqrt{2}}(1, -i\ \mathrm{sgn}\beta)^T$, we find a zero energy eigenstate $|\Phi_{k0}\rangle = |0\rangle_k |\downarrow\rangle$ and nonzero energy eigenstates

$$|\Phi_{kn\pm}\rangle = \frac{1}{\sqrt{2}}\left(|n-1\rangle_k |\uparrow\rangle \pm i\, |n\rangle_k |\downarrow\rangle \right), \tag{2.9}$$

where the subscript $\pm$ denotes states with energies $\pm\sqrt{2|\beta|v_\Delta v_\mathrm{f} n}$ (with integer $n \geq 1$). Here, $|n\rangle_k$ is the nth eigenstate of a harmonic oscillator centered at k/β, with a mean square width $\langle x^2\rangle = (n+1/2)\frac{v_\mathrm{f}}{|\beta| v_\Delta}$. We confirm these findings below within a lattice model of a d-wave superconducting strip.

2.3.2 Pseudo-LLs from hopping variations

Next, let us consider a uniform spatial gradient in the hopping along the $[1,1]$ direction, given by $\delta t_{+x}(\mathbf{r}) = \delta t_{+y}(\mathbf{r}) = -(x_a/a_0 + x_b/a_0 + 1/2)t_s$, where t_s sets the scale of the hopping distortion. This results in $g_\ell(\mathbf{r}) = 0$ and, in local coordinates, $f_1(\mathbf{r}) = \beta v_\mathrm{f} x$ and $f_2(\mathbf{r}) = \beta v_\mathrm{f} y$, where $\beta \equiv 4\sqrt{2}\frac{t_s}{v_\mathrm{f} a_0}\cos K$. This, in turn, leads to $\vec{\mathcal{A}}^{(1)} = (\beta x, 0)$, which corresponds to zero pseudo-magnetic field, while $\vec{\mathcal{A}}^{(2)} = (\beta y, 0)$ yields a pseudo-magnetic field $\vec{\mathcal{B}}^{(2)} = -\beta\hat{z}$, which supports pseudo-LL energies identical to the case with gap variation for the same choice of β (see Appendix C). A similar pseudo-vector potential can also be realized by a spatially varying nematic distortion of the second-neighbor hopping, with $\delta t_{+x+y}(\mathbf{r}) = -(x_a/a_0 + x_b/a_0 + 1)t_s$ and $\delta t_{+x-y}(\mathbf{r}) = (x_a/a_0 + x_b/a_0)t_s$, which yields $\vec{\mathcal{B}}^{(1)} = 0$ and $\vec{\mathcal{B}}^{(2)} = -\beta\hat{z}$, with $\beta \equiv 4\sqrt{2}\frac{t_s}{v_\mathrm{f} a_0}\sin^2 K$. We note that while these examples are 'gauge equivalent' to the earlier gap variation case, their physical realizations are distinct since we are changing the hopping rather than the gap, thus directly controlling the 'vector potential'.

2.4 Lattice model results

To check the validity of the low-energy linearized Dirac theory, we numerically diagonalized the full lattice Bogoliubov-deGennes (BdG) Hamiltonian using a strip geometry with $(1,1)$ edges (see Fig. 2.1(b)). The strip width is W; the transverse direction, along which periodic boundary conditions were used, has length $L \gg W$. Analogous results for the $(1,0)$-edged strip are presented in Appendix F. We pick a nearest neighbor hopping amplitude $t = 1$, next-neighbor hopping $t' = -0.25t$, electron filling $\bar{n} = 0.85$, and a d-wave gap $\Delta_d = 0.25t$, such that $v_\mathrm{f}/v_\Delta \approx 13$; these parameters are chosen so as to be representative of the hole-doped cuprate SCs.

Fig. 2.2(a) shows the spectrum of the $(1,1)$-edged strip as a function of the momentum k_L along the long direction L, in the absence of any imposed spatial variation for $W = 500\sqrt{2}a_0$. The spectrum exhibits d-wave Dirac nodes projected onto the Brillouin zone of the strip; the velocity anisotropy $v_\mathrm{f}/v_\Delta \gg 1$ is evident in the dispersion slopes of the outer versus inner nodes. In addition, we find zero energy Andreev bound states (ABSs) expected for a d-wave

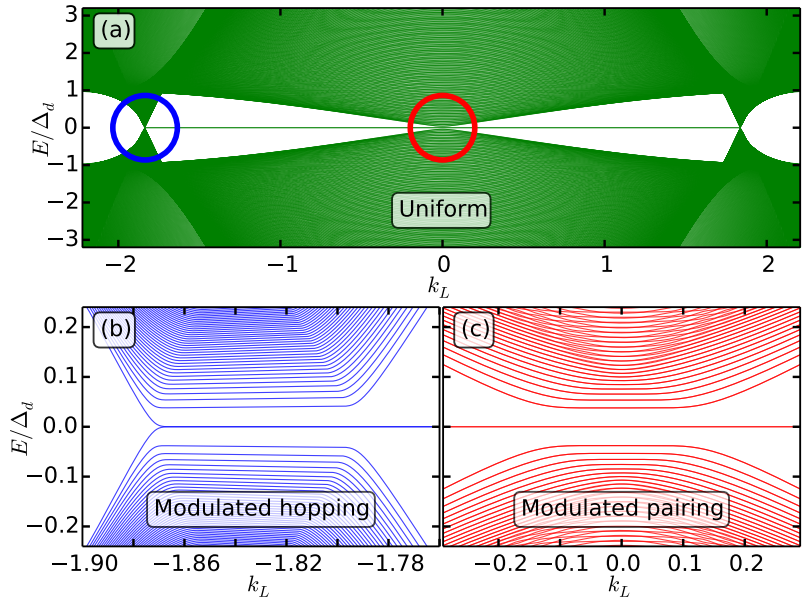

Figure 2.2: (Color online) (a) Spectrum of uniform d-wave SC on a $(1,1)$-edged strip versus momentum k_L along the L-direction, showing Dirac nodes and zero energy ABSs. Circles indicate regions shown in the next two panels. (b) Formation of flat pseudo-Landau levels near the outer Dirac nodes due to uniform hopping-amplitude gradient in the [1,1] direction; shown here is the near-node region indicated in (a). (c) Similar to (b) but with extended s-wave pairing gradient, which induces pseudo-LLs near the central Dirac node indicated in panel (a).

SC in this geometry [104, 222–224].

Fig. 2.2(b) shows the spectrum with a nonzero gradient in the hopping amplitude across the strip width, which leads to a pseudo-LL spectrum at the outer Dirac nodes; we have chosen to plot the spectrum near the Dirac node indicated by the circle in Fig. 2.2(a), for strip width $W = 500\sqrt{2}a_0$ and a maximum change $\delta t \sim 0.1t$ at the edge. Fig. 2.2(c) shows the effect of an extended s-wave pairing gradient along the strip width, which leads to pseudo-LL formation at the central Dirac node. Here, we have chosen $W = 2000\sqrt{2}a_0$ and a maximum s-wave gap $\Delta_s \sim 0.4\Delta_d$ at the edge. The low energy spectra in Fig. 2.2(b) and (c) are in quantitative agreement with our analytical results. The spectrum for the $(1,0)$-edged strip (see Appendix F) displays similar strain induced pseudo-LLs; the key difference is in the absence of ABSs for the unstrained d-wave SC in this geometry.

2.5 Experimental signature of pseudo-LLs

As in the case of strained graphene, scanning tunneling spectroscopy (STS) experiments which probe the TDOS may provide the most direct route to observing the QP pseudo-LLs. For weak pseudo-magnetic fields, the peaks in density of states due to pseudo-LLs may be visible in microwave spectroscopy. Below, we first provide analytical expressions for the bulk TDOS expected within our continuum low energy theory. We then present numerical results

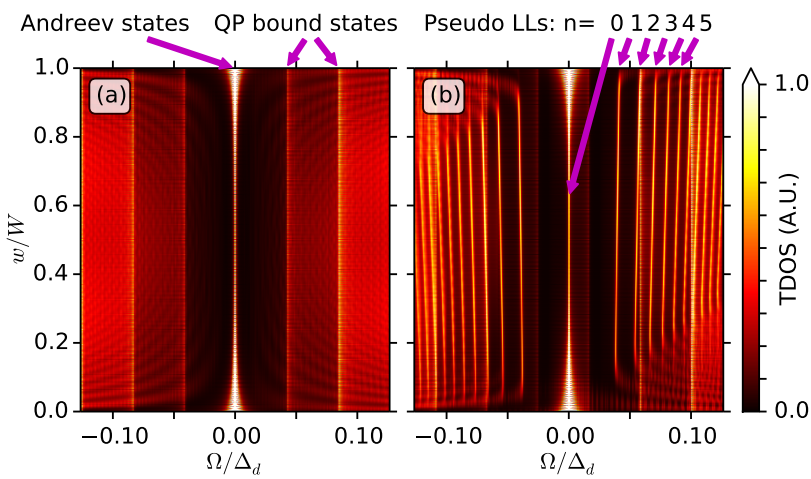

Figure 2.3: (Color online) Low energy TDOS versus energy Ω/Δ_d (scaled to the d-wave gap), from diagonalization of BdG Hamiltonian in the strip geometry, plotted across scaled strip width $0 < w/W < 1$. (a) Uniform d-wave SC, showing ABSs near zero energy localized near $w/W = 0, 1$, and QP bound state TDOS exhibiting rapid spatial oscillations. (b) Hopping gradient case showing extra pseudo-LL peaks.

on the lattice model (see Fig. 2.3) which goes beyond the continuum theory by incorporating the effects of quantum confinement of the Bogoliubov QPs to the strip, as well as the impact of ABSs at the edges.

In tunneling experiments, the TDOS in the continuum theory will have two contributions in the bulk. At nodes where the vector potential acts as pure gauge, it will only induce a phase shift for the fermion operators, leading to a TDOS contribution identical to a uniform d-wave SC. At nodes where the QPs sense a pseudo-magnetic field, there will be discrete pseudo-LLs. These lead to a total TDOS (details in Appendix D)

$$N(\Omega) \approx \frac{|\Omega|}{\pi v_{\mathrm{f}} v_{\Delta}} + \frac{|\beta|}{\pi} \sum_n \delta(\Omega - \lambda_n) \tag{2.10}$$

where $n = 0, \pm 1, \pm 2, \ldots$, and $\lambda_n = \sqrt{2\beta v_{\mathrm{f}} v_{\Delta} |n|}\mathrm{sgn}(n)$.

We have also computed the TDOS numerically for the lattice model in the above strip geometry. Confinement to the strip then leads to QP subbands with minima at discrete energies $\sim p\pi v_{\Delta}/W$ and $\sim p\pi v_{\mathrm{f}}/W$ for nodes $\mathbf{K}_1, \mathbf{K}_2$ respectively ($p =$ nonzero integer), as well as ABSs at the strip edges. As seen from Fig. 2.3, the TDOS for the strip exhibits three key features. (i) Without or with a gradient in the hopping amplitude, we see the zero energy peaks in the TDOS at the top and bottom edges reflecting the presence of ABSs; the spectral weight from these ABSs weakly leaks into the bulk. As shown in Appendix F, the ABSs and their contribution to the TDOS is absent for a (1,0)-edged strip. (ii) In the bulk (i.e., away from the edges), one set of indicated peaks exhibits rapid spatial oscillation of the TDOS across the strip width. These peaks arise when the energy Ω crosses the minimum Ω_0^s (at $k_L = 0$) of each subband s in the spectrum, leading to a $\sim 1/\sqrt{\Omega - \Omega_0^s}$

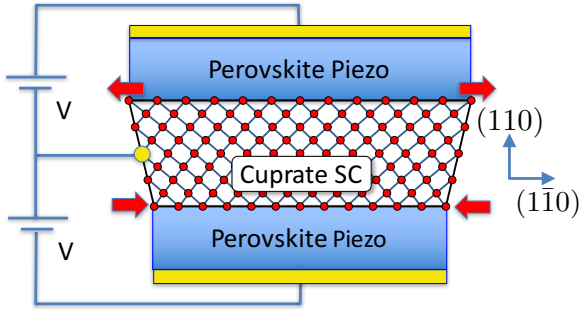

Figure 2.4: (Color online) Trilayer heterostructure with cuprate SC thin film epitaxially sandwiched between two piezoelectric perovskite films along the (110) surface. An inhomogeneous strain can be induced in the cuprate layer by asymmetrically polarizing the two piezo layers. Metallic outer gates (yellow regions) are used to apply the piezo voltages, with the cuprate layer serving as the common inner gate. For typical values of piezo constant ($d_{31} \sim$ 50-275pm/V) and dielectric breakdown field ($\sim$ 25MV/m) for piezoelectric perovskites [225,226] such as $Pb(Zr_xTi_{1-x})O_3$, we estimate that lattice strains $\sim$ 0.1-1% can be induced in the cuprate layer.

divergence in the TDOS. These QP bound states (see Appendix E) arise due to internode scattering $\mathbf{K}_1 \leftrightarrow -\mathbf{K}_1$. There are additional weaker features with longer-length-scale spatial variations arising from intranode scattering at $\pm\mathbf{K}_2$. Both contributions are present even in the absence of a gradient; see Fig. 2.3(a). (iii) Finally, the hopping gradient induces an extra set of indicated pseudo-LL peaks seen in Fig. 2.3(b) where the TDOS is nearly constant across the strip. The spatial dependence of the TDOS distinguishes the pseudo-LL peaks from QP bound states.

2.6 Experimental realizations

2.6.1 Strained nanowires or films

One route to tuning the spatial variation of the electron hopping and pairing amplitudes discussed above is to strain a cuprate thin film or nanowire. Unlike graphene, which has a simple single-particle description of its electronic bands, it is necessary here to include electron interactions in order to study the microscopic impact of strain on the d-wave SC. The cuprates may be modelled by a tJ Hamiltonian, $H_{tJ} = -g_t \sum_{i,j,\sigma} t_{ij} c^\dagger_{i\sigma} c_{j\sigma} + g_J J \sum_{\langle ij \rangle} \vec{S}_i \cdot \vec{S}_j$, with *bare* nearest and next-neighbor hoppings t_0 and $t'_0 \approx -0.3t_0$ respectively, and nearest-neighbor spin exchange $J = 4t_0^2/U \approx 0.3t_0$. We set $t_0 = 450$meV which leads to $J = 135$meV. The coefficients g_t, g_J represent renormalization factors that crudely account for strong correlation effects. Motivated by slave-boson [227] and renormalized mean field theory calculations [119,125], we pick $g_t = 2p/(1+p)$ and $g_J = 1$, where p is the hole doping (see Appendix G for details). Such a mean field approach captures a variety of experimental observations on the d-wave cuprate SCs; we therefore view it as a useful tool to estimate the pseudo-LL gap.

Here, we consider the effects of inhomogeneous strain that can be induced using a piezoelectric thin-film heterostructure schematically depicted and discussed in Fig. 2.4. Such piezo-induced strain will lead to a gradient in the hopping $\delta t_0(\mathbf{r})$ as well as a change in the superexchange interaction $\delta J(\mathbf{r}) \approx (8t_0/U)\delta t_0(\mathbf{r})$ across the strip. This induces a gradient in the effective hopping and pairing amplitude in the BdG equation. Raman scattering studies of La_2CuO_4 under hydrostatic pressure [228] indicate that a $\mp 0.5\%$ change in the lattice constant leads to $\delta J/J \approx \pm 5\%$, indirectly implying a change in the bare hopping amplitude $\delta t_0/t_0 \approx \pm 2.5\%$ in the underlying tJ model. A self-consistent solution to the mean field equations in the SC state at a hole doping $p = 0.15$ shows that such a uniform change leads to a $\approx \pm 7\%$ change in the d-wave pairing gap and $\approx \pm 3\%$ change in the renormalized hopping. A gradient in the d-wave gap does not induce any pseudo-LLs; however, the hopping gradient can in fact induce pseudo-LLs as discussed above. For a (110)-edged film of thickness $\sim 700a_0$, or a nanowire of similar width (≈ 270nm) which is experimentally realizable [229] and similar to the strip geometry explored here, we estimate that a hopping gradient with a realistic 0.5-1% maximal strain across the sample will generate a first excited pseudo-LL at $E_1 \sim 1$meV; this can be probed by c-axis tunneling. A fully self-consistent inhomogeneous BdG study of this physics is challenging due to the large system sizes involved; we defer this to future work.

2.6.2 Proximity to nematic order

A different route to realizing pseudo-LLs is to note that the onset of nematic order in a tetragonal d-wave SC spontaneously breaks the C_4 point group symmetry and will induce an extended s-wave component to the pair field [220]. There is evidence that the cuprates are proximate to such a QPT [230–235], so that an edge-induced s-wave pairing component will exhibit slow spatial decay, leading naturally to a gap variation needed to form pseudo-LLs. Tuning near such a critical point, or using proximity effect coupling to an s-wave SC, can tune the decay length and amplitude of the s-wave gap, thus controlling the pseudo-magnetic field and permitting further experimental tests.

2.7 Summary

We have proposed inhomogeneously strained nodal SCs as systems to realize pseudo-gauge fields and pseudo-LLs for Bogoliubov QPs, and suggested experimental routes and signatures to observe such physics in candidate materials such as the cuprate d-wave SCs. We note that even accidental SC Dirac nodes will show similar physics. Further research directions include understanding the impact of such inhomogeneous strains on the superconducting transition temperature, its interplay with real magnetic fields and vortices, and extensions to materials like $CeCoIn_5$, iron pnictides, and candidate topological SCs like Sr_2RuO_4.

Note Added: After submission of our manuscript, a closely related work appeared by Emilian Nica and Marcel Franz (arXiv:1709.01158). Our results, where they overlap, are in agreement.

Acknowledgments

This research was funded by the National Science and Engineering Research Council of Canada. AP acknowledges the support and hospitality of the International Center for Theoretical Sciences (Bangalore) during the completion of this manuscript.

Appendix 2.A Absence of "scalar gauge potential" in BdG equation

Inhomogeneous strain effects also lead to a deformation potential, which in graphene produces a *scalar* gauge potential in addition to the pseudo-vector potential [91,96,194,207–209]. Here, we argue that no such scalar potential – which may significantly alter the low-energy LL structure, or even cause its collapse [209] – can arise in time-reversal symmetric spin-singlet superconducting systems, such as the one we consider.

The key physical idea is that the BdG Hamiltonian for a singlet SC with time-reversal symmetry only permits 2 of the 4 Pauli matrices – the corresponding coefficients are in fact the two components of the vector potential identified in the main body of the Letter. Thus, any analog of the 'scalar deformation potential' here will necessarily break time-reversal symmetry or lead to singlet-triplet mixing. Such terms will be allowed in a more general setting, for example if spin orbit coupling is present and inversion symmetry or time-reversal symmetry is broken, but not in the cases studied here.

The Pauli matrix components that can enter the Hamiltonian of Equation 4 of the manuscript are constrained by symmetry. This is most easily seen by considering the BdG Hamiltonian in real space,

$$H_{\mathrm{BdG}} = \sum_{i,j} \psi_i^\dagger h_{ij} \psi_j, \tag{2.11}$$

$$h_{ij} = \begin{pmatrix} d_{ij}^0 + d_{ij}^3 & \Delta_{ij} \\ \Delta_{ji}^* & d_{ij}^0 - d_{ij}^3 \end{pmatrix}, \tag{2.12}$$

where $\psi_i^\dagger = (c_{i\uparrow}^\dagger, c_{i\downarrow})$ is the Nambu spinor at site i, and $d_{ij}^0, d_{ij}^3, \Delta_{ij}$ are complex numbers, with hermiticity imposing the constraint that $d_{ij}^0 = (d_{ji}^0)^*$ and $d_{ij}^3 = (d_{ji}^3)^*$.

- Time-reversal symmetry, which sends $c_{i\uparrow} \to c_{i\downarrow}$, $c_{i\downarrow} \to -c_{i\uparrow}$, and complex-conjugates all complex numbers, leads to the additional restrictions (i) $d_{ij}^0 = 0$ and (ii) $\Delta_{ij} = \Delta_{ji}^*$.

- Spin rotation symmetry and singlet pairing further imposes the constraints $d^3_{ij} = (d^3_{ij})^*$ and $\Delta_{ij} = \Delta^*_{ij}$.

With these ingredients, the Hamiltonian matrix $h_{ij} = d^3_{ij}\sigma^3 + \Delta_{ij}\sigma^1$, where d^3_{ij} and Δ_{ij} are real numbers. Thus, time-reversal symmetry and spin-rotation symmetry respectively require that the coefficients of σ^0 (which corresponds to a valley-odd chemical potential) and σ^2 (which corresponds to a complex pairing component) both vanish.

Such a Hamiltonian captures a BdG SC with arbitrary spatial modulations in hopping and pairing amplitudes, and an appropriate low-energy 'Dirac node' expansion recovers Equation 4 of our manuscript, and only permits the two components of the vector potential which we have shown leads to the formation of pseudo-LLs. Any additional 'scalar potential' is thus symmetry forbidden. Breaking such symmetries, for instance with a supercurrent that breaks time-reversal symmetry, leads to a Doppler shift for the QPs, which is an analog of a 'scalar potential'.

Appendix 2.B Dirac BdG solution - gap variations

Start with the Hamiltonian at node $\ell = 1$ for the case discussed in the main text where pseudo-LLs arise from gap variations.

$$H = \left[-iv_{\mathrm{f}}\sigma^z\partial_x + \beta v_\Delta \sigma^x (x - \frac{k}{\beta})\right] \tag{2.13}$$

Note that ($\mathrm{sgn}\beta\ \sigma^y$) anticommutes with this Hamiltonian, so that if $|\Phi\rangle$ is an eigenstate of H with energy E, then ($\mathrm{sgn}\beta\ \sigma^y$) $|\Phi\rangle$ is a solution with energy $-E$. (Here, $\mathrm{sgn}\beta = \beta/|\beta|$), This is the BdG particle-hole symmetry. Let us define

$$-i\partial_x = i\sqrt{\frac{|\beta|v_\Delta}{2v_{\mathrm{f}}}}(a^\dagger - a) \tag{2.14}$$

$$(x - \frac{k}{\beta}) = \sqrt{\frac{v_{\mathrm{f}}}{2|\beta|v_\Delta}}(a^\dagger + a) \tag{2.15}$$

so we get

$$H = \sqrt{2|\beta|v_{\mathrm{f}}v_\Delta}\left[a^\dagger\frac{(\sigma^x\mathrm{sgn}\beta + i\sigma^z)}{2} + a\frac{(\sigma^x\mathrm{sgn}\beta - i\sigma^z)}{2}\right] \tag{2.16}$$

Define spinors

$$|\uparrow\rangle \equiv \frac{1}{\sqrt{2}}\begin{pmatrix}1\\ i\ \mathrm{sgn}\beta\end{pmatrix}; |\downarrow\rangle \equiv \frac{1}{\sqrt{2}}\begin{pmatrix}1\\ -i\ \mathrm{sgn}\beta\end{pmatrix} \tag{2.17}$$

Then Hamiltonian is of the Jaynes-Cummings type,

$$H = \sqrt{2|\beta|v_{\mathrm{f}}v_\Delta}\left[ia^\dagger\mathcal{S}^- - ia\mathcal{S}^+\right] \tag{2.18}$$

where $\mathcal{S}^{\pm}$ act as raising/lowering operators on the above spin-1/2 states. Let $|n\rangle$ denote harmonic oscillator states (with $n \geq 0$) centered at k/β which are generated by $a, a^{\dagger}$. Then, we have a zero energy eigenstate

$$|\Phi_0\rangle = |0\rangle\,|\downarrow\rangle \tag{2.19}$$

and nonzero energy solutions

$$|\Phi_{n\pm}\rangle = \frac{|n-1\rangle\,|\uparrow\rangle \pm i\,|n\rangle\,|\downarrow\rangle}{\sqrt{2}} \tag{2.20}$$

with respective energies $\pm\sqrt{2|\beta|v_{\mathrm{f}}v_{\Delta}n}$. More explicitly, the wavefunctions are given by

$$\Phi_{k0}(x) = \frac{1}{\sqrt{2}}\varphi_0(x - \frac{k}{\beta})\begin{pmatrix} 1 \\ -i\mathrm{sgn}\beta \end{pmatrix} \tag{2.21}$$

$$\Phi_{kn\pm}(x) = \frac{1}{2}\begin{pmatrix} \varphi_{n-1}(x - \frac{k}{\beta}) \pm i\varphi_n(x - \frac{k}{\beta}) \\ \mathrm{sgn}\beta(i\varphi_{n-1}(x - \frac{k}{\beta}) \pm \varphi_n(x - \frac{k}{\beta})) \end{pmatrix} \tag{2.22}$$

where $\varphi_n(x)$ is the nth harmonic oscillator ground state. We can then define quasiparticle operators γ for the node pair $\ell = \pm 1$, so that

$$\begin{aligned}\Psi_{1\alpha}(\mathbf{r}) = \begin{pmatrix} \psi_{1,\alpha}(\mathbf{r}) \\ \epsilon_{\alpha\nu}\psi^{\dagger}_{-1,\nu}(\mathbf{r}) \end{pmatrix} = \frac{1}{\sqrt{L}}\sum_k \mathrm{e}^{iky}\Bigg[&\gamma_{0,\alpha}(k)\Phi_{k0}(x) \\ &+ \sum_{n>0}\begin{pmatrix} \Phi_{kn+}(x) & \Phi_{kn-}(x) \end{pmatrix}\begin{pmatrix} \gamma_{n,1,\alpha}(k) \\ \epsilon_{\alpha\nu}\gamma^{\dagger}_{n,-1,\nu}(-k) \end{pmatrix}\Bigg]\end{aligned} \tag{2.23}$$

In terms of these, the Hamiltonian is given by

$$H = \sum_{k,\alpha,n>0}\sqrt{2|\beta|v_{\mathrm{f}}v_{\Delta}n}\left(\gamma^{\dagger}_{n1\alpha}(k)\gamma_{n1\alpha}(k) + \gamma^{\dagger}_{n2\alpha}(k)\gamma_{n2\alpha}(k)\right) \tag{2.24}$$

Appendix 2.C Dirac BdG solution - hopping variations

Start with the Hamiltonian at node $\ell = 2$ for the case discussed in the main text where pseudo-LLs arise from hopping variations. Assume plane waves along the x-direction. Then

$$H = \beta v_{\mathrm{f}}\sigma^z(y + \frac{k}{\beta}) - iv_{\Delta}\sigma^x\partial_y \tag{2.25}$$

Let us define

$$-i\partial_y = i\sqrt{\frac{|\beta|v_{\mathrm{f}}}{2v_\Delta}}(a^\dagger - a) \tag{2.26}$$

$$(y + \frac{k}{\beta}) = \sqrt{\frac{v_\Delta}{2|\beta|v_{\mathrm{f}}}}(a^\dagger + a) \tag{2.27}$$

so we get

$$H = \sqrt{2|\beta|v_{\mathrm{f}}v_\Delta}\left[a^\dagger\frac{(\sigma^z\mathrm{sgn}\beta + i\sigma^x)}{2} + a\frac{(\sigma^z\mathrm{sgn}\beta - i\sigma^x)}{2}\right] \tag{2.28}$$

Define spinors

$$|\uparrow\rangle \equiv \frac{1}{\sqrt{2}}\begin{pmatrix}1\\ -i\ \mathrm{sgn}\beta\end{pmatrix}; |\downarrow\rangle \equiv \frac{1}{\sqrt{2}}\begin{pmatrix}1\\ i\ \mathrm{sgn}\beta\end{pmatrix} \tag{2.29}$$

Then Hamiltonian is of the Jaynes-Cummings type,

$$H = \sqrt{2|\beta|v_{\mathrm{f}}v_\Delta}\left[ia^\dagger\mathcal{S}^- - ia\mathcal{S}^+\right] \tag{2.30}$$

where $\mathcal{S}^\pm$ act as raising/lowering operators on the above spin-1/2 states. Let $|n\rangle$ denote harmonic oscillator states (with $n \geq 0$) centered at $y = -k/\beta$ which are generated by $a, a^\dagger$. Then, we have a zero energy eigenstate

$$|\Phi_0\rangle = |0\rangle\,|\downarrow\rangle \tag{2.31}$$

and nonzero energy solutions

$$|\Phi_{n\pm}\rangle = \frac{|n-1\rangle\,|\uparrow\rangle \pm i\,|n\rangle\,|\downarrow\rangle}{\sqrt{2}} \tag{2.32}$$

with respective energies $\pm\sqrt{2|\beta|v_{\mathrm{f}}v_\Delta n}$. More explicitly, the wavefunctions are given by

$$\Phi_{k0}(y) = \frac{1}{\sqrt{2}}\varphi_0(y + \frac{k}{\beta})\begin{pmatrix}1\\ i\mathrm{sgn}\beta\end{pmatrix} \tag{2.33}$$

$$\Phi_{kn\pm}(y) = \frac{1}{2}\begin{pmatrix}\varphi_{n-1}(y + \frac{k}{\beta}) \pm i\varphi_n(y + \frac{k}{\beta})\\ -\mathrm{sgn}\beta(i\varphi_{n-1}(y + \frac{k}{\beta}) \pm \varphi_n(y + \frac{k}{\beta}))\end{pmatrix} \tag{2.34}$$

where $\varphi_n(y)$ is the nth harmonic oscillator ground state.

Appendix 2.D Tunneling density of states (TDOS)

2.D.1 Uniform case

The superconducting local TDOS for spin-α for a uniform d-wave SC is given by

$$N_\alpha(\mathbf{r},\Omega) = \int \frac{d^2\mathbf{k}}{(2\pi)^2}\left[u_{\mathbf{k}}^2\delta(\Omega - E_{\mathbf{k}}) + v_{\mathbf{k}}^2\delta(\Omega + E_{\mathbf{k}})\right] \tag{2.35}$$

where $u_{\mathbf{k}}^2 = \frac{1}{2}(1+\xi_{\mathbf{k}}/E_{\mathbf{k}})$, $v_{\mathbf{k}}^2 = \frac{1}{2}(1-\xi_{\mathbf{k}}/E_{\mathbf{k}})$, and $E_{\mathbf{k}} = \sqrt{\xi_{\mathbf{k}}^2 + \Delta_{\mathbf{k}}^2}$. We can linearize the dispersion around the 4 nodes (labelled $\ell = \pm 1, \pm 2$), which leads to

$$N_\alpha(\mathbf{r},\Omega) = \sum_\ell \int^\Lambda \frac{d^2q}{(2\pi)^2}\frac{1}{2}\left[(1+\frac{\vec{v}_{\mathrm{f}}^{(\ell)}\cdot\vec{q}}{\mathcal{E}_{\mathbf{q}}})\delta(\Omega - \mathcal{E}_{\mathbf{q}}) + (1-\frac{\vec{v}_{\mathrm{f}}^{(\ell)}\cdot\vec{q}}{\mathcal{E}_{\mathbf{q}}})\delta(\Omega + \mathcal{E}_{\mathbf{q}})\right] \tag{2.36}$$

where $\mathcal{E}_{\mathbf{q}} = \sqrt{v_{\mathrm{f}}^2 q_\perp^2 + v_\Delta^2 q_\parallel^2}$ and the momentum cutoff Λ ensures the same total number of momentum states. Doing the integral, we find

$$N_\alpha(\mathbf{r},\Omega) = 2\int^\Lambda \frac{dq_\parallel dq_\perp}{(2\pi)^2}\left[\delta(\Omega - \sqrt{v_{\mathrm{f}}^2 q_\perp^2 + v_\Delta^2 q_\parallel^2}) + \delta(\Omega + \sqrt{v_{\mathrm{f}}^2 q_\perp^2 + v_\Delta^2 q_\parallel^2})\right] \tag{2.37}$$

Rescaling $v_{\mathrm{f}} q_\parallel = Q_1$ and $v_\Delta q_\perp = Q_2$, with $Q = \sqrt{Q_1^2 + Q_2^2}$, we find

$$N_\alpha(\mathbf{r},\Omega) = 2\int^\Lambda \frac{dQ}{2\pi v_{\mathrm{f}} v_\Delta} Q\left[\delta(\Omega - Q) + \delta(\Omega + Q)\right] \tag{2.38}$$

with an appropriate choice $\Lambda = \sqrt{\pi v_{\mathrm{f}} v_\Delta}$. Of course, this linearized description will break down at a lower energy scale $\sim v_\Delta/a_0$, where a_0 is the lattice spacing. This yields, for $|\Omega| \lesssim v_\Delta/a_0 \ll \Lambda$,

$$N(\mathbf{r},\Omega) = \sum_\alpha N_\alpha(\mathbf{r},\Omega) = \frac{2|\Omega|}{\pi v_{\mathrm{f}} v_\Delta} \tag{2.39}$$

2.D.2 Pseudo-Landau Level case: Gap variations

Consider the gap variation example discussed in the main text. Then, fermions at two of the Dirac points only see a phase change from the vector potential, which does not change the density of states, leading to a contribution from $\ell = \pm 2$ given by

$$N_2(\mathbf{r},\Omega) = \frac{|\Omega|}{\pi v_{\mathrm{f}} v_\Delta}. \tag{2.40}$$

This is half the total density of states in the uniform case. The contribution from the other node pair $N_1(\mathbf{r},\Omega)$ is expected to reflect the formation of pseudo-LLs. The Green function

for node pair $\ell = \pm 1$ reduces to

$$\mathcal{G}_\alpha^{(\ell=1)}(\mathbf{r}, i\Omega_m) = \frac{1}{2L}\sum_k \Bigg[\frac{\varphi_0^2(x-\frac{k}{\beta})}{i\Omega_m - E_0} + \frac{1}{2}\sum_{n>0}\left(\varphi_n^2(x-\frac{k}{\beta}) + \varphi_{n-1}^2(x-\frac{k}{\beta})\right)\left(\frac{1}{i\Omega_m - E_n} + \frac{1}{i\Omega_m + E_n}\right)\Bigg] \quad (2.41)$$

where $E_0 = 0$. Summing over spins and $\ell = \pm 1$, this leads to

$$N_1(\mathbf{r}, \Omega) = \frac{2}{L}\sum_k \Bigg[\varphi_0^2(x-\frac{k}{\beta})\delta(\Omega) + \frac{1}{2}\sum_{n>0}\left(\varphi_n^2(x-\frac{k}{\beta}) + \varphi_{n-1}^2(x-\frac{k}{\beta})\right)\left(\delta(\Omega - E_n) + \delta(\Omega + E_n)\right)\Bigg] \quad (2.42)$$

Deep in the bulk, $N_1(\mathbf{r}, \Omega)$ will be independent of $\mathbf{r}$, and we can approximate it as

$$N_1(\mathbf{r}, \Omega) \approx \frac{|\beta|}{\pi}\left[\delta(\Omega) + \sum_{n>0}\left(\delta(\Omega - E_n) + \delta(\Omega + E_n)\right)\right] \quad (2.43)$$

which can be recast in the more compact form

$$N_1(\mathbf{r}, \Omega) \approx \frac{|\beta|}{\pi}\sum_n \delta(\Omega - \lambda_n) \quad (2.44)$$

where $n = 0, \pm 1, \pm 2, \ldots$, with $\lambda_n = \sqrt{2\beta v_{\mathrm{f}} v_\Delta |n|}\mathrm{sgn}(n)$. Thus, the total density of states, $N_1(\mathbf{r}, \Omega) + N_2(\mathbf{r}, \Omega)$ will reflect a combination of the pseudo-LL spectrum as well as the Dirac density of states of the uniform d-wave SC.

Appendix 2.E *d*-wave SC in a narrow strip

In this section we study singular contributions to the TDOS which come from quantization of the quasiparticle momentum transverse to the strip. Just in this section, we find it convenient to retain the full BdG equation, and linearize around the Dirac nodes only at the end. We begin with the BdG Hamiltonian,

$$\hat{H}(k_L) = \begin{pmatrix} \xi(k_L, -i\partial_w) & \Delta(k_L, -i\partial_w) \\ \Delta(k_L, -i\partial_w) & -\xi(k_L, -i\partial_w) \end{pmatrix}, \quad (2.45)$$

where $0 < w < W$ is the transverse coordinate, and k_L, k_W will denote momenta along the strip length and strip width (L, W directions) respectively. For a (110) edge, we have $\xi(k_L, -k_W) = \xi(k_L, k_W)$ and $\Delta(k_L, -k_W) = -\Delta(k_L, k_W)$. We are looking for states which obey the strip boundary conditions, i.e., eigenfunctions, $\psi(w)$, of $\hat{H}$ which have a

vanishing charge density at the strip edges, $\psi^\dagger(0)\tau^z\psi(0) = \psi^\dagger(W)\tau^z\psi(W) = 0$. A plane wave eigenfunction with positive eigenvalue $\varepsilon(k_L, k_W) = \sqrt{\xi^2(k_L, k_W) + \Delta^2(k_L, k_W)}$ is given by

$$\phi^+(k_L, k_W; w) = \begin{pmatrix} u(k_L, k_W) \\ v(k_L, k_W) \end{pmatrix} e^{ik_W w}, \tag{2.46}$$

where

$$|u(k_L, k_W)|^2 = \frac{1}{2}\left(1 + \frac{\xi(k_L, k_W)}{\varepsilon(k_L, k_W)}\right), \tag{2.47}$$

and

$$|v(k_L, k_W)|^2 = \frac{1}{2}\left(1 - \frac{\xi(k_L, k_W)}{\varepsilon(k_L, k_W)}\right). \tag{2.48}$$

Since $\Delta(k_L, k_W)$ is a real function for the d-wave SC we are considering, it is sufficient to take $u(k_L, k_W) > 0$ and (sign $v(k_L, k_W)$) = (sign $\Delta(k_L, k_W)$), thus, $u(k_L, -k_W) = u(k_L, k_W)$ and $v(k_L, -k_W) = -v(k_L, k_W)$. A plane wave eigenfunction with negative energy $-\varepsilon(k_L, k_W)$ is given by

$$\phi^-(k_L, k_W; w) = \begin{pmatrix} v(k_L, k_W) \\ -u(k_L, k_W) \end{pmatrix} e^{ik_W w}. \tag{2.49}$$

To construct a state which obeys the boundary conditions, we consider a superposition of states with opposite k_W,

$$\begin{aligned} \psi^+(k_L, k_W > 0, w) &= \phi^+(k_L, k_W, w) + r(k_L, k_W)\phi^+(k_L, -k_W) \\ &= \begin{pmatrix} u(k_L, k_W) \\ v(k_L, k_W) \end{pmatrix} e^{ik_W w} + r(k_L, k_W) \begin{pmatrix} u(k_L, k_W) \\ -v(k_L, k_W) \end{pmatrix} e^{-ik_W w}. \end{aligned} \tag{2.50}$$

The charge density for this state is given by (dependence on k_L and k_W implicit)

$$\begin{aligned} \rho^+(w) &= \psi^{+\dagger}(w)\tau^z\psi^+(w). \\ &= u^2(1 + |r|^2 + 2\mathrm{Re}\,(re^{-i2k_W w})) - v^2(1 + |r|^2 - 2\mathrm{Re}\,(re^{-i2k_w W})) \\ &= (u^2 - v^2)(1 + |r|^2) + 2\mathrm{Re}\,(re^{-i2k_W w}), \end{aligned} \tag{2.51}$$

where $\mathrm{Re}\,(z)$ denotes the real part of z. Finite size quantization sets as usual $k_W = \pi n/W$, where $n = 0, 1, 2...$, while demanding that ρ^+ vanish at the strip edges results in

$$(u^2 - v^2)(1 + |r|^2) + 2\mathrm{Re}\,(r) = 0. \tag{2.52}$$

Since, $-1 \leq u^2 - v^2 \leq 1$, r is always real. Thus, the eigenstates are given by

$$\psi_n^+(k_L; w) = \begin{pmatrix} u_n(k_L) \\ v_n(k_L) \end{pmatrix} e^{i\pi n w/W} + r_n(k_L) \begin{pmatrix} u_n(k_L) \\ -v_n(k_L) \end{pmatrix} e^{-i\pi n w/W}. \tag{2.53}$$

Similar states with negative energy are given by

$$\psi_n^-(k_L;w) = \begin{pmatrix} v_n(k_L) \\ -u_n(k_L) \end{pmatrix} e^{i\pi nw/W} + r_n(k_L) \begin{pmatrix} -v_n(k_L) \\ -u_n(k_L) \end{pmatrix} e^{-i\pi nw/W}. \tag{2.54}$$

The TDOS is given by

$$N(\Omega,w) = \frac{1}{2}\int \frac{dk_L}{2\pi} \sum_{n=0}^{\infty} \sum_{s=\pm} \psi_n^{s\dagger}(k_L,w)(\tau^0 + s\tau^z)\psi_n^s(k_L,w)\delta(\Omega - s\varepsilon_n(k_L)) \tag{2.55}$$

Focusing on positive energies,

$$N(\Omega>0,w) = 2\int \frac{dk_L}{2\pi} \sum_n u_n^2(k_L)\left(1 + r_n^2(k_L) + 2r_n(k_L)\cos\frac{\pi nw}{W}\right)\delta(\Omega - \varepsilon_n(k_L)) \tag{2.56}$$

The main low energy contributions to the TDOS in a d-wave SC come from the vicinity of the nodes. We are further focusing on the nodes at $k_L = 0$ and $k_W = \pm K_F$, thus, for $k_W > 0$, $\xi \simeq v_{\mathrm{f}}(n\pi/W - K_F)$, $\Delta \simeq v_\Delta k_L$, and $\varepsilon \simeq \sqrt{v_{\mathrm{f}}^2(n\pi/W - K_F)^2 + v_\Delta^2 k_L^2}$. Changing integration variables we have

$$\begin{aligned} N(\Omega>0,w) &= 2\int_{v_{\mathrm{f}}|n\pi/W - K_F|}^{\infty} \frac{\varepsilon d\varepsilon}{2\pi} \sum_n \frac{1}{v_\Delta k_n(\varepsilon)} u_n^2(\varepsilon)\left(1 + r_n^2 + 2r_n\cos\frac{\pi nw}{W}\right)\delta(\Omega - \varepsilon) \\ &= \sum_n \Theta(\Omega - v_{\mathrm{f}}|n\pi/W - K_F|)\frac{\Omega}{\pi}\frac{1}{v_\Delta k_n(\Omega)} u_n^2(\Omega)\left(1 + r_n^2 + 2r_n\cos\frac{\pi nw}{W}\right), \end{aligned} \tag{2.57}$$

where $k_n(\Omega) = \sqrt{\Omega^2 - (v_{\mathrm{f}} n\pi/w - K)^2}/v_\Delta$, and $u_n^2(\Omega) = (1 + v_{\mathrm{f}}(n\pi/w - K_F)/\Omega)/2$. Since there are always values of w for which the term in the above parentheses is finite, we find that there are contributions at $\Omega = v_{\mathrm{f}}|n\pi/W - K_F|$ which diverge as $1/\sqrt{\Omega^2 - (v_{\mathrm{f}} n\pi/W - K_F)^2}$.

Appendix 2.F Pseudo-Landau levels of strained d-wave SC in the (1,0)-edged strip geometry

Numerical diagonalization of the lattice BdG Hamiltonian was also performed for a $(1,0)$-edged strip. Again, the strip's width is W, and the transverse direction, along which periodic boundary conditions were used, has length $L \gg W$. Parameters t, t', $\bar{n}$, and Δ_d are taken to be the same as in the $(1,1)$-edged case considered in the main text.

Fig. 2.5(a) shows the spectrum of the strip as a function of the momentum k_L along the long direction L in the absence of any imposed spatial variation. The spectrum exhibits the d-wave Dirac nodes projected onto the Brillouin zone of the strip. As expected with $(1,0)$ edges, zero-energy ABSs are absent from the spectrum. A circle indicates the near-node region in which we have chosen to plot the spectra of panels (b) and (c).

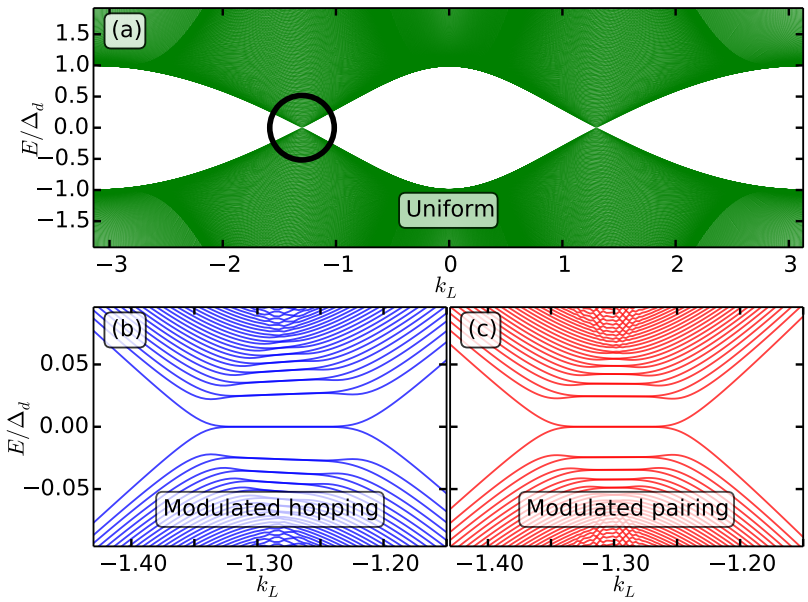

Figure 2.5: (Color online) (a) Spectrum of uniform d-wave SC on a $(1,0)$-edged strip versus momentum k_L along the L-direction showing Dirac nodes. Note that there are no zero energy ABSs in this geometry. Circle indicates region shown in the next two panels. (b) Formation of flat pseudo-Landau levels in the low-energy regime due to uniform hopping-amplitude gradient in the $[1,0]$ direction; shown here is the near-node region indicated in (a). (c) Similar to (b) but with extended s-wave pairing gradient.

Fig. 2.5(b) shows the spectrum in the presence of a nonzero gradient in the hopping amplitude across the strip width (in the $[1,0]$ direction), which leads to a pseudo-LL spectrum at both Dirac nodes; we have chosen $W = 3000a_0$ and a maximum change $\delta t \sim 0.25t$ at the edge. Fig. 2.5(c) shows the effect of an extended s-wave pairing gradient across the strip width, also leading to pseudo-LL formation at both Dirac nodes. Here, we have chosen $W = 3000a_0$ and a maximum s-wave gap $\Delta_s \sim 0.25\Delta_d$ at the edge. The low energy spectra in Fig. 2.5(b) and (c) are in quantitative agreement with our analytical results.

Appendix 2.G Mean field equations for correlated d-wave SC with strain

We start from the usual tJ model in the main text

$$H_{tJ} = -g_t \sum_{i,j,\alpha} t_{0,ij} c^\dagger_{i\alpha} c_{j\alpha} + g_J J \sum_{\langle ij \rangle} \vec{S}_i \cdot \vec{S}_j \tag{2.58}$$

where the *bare* nearest neighbor and next-neighbor hoppings are $t_0 = 1$ and $t'_0 = -0.3t_0$ respectively, the antiferromagnetic exchange coupling $J = 4t_0^2/U = 0.3t_0$, and the renormalization factors $g_t = 2p/(1+p)$, $g_J = 1$ account for strong correlation effects in a mean field manner. Note that g_t is chosen in line with renormalized mean field theory, while we have

set $g_J = 1$ similar to what one expects from slave boson mean field theory. At any rate, we should only view this as an effective model to obtain a variational d-wave superconducting ground state, with results which approximately reproduce experimental data. Doing a full Hartree-Fock-Bogoliubov mean field theory of the superexchange term, we arrive at the mean field Hamiltonian

$$H_{\mathrm{MFT}} = \sum_{\mathbf{k}\alpha} \xi_{\mathbf{k}} c^\dagger_{\mathbf{k}\alpha} c_{\mathbf{k}\alpha} - \sum_{\mathbf{k}} \Delta_{\mathbf{k}} (c^\dagger_{\mathbf{k}\uparrow} c^\dagger_{-\mathbf{k}\downarrow} + c_{-\mathbf{k}\downarrow} c_{\mathbf{k}\uparrow}), \tag{2.59}$$

where $\xi_{\mathbf{k}} = -2(g_t t_0 + \frac{3}{4} g_J J\chi)(\cos k_x + \cos k_y) - 4 g_t t'_0 \cos k_x \cos k_y$ is set by the effectively renormalized hoppings (which appear in our BdG calculations in the paper), $t = (g_t t_0 + \frac{3}{4} g_J J\chi)$ and $t' = g_t t'_0$, while the pairing gap $\Delta_{\mathbf{k}} = \frac{3}{2} g_J J \Delta_0 (\cos k_x - \cos k_y)$. The mean field equations determining χ, Δ_0 and the mean electron density $\bar{n} \equiv 1 - p$ are given by

$$\Delta_0 = \frac{1}{2N} \sum_{\mathbf{k}} \frac{\Delta_{\mathbf{k}}}{2E_{\mathbf{k}}} (\cos k_x - \cos k_y) \tag{2.60}$$

$$\chi = \frac{1}{4N} \sum_{\mathbf{k}} (1 - \frac{\xi_{\mathbf{k}}}{E_{\mathbf{k}}})(\cos k_x + \cos k_y) \tag{2.61}$$

$$\bar{n} = \frac{1}{N} \sum_{\mathbf{k}} (1 - \frac{\xi_{\mathbf{k}}}{E_{\mathbf{k}}}) \equiv 1 - p \tag{2.62}$$

where $E_{\mathbf{k}} = \sqrt{\xi^2_{\mathbf{k}} + \Delta^2_{\mathbf{k}}}$. We solve these equations self-consistently assuming $t_0 \to t_0(1+\varepsilon)$ and $J \to J(1+2\varepsilon)$, where the (small) fractional change ε in the hopping and exchange interaction is determined by the strain which affects the lattice constant; see main text. (The factor of 2ε in J reflects its dependence on hopping as $\sim t_0^2$.)

We pick the bare hopping $t_0 = 450$meV, which leads to $J = 135$meV (corresponding to $U/t_0 \approx 13$). For hole doping $p = 0.15$, and for the unstrained case $\varepsilon = 0$, we find that the renormalized hoppings satisfy $t' = -0.25t$, and an anti-nodal gap $3 g_J J \Delta_0 \approx 24$meV at $(\pi, 0)$. In addition, with the lattice constant $a_0 = 3.85$Å, we find a nodal Fermi velocity $v_{\mathrm{f}} \approx 1.3$eV-Å, and a ratio of Fermi velocity to gap velocity $v_{\mathrm{f}}/v_\Delta \approx 20$. These are in reasonable agreement with results for the optimally doped cuprates. Incorporating ε, and solving the mean field equations, we find the results for the strain dependence of the hopping and pairing quoted in the main text.

Chapter 3

Orbital Edelstein effect from density-wave order[1]

3.1 Introduction

The field of magnetoelectric effects has seen a revival in interest in the past decades on several fronts. The discovery and study of multiferroicity in correlated materials has uncovered unconventional mechanisms which can give rise to a large effective magnetoelectric coupling [147, 148, 236–241]. Similarly, the discovery of three-dimensional (3D) topological insulators has led to an exploration of novel magnetoelectric effects due to emergent axion electrodynamics in such topological phases [242–251]. The wide interest in such magnetoelectric effects stems partly from the technological potential of controlling charge degrees of freedom via magnetic fields or, conversely, tuning magnetism via an applied electric field.

A prominent example of such a magnetoelectric effect is the nonequilibrium phenomenon of current-induced magnetization, which is also termed *kinetic magnetoelectric effect* (KME) [144, 252]. The intrinsic-spin variant of this effect, wherein a charge current in a spin-orbit-coupled conductor gives rise to bulk spin polarization and, hence, a net magnetization, is referred to as the *Edelstein effect* or the *inverse spin-galvanic effect* [156, 157] and has been under study for several decades [253]. A great deal of experimental work has focused on the Edelstein effect in 2D systems, notably in thin-film semiconductors [158, 254–258] and at metal surfaces [259]. However, experiments on 3D materials have been scant, although some recent studies have reported its observation in trigonal tellurium [169, 260].

In recent years, it has come to light that 3D systems can have an intrinsic orbital contribution to the KME, analogous to the spin part and arising as a consequence of the orbital magnetic moment of Bloch bands [144, 151, 152, 160, 162, 261–264], notably in trigonal selenium and tellurium. Whereas the ordinary Edelstein effect (hereafter referred to as the *spin* Edelstein effect, SEE) relies on crystalline spin-orbit coupling (SOC) to give Bloch

[1] Chapter adapted from Ref. 2, i.e., Geremia Massarelli, Bryce Wu, and Arun Paramekanti, *Phys. Rev. B*, 100:075136 (2019). Copyright 2019 by the American Physical Society.

states a spin texture and, hence, is limited by the size of the SOC, the *orbital Edelstein effect* (OEE), also referred to as the *inverse gyrotropic magnetic effect* [160], is determined solely by the geometry of the crystal [151, 162].

Chiral crystals are a subset of those that can exhibit the KME. Previous studies have considered trigonal selenium and tellurium and viewed their chiral nature as descending from a charge-density-wave (CDW) instability of a hypothetical parent phase [265], and others have studied optical gyrotropy as a probe for symmetry breaking in the chiral CDW phase of $1T$-$TiSe_2$ [266] and in stripe-ordered cuprates [267]. It has also been shown that Weyl nodes at the Fermi level can yield a large intrinsic contribution to the KME [151, 162].

Our work builds on this theme, and explores the KME induced by symmetry breaking in a system with line nodes protected by nonsymmorphic symmetries in the electronic band structure. The resulting phase is a nonchiral but gyrotropic crystal, and we study the concomitant temperature-dependent KME as a probe of the density-wave order. Below, we briefly review the OEE, before introducing our model Hamiltonian and presenting its theoretical study. Our work suggests that line node semimetals which are weakly gapped by charge order might be a promising place to search for large OEE.

3.2 Orbital Edelstein effect

Electrons in crystalline solids form Bloch bands with an intrinsic spin magnetic moment

$$\mathbf{s}_{\mathbf{k}n} = -\frac{ge}{2m_{\mathrm{e}}}\langle u_{\mathbf{k}n}|\mathbf{s}|u_{\mathbf{k}n}\rangle, \tag{3.1}$$

where $\mathbf{s} = \hbar\boldsymbol{\sigma}/2$ is the spin operator for the electrons and the electron charge is $(-e)$. The modern theory of magnetization in solids [168, 268–270] has discovered that such Bloch bands also host an intrinsic orbital magnetic moment given by

$$\mathbf{m}_{\mathbf{k}n} = \frac{e}{2\hbar}\mathrm{Im}\,\langle\nabla_{\mathbf{k}}u_{\mathbf{k}n}| \times (H_{\mathbf{k}} - \varepsilon_{\mathbf{k}n})|\nabla_{\mathbf{k}}u_{\mathbf{k}n}\rangle, \tag{3.2}$$

where $H_{\mathbf{k}}$ is the Bloch Hamiltonian, n is the band index, and $H_{\mathbf{k}}|u_{\mathbf{k}n}\rangle = \varepsilon_{\mathbf{k}n}|u_{\mathbf{k}n}\rangle$. This orbital magnetization has been shown to arise from the self-rotation of wavepackets in the semiclassical theory of electron dynamics [268, 271]. Since $\mathbf{m}_{\mathbf{k}n} \to -\mathbf{m}_{-\mathbf{k}n}$ under time reversal and $\mathbf{m}_{\mathbf{k}n} \to \mathbf{m}_{-\mathbf{k}n}$ under spatial inversion, it is clear that at least one of these symmetries must be broken in order for $\mathbf{m}_{\mathbf{k}n}$ to not be identically zero.

From the viewpoint of semiclassical dynamics, given an electron distribution function $f_{\mathbf{k}n}$, the intrinsic contribution to the net electronic magnetization is given by [144, 168, 271]

$$\mathbf{M} = \frac{1}{\mathcal{V}}\sum_{\mathbf{k}n} f_{\mathbf{k}n}\left(\mathbf{m}_{\mathbf{k}n} + \mathbf{s}_{\mathbf{k}n}\right), \tag{3.3}$$

where $\mathcal{V}$ is the crystal volume. In thermodynamic equilibrium for a time-reversal symmetric

system, the Fermi-Dirac distribution, $f^0_{\mathbf{k}n} = f(\varepsilon_{\mathbf{k}n} - \mu)$ forces a zero net magnetization $\mathbf{M} = 0$ because of cancellation between contributions from opposite crystal momenta [151]. However, an asymmetric distribution function, such as that arising from an applied electric field, can generally give rise to nonzero net bulk magnetization.

Explicitly, to lowest order in an applied uniform DC electric field $\mathbf{E}$, the distribution function becomes [161]

$$f_{\mathbf{k}n} = f^0_{\mathbf{k}n} + e\tau(\mathbf{E}\cdot\mathbf{v}_{\mathbf{k}n})\left.\frac{\mathrm{d}f}{\mathrm{d}\xi}\right|_{\xi=\varepsilon_{\mathbf{k}n}-\mu}, \tag{3.4}$$

where $\mathbf{v}_{\mathbf{k}n}$ is the electronic group velocity and τ is the impurity-scattering relaxation time in relaxation-time approximation. Hence, the magnetization arises as a linear response to an applied electric field,

$$M_\kappa = \alpha_{\kappa\lambda}E_\lambda, \tag{3.5}$$

with the linear response tensor

$$\alpha_{\kappa\lambda} = \alpha^{\mathrm{orb}}_{\kappa\lambda} + \alpha^{\mathrm{spin}}_{\kappa\lambda} \tag{3.6a}$$

$$= \tau e\frac{1}{\mathcal{V}}\sum_{\mathbf{k},n}\left.\frac{\mathrm{d}f}{\mathrm{d}\xi}\right|_{\xi=\varepsilon_{\mathbf{k}n}-\mu}(m_{\mathbf{k}n,\kappa} + s_{\mathbf{k}n,\kappa})\, v_{\mathbf{k}n,\lambda}, \tag{3.6b}$$

where κ and λ are Cartesian indices. The tensors α^{spin} and α^{orb} respectively describe the SEE and the OEE.

The form of the tensor α is significantly constrained by crystal symmetry [150,151,253,272]. Indeed, α is an axial rank-two tensor since it relates a polar vector, $\mathbf{E}$, to a axial vector, $\mathbf{M}$. Crystal classes whose point-group symmetries allow for nonzero axial rank-two response tensors are known as *gyrotropic*. The reason for this name is that the tensor governing natural optical activity, or *gyrotropy*, transforms in the same way as α; thus KME and optical gyrotropy go hand in hand.

We note that the same symmetry constraints govern the appearance of nonzero spin and orbital contributions to α, so both are expected to arise together, and there is no clear route to disentangling them experimentally in a 3D system [151,169]. Indeed, the authors of Ref. 169 conclude by speculating that the current-induced magnetization they observe in trigonal tellurium may be due not only to the well-known SEE, but also to the OEE.

3.3 Model

As an example of the OEE brought about by symmetry breaking, we consider a tight-binding toy model of electrons moving in the tetragonal crystal shown in Fig. 3.1, consisting of identical atoms arranged in layered square lattices. We assume a single isotropic orbital, and ignore the electron spin hereafter; for this reason, there is no spin contribution to α

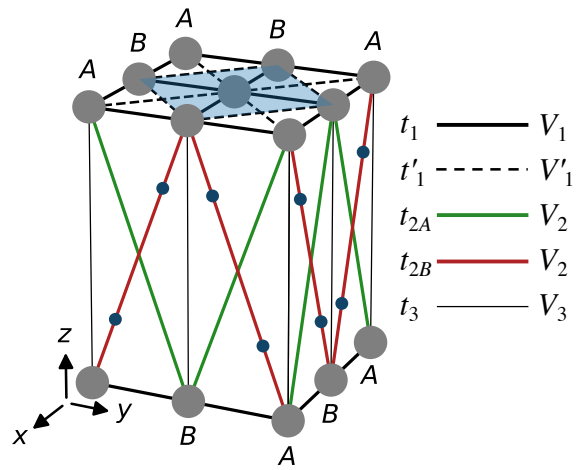

Figure 3.1: (Color online) Tetragonal crystal structure showing identical atoms (large gray spheres) on the A and B sublattices, with a legend for hopping amplitudes and repulsion strengths. Primitive translations $\mathbf{a}$, $\mathbf{b}$, and $\mathbf{c}$ are defined in the main text. The volume shown corresponds to two unit cells as defined in Sec. 3.3, and the projection of the unit cell onto the x-y plane is shaded in blue. The secondary atoms (small dark-blue spheres) are *not* considered in the tight-binding model, as discussed in the main text.

in this work. There are many cases where this is a useful starting point. In crystals with density-wave order driven by nearest-neighbor (NN) electronic repulsion, such as we will consider below, both spin components behave in the same manner—including spin then only leads to an extra factor of two in certain equations below. The other case in which spin may be ignored is in spin-polarized systems, which might be a useful description of states in a large energy interval around the Fermi energy in strong ferromagnets (i.e., in half-metals).

We define the x-y-plane NN lattice constant to be a_0 and the lattice constant along the stacking direction $\hat{\mathbf{z}}$ to be c. In the x-y planes, we include NN hopping t_1 and next-nearest-neighbor (NNN) hopping t'_1. In the y-z and z-x planes, we include NN hopping t_3 and the peculiar NNN hoppings depicted in Fig. 3.1, with $t_{2A} \neq t_{2B}$. Although the atoms are chemically identical, this last choice differentiates A and B sublattices, requiring us to use a two-atom unit cell with primitive translations $\mathbf{a} = a_0(\hat{\mathbf{x}} - \hat{\mathbf{y}})$, $\mathbf{b} = a_0(\hat{\mathbf{x}} + \hat{\mathbf{y}})$, and $\mathbf{c} = c\hat{\mathbf{z}}$. Hereafter, this unit cell is referred to as *the unit cell* and its first Brillouin zone, as *the first Brillouin zone*. The crystal's space group is $P4/nbm$, and its associated crystal class is $4/mmm$. Importantly, this crystal has centers of inversion at the middle point of every x-y-plane NN bond. We use the following values for the hopping parameters: $t'_1 = 0.7\,t_1$, $t_{2A} = 0.1\,t_1$, $t_{2B} = 0.4\,t_1$, and $t_3 = 0.5\,t_1$; we have checked that our results are qualitatively robust upon tuning these parameters.

The nonequivalence of the hopping amplitudes t_{2A} and t_{2B} giving rise to $P4/nbm$ symmetry may be rationalized as depicted in Fig. 3.1: if a secondary set of atoms (shown in dark blue) is present only along the red bonds—which would be consistent with the space-group symmetry of the model—and their energy levels are far from the Fermi energy, their dynamics could be integrated out, with the end result of renormalizing the hopping

amplitude between the primary atoms (shown in gray), effectively leading to $t_{2A} \neq t_{2B}$. The same reasoning holds if there are additional secondary atoms on the green bonds *provided they are of a species different from those on the red bonds.*

As is true for any crystal class with inversion symmetry, $4/mmm$ is nongyrotropic [150, 272]. However, if the symmetry of the crystal were to be reduced, for instance by the onset of CDW order, the inversion symmetry could be broken and, indeed, the ordered structure could fall into a gyrotropic class. Below, we first study the band structure of this model in the absence of interactions, before turning to the impact of electronic repulsion.

3.3.1 Non-interacting band structure

The non-interacting Hamiltonian is

$$K = \sum_{\alpha,\beta} \sum_{i,j} -t_{ij}^{\alpha\beta} c_i^{\alpha\dagger} c_j^{\beta}, \tag{3.7}$$

where $c_i^{\alpha\dagger}$ creates an electron on sublattice α of unit cell i (that is, on the atom at position $\mathbf{r}_i^{\alpha}$). In momentum space,

$$K = \sum_{\mathbf{k}} \psi_{\mathbf{k}}{}^{\dagger} \left(d_{\mathbf{k}}^0 + \vec{d}_{\mathbf{k}} \cdot \vec{\tau} \right) \psi_{\mathbf{k}}, \tag{3.8}$$

where $c_{\mathbf{k}}^{\alpha} = N^{-1/2} \sum_i \mathrm{e}^{-\mathrm{i}\mathbf{k}\cdot\mathbf{r}_i^{\alpha}} c_i^{\alpha}$, N is the number of unit cells, $\vec{\tau}$ is the vector of Pauli matrices (acting in sublattice space), and $\psi_{\mathbf{k}}{}^{\dagger} = \begin{pmatrix} c_{\mathbf{k}}^{A\dagger} & c_{\mathbf{k}}^{B\dagger} \end{pmatrix}$. Because of time-reversal symmetry, the hopping amplitudes $t_{ij}^{\alpha\beta}$ are necessarily real valued. We will measure momenta in units of inverse lattice spacing, setting $a = c = 1$ henceforth. With this, we arrive at

$$d_{\mathbf{k}}^0 = -2t_3 \cos(k_c) - 2t_1' \Big(\cos(k_a) + \cos(k_b) \Big) \tag{3.9a}$$

$$d_{\mathbf{k}}^1 = -4 \cos\left(\frac{k_a}{2}\right) \cos\left(\frac{k_b}{2}\right) \Big(t_1 + (t_{2A} + t_{2B}) \cos(k_c) \Big) \tag{3.9b}$$

$$d_{\mathbf{k}}^2 = 4(t_{2A} - t_{2B}) \cos\left(\frac{k_a}{2}\right) \cos\left(\frac{k_b}{2}\right) \cos(k_c) \tag{3.9c}$$

$$d_{\mathbf{k}}^3 = 0. \tag{3.9d}$$

The product $\Pi\Theta$ of the aforementioned inversion symmetry Π with the Hamiltonian's time-reversal symmetry Θ constrains $d_{\mathbf{k}}^3 \equiv 0$ identically; for this reason, band touchings for this crystal will generically arise as line nodes, as seen in the non-interacting band structure (top panel of Fig. 3.6). More specifically, the nonsymmorphic symmetries present in the space group $P4/nbm$ give rise to band touchings along high-symmetry lines (see Appendix 3.C); Fig. 3.2 shows the location of these lines in the Brillouin zone.

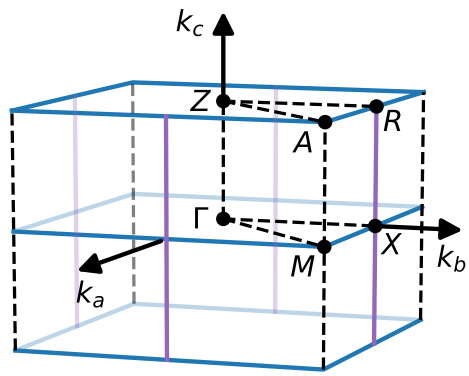

Figure 3.2: (Color online) Location of the line nodes (solid lines, shown in color) present in the symmetric phase within the first Brillouin zone as defined in Sec. 3.3. High-symmetry points are labeled.

3.3.2 Repulsive interactions

Next, we include repulsive interactions between NNs and NNNs; that is,

$$V = \frac{1}{2} \sum_{(i,\alpha)\neq(j,\beta)} V_{ij}^{\alpha\beta} n_i^\alpha n_j^\beta, \tag{3.10}$$

where $n_i^\alpha = c_i^{\alpha\dagger} c_i^\alpha$ is the number operator for the atom (i, α) and we take $V_{ij}^{\alpha\beta} = V_{ji}^{\beta\alpha}$. We take nonzero repulsions $V_{ij}^{\alpha\beta}$ on the same bonds as the hopping amplitudes and use a similar naming scheme, as shown in Fig. 3.1. Note that, unlike for the hopping amplitudes $t_{2A} \neq t_{2B}$, we take the repulsion strengths to be V_2 on both the red and green bonds—this choice serves as a representative slice through the full parameter space and illustrates some of the key ideas. Hence, the full Hamiltonian is given by $H = K + V$, and has the same (nongyrotropic) space-group symmetry $P4/nbm$ as K.

Spontaneous symmetry breaking (SSB), however, could reduce the symmetry of the crystal. A simple scenario is a CDW phase in which the densities on the A and B atoms are unequal, in which case the space group becomes $P\bar{4}2m$, whose crystal class—$\bar{4}2m$—is gyrotropic.

We note that in the absence of spin order, a Hubbard term $U \sum_i n_{i\uparrow} n_{i\downarrow}$ would modify the mean-field (MF) Hamiltonian by a mere uniform offset in the chemical potential μ. Hence, as we will restrict ourselves to ansätze without spin order, we do not bother including the Hubbard interaction.

We performed a MF calculation of the CDW order in the above system, allowing for a finite set of commensurate wavevectors. The ordering wavevectors favored by the interaction were identified by considering a simple model of classical charges resting at each atomic site of the crystal of Fig. 3.1—see Appendix 3.A. Based on this, the four ordering wavevectors

included in the ansatz are

$$\mathbf{Q}_0 = 0, \qquad \mathbf{Q}_1 = \pi\hat{\mathbf{a}} + \pi\hat{\mathbf{b}},$$
$$\mathbf{Q}_2 = \pi\hat{\mathbf{c}}, \qquad \mathbf{Q}_3 = \pi\hat{\mathbf{a}} + \pi\hat{\mathbf{b}} + \pi\hat{\mathbf{c}}.$$

The order parameters for the mean-field theory are the Fourier amplitudes $\rho^{\alpha}_{\mathbf{Q}}$ for the $\mathbf{Q}$ listed above, where $\alpha \in \{A, B\}$. However, we find it convenient to express the amplitudes on the A and B sublattices in terms of a symmetric and an antisymmetric part, respectively defined as

$$\rho^{\mathrm{s}}_{\mathbf{Q}} := \frac{\rho^{A}_{\mathbf{Q}} + \rho^{B}_{\mathbf{Q}}}{2}, \tag{3.11a}$$
$$\rho^{\mathrm{a}}_{\mathbf{Q}} := \frac{\rho^{A}_{\mathbf{Q}} - \rho^{B}_{\mathbf{Q}}}{2}. \tag{3.11b}$$

Since $\rho^{\mathrm{s}}_{\mathbf{Q}_0} = \rho$, the electron filling, we are left with 7 independent MFs.

3.4 Results

3.4.1 Mean-field theory of charge-density-wave order

We focus on a cut of parameter space parametrized by g such that

$$V_1 = g, \qquad V_1' = \frac{g}{2}, \qquad V_2 = \frac{g}{2}, \qquad V_3 = \frac{g}{2}. \tag{3.12}$$

According to the model of electrostatic charges, at these relative repulsion values (marked by a white star in Fig. 3.10), the interaction most favors an ordering with $\rho^{\mathrm{a}}_{\mathbf{Q}_0} \neq 0$; however, the region of parameter space with $\rho^{\alpha}_{\mathbf{Q}_3} \neq 0$ most favored is nearby (see Appendix 3.A).

The MF calculation, for which the zero-temperature phase diagram is shown in Fig. 3.3, does indeed identify a swath of pure $\rho^{\mathrm{a}}_{\mathbf{Q}_0} \neq 0$ order for sufficiently large g and for approximately $0.3 < \rho < 0.6$—call this *Phase I*. In addition to this phase, at high and low filling, we discover regions where multiple CDW modes coexist (specifically, $\mathbf{Q}_0$ and $\mathbf{Q}_3$); that is, $\rho^{\mathrm{a}}_{\mathbf{Q}_0} \neq 0$ and $\rho^{\alpha}_{\mathbf{Q}_3} \neq 0$ (where α is either A or B)—call these regions *Phase II*. The orders in these phases are depicted in insets to Fig. 3.3.

For $g/t_1 \gg 1$, we observe that the phase diagram is approximately symmetric under $\rho \to 0.5 - \rho$; this is expected given the particle-hole symmetry of V, which becomes an approximate symmetry of H when K is nonzero but small compared with V. The system is insulating at zero temperature along lines shown as dashed in the phase diagram. These lines are located at fillings 1/4, 1/2, and 3/4, and each terminate at a point corresponding to a metal-insulator transition at commensurate filling. We can qualitatively understand the appearance of these insulating phases at commensurate fillings as follows. The classical picture in Appendix 3.A, appropriate in the large-g limit, favors the $\mathbf{Q}_0$ charge-ordered

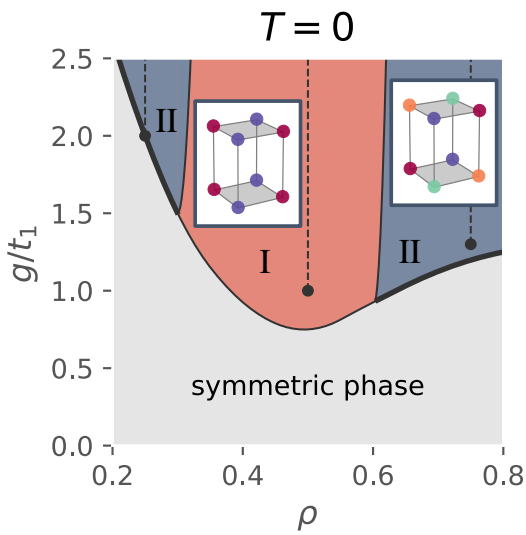

Figure 3.3: (Color online) CDW phases arising in the MF study as a function of the electronic filling ρ and g (which parametrizes the repulsion strength). Continuous and discontinuous transitions are respectively shown as thin and thick solid lines, while insulating lines, which occur at fillings 1/4, 1/2, and 3/4, are dashed. The nature of Phases I and II is described in the text.

state for our choice of interaction parameters. It is pictorially clear from Fig. 3.3 that this ordered state can be a stable "atomic" insulator at 1/2 filling. However, at 1/4 and 3/4 filling, this charge-ordered state will continue to host a gapless Fermi surface. Instead, at these other commensurate fillings, it is advantageous to have a secondary $\mathbf{Q}_3$ order which doubles the unit cell, permitting a gapped lowest band, again stabilizing a simple "atomic" charge-ordered insulator as is again pictorially clear from Fig. 3.3.

The phase diagram at $\rho = 0.5$ as a function of T and g is shown in Fig. 3.4 and reveals that raising the system temperature progressively suppresses Phase-I order.

3.4.2 Magnetoelectric response in Phase I

We study the temperature-dependent SSB-induced OEE in broken-symmetry Phase I, whose sole order parameter is $\rho^{\mathrm{a}}_{\mathbf{Q}_0}$. The other phases of the mean-field theory, such as Phase II, involve additional breaking of translational symmetry; this enlarges the unit cell and leads to more bands, making the analysis less transparent. Figure 3.5 shows the evolution of $\rho^{\mathrm{a}}_{\mathbf{Q}_0}$ and the components of the response tensor α^{orb} at half filling ($\rho = 0.5$) and fixed interaction strength ($g = 1.5\,t_1$). The phase transition, which is seen to be continuous, takes place at $k_{\mathrm{B}}T_{\mathrm{c}} \approx 1.4\,t_1$.

As alluded to previously, the point-group symmetry in Phase I is the $\bar{4}2m$, and a symmetry analysis (Appendix 3.D) reveals that symmetry constrains the response tensor α

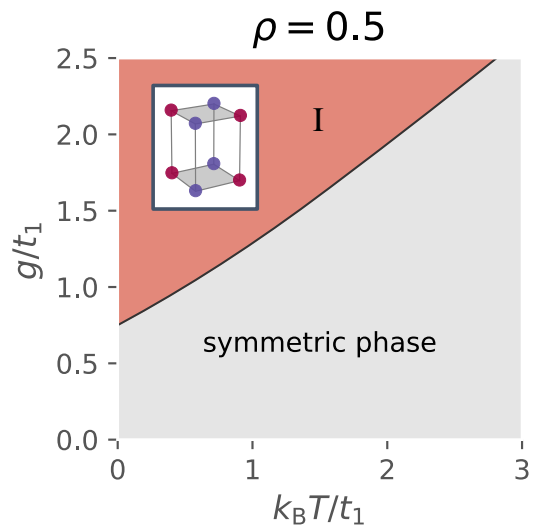

Figure 3.4: (Color online) CDW phases arising in the MF study at half filling ($\rho = 0.5$) as a function of temperature and g (which parametrizes the repulsion strength). The transition into Phase I from the symmetric phase is continuous. The nature of Phase I is described in the text.

to the form [150]

$$\alpha = \begin{pmatrix} \alpha_{aa} & & \\ & -\alpha_{aa} & \\ & & 0 \end{pmatrix}. \tag{3.13}$$

As seen in the lower panel of Fig. 3.5, the calculated α^{orb} is indeed of this form. The nonmonotonicity of α^{orb} is understood via the MF band structure, shown in Fig. 3.6. The top panel shows the high-temperature band structure; specifically, $k_B T = 2.00\, t_1$. Although the system is in a metallic phase with many states within $k_B T$ (gray shading) from the chemical potential μ (dashed line), in the high-symmetry phase, $\mathbf{m}_{\mathbf{k}n} = 0$ identically, so $\alpha^{\text{orb}} = 0$. The middle panel shows the band structure at an intermediate temperature $k_B T = 1.20\, t_1$ (near the peak in the α^{orb}); this is below the transition temperature, where the Phase-I charge order breaks inversion symmetry (along with the nonsymmorphic symmetries) and splits the bands throughout the Brillouin zone. The reduced symmetry of this phase allows gyrotropic response, so $\alpha^{\text{orb}} \neq 0$. As the temperature is further lowered, the size of the band splitting increases and a full gap develops, with μ within this gap as expected at half filling (lower panel of Fig. 3.5). Hence, it is clear that in the low-temperature limit, as the sum in Eq. 3.6 approaches a Fermi-surface integral, α^{orb} should again vanish.

3.4.3 Role of line nodes

In this subsection, we inspect the contribution of the gapped-out line nodes to the magnetoelectric response tensor α^{orb} in Phase I. We find that these constitute the dominant sources of orbital magnetic moment $\mathbf{m}_{\mathbf{k}n}$ in the Brillouin zone and the dominant contribution to

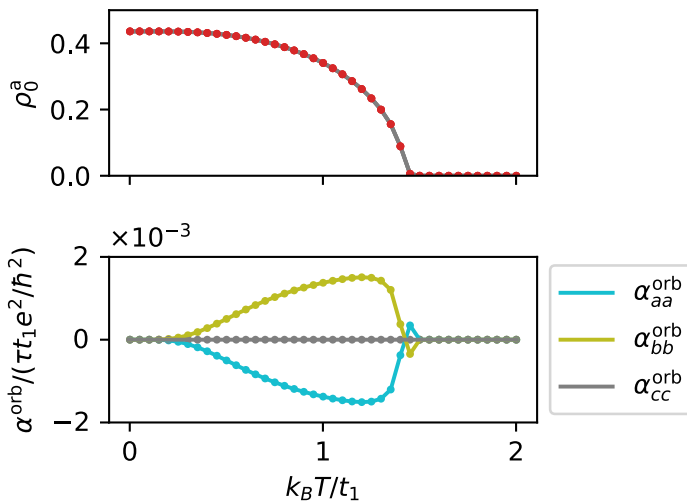

Figure 3.5: (Color online) Evolution of the magnetoelectric response through a phase transition with $g = 1.5t_1$ and $\rho = 0.5$. TOP PANEL Order parameter $\left(\rho^{a}_{\mathbf{Q}_0}\right)$ as a function of temperature. BOTTOM PANEL Components of the OEE response tensor α^{orb} as a function of temperature. Components that are not shown are identically zero.

α^{orb}. First, we obtain analytical expressions for the orbital magnetic moment $\mathbf{m}_{\mathbf{k}n}$ in the vicinity of these nodes; then, we compare with data computed from the lattice model.

In Phase I, the charge order breaks the inversion symmetry Π (together with the nonsymmorphic symmetries); accordingly, in the MF Hamiltonian for Phase I, $d^3_{\mathbf{k}}$ is no longer constrained to be zero; hence the disappearance of the band touchings. Rather, $d^3_{\mathbf{k}}$ is set by the Phase-I order parameter $\rho^{a}_{\mathbf{Q}_0}$. As a shorthand, define

$$\nu := \tilde{\rho}^{a}_{\mathbf{Q}_0}, \tag{3.14}$$

where $\tilde{\rho}^{a}_{\mathbf{Q}_0}$, defined in Appendix 3.B, is proportional to the Phase-I order parameter $\rho^{a}_{\mathbf{Q}_0}$.

In the high-symmetry phase, three independent line nodes exist in the first Brillouin zone (Fig. 3.2): (i) the X-R segment, (ii) the X-M segment, and (iii) the R-A segment—all other line nodes are related by the symmetry of Phase I. We expand about these (now-gapped) line nodes, denoting small deviations in momentum by $\tilde{\mathbf{k}}$. In the neighborhood of the (gapped) nodes, we have

(i) $k_a = \pi + \tilde{k}_a, \quad k_b = \tilde{k}_b, \quad -\pi < k_c \leq \pi$

$$d^0_{\mathbf{k}} = -2t_3 \cos(k_c) \tag{3.15a}$$

$$d^1_{\mathbf{k}} = 2\Big(t_1 + (t_{2A} + t_{2B})\cos(k_c)\Big)\tilde{k}_a \tag{3.15b}$$

$$d^2_{\mathbf{k}} = 2(t_{2A} - t_{2B})\sin(k_c)\tilde{k}_b \tag{3.15c}$$

$$d^3_{\mathbf{k}} = \nu \tag{3.15d}$$

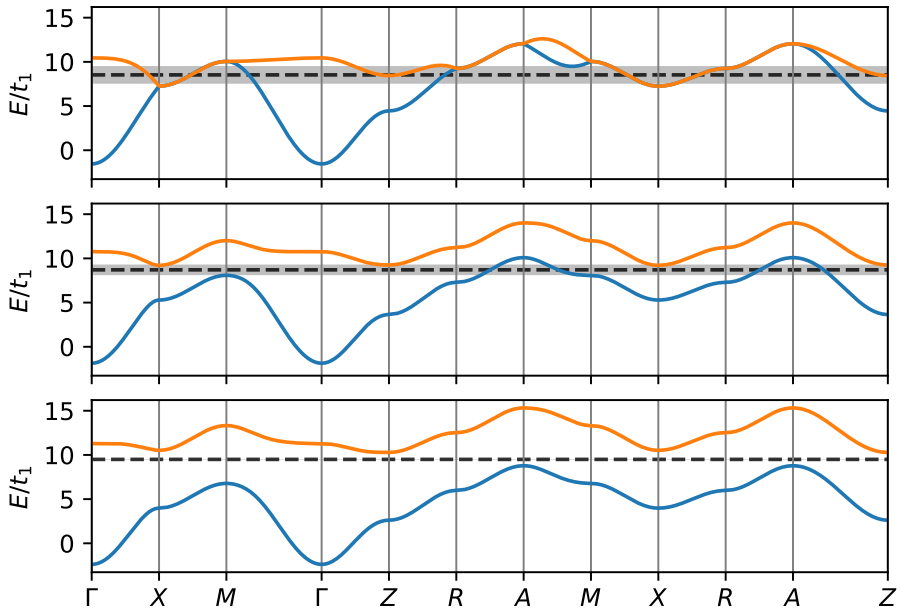

Figure 3.6: (Color online) Mean-field band structure at half filling (with parameters as specified in the main text) at three different temperatures: $k_\mathrm{B}T/t_1 = 2.00$ (top), 1.20 (middle), and 0.05 (bottom). The black dotted lines show the location of the chemical potential μ at each temperature, and the shaded areas centered at μ show the width $k_\mathrm{B}T$.

(ii) $-\pi < k_a < \pi, \quad k_b = \pi + \tilde{k}_b, \quad k_c = \tilde{k}_c$

$$d^0_{\mathbf{k}} = -2t_3 + 2t_1'(1 - \cos(k_a)) \tag{3.16a}$$

$$d^1_{\mathbf{k}} = 2(t_1 + t_{2A} + t_{2B}) \cos\left(\frac{k_a}{2}\right) \tilde{k}_b \tag{3.16b}$$

$$d^2_{\mathbf{k}} = 4(t_{2A} - t_{2B}) \sin\left(\frac{k_a}{2}\right) \tilde{k}_c \tag{3.16c}$$

$$d^3_{\mathbf{k}} = \nu \tag{3.16d}$$

(iii) $-\pi < k_a < \pi, \quad k_b = \pi + \tilde{k}_b, \quad k_c = \pi + \tilde{k}_c$

$$d^0_{\mathbf{k}} = 2t_3 + 2t_1'(1 - \cos(k_a)) \tag{3.17a}$$

$$d^1_{\mathbf{k}} = 2(t_1 - t_{2A} - t_{2B}) \cos\left(\frac{k_a}{2}\right) \tilde{k}_b \tag{3.17b}$$

$$d^2_{\mathbf{k}} = -4(t_{2A} - t_{2B}) \sin\left(\frac{k_a}{2}\right) \tilde{k}_c \tag{3.17c}$$

$$d^3_{\mathbf{k}} = \nu. \tag{3.17d}$$

For a two-band model with Bloch Hamiltonian $H_{\mathbf{k}} = d^0_{\mathbf{k}}\tau^0 + \vec{d}_{\mathbf{k}} \cdot \vec{\tau}$, $\mathbf{m}_{\mathbf{k}n}$ is the same for

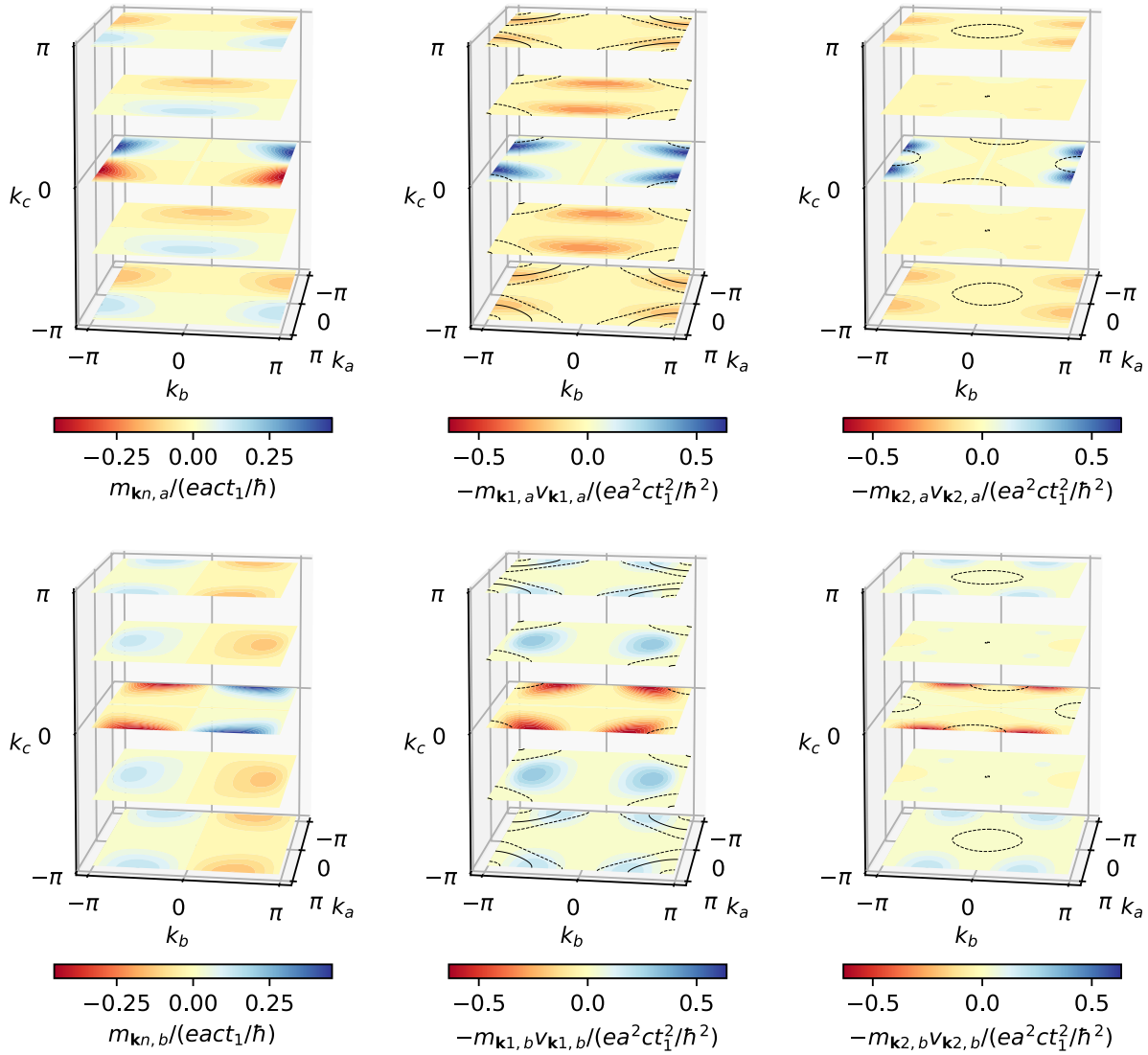

Figure 3.7: (Color online) Magnetic moment $m_{\mathbf{k}n,\kappa}$ and product $-m_{\mathbf{k}n,\kappa}v_{\mathbf{k}n,\kappa}$ for bands $n \in \{1,2\}$ and components $\kappa \in \{a,b\}$ at $k_\mathrm{B}T = 1.20\,t_1$. (Note that $\mathbf{m}_{\mathbf{k}n}$ is the same for both bands.) For clarity, the first Brillouin zone is not drawn to scale. The largest contributions to these two quantities are attributable to the line nodes depicted in Fig. 3.2. The solid lines in middle and right panels depict $\varepsilon_{\mathbf{k}n} = \mu$ surfaces. The dashed lines show $\varepsilon_{\mathbf{k}n} = \mu \pm k_\mathrm{B}T$ surfaces, which delimit the region most heavily weighted in the integral of Eq. 3.13. The slices shown are $k_c = -\pi$, $-\pi/2$, 0, $\pi/2$, and π.

both bands and can be written in the closed form [151,160]

$$m_{\mathbf{k}n,\kappa} = -\frac{e}{2\hbar}\sum_{\lambda\zeta}\varepsilon_{\kappa\lambda\zeta}\frac{\vec{d}_{\mathbf{k}}}{|\vec{d}_{\mathbf{k}}|^2}\cdot\left(\frac{\partial\vec{d}_{\mathbf{k}}}{\partial k_\lambda}\times\frac{\partial\vec{d}_{\mathbf{k}}}{\partial k_\zeta}\right), \tag{3.18}$$

where κ, λ, and ζ are Cartesian indices.

In the neighborhood of a (gapped) line node in the $\hat{\mathbf{a}}$ direction, the Hamiltonian can generically be expressed as

$$d^0_{\mathbf{k}} = f(k_a), \qquad \vec{d}_{\mathbf{k}} = \left(g_1(k_a)\tilde{k}_b,\ g_2(k_a)\tilde{k}_c,\ h(k_a)\right), \tag{3.19}$$

where f, g_1, g_2, and h are functions of k_a, and, hence, the components of $\mathbf{m}_{\mathbf{k}n}$ are given by

$$m_{\mathbf{k}n,a} = \frac{e}{2\hbar}\frac{1}{|\vec{d}_{\mathbf{k}}|^2}g_1g_2h \tag{3.20a}$$

$$m_{\mathbf{k}n,b} = \frac{e}{2\hbar}\frac{\tilde{k}_b}{|\vec{d}_{\mathbf{k}}|^2}g_2(g_1h' - g_1'h) \tag{3.20b}$$

$$m_{\mathbf{k}n,c} = \frac{e}{2\hbar}\frac{\tilde{k}_c}{|\vec{d}_{\mathbf{k}}|^2}g_1(g_2h' - g_2'h), \tag{3.20c}$$

where primes denote differentiation of the single-variable functions. To describe a line node in another direction, the indices in Eqs. 3.19 and 3.20 must be changed appropriately. We see that the longitudinal component $m_{\mathbf{k}n,a}$ is greatest at the (gapped) node itself (i.e., at $\tilde{k}_b = \tilde{k}_c = 0$, where $|\vec{d}_{\mathbf{k}}|^2$ is minimized), whereas the transverse components $m_{\mathbf{k}n,b}$ and $m_{\mathbf{k}n,c}$ are sizeable in the neighborhood of the (gapped) node but vanish at the (gapped) node itself.

Figure 3.7 shows the orbital magnetic moment $m_{\mathbf{k}n,\kappa}$ as well as the product $-m_{\mathbf{k}n,\kappa}v_{\mathbf{k}n,\kappa}$ for bands $n \in \{1,2\}$ and components $\kappa \in \{a,b\}$ calculated from the lattice model—these are directly relevant to the non-vanishing components of α^{orb}. The parameters used are the same as for the middle panel of Fig. 3.6. As shown by Eq. 3.6, up to constant factors, the integrand for $\alpha^{\mathrm{orb}}_{\kappa\kappa}$ is $-m_{\mathbf{k}n,\kappa}v_{\mathbf{k}n,\kappa}$ multiplied by $-\mathrm{d}f/\mathrm{d}\xi|_{\xi=\varepsilon_{\mathbf{k}n}-\mu}$, a positive weighting factor concentrated within $k_{\mathrm{B}}T$ around the chemical potential μ. Hence, the equal-energy surfaces at $\varepsilon_{\mathbf{k}n} = \mu$ (solid black lines) and $\varepsilon_{\mathbf{k}n} = \mu \pm k_{\mathrm{B}}T$ (dashed black lines) reveal the main contributions to the integral—generically, these are the (gapped) line nodes. In particular, at this temperature, for our choice of parameters, the largest contributions to α^{orb} are from the (gapped) line nodes at $k_c = \pm\pi$.

As outlined in Appendix 3.D, the data of Fig. 3.7 reflects all the symmetries of the point group $\bar{4}2m$ of Phase I as well as time-reversal symmetry, which dictates $\mathbf{m}_{\mathbf{k}n} = -\mathbf{m}_{-\mathbf{k}n}$ and $\mathbf{v}_{\mathbf{k}n} = -\mathbf{v}_{-\mathbf{k}n}$. The large values of $\mathbf{m}_{\mathbf{k}n}$ are attributable to the presence of line nodes and are as expected from Eqs. 3.20: focusing on $m_{\mathbf{k}n,a}$, for the slices $k_c = \pm\pi/2$, we see the signature of line node (i) (transverse to $\hat{\mathbf{a}}$), for which $m_{\mathbf{k}n,a} \to 0$ in proximity to the node, and for the slices $k_c = 0$ and $k_c = \pm\pi$, we also recognize contributions from line nodes (ii)

and (iii) (longitudinal to $\hat{\mathbf{a}}$), which are largest at the locus of the line nodes. The product $-m_{\mathbf{k}n,\kappa}v_{\mathbf{k}n,\kappa}$ still retains the general form of $m_{\mathbf{k}n,\kappa}$, though with a modified symmetry that allows a nonzero integral over the Fermi surface.

The difference in the magnitude of the longitudinal contributions at $k_c = 0$ and $k_c = \pm\pi$ can be retraced to the different $g_1(k_a)$ for line nodes (ii) and (iii): while $g_1(k_a) = 2(t_1 + t_{2A} + t_{2B})\cos(k_a/2)$ for the former, $g_1(k_a) = 2(t_1 - t_{2A} - t_{2B})\cos(k_a/2)$ for the latter, and $|t_1 + t_{2A} + t_{2B}| > |t_1 - t_{2A} - t_{2B}|$ with our parameter values.

3.5 Discussion and conclusion

It is sometimes overlooked that gyrotropy can arise without chiral or time-reversal symmetry breaking [253, 267]. Since the point group $\bar{4}2m$ of the Phase-I order contains mirror symmetries (in our coordinates, one perpendicular to $\hat{\mathbf{x}}$ and another perpendicular to $\hat{\mathbf{y}}$), the ground state of this broken-symmetry phase is an example of a nonchiral gyrotropic structure. This is unlike many of the examples of the OEE studied so far [151, 162], such as trigonal selenium and tellurium [144, 152]. Furthermore, it constitutes a concrete example of longitudinal magnetization induced by a current in a mirror-symmetric structure, which had been implied to be disallowed by symmetry [162]. While longitudinal magnetization is forbidden by mirrors perpendicular or parallel to the current, it is not forbidden by mirrors at 45° angles from the current, such as those in Phase I.

Similarly to a previously studied model [151], a picture of current flowing through solenoidal paths in the crystal provides a qualitative understanding of the OEE in Phase I. Furthermore, this picture makes physically clearer why the OEE response vanishes (i) when $t_{2A} = t_{2B}$—hence giving an intuitive explanation for the necessity of assuming $t_{2A} \neq t_{2B}$ from the start—and (ii) in the absence of charge order, that is, when the atoms are indistinguishable. We imagine a current $\mathbf{j}$ driven in the $\hat{\mathbf{b}}$ direction: the simplest solenoid-like paths that result in net displacement purely in the $\hat{\mathbf{b}}$ direction are shown in Figs. 3.8 and 3.9.

(i) Each row of atoms, whether on sublattice A or B, is surrounded by a solenoid traced out of t_{2A} (green) hoppings and another traced out of t_{2B} (red) hoppings (Fig. 3.8). These two solenoids are of opposite helicities given the current $\mathbf{j}$, and if $t_{2A} = t_{2B}$, their induced magnetic fields cancel identically, precluding any current-induced magnetization whether in the symmetric phase or in a charge-ordered phase. Indeed, if $t_{2A} = t_{2B}$, there exist additional mirror planes (perpendicular to $\hat{\mathbf{a}}$ and to $\hat{\mathbf{b}}$) that interchange the two solenoids, but these mirrors are absent for $t_{2A} \neq t_{2B}$.

(ii) If $t_{2A} \neq t_{2B}$, let us presume without loss of generality that t_{2B} (in red) is dominant and ignore the t_{2A} solenoids. Figure 3.9 shows that, given the current $\mathbf{j}$, a solenoid whose central axis is a row of A sites is of helicity opposite to one whose central axis is a row of B sites. If the atoms on the two sublattices are indistinguishable, the magnetic fields induced

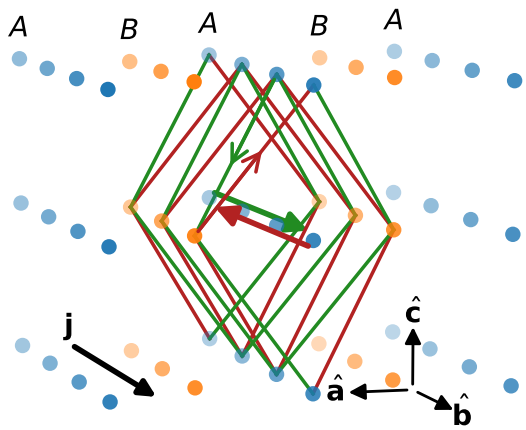

Figure 3.8: (Color online) For a current $\mathbf{j}$ oriented in the $\hat{\mathbf{b}}$ direction, solenoid-like paths due to the t_{2A} hoppings (green) and the t_{2B} hoppings (red) have opposite helicity. If $t_{2A} = t_{2B}$, the magnetizations from the two solenoids cancel. Crystal is not drawn to scale.

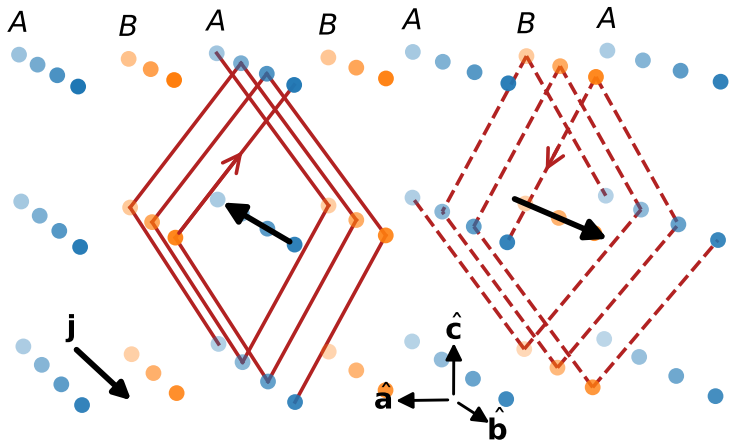

Figure 3.9: (Color online) For a current $\mathbf{j}$ oriented in the $\hat{\mathbf{b}}$ direction, solenoid-like paths with their axis along A atoms (solid lines) have opposite helicity to those with their axis along B atoms (dashed lines). If the atoms are indistinguishable, the magnetizations from the two solenoids cancel on average. Crystal is not drawn to scale.

by these two solenoids are equal and opposite and cancel when averaged over several lattice spacings. If the A and B atoms are distinguishable, however, the two sets of solenoids are distinct and can give rise to net magnetization. Indeed, the glide planes G_a and G_b (defined in Appendix 3.C) of the symmetric phase interchange the dotted-line and solid-line solenoids; however, these glide planes are broken in Phase I.

It is surprising *a priori* that such a solenoid picture can exist in a nonchiral crystal (previous examples have focused on chiral structures and the helicity that naturally arises therefrom [144, 151, 162]); however, the two mirror symmetries of point group $\bar{4}2m$—one perpendicular to $\hat{\mathbf{x}}$ and the other perpendicular to $\hat{\mathbf{y}}$—do not bring the solenoids into themselves, but rather exchange the $\hat{\mathbf{a}}$-axis solenoids with the $\hat{\mathbf{b}}$-axis solenoids. Hence, instead of forbidding a magnetoelectric response, the mirrors explain why the OEE coefficients

along the $\hat{\mathbf{a}}$ and $\hat{\mathbf{b}}$ axes are opposite in sign, since the current is a polar vector and the magnetization is an axial vector.

In summary, we have discussed a simple model of a crystal with lines nodes and shown how charge order can lead to a nonzero OEE. Such an OEE could be probed by nuclear magnetic resonance experiments. We have also discussed how the magnetoelectric response has a large contribution arising from the vicinity of line nodes. Our work suggests that line node semimetals which are weakly gapped by charge order might be a promising place to search for large OEE.

Note added: While completing this manuscript, we came across a recent theory preprint (arXiv:1903.01103v1) [273] which discusses the OEE induced by quadrupolar symmetry breaking in certain diamond lattice materials. While some of the ideas in that preprint overlap with our work, many of the details we consider (lattice structure, type of ordering and line-node analysis) are significantly different.

Acknowledgements

We thank D. A. Pesin for fruitful discussions. This research was funded by the Natural Sciences and Engineering Research Council of Canada and the Canadian Institute for Advanced Research. G. M. is supported by the *Fonds de recherche du Québec - Nature et technologies*. This research was enabled in part by support provided by Compute Ontario, Westgrid and Compute Canada. Computations were performed on the Niagara supercomputer at the SciNet HPC Consortium. SciNet is funded by the Canada Foundation for Innovation, the Government of Ontario, Ontario Research Fund - Research Excellence, and the University of Toronto.

Appendix 3.A Classical phase diagram

The charge ordered states favored by the interaction of Eq. 3.10 were identified by determining the energy of CDW modes in a classical picture of electrostatic charges by Fourier transforming and minimizing the repulsive interaction in momentum space. In Fig. 3.10, we show using which state has the lowest energy (according to V) as a function of the (relative) sizes of the repulsion strengths V_1, V_1', V_2, and V_3; the white star shows the relative parameter values used in the MF calculation. The ansatz for the mean-field theory described in the main text was chosen to potentially allow all the ground states that occur in this simplified model.

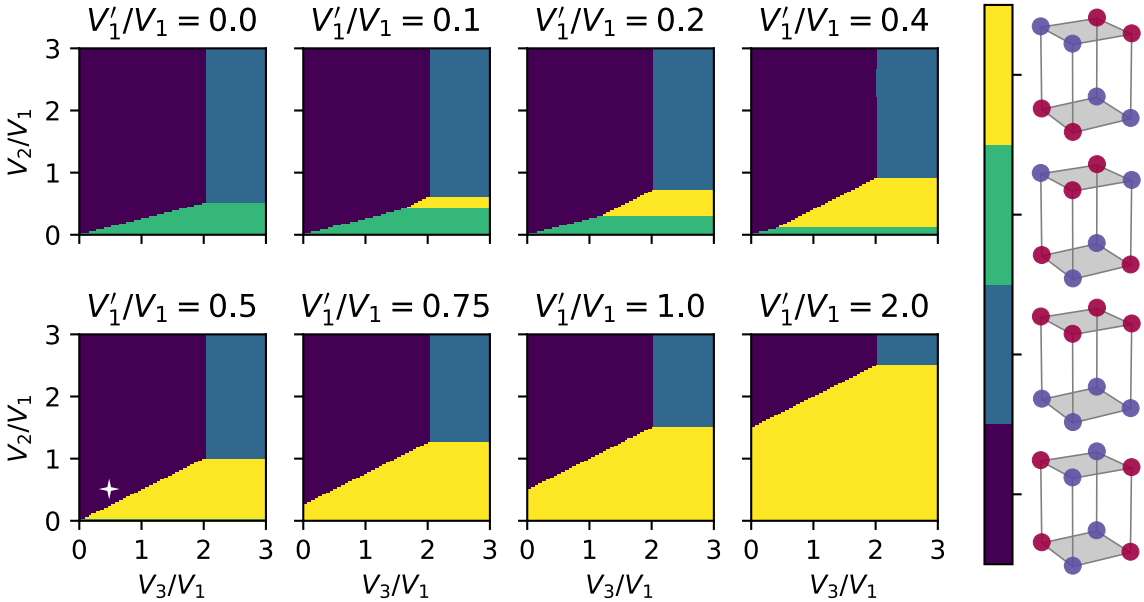

Figure 3.10: (Color online) Phase diagram showing the lowest-energy charge ordered states resulting from a model of electrostatic charges subject to the interaction of Eq. 3.10; the colors correspond to the indicated charge ordering patterns. The white star shows the relative parameter values used in the MF calculation.

Appendix 3.B Details of the mean-field calculation

Here, we provide additional information regarding the self-consistent MF calculation of the CDW order. The electronic interaction of Eq. 3.10 was decomposed in the density channel, giving rise to the following MF interaction term:

$$V_{\mathrm{MF}} = \frac{1}{2} \sum_{(i,\alpha)\neq(j,\beta)} V_{ij}^{\alpha\beta} \left(\rho_i^\alpha n_j^\beta + n_i^\alpha \rho_j^\beta \right) \tag{3.21a}$$

$$= N \sum_{\mathbf{q}}^{\mathrm{BZ}} \sum_{\alpha\beta} V_{\mathbf{q}}^{\alpha\beta} \rho_{\mathbf{q}}^{\alpha *} n_{\mathbf{q}}^\beta . \tag{3.21b}$$

Here, N is the number of unit cells in the crystal, $\rho_{\mathbf{q}}^\alpha = N^{-1} \sum_i \mathrm{e}^{-\mathrm{i}\mathbf{q}\cdot\mathbf{R}_i} \rho_i^\alpha$ (and likewise for $n_{\mathbf{q}}^\alpha$), and $V_{\mathbf{q}}^{\alpha\beta}$ is the Fourier transform of $V_{ij}^{\alpha\beta}$, which is invariant under simultaneous translation of i and j.

Choosing a closed set of commensurate wavevectors $\{\mathbf{Q}\}$ defines a *reduced Brillouin zone* (RBZ), which is mapped to the full Brillouin zone under addition of the wavevectors $\mathbf{Q}$. This property allows us to rewrite the integral of reciprocal-space-periodic functions as

$$\sum_{\mathbf{k}}^{\mathrm{BZ}} f(\mathbf{k}) = \sum_{\mathbf{Q}} \sum_{\mathbf{k}}^{\mathrm{RBZ}} f(\mathbf{k}+\mathbf{Q}), \tag{3.22}$$

where the domain of the momentum sums is indicated above the summation symbol. Hence, we diagonalized the Hamiltonian $H_{\mathrm{MF}} = K + V_{\mathrm{MF}}$ in the RBZ by writing it in the form

$$K = \sum_{\mathbf{k}}^{\mathrm{RBZ}} \sum_{\alpha\beta} \sum_{\mathbf{Q}} {c^{\alpha}_{\mathbf{k}+\mathbf{Q}}}^{\dagger} h^{\alpha\beta}_{\mathbf{k}+\mathbf{Q}} c^{\beta}_{\mathbf{k}+\mathbf{Q}} \tag{3.23}$$

$$V_{\mathrm{MF}} = \sum_{\mathbf{k}}^{\mathrm{RBZ}} \sum_{\alpha} \sum_{\mathbf{Q}\mathbf{Q}'} {c^{\alpha}_{\mathbf{k}+\mathbf{Q}}}^{\dagger} \tilde{\rho}^{\alpha}_{\mathbf{Q}-\mathbf{Q}'} c^{\alpha}_{\mathbf{k}+\mathbf{Q}'}, \tag{3.24}$$

where $\tilde{\rho}^{\alpha}_{\mathbf{Q}} = \sum_{\beta} V^{\alpha\beta}_{\mathbf{Q}} \rho^{\beta}_{\mathbf{Q}}$ and $h^{\alpha\beta}_{\mathbf{k}}$ is the Bloch Hamiltonian, in our case given in Eq. 3.8 as $h_{\mathbf{k}} = d^0_{\mathbf{k}} + \vec{d}_{\mathbf{k}} \cdot \vec{\tau}$. Starting from a series of randomized values for the MFs $\rho^{\alpha}_{\mathbf{Q}}$, we iterated until the computed expectation values agree with the input MFs to within 10^{-6}. We compared the Helmholtz free energy F of the different ground states thusly obtained and selected the one with minimal F at every point in parameter space.

Appendix 3.C Nonsymmorphic symmetries and protection of the gapless lines in the high-symmetry phase

In this appendix, we show how the nonsymmorphic symmetries present in the space group $P4/nbm$ (that of the bare crystal in the absence of charge order) constrain the location of gapless lines via a Kramers-like degeneracy of the spinless fermions [78, 80]. Three independent nonsymmorphic symmetries are present in the group. In Seitz notation and with respect to an origin at an inversion center, they are

$$G_a = \left\{ m_a \middle| \frac{\mathbf{b}}{2} \right\}, \tag{3.25a}$$

$$G_b = \left\{ m_b \middle| \frac{\mathbf{a}}{2} \right\}, \tag{3.25b}$$

$$G_c = \left\{ m_c \middle| \frac{\mathbf{a}+\mathbf{b}}{2} \right\}. \tag{3.25c}$$

Each of these symmetries composed with time reversal gives rise to Kramers-like degeneracies along certain high-symmetry lines in momentum space. In order to obtain a Kramers-like degeneracy at momentum $\mathbf{k}$ due to an antiunitary operator $\tilde{\Theta}$, two conditions must be fulfilled: (i) $\tilde{\Theta}$ must map $\mathbf{k}$ to itself up to a reciprocal lattice vector, and (ii) for any $|\psi\rangle$ within the fixed-$\mathbf{k}$ subspace, we must have $\tilde{\Theta}^2 |\psi\rangle = -|\psi\rangle$ (that is, $\tilde{\Theta}$ must "square to -1").

For instance, under the action of $\tilde{\Theta} = \Theta G_a$,

$$\Theta G_a |k_a, k_b, k_c, \alpha\rangle = \begin{cases} |k_a, -k_b, -k_c, B\rangle^* & \alpha = A \\ \mathrm{e}^{-\mathrm{i}\mathbf{k}\cdot\mathbf{b}} |k_a, -k_b, -k_c, A\rangle^* & \alpha = B, \end{cases} \tag{3.26}$$

while under the action of $\tilde{\Theta}^2 = (\Theta G_a)^2$,

$$(\Theta G_a)^2 \left|\mathbf{k}, \alpha\right\rangle = \mathrm{e}^{-\mathrm{i}k_b} \left|\mathbf{k}, \alpha\right\rangle \quad \forall \alpha, \tag{3.27}$$

where $\mathbf{k} = k_a \hat{\mathbf{a}} + k_b \hat{\mathbf{b}} + k_c \hat{\mathbf{c}}$ and $\left|\mathbf{k}, \alpha\right\rangle = N^{-1/2} \sum_i \mathrm{e}^{-\mathrm{i}\mathbf{k}\cdot\mathbf{r}_i^\alpha} \left|i, \alpha\right\rangle$. It is then easy to see that the set of points at which conditions (i) and (ii) are fulfilled is

$$\left\{\mathbf{k} \in 1^{\mathrm{st}} \text{ BZ} \;\middle|\; k_b = \pi \text{ and } k_c \in \{0, \pi\}\right\}. \tag{3.28a}$$

Similarly, taking $\tilde{\Theta} = \Theta G_b$ and $\tilde{\Theta} = \Theta G_c$ respectively give Kramers-like degeneracies at momenta in the sets

$$\left\{\mathbf{k} \in 1^{\mathrm{st}} \text{ BZ} \;\middle|\; k_b \in \{0, \pi\} \text{ and } k_c = \pi\right\}. \tag{3.28b}$$

and

$$\left\{\mathbf{k} \in 1^{\mathrm{st}} \text{ BZ} \;\middle|\; (k_a, k_b) = (0, \pi) \text{ or } (k_a, k_b) = (\pi, 0)\right\}. \tag{3.28c}$$

Hence, we have shown that the existence and location of the line nodes shown Fig. 3.2 are determined by the nonsymmorphic symmetries of the space group combined with time reversal symmetry.

Appendix 3.D Crystal class $\bar{4}2m$

As stated in the main text, the (macroscopic) point group of Phase I is $\bar{4}2m$. With respect to the coordinates used above, the elements of the point group $\bar{4}2m$ are as follows.

- E, the identity;
- $\bar{4}_c$ and $\bar{4}_c^{-1}$, a fourfold rotoinversion axis parallel to $\hat{\mathbf{c}}$ and its inverse, respectively;
- $2_c = \bar{4}_c^2$, a twofold rotation axis parallel to $\hat{\mathbf{c}}$;
- 2_a and 2_b, twofold rotation axes parallel to $\hat{\mathbf{a}}$ and $\hat{\mathbf{b}}$, respectively;
- m_{d_1} and m_{d_2}, mirror planes perpendicular to $(\hat{\mathbf{a}} + \hat{\mathbf{b}})/\sqrt{2}$ and $(\hat{\mathbf{a}} - \hat{\mathbf{b}})/\sqrt{2}$, respectively.

Under an (active) rigid-body transformation R, the axial rank-two tensor α transforms as [150]

$$\alpha_{\kappa\lambda} \to \alpha'_{\kappa\lambda} = \det(R) \sum_{\zeta\eta} R_{\kappa\zeta} R_{\lambda\eta} \alpha_{\zeta\eta}, \tag{3.29}$$

where $\det(R) = 1$ for a transformation that preserves the parity of the axes and $\det(R) = -1$ for one that changes it. If $R \in \bar{4}2m$ [that is, R is a (macroscopic) symmetry of the crystal], then the response tensor must obey $\alpha = \alpha'$; this restricts the possible entries of the response tensor and, for $\bar{4}2m$, leads to the form shown in Eq. 3.13.

The point-group symmetry also constrains the form of the polar vector $\mathbf{v}_{\mathbf{k}n}$ and of the axial vector $\mathbf{m}_{\mathbf{k}n}$. For any transformation R in the point group,

$$\mathbf{v}_n(\mathbf{k}) = R\,\mathbf{v}_n(R^{-1}\mathbf{k}) \tag{3.30a}$$

$$\mathbf{m}_n(\mathbf{k}) = \det(R) R\,\mathbf{m}_n(R^{-1}\mathbf{k}), \tag{3.30b}$$

where we have used functional notation for the crystal momenta in order to avoid excessive indexing.

For example, if $R = \bar{4}_c$, then

$$\bar{4}_c\mathbf{k} = \begin{pmatrix} k_b \\ -k_a \\ -k_c \end{pmatrix}, \tag{3.31}$$

and so

$$\begin{pmatrix} v_{n,a}(\mathbf{k}) \\ v_{n,b}(\mathbf{k}) \\ v_{n,c}(\mathbf{k}) \end{pmatrix} = \begin{pmatrix} +v_{n,b}\left(\bar{4}_c^{-1}\mathbf{k}\right) \\ -v_{n,a}\left(\bar{4}_c^{-1}\mathbf{k}\right) \\ -v_{n,c}\left(\bar{4}_c^{-1}\mathbf{k}\right) \end{pmatrix} \tag{3.32a}$$

$$\begin{pmatrix} m_{n,a}(\mathbf{k}) \\ m_{n,b}(\mathbf{k}) \\ m_{n,c}(\mathbf{k}) \end{pmatrix} = \begin{pmatrix} -m_{n,b}\left(\bar{4}_c^{-1}\mathbf{k}\right) \\ +m_{n,a}\left(\bar{4}_c^{-1}\mathbf{k}\right) \\ +m_{n,c}\left(\bar{4}_c^{-1}\mathbf{k}\right) \end{pmatrix}. \tag{3.32b}$$

This and other constraints are consistent with the data of Fig. 3.7, as is clear by inspection.

Chapter 4

Krein-unitary Schrieffer-Wolff transformation and band touchings in bosonic Bogoliubov-de Gennes and other Krein-Hermitian Hamiltonians[1]

4.1 Introduction

Non-Hermitian Hamiltonians have become a central field of study in condensed-matter physics in the last decades [274]. Important examples of systems governed by non-Hermitian Hamiltonians are quadratic bosonic Bogoliubov–de Gennes (BdG) Hamiltonians [275, 276], which have been the subject of renewed interest recently in the context of topological systems [57, 58, 187, 277–283], and so-called "PT-symmetric" non-Hermitian Hamiltonians, which initially attracted interest because they could give rise to real spectra despite not being Hermitian [284, 285]. Note that in the context of non-Hermitian Hamiltonians, a "PT symmetry" has come to refer to, loosely, any antilinear symmetry whose linear part is involutory (see Ref. 187, Sec. 3.1 for a careful discussion), and not necessarily to space-time inversion symmetry. Both these examples fall into a class of non-Hermitian Hamiltonians called *Krein Hermitian* [187, 286–293], also referred to in the literature as "pseudo-Hermitian" [58, 187, 188, 286–289] or "para-Hermitian" [186].

Krein-Hermitian Hamiltonians are Hermitian with respect to an indefinite, nondegenerate inner product, rather than the conventional positive-definite inner product [186]. They have spectral properties that enable them to describe stable physical systems: the phase diagram of a Krein-Hermitian Hamiltonian typically includes *dynamically stable* regions, in which the Hamiltonian is diagonalizable with real eigenvalues and with eigenvectors that

[1] Chapter adapted from Ref. 4, i.e., Geremia Massarelli, Ilia Khait, and Arun Paramekanti, *Phys. Rev. B*, 106:144434 (2022). Copyright 2022 by the American Physical Society.

are orthonormal with respect to the indefinite inner product. Lately, the mathematics of Krein-Hermitian Hamiltonians and Krein spaces more generally have seen growing interest and adoption among theoretical physicists as a tool to approach these specific non-Hermitian problems [58, 186, 187, 292].

The Schrieffer-Wolff (SW) transformation [294], also known as the Löwdin partitioning method [295], has been the object of renewed interest in recent years. Novel non-perturbative approaches have yielded new results, like the expansion's radius of convergence and closed-form expressions to all orders [294]. Moreover, the SW approach has been generalized to obtain non-unitary similarity transformations of (non-Hermitian) Liouvillian operators in order to perturbatively eliminate fast degrees of freedom in dissipative quantum systems [296, 297].

Previously, perturbative transformations have been used in bosonic BdG Hamiltonians specifically to eliminate boson pairing terms [278, 298–301]. Other recent works have simply assumed more or less implicitly that, in regards to perturbation theory and effective Hamiltonians, Krein-Hermitian Hamiltonians can be treated the same as Hermitian Hamiltonians. However, a systematic study highlighting differences and similarities between them in this regard has been lacking. In Sec. 4.3, we formulate a general perturbative SW transformation for dynamically stable, finite-dimensional Krein-Hermitian Hamiltonians, yielding a reduced effective Hamiltonian that is Krein Hermitian in a reduced space and is sure to be Krein-unitarily diagonalizable. Unlike previous work on general non-Hermitian SW transformations [296, 297], our transformation is explicitly Krein unitary; further, we highlight the implications of Krein stability theory on the effective Hamiltonian and its diagonalizability. In particular, it is safe to perturbatively study degenerate and near-degenerate states as long as they have the same (nonzero) Krein signature, since small perturbations cannot drive them to dynamical instability.

Aside from the practical applications of a SW transformation for Krein-Hermitian Hamiltonians, our results allow a justification for the use of reduced Hamiltonians describing a subset of contiguous energy bands in a Krein-Hermitian system, as discussed in Sec. 4.4. In particular, we clarify why adjacent positive-energy bands of thermodynamically stable systems can simply be described by a Hermitian reduced Hamiltonian, even though the larger Hamiltonian they originate from is Krein Hermitian.

We use this observation to justify codimension-based arguments for band touchings in bosonic BdG Hamiltonians, focusing on magnons for concreteness. Such arguments are well known for Hermitian Hamiltonians [302]. We then revisit known results on topological band touchings and the consequences of space-time inversion symmetry in magnon systems, based solely on codimension and symmetry arguments. In short, the behavior hinges on the fact that space-time inversion squares to $+1$ for bosons [303]. We focus on Dirac points and gapless lines in the magnon spectrum of Cu_3TeO_6 [303–305] and gapless lines in the magnon spectrum of $CoTiO_3$ [306, 307], both part of a recent drive to identify topological

band touchings in bosonic systems.

Appendix 4.A contains details on the SW transformation for Krein-Hermitian matrices, and Appendix 4.C discusses magnons in linear spin-wave theory as well as the implementation of spin-space-group symmetries on the linear spin-wave Hamiltonian.

To avoid confusion with the aforementioned notion of "PT symmetry" in the context of non-Hermitian Hamiltonians, we refer to space-time inversion symmetry as *magnetic inversion* symmetry rather than "PT symmetry". The Krein Hermiticity—equivalent to so-called "PT symmetry" [187]—of bosonic BdG Hamiltonians stems solely from the bosonic commutation relations and holds regardless of the system's physical symmetries.

4.2 Bosonic BdG Hamiltonians

In this section, we review the mathematics of quadratic BdG Hamiltonians of bosons, which will be our main focus in this work, though our results have broader applicability. This keeps the article self-contained, and allows us to introduce necessary notions and definitions.

Consider a bosonic Fock space made up of countably many single-particle states, and a quadratic Hermitian Hamiltonian $\hat{H}$ in that space. Although the second-quantized Hamiltonian $\hat{H}$ is Hermitian and the bosonic Fock space is necessarily of infinite dimension, the "single-particle Hamiltonian" that governs the time evolution and determines the spectrum of the non-interacting bosons is finite dimensional and, in general, as we will see, Krein Hermitian. For concreteness, we assume the system has (either discrete or continuous) translational invariance, allowing us to write

$$\hat{H} = \frac{1}{2}\sum_{\mathbf{k}} \hat{\Phi}^\dagger_{\mathbf{k}} H_{\mathbf{k}} \hat{\Phi}_{\mathbf{k}}, \tag{4.1}$$

where $\hat{\Phi}^\dagger_{\mathbf{k}} = [b^\dagger_{\mathbf{k},1}, \ldots, b^\dagger_{\mathbf{k},n}, b_{-\mathbf{k},1}, \ldots, b_{-\mathbf{k},n}]$ is the Nambu spinor, and $b_{\mathbf{k}\alpha}$ is the annihilation operator for the state with wave vector $\mathbf{k}$ and "flavor" $\alpha \in \{1, \ldots, n\}$; the extension of our results to systems without translational invariance presents no difficulties. In the case of discrete translational invariance, the momentum sum is restricted to a Brillouin zone, while in the case of continuous translational invariance, it is not restricted. In magnon systems such as those considered in Sec. 4.3 and Appendix 4.C, $\mathbf{k}$ is summed over the magnetic Brillouin zone and α labels the different spins within the magnetic unit cell. Notice that for clarity, we use hats on Hilbert-space operators like $\hat{H}$, but not on coefficient matrices like $H_{\mathbf{k}}$.

The redundancy inherent in the Nambu formalism is eliminated by choosing the Hermitian coefficient matrix $H_{\mathbf{k}}$ to satisfy the particle-hole (PH) constraint, $\tau^1 H_{\mathbf{k}} \tau^1 = H^*_{-\mathbf{k}}$. Here and throughout the article, τ^μ, short for $\tau^\mu \otimes \mathbb{1}_n$, are the Pauli matrices in Nambu space.

Note that if the system is particle conserving, $H_{\mathbf{k}}$ is block diagonal in the Nambu space, in which case the spectrum of $\hat{H}$ and the system's time evolution are simply determined by

the unitary eigendecomposition of $H_{\mathbf{k}}$.

4.2.1 Diagonalization

Unlike for fermions, a Bogoliubov transformation for bosons is not simply achieved by the eigendecomposition of the coefficient matrix $H_{\mathbf{k}}$, as such a transformation does not preserve the bosonic canonical commutation relations [80, 189, 275, 276, 308]. Writing the transformation to a new bosonic Nambu spinor $\hat{\Gamma}_{\mathbf{k}}$ as $\hat{\Phi}_{\mathbf{k}} = T_{\mathbf{k}}\hat{\Gamma}_{\mathbf{k}}$, meaning

$$\hat{H} = \frac{1}{2}\sum_{\mathbf{k}} \hat{\Gamma}^{\dagger}_{\mathbf{k}}(T^{\dagger}_{\mathbf{k}}H_{\mathbf{k}}T_{\mathbf{k}})\hat{\Gamma}_{\mathbf{k}}, \tag{4.2}$$

the $2n \times 2n$ transformation matrix $T_{\mathbf{k}}$ must fulfill

$$T^{\dagger}_{\mathbf{k}}\tau^3 T_{\mathbf{k}} = T_{\mathbf{k}}\tau^3 T^{\dagger}_{\mathbf{k}} = \tau^3 \tag{4.3}$$

in order to preserve the bosonic commutation relations. Hence, in general, $T_{\mathbf{k}}$ is not unitary, and the transformation on $H_{\mathbf{k}}$ is not a similarity transformation [2]. A matrix satisfying the constraint of Eq. (4.3) has been called *paraunitary* in the physics literature [275].

In order to give rise to the eigenmodes of $\hat{H}$, the transformation $T_{\mathbf{k}}$ should be chosen such that $T^{\dagger}_{\mathbf{k}}H_{\mathbf{k}}T_{\mathbf{k}}$ is diagonal with real entries. If this is possible, the Hamiltonian can be written in its eigenbasis as

$$\hat{H} = \sum_{\mathbf{k}}\sum_{\alpha=1}^{n} \epsilon_{\mathbf{k},\alpha}\frac{\gamma^{\dagger}_{\mathbf{k},\alpha}\gamma_{\mathbf{k},\alpha} + \gamma_{\mathbf{k},\alpha}\gamma^{\dagger}_{\mathbf{k},\alpha}}{2}, \tag{4.4}$$

where we have used the fact that the particle-hole constraint ensures the modes at $\mathbf{k}$ and $-\mathbf{k}$ have the same energies and appropriately related eigenvectors. As we shall see in reviewing Krein theory, that $H_{\mathbf{k}}$ is positive definite, which we denote $H_{\mathbf{k}} > 0$, is a sufficient condition for there to exist a paraunitary $T_{\mathbf{k}}$ such that $T^{\dagger}_{\mathbf{k}}H_{\mathbf{k}}T_{\mathbf{k}}$ is diagonal with real, strictly positive entries [3].

The Hamiltonian $\hat{H}$ is *thermodynamically stable*, meaning it is bounded below, if and only if $H_{\mathbf{k}} \geq 0$ at all $\mathbf{k}$ [58]. In a linear spin-wave system, for example, $H_{\mathbf{k}} \geq 0$ holds as long as the underlying classical ground state is a local minimum of the classical energy. In many physical systems for which $H_{\mathbf{k}}$ is positive semidefinite but not positive definite, the zero eigenspace corresponds to the Goldstone mode; in such systems, $H_{\mathbf{k}} > 0$ for $\mathbf{k} \neq 0$ [58, 276].

Finally, we point out that the transformed coefficient matrix $T^{\dagger}_{\mathbf{k}}H_{\mathbf{k}}T_{\mathbf{k}}$ can be rewritten

[2] In general, a matrix transformation $P^{\dagger}AP$, where P is invertible, is known as a congruence transformation. Congruence transformations and similarity transformations overlap when P is unitary.

[3] It seems this was initially proven in the physics literature using a constructive approach based on the Cholesky decomposition of $H_{\mathbf{k}}$ [275], rather than using the tools from Krein theory.

using the paraunitarity constraint of Eq. (4.3):

$$T_{\mathbf{k}}^{\dagger} H_{\mathbf{k}} T_{\mathbf{k}} = \tau^3 \Big(T_{\mathbf{k}}^{-1} (\tau^3 H_{\mathbf{k}}) T_{\mathbf{k}} \Big). \tag{4.5}$$

Since τ^3 is diagonal, this form shows that the spectrum and the transformation $T_{\mathbf{k}}$ can be found from the (nonunitary) eigendecomposition of the non-Hermitian matrix $\tau^3 H_{\mathbf{k}}$. Since it determines the spectrum and governs the system's time evolution [187], we refer to $\tau^3 H_{\mathbf{k}}$ as the *single-particle Hamiltonian.* The properties of the single-particle Hamiltonian, and of Krein-Hermitian Hamiltonians more generally, are reviewed in Sec. 4.3.1.

4.2.2 Unitary transformations

We also review how a unitary transformation on the Hamiltonian $\hat{H}$ of Eq. (4.1) translates to a paraunitary transformation on the single-particle Hamiltonian $\tau^3 H_{\mathbf{k}}$ [276, 278, 301]. To see this, consider the transformed Hamiltonian $\hat{\tilde{H}} = \mathrm{e}^{-\hat{W}} \hat{H} \mathrm{e}^{\hat{W}}$, where $\mathrm{e}^{\hat{W}}$ is a unitary transformation in the Fock space generated by the skew-Hermitian generator $\hat{W}$, and rewrite it using the following expansion:

$$\hat{\tilde{H}} = \mathrm{e}^{-\hat{W}} \hat{H} \mathrm{e}^{\hat{W}} = \hat{H} + [\hat{H}, \hat{W}] + \frac{1}{2!} [[\hat{H}, \hat{W}], \hat{W}] + \dots \tag{4.6}$$

In order for the transformation to keep the Hamiltonian quadratic, its generator $\hat{W}$ must itself be quadratic: $\hat{W} = \frac{1}{2} \sum_{\mathbf{k}} \hat{\Phi}_{\mathbf{k}}^{\dagger} W_{\mathbf{k}} \hat{\Phi}_{\mathbf{k}}$, where $W_{\mathbf{k}}$ is a skew-Hermitian $2n \times 2n$ matrix. Furthermore, imposing the PH constraint on $W_{\mathbf{k}}$ (i.e., $\tau^1 W_{\mathbf{k}} \tau^1 = W_{-\mathbf{k}}^{\top}$) will ensure the coefficient matrix for $\hat{\tilde{H}}$ is PH symmetric, in addition to eliminating the redundancy in $W_{\mathbf{k}}$ intrinsic to the Nambu formalism.

Using the bosonic commutation relations $[\Phi_{\mathbf{k}}^a, \Phi_{\mathbf{p}}^{b\,\dagger}] = (\tau^3)^{ab} \delta_{\mathbf{p},\mathbf{k}}$, where a and $b \in \{1, \dots, 2n\}$, and the PH constraint $\tau^1 H_{\mathbf{k}} \tau^1 = H_{-\mathbf{k}}^{\top}$, one finds that the commutator is given by

$$[\hat{H}, \hat{W}] = \frac{1}{2} \sum_{\mathbf{k}} \hat{\Phi}_{\mathbf{k}}^{\dagger} (H_{\mathbf{k}}, W_{\mathbf{k}}) \hat{\Phi}_{\mathbf{k}}, \tag{4.7}$$

where $(H_{\mathbf{k}}, W_{\mathbf{k}}) \coloneqq H_{\mathbf{k}} \tau^3 W_{\mathbf{k}} - W_{\mathbf{k}} \tau^3 H_{\mathbf{k}}$ is a τ^3-intertwined commutator, which arises from the bosonic commutation relations. Since $H_{\mathbf{k}}$ and $W_{\mathbf{k}}$ are PH symmetric, so is $(H_{\mathbf{k}}, W_{\mathbf{k}})$; hence, the result of Eq. (4.7) can be iterated to find all orders of $\hat{\tilde{H}}$ and the transformed Hamiltonian of Eq. (4.6) takes the form

$$\begin{aligned} \hat{\tilde{H}} &= \frac{1}{2} \sum_{\mathbf{k}} \hat{\Phi}_{\mathbf{k}}^{\dagger} \Big(H_{\mathbf{k}} + (H_{\mathbf{k}}, W_{\mathbf{k}}) + \frac{1}{2!} ((H_{\mathbf{k}}, W_{\mathbf{k}}), W_{\mathbf{k}}) + \dots \Big) \hat{\Phi}_{\mathbf{k}} \\ &= \frac{1}{2} \sum_{\mathbf{k}} \hat{\Phi}_{\mathbf{k}}^{\dagger} \Big(\tau^3 \mathrm{e}^{-\tau^3 W_{\mathbf{k}}} \tau^3 H_{\mathbf{k}} \mathrm{e}^{\tau^3 W_{\mathbf{k}}} \Big) \hat{\Phi}_{\mathbf{k}} \\ &= \frac{1}{2} \sum_{\mathbf{k}} \hat{\Phi}_{\mathbf{k}}^{\dagger} \underbrace{\tau^3 T_{\mathbf{k}}^{-1} \tau^3}_{T_{\mathbf{k}}^{\dagger}} H_{\mathbf{k}} T_{\mathbf{k}} \hat{\Phi}_{\mathbf{k}}. \end{aligned} \tag{4.8}$$

In the last line, we have introduced the paraunitary transformation $T_{\mathbf{k}} := \mathrm{e}^{\tau^3 W_{\mathbf{k}}}$; indeed, any $2n \times 2n$ paraunitary matrix can be generated in this way with a skew-Hermitian matrix $W_{\mathbf{k}}$. Furthermore, the transformation $T_{\mathbf{k}}$ inherits a particle-hole constraint from that of $W_{\mathbf{k}}$, i.e., $\tau^1 T_{\mathbf{k}} \tau^1 = T^*_{-\mathbf{k}}$ [4].

Equation (4.8) shows that a unitary transformation $\hat{H} \to \mathrm{e}^{-\hat{W}} \hat{H} \mathrm{e}^{\hat{W}}$ on the second-quantized Hamiltonian has a paraunitary representation $\tau^3 H_{\mathbf{k}} \to T_{\mathbf{k}}^{-1} \tau^3 H_{\mathbf{k}} T_{\mathbf{k}}$ on the single-particle Hamiltonian. Since the single-particle Hamiltonian undergoes a similarity transformation, the invariance of the spectrum is manifest.

Had the ladder operators been fermionic and obeyed anticommutation relations rather than commutation relations, the unitary transformation on the second-quantized Hamiltonian would have had a more familiar unitary representation on the single-particle Hamiltonian.

4.3 Krein-Hermitian Hamiltonians and perturbation theory

In this section, we show that the SW transformation can be used to formulate a Krein-unitary perturbation theory for finite-size Krein-Hermitian Hamiltonians within a dynamically stable phase. A Hamiltonian is *dynamically stable* [5], meaning the time evolution it generates is bounded, iff the Hamiltonian is diagonalizable with real eigenvalues [187].

Since single-particle BdG Hamiltonians $\tau^3 H_{\mathbf{k}}$ and paraunitary transformations $T_{\mathbf{k}}$ are, respectively, Krein Hermitian and Krein unitary with respect to τ^3, our results allow for a perturbation theory perturbatively yielding bosonic eigenmodes as well as mode energies.

We begin by briefly reviewing necessary aspects of Krein spaces, and then present the perturbation theory.

4.3.1 Krein spaces

Although the single-particle Hamiltonian $\tau^3 H_{\mathbf{k}}$ is not Hermitian, it is Hermitian with respect to an indefinite inner product with metric τ^3, $\langle \phi, \psi \rangle_{\tau^3} := \phi^\dagger \tau^3 \psi$, in the sense that $\langle \tau^3 H \phi, \psi \rangle_{\tau^3} = \langle \phi, \tau^3 H \psi \rangle_{\tau^3}$ for any vectors ϕ and $\psi \in \mathbb{C}^{2n}$. Vector spaces endowed with an indefinite, nondegenerate inner product in addition to a positive-definite inner product are called *Krein spaces* [186, 309, 310]. While $\tau^3 H_{\mathbf{k}}$ may fail to be diagonalizable or to have real eigenvalues because it is non-Hermitian, these possibilities are narrowly constrained because of its *Krein Hermiticity*.

Consider a Krein space of dimension n_{K} with indefinite inner product $\langle \phi, \psi \rangle_\eta := \phi^\dagger \eta \psi$, where the Hermitian metric η is indefinite and nondegenerate. The *Krein adjoint* of a matrix

[4] The various expressions of PH symmetry all arise in the same way, from the redundancy of the Nambu spinors. On the (Hermitian) Bloch-BdG matrix, it reads as $\tau^1 H_{\mathbf{k}} \tau^1 = H^*_{-\mathbf{k}} = H^\top_{-\mathbf{k}}$. On the transformation matrix, it reads as $\tau^1 T_{\mathbf{k}} \tau^1 = T^*_{-\mathbf{k}}$, making the transformed Bloch-BdG matrix P-H symmetric. On the (skew-Hermitian) generator $W_{\mathbf{k}}$, it reads as $\tau^1 W_{\mathbf{k}} \tau^1 = W^\top_{-\mathbf{k}} = -W^*_{-\mathbf{k}}$.

[5] Note that dynamical stability and thermodynamic stability are fully independent concepts: Krein-Hermitian Hamiltonians can be both, either, or neither [187].

A is given by

$$A^\sharp := \eta^{-1} A^\dagger \eta, \tag{4.9}$$

since $\langle A\phi, \psi\rangle_\eta = \langle \phi, A^\sharp \psi\rangle_\eta$ for any vectors ϕ and $\psi \in \mathbb{C}^{n_\mathrm{K}}$. The concepts of Krein-Hermitian matrices ($K^\sharp = K$) and Krein-unitary matrices ($T^\sharp T = T T^\sharp = \mathbb{1}$) follow. Furthermore, a *Krein-antiunitary* operator Z can be written $Z = KT$ in a suitable basis, where K is the operation of complex conjugation and T is a Krein-unitary operator [311]. Note that a change of basis (to "normal coordinates") can make η diagonal with entries ± 1; specifically, diagonalization followed by a scaling transformation [6]. From here on, we assume the metric η has this form, with n_+ entries of $+1$ and $n_- = n_\mathrm{K} - n_+$ entries of -1, which considerably simplifies the treatment.

The Krein space that naturally arises in bosonic BdG theory has metric $\eta = \tau^3 \otimes \mathbb{1}_n$, with $n_- = n_+ = n$: the single-particle Hamiltonian $K = \tau^3 H$ and paraunitary transformations T are, respectively, Krein Hermitian and Krein unitary with respect to τ^3 [7]. The PH constraint of bosonic systems is not, however, a general feature of Krein-Hermitian Hamiltonians; indeed, the momentum-space single-particle Hamiltonian *at a given* $\mathbf{k}$ does not in general obey such a constraint, unless an inversion-like symmetry relating $\mathbf{k}$ and $-\mathbf{k}$ is present.

Dynamical stability and perturbations The eigenvalues of a Krein-Hermitian matrix K are either real or come in complex-conjugate pairs [58, 187, 188, 276]. An eigenvector ψ corresponding to a non-real eigenvalue has null signature ($\langle \psi, \psi\rangle_\eta = 0$), while one corresponding to a real eigenvalue can have positive ($\langle \psi, \psi\rangle_\eta > 0$), negative ($\langle \psi, \psi\rangle_\eta < 0$), or null signature. If all the vectors in the eigenspace of an eigenvalue λ have the same nonzero signature, the eigenspace is said to have *definite signature*; otherwise, it has *indefinite signature*. According to Krein stability theory [58, 187], if each eigenspace of K has definite signature, a perturbed Hamiltonian $K + \epsilon K'$ for sufficiently small ϵ is diagonalizable with real eigenvalues; that is, it is dynamically stable [8]. Furthermore, its eigenvectors can be chosen to be orthonormal with respect to the Krein inner product. Conversely, if K has an indefinite eigenspace, either with or without nontrivial Jordan blocks, then K either has non-real eigenvalues or there are arbitrarily small perturbations that make them non-real, meaning K is either dynamically unstable or at a phase boundary of dynamical stability.

If $K = K^\sharp$ is positive definite with respect to the Krein inner product, i.e., $\langle \phi, K\phi\rangle_\eta > 0$ for any nonzero ϕ, all its eigenspaces automatically have definite signature, so it is within a dynamically stable phase [58, 186, 187]. Furthermore, it has n_+ eigenstates with positive

[6] To see this, write η in its eigenbasis, $\eta = U\eta_\mathrm{d}U^\dagger$, and note that $\eta = (U\sqrt{\operatorname{abs}\eta_\mathrm{d}})\operatorname{sgn}\eta_\mathrm{d}(\sqrt{\operatorname{abs}\eta_\mathrm{d}}U^\dagger) = V^\dagger \operatorname{sgn}\eta_\mathrm{d} V$, where $V = \sqrt{\operatorname{abs}\eta_\mathrm{d}}U^\dagger$ and the sgn and abs functions act elementwise. It is easy to see that $\langle \phi, \psi\rangle_\eta = \langle V\phi, V\psi\rangle_{\operatorname{sgn}\eta_\mathrm{d}}$, K is Krein Hermitian with respect to η iff VKV^{-1} is Krein Hermitian with respect to $\operatorname{sgn}\eta_\mathrm{d}$, etc.

[7] When η is diagonal with entries ± 1, the columns of a Krein-unitary matrix T are orthonormal with respect to the Krein inner product.

[8] For Krein-Hermitian matrices, dynamical stability is equivalent to the concept of "Krein spectrality" [186, Sec. III A 1].

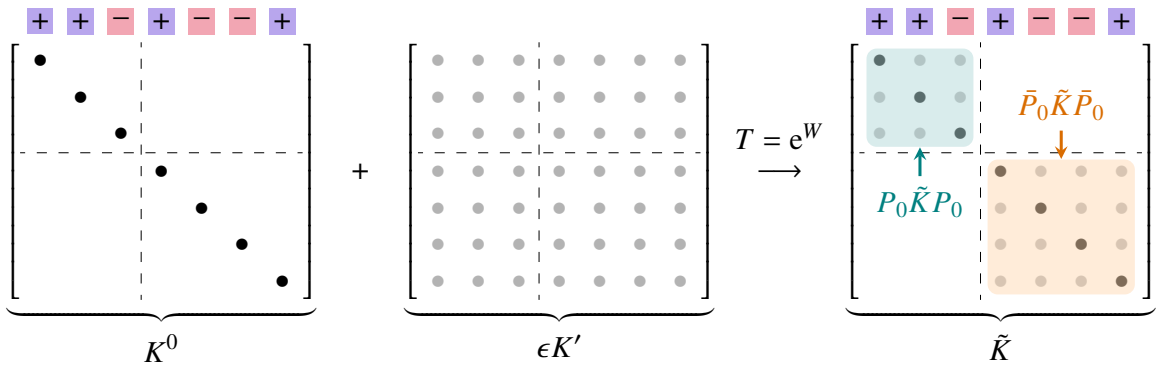

Figure 4.1: Schematic depiction of the SW transformation for Krein-Hermitian matrices, shown in the eigenbasis of the unperturbed Hamiltonian K^0. The Krein-unitary transformation T block-diagonalizes the perturbed Hamiltonian with respect to the subspace $\mathcal{P}_0$, and the effective Hamiltonian in the subspace $\mathcal{P}_0$ is $P_0\tilde{K}P_0$. The signs above the columns of K^0 show the Krein signatures of its eigenvectors; in the case shown here, $m_+ = 2$ and $m_- = 1$. This implies that the eigenstates of $P_0\tilde{K}P_0$ will have the same signatures, as illustrated schematically by the signs above the columns of $\tilde{K}$.

signature and positive energy, and $n_- = n_\mathrm{K} - n_+$ eigenstates with negative signature and negative energy. Taking $K = \tau^3 H$, K is clearly positive definite with respect to τ^3 iff $H > 0$. Once the eigenstates ψ of K are chosen to be orthonormal with respect to the Krein inner product, the claim made in Sec. 4.2.1—that $H > 0$ implies there is a paraunitary T such that $T^\dagger H T$ is diagonal with real, positive entries—follows. (Note, however, that dynamically stable phases can also exist if K is not positive definite with respect to the Krein inner product, as exemplified in Ref. 187.)

4.3.2 Schrieffer-Wolff transformation for Krein-Hermitian Hamiltonians

We now demonstrate that within a dynamically stable phase, the perturbative SW transformation can be generally formulated in terms of Krein-unitary transformations. Applied to single-particle boson Hamiltonians, the transformation yields a reduced single-particle Hamiltonian with proper bosonic eigenmodes.

The SW transformation is used to study the effect of a perturbation on a subset of contiguous energy states of a (traditionally) Hermitian Hamiltonian [294,295]. This *subspace of interest* is often, but not necessarily, made up of the low-energy states of the unperturbed Hamiltonian. The transformation is defined as a unitary rotation that block-diagonalizes the perturbed Hamiltonian; the block corresponding to the subspace of interest then yields an effective Hamiltonian for those states. The transformation as well as the effective Hamiltonian can be expressed perturbatively, order by order in terms of the perturbation. One of the considerable strengths of this method is its ability to deal on an equal footing with perturbations of degenerate as well as nondegenerate states, avoiding the complications that arise in Rayleigh-Schrödinger perturbation theory, for example [295,312].

The canonical transformations for Krein-Hermitian Hamiltonians are Krein-unitary trans-

formations: they preserve Krein Hermiticity, and leave eigenspace signatures unchanged. We adapt the SW procedure to Krein-Hermitian Hamiltonians within a dynamically stable regime, showing that it naturally yields a Krein-unitary transformation that block-diagonalizes the Krein-Hermitian Hamiltonian order by order in the perturbation, producing an effective Hamiltonian that is also Krein Hermitian. Krein stability theory ensures that for sufficiently small perturbations, the effective Hamiltonian at any order is also dynamically stable. Applied to single-particle boson Hamiltonians, the transformation will yield canonical boson modes.

Consider a perturbed η-Krein-Hermitian $n_{\mathrm{K}} \times n_{\mathrm{K}}$ Hamiltonian

$$K = K^0 + \epsilon K', \tag{4.10}$$

where K^0 is within a dynamically stable regime and has a known Krein-orthonormal eigendecomposition, $K^0 t_i = E_i^0 t_i$ with $t_i^\dagger \tau^3 t_j = \pm\delta_{ij}$, and $\epsilon \in \mathbb{R}$ controls the smallness of the perturbation. Let S_0 denote a subset of energy-contiguous eigenstates of K^0, comprised of m_+ positive-signature states and m_- negative-signature states, and gapped from the rest of the spectrum. Let $\mathcal{P}_0$ denote the subspace spanned by the eigenstates in S_0. We wish to block-diagonalize the perturbed Hamiltonian K in the subspace $\mathcal{P}_0$ using a Krein-unitary transformation (see the schematic depiction in Fig. 4.1). Associated with the subspace $\mathcal{P}_0$ is a unique Krein-orthogonal projector $P_0 = P_0^2 = P_0^\sharp$ [9], where

$$P_0 = \sum_{i \in S_0} \frac{t_i t_i^\dagger \eta}{t_i^\dagger \eta t_i}. \tag{4.11}$$

Schematically, in the eigenbasis of K^0, any matrix A can be written

$$\begin{aligned} A &= P_0 A P_0 + P_0 A \bar{P}_0 + \bar{P}_0 A P_0 + \bar{P}_0 A \bar{P}_0 \\ &= \left[\begin{array}{c|c} P_0 A P_0 & P_0 A \bar{P}_0 \\ \hline \bar{P}_0 A P_0 & \bar{P}_0 A \bar{P}_0 \end{array}\right], \end{aligned} \tag{4.12}$$

where $\bar{P}_0 \coloneqq \mathbb{1} - P_0$. We use the notation $A_{\mathrm{b}} \coloneqq P_0 A P_0 + \bar{P}_0 A \bar{P}_0$ and $A_{\mathrm{o}} \coloneqq P_0 A \bar{P}_0 + \bar{P}_0 A P_0$ for the parts of A that are, respectively, block diagonal and block off-diagonal in the subspace $\mathcal{P}_0$ [10].

We seek a paraunitary transformation T, generated by a skew-Krein-Hermitian matrix $W = -W^\sharp$,

$$\tilde{K} = T^\sharp K T = \mathrm{e}^{-W} K \mathrm{e}^{W}, \tag{4.13}$$

[9] In general, a non-orthonogal projection can be written $P = \sum_{i \in S} e_i \, \omega_i^\dagger$, where $\{e_i\}$ is a basis of the vector space and S is a subset of the basis vectors. Furthermore, $\{\omega_i\}$ is the basis of the dual space, chosen to satisfy the biorthogonality condition $\omega_i^\dagger e_j = \delta_{ij}$. For a Krein-orthogonal basis $\{t_i\}$, the dual basis vector ω_i depends only on the basis vector t_i: $\omega_i = \eta \, t_i / (t_i^\dagger \eta t_i)$.

[10] Please bear in mind the difference between the digit "0" (zero) and the letter "o".

to block-diagonalize the Hamiltonian in the subspace $\mathcal{P}_0$, meaning $\tilde{K}_\mathrm{o} = 0$. This can be achieved by choosing the generator W to be purely block off-diagonal, $W_\mathrm{b} = 0$ [11]. The parameter ϵ is assumed small enough to keep K dynamically stable, and to preserve an energy gap between the states in $\mathcal{P}_0$ and those not in $\mathcal{P}_0$; hence, there is an unambiguous correspondence between the unperturbed states in $\mathcal{P}_0$ and the smoothly connected eigenstates of the effective Hamiltonian.

The $\mathcal{P}_0$ block of the transformed Hamiltonian, $P_0\tilde{K}P_0$, is Krein Hermitian with metric $P_0\eta P_0$, meaning it has m_+ positive-signature eigenstates and m_- negative-signature eigenstates (see Fig. 4.1); these states are smoothly connected to the unperturbed states in S_0. We note that if the subset of interest is comprised only of positive-signature states, meaning $m_- = 0$, the effective Hamiltonian for the $\mathcal{P}_0$ subspace is Hermitian, since $P_0\eta P_0 = \mathbb{1}_{m_+}$.

Perturbative expansion We adapt the procedure of Ref. 295 to Krein-Hermitian and Krein-unitary matrices. Employing the expansion

$$\begin{aligned}\tilde{K} = T^\sharp K T &= \mathrm{e}^{-W} K \mathrm{e}^{W} \\ &= K + [K, W] + \frac{1}{2!}[[K, W], W] + \dots,\end{aligned} \tag{4.14}$$

using the assumption $W_\mathrm{b} = 0$, and demanding that $\tilde{K}_\mathrm{o} = 0$, we find the following equations defining $W = \epsilon W^{(1)} + \epsilon^2 W^{(2)} + \dots$ order by order in the perturbation K':

$$[K^0, W^{(1)}] = -K'_\mathrm{o}, \tag{4.15a}$$

$$[K^0, W^{(2)}] = -[K'_\mathrm{b}, W^{(1)}], \tag{4.15b}$$

$$[K^0, W^{(3)}] = -[K'_\mathrm{b}, W^{(2)}] - \frac{1}{3}[[K'_\mathrm{o}, W^{(1)}], W^{(1)}], \tag{4.15c}$$

$$\vdots$$

These equations are compatible with $W^{(j)\sharp} = -W^{(j)}$, i.e., with the assumption that T is Krein unitary at all orders. Indeed, the first few orders of $W = \sum_{l=1}^{+\infty} \epsilon^l W^{(l)}$ and of the transformed Hamiltonian $\tilde{K} =: \sum_{l=0}^{+\infty} \epsilon^l \tilde{K}^{(l)}$ are explicitly solved for in Appendix 4.A, showing that the generator W is indeed skew-Krein-Hermitian, and the effective Hamiltonian $P_0\tilde{K}P_0$ is Krein Hermitian with respect to $P_0\eta P_0$.

We note that if the Hamiltonian K is purely real, the transformation yields a purely real effective Hamiltonian $\tilde{K}$ to all orders in the perturbation. This is verified explicitly for the first few orders in Appendix 4.A, and holds to all orders.

Our findings agree with prior results on the first-order contribution $\tilde{K}^{(1)}$ found by applying degenerate perturbation theory to two *degenerate* states of a para-Hermitian Hamiltonian [277, 313, 314]. We stress once again, however, that the SW approach does not

[11] Clearly, this condition does not uniquely specify W or T. In Appendix 4.A, we perturbatively derive the "canonical" choice [296] of W, with which W is block off-diagonal.

have certain limitations of a Rayleigh-Schrödinger perturbation theory and treats degenerate, quasidegenerate, and nondegenerate states on the same footing [295, 312].

Range of validity For Hermitian matrices, the perturbative SW transformation is well controlled as long as the subspace of interest is gapped from the rest of the spectrum [294,295]. For Krein-Hermitian matrices, we additionally require that the perturbed Hamiltonian remain within a dynamically stable region in order for eigenvalues to remain real, and for eigenvectors to be orthonormal with respect to the Krein inner product. Furthermore, at points of non-diagonalizability, eigenvectors have a non-analytic dependence on perturbations [190, 191], and since dynamical-stability phase boundaries are mostly composed of non-diagonalizable points (called *exceptional points*) [187], they can constitute an obstruction to the convergence of a perturbation series.

In previous work, ranges of validity for the SW transformation were determined in terms of bounds on the norm $\|H'\|$ of a perturbation H' ensuring that the gaps between the subspace of interest and the rest of the spectrum remain sufficiently large [294]. This simple picture was possible because the eigenvalues of a Hermitian matrix H (and of normal matrices more generally) shift at most by $\|H'\|$ under the effect of a perturbation H', regardless of the details of H [190, 191, 294]. Here, $\|\cdot\|$ is the operator norm, equal to the largest singular value, but equal in general to the largest eigenvalue (in absolute value) *only* for a normal matrix.

In contrast, the eigenvalues of a non-normal matrix A can shift by more than $\|A'\|$ under the effect of a perturbation A' (contra Ref. 296), and the set of points at which the eigenvalues can end up depends on the details of A [190, 191]. This makes the task of formulating sufficient conditions for the non-closing of relevant gaps more complex. In mathematics, the notion of *pseudospectra* explores this striking difference between normal and non-normal matrices in regards to perturbations and eigenvalues [190, 191].

For a Krein-Hermitian matrix K^0 satisfying $\eta K^0 > 0$ [12], there is a simple condition under which a perturbed Hamiltonian $K^0 + K'$ remains dynamically stable and Krein-unitarily diagonalizable [58, Sec. IV C]: assuming $\|K'\| < \|(K^0)^{-1}\|^{-1}$, no eigenvalues of $K^0 + K'$ can reach zero, implying the perturbed Hamiltonian remains within the dynamically stable phase. Note that $\|(K^0)^{-1}\|^{-1}$—the smallest singular value of K^0 [190, Sec. II]—constitutes a lower bound for the smallest eigenvalue (in absolute value) of K^0, but since K^0 is non-normal, it is not in general equal to its smallest eigenvalue (contra Ref. 58).

The formulation of more general bounds on allowable perturbations K', and the derivation of a radius of convergence such as that which exists for perturbative SW transformations on Hermitian Hamiltonians [294], are left for future work.

[12] It is easy to convince oneself that ηK^0 is positive definite in the ordinary sense if and only if K^0 is positive definite with respect to the Krein inner product, with the consequences laid out at the end of Sec. 4.3.1.

4.4 Band touchings and codimension in magnon systems

In Hermitian systems, the standard SW transformation allows one to obtain, at least locally in momentum space, an effective Hamiltonian describing a contiguous subset of bands [315–319]. The transformation, which can in principle be carried out to any order, also justifies the existence of an effective reduced Hamiltonian that exactly describes contiguous bands if sufficiently large gaps separate them from the rest of the spectrum, again, locally in momentum space.

In linear spin-wave theory, magnons are generally described by a bosonic BdG Hamiltonian of the form of Eq. (4.1), with a Krein-Hermitian single-particle Hamiltonian (see Appendix 4.C for an overview of linear spin-wave theory). The Krein-Hermitian SW transformation we formulate explains why such effective reduced descriptions can also be used for Krein-Hermitian systems, and clarifies the properties of the effective reduced Hamiltonian in such cases. With these facts in hand, we revisit results on the codimensions of generic band touchings (i.e., those not at high-symmetry momenta) of noninteracting magnon systems with and without magnetic inversion symmetry—a term which, as explained in Sec. 4.1, we use to refer to space-time inversion symmetry. We comment on high-symmetry momenta at the end of the section.

Quadratic magnon Hamiltonians in three dimensions (3D) with magnetic inversion symmetry are known to exhibit either topologically protected Dirac points or topologically protected gapless lines, depending on the classical spin order and on other symmetries of the system [303]. This behavior makes them in part analogous to quadratic Hamiltonians of spinless electrons in 3D, which also generically exhibit gapless lines in the presence of space-time-inversion symmetry [60, 302, 320–322]. The source of this commonality is that both are integer-spin particles, for which space-time inversion squares to $+1$ [16, 323]; however, the magnon case can exhibit richer behavior because of the larger set of possible symmetries. The symmetries of magnetically ordered systems and their implementation on magnon Hamiltonians are discussed in Appendix 4.C.

Since our findings justify an effective two-band model for bosonic BdG Hamiltonians, we can use simple codimension counting approaches familiar from fermionic systems [50, 65, 302] to understand the emergence of generic gapless features in magnon spectra, giving a useful complementary understanding of the topologically protection.

Given a Bloch coefficient matrix function $H_{\mathbf{k}}$, we first maximally block-diagonalize it using all the ($\mathbf{k}$-conserving) unitary symmetries of the Hamiltonian; for example, the spin-rotation symmetry in the example from Ref. 303 mentioned above, further elaborated on below. This gives rise to "symmetryless" blocks $\{H^a_{\mathbf{k}}\}$ whose dependence on $\mathbf{k}$ should be generic [16]. Then, we consider the action of magnetic inversion symmetries—which are antiunitary—on the symmetryless blocks to understand the generic band touchings that occur within them.

4.4.1 Two-band effective Hamiltonian for magnon systems

Consider a symmetryless block as described above, at least of size 2×2. At a wave vector $\mathbf{k}_0$ at which $H_{\mathbf{k}_0} > 0$, the magnon spectrum at $\mathbf{k}_0$ and neighboring wave vectors is given by the set of positive eigenvalues of the τ^3-Krein-Hermitian matrix $\tau^3 H_{\mathbf{k}}$. Assume two positive eigenvalues of $\tau^3 H_{\mathbf{k}}$, spanning a subspace $\mathcal{P}_0$, are separated from the rest of the spectrum by nonzero gaps. In the neighborhood of $\mathbf{k}_0$, we can write

$$\tau^3 H_{\mathbf{k}} = \tau^3 H_{\mathbf{k}_0} + \tau^3 \left(H_{\mathbf{k}} - H_{\mathbf{k}_0} \right), \tag{4.16}$$

with the second term on the right-hand side acting as a "small" perturbation of the first term.

For every $\mathbf{k}$ in a sufficiently small neighborhood of $\mathbf{k}_0$, the SW transformation for Krein-Hermitian Hamiltonians presented in the previous section gives an effective Hamiltonian $P_0(\widetilde{\tau^3 H_{\mathbf{k}}})P_0$ (as defined in and after Eq. (4.13)) for the subspace $\mathcal{P}_0$, which faithfully reproduces the band structure. We reiterate that the SW method is especially well suited for the study of band touchings and their neighborhoods. Since $\mathcal{P}_0$ contains only positive-signature bands, the effective Hamiltonian is Hermitian. In the eigenbasis of $\tau^3 H_{\mathbf{k}_0}$, it is given by

$$P_0(\widetilde{\tau^3 H_{\mathbf{k}}})P_0 = d^0_{\mathbf{k}} \sigma^0 + \vec{d}_{\mathbf{k}} \cdot \vec{\sigma}, \tag{4.17}$$

where $(\sigma^0, \vec{\sigma})$ are the Pauli matrices in the two-dimensional subspace $\mathcal{P}_0$ and where $d^\mu_{\mathbf{k}}, \mu \in \{0, 1, 2, 3\}$ are real.

Importantly, the expressions for the effective Krein-Hermitian Hamiltonian (Appendix 4.A) reveal that if $H_{\mathbf{k}}$ is real, so is the effective Hamiltonian $P_0(\widetilde{\tau^3 H_{\mathbf{k}}})P_0$, forcing the term proportional to σ^2 to vanish, and meaning that the two bands touch iff the functions $d^1_{\mathbf{k}}$ and $d^3_{\mathbf{k}}$ vanish simultaneously. In that case, except at high-symmetry momenta, band touchings that are stable against symmetry-preserving perturbations will generically have a codimension of two, with twofold degeneracy. Otherwise, they would have a codimension of three, with twofold degeneracy.

4.4.2 Constraint of magnetic inversion symmetry and examples

If a spin Hamiltonian and its classical ground state are invariant under a symmetry transformation, then the Bloch coefficient matrix $H_{\mathbf{k}}$ of the associated magnon Hamiltonian admits a representation of that symmetry (see Appendix 4.C for a general discussion). Magnetic inversion symmetry plays a prominent role in the present discussion, and Fig. 4.2(a) depicts a pair of spins that are left invariant by magnetic inversion symmetry: spatial inversion interchanges the spins (while leaving the spin direction unaffected), and time reversal reverses the spin directions, returning the system to its initial configuration. Hence, provided the spin Hamiltonian has only terms even in spin operators, magnetic inversion symmetry will

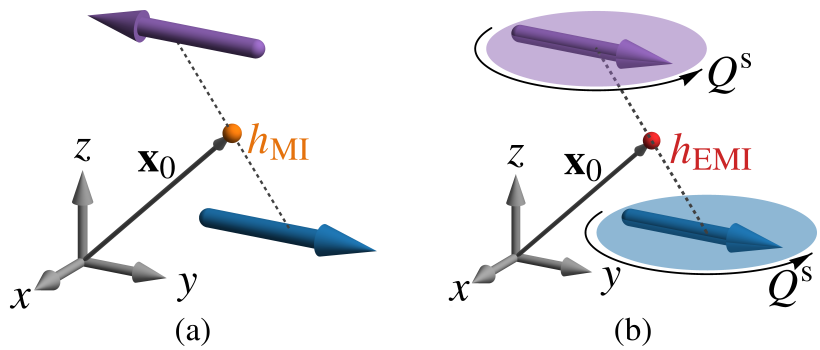

Figure 4.2: (a) Schematic depiction of spins left invariant by a magnetic inversion symmetry $h_{\mathrm{MI}} = \{P|2\mathbf{x}_0\}T$ whose inversion center, shown in orange, is located at $\mathbf{x}_0$. (b) Spins left invariant by an effective magnetic inversion symmetry $h_{\mathrm{EMI}} = \{P; Q^{\mathrm{s}}|2\mathbf{x}_0\}T$ whose inversion center, shown in red, is located at $\mathbf{x}_0$. The spin rotation Q^{s}, which is only allowed if the spin Hamiltonian lacks certain SOCs, effectively "undoes" the effect of time reversal and returns the spins to their initial configuration, as detailed in Sec. 4.4.2.2.

have an implementation on $H_{\mathbf{k}}$ in such a scenario. In Seitz notation, a magnetic inversion symmetry with inversion center $\mathbf{x}_0$ (see Fig. 4.2(a)) takes the form $h_{\mathrm{MI}} = \{P|2\mathbf{x}_0\}T$ [83], where P denotes inversion with respect to the origin and T denotes time reversal. The translational part $2\mathbf{x}_0$ depends on the choice of origin and will mostly be unimportant in the present discussion.

As shown in Appendix 4.C, the constraint due to magnetic inversion in a magnon system is generally $H_{\mathbf{k}} = V^\dagger H_{\mathbf{k}}^* V$, where V is a paraunitary, unitary, particle-hole symmetric, and also symmetric matrix. This implies that $VV^* = +\mathbb{1}$, i.e., that magnetic inversion squares to $+1$ [16]; indeed, this must be the case for integer-spin excitations [302, 312], like the magnon. Furthermore, because $VV^* = +\mathbb{1}$, there must exist a basis in which the constraint takes the simple form $H_{\mathbf{k}} = H_{\mathbf{k}}^*$; see Appendix 4.C.

This basis, however, may not coincide with that in which $H_{\mathbf{k}}$ is maximally block-diagonalized into symmetryless blocks. If, under magnetic inversion, a symmetryless block $H_{\mathbf{k}}^a$ is mapped to itself ($H_{\mathbf{k}}^a = \tilde{V}^\dagger H_{\mathbf{k}}^{a*} \tilde{V}$ for some $\tilde{V}$), then magnetic inversion admits a representation within that block, and its generic band touchings are twofold degenerate and have codimension two instead of three. If two blocks $H_{\mathbf{k}}^a$ and $H_{\mathbf{k}}^{a'}$ are mapped to each other ($H_{\mathbf{k}}^a = \tilde{V}^\dagger H_{\mathbf{k}}^{a'*} \tilde{V}$ for some $\tilde{V}$), then they have the same energy eigenvalues, so their generic band touchings are fourfold degenerate with codimension three.

We now discuss some examples of magnon band touchings from the literature and illustrate how the codimension approach can be useful for quickly understanding the generic features.

4.4.2.1 Magnetic inversion and spin-rotation symmetries

The scenario considered in Ref. 303 is that of a 3D collinear antiferromagnetic spin system with magnetic inversion symmetry (see Fig. 1 of Ref. 303), with and without spin-rotation

symmetry. If the system has a spin-rotation symmetry about an axis, say $\hat{z}$, the excitations conserve the quantum number S_z. This is a $\mathbf{k}$-independent symmetry that allows a block-diagonalization of $H_{\mathbf{k}}$,

$$H_{\mathbf{k}} = \left[\begin{array}{c|c} H_{\mathbf{k}}^{+} & \\ \hline & H_{\mathbf{k}}^{-} \end{array}\right], \tag{4.18}$$

into sectors corresponding to excitations with $S_z = \pm 1$ [303] (see Appendix 4.C for details). In this case, magnetic inversion interchanges $+\hat{z}$ spins and $-\hat{z}$ spins, hence mapping the two blocks to each other and making the spectrum everywhere doubly degenerate. Then, assuming the blocks are symmetryless, the generically occurring band touchings are fourfold-degenerate isolated points; as explained in Ref. 303, they are made up of Weyl points with opposite monopole charges, making them Dirac points.

If the spin-rotation symmetry is broken by certain spin-orbit-coupling (SOC) terms in the Hamiltonian or by canting of the spins, but the magnetic inversion symmetry is preserved, then $H_{\mathbf{k}}$ can no longer be block-diagonalized into definite-spin sectors. Assuming $H_{\mathbf{k}}$ is a symmetryless block, its generic gapless manifolds are doubly-degenerate lines.

Of course, an analysis based simply on the codimension of the generic gapless manifolds does not tell the whole story [302]. For instance, it does not capture the $\mathbb{Z}_2$ monopole charge carried by the the Dirac nodes and gapless lines in this example [303], which explains why the two can evolve into each other, but cannot—contrary to other gapless lines—gap out without encountering an opposite charge [60, 302, 320]. Nonetheless, the simplicity of this analysis makes it complementary to other approaches.

In Ref. 303, the authors propose Cu_3TeO_6 as a material nearly at the cusp between these two scenarios. Indeed, Heisenberg interactions (which have spin-rotation symmetry) appear to be dominant in this compound; thus, in the absence of subdominant interactions, we expect Dirac points in the band structure. However, weak SOC likely breaks the spin-rotation symmetry and deforms the Dirac points to small gapless lines. Indeed, Dirac points have recently been observed in experiment, though they may be gapless lines that are too small to be resolved with current resolutions [304, 305].

4.4.2.2 Effective magnetic inversion and Heisenberg ferromagnets

We can contrast the scenario of Sec. 4.4.2.1 with one in which the magnetic inversion symmetry is replaced with an *effective* magnetic inversion symmetry that leaves the spin direction unchanged, an example of which is considered in Ref. 324. Such a symmetry is possible in the absence of certain SOCs, and necessarily acts differently in position space and spin space. Using a modified Seitz notation (see Appendix 4.C), we denote the effective magnetic inversion as $h_{\mathrm{EMI}} = \{P; Q^{\mathrm{s}} | 2\mathbf{x}_0\}T$; here, Q^{s} is a *spin* rotation by π about some suitable axis that serves to return the spin to its original direction and undo the effect of time reversal on the classical order, as depicted schematically in Fig. 4.2(b).

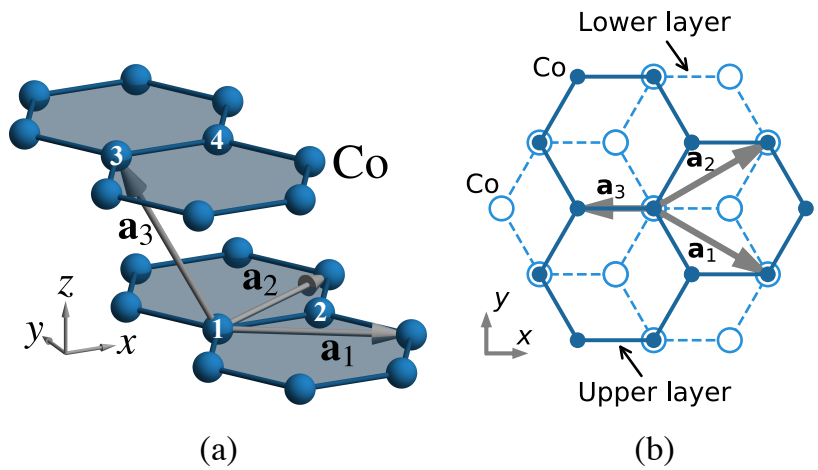

Figure 4.3: Crystal structure of the magnetic Co^{2+} ions in $CoTiO_3$. Two layers are shown, both as a 3D illustration in panel (a) and as a projection along the stacking direction $\hat{z}$ in panel (b). The crystal's primitive lattice vectors $\mathbf{a}_1$, $\mathbf{a}_2$, and $\mathbf{a}_3$ are shown; the magnetic order (depicted in Fig. 4.4) doubles the third one to $2\mathbf{a}_3$. Sublattice indices 1, 2, 3, and 4 of the magnetic unit cell are shown in panel (a).

If spin-rotation symmetry about an axis is present, the Bloch Hamiltonian can again be block-diagonalized into spin-conserving sectors, as in Eq. (4.18). However, rather than interchanging the sectors, h now maps each sector to itself. Therefore, the intra-sector band touchings will generically have codimension two and twofold degeneracy (assuming each sector is symmetryless). Of course, inter-sector band touchings can also occur; since they involve bands with different spin quantum numbers, their touchings will generically be of codimension one with twofold degeneracy.

On the other hand, if the spin-rotation symmetry is broken, leaving the Bloch Hamiltonian symmetryless, any codimension-one band touchings either gap out or are reduced to codimension two.

The situation considered in Ref. 324, a spin model with Heisenberg interactions and ferromagnetic order, falls within this category. The effective magnetic inversion $h = \{P; R(\pi\hat{n})|\boldsymbol{\tau}\}T$, where $R(\pi\hat{n})$ is a spin rotation of π about an axis $\hat{n}$ perpendicular to the spin direction and $\boldsymbol{\tau}$ is some origin-dependent translation, protects the nodal lines. As the authors mention, certain SOCs, like the Dzyaloshinskii-Moriya (DM) interaction, would gap out the nodal lines completely or downgrade them to Weyl points. In our present language, it is those interactions that are incompatible with the symmetry h that will generically gap out nodal lines.

4.4.2.3 Nodal lines in a stacked honeycomb quantum magnet

We next discuss $CoTiO_3$, an example of a stacked honeycomb quantum magnet that has been the object of recent interest. $CoTiO_3$ has an ilmenite structure and space group $R\bar{3}$: its magnetic Co^{2+} ions form stacked honeycomb layers with ABC-type stacking [306, 307, 325],

depicted in Fig. 4.3. It becomes magnetically ordered below $T_{\mathrm{N}} \approx 38\,\mathrm{K}$, with ferromagnetic order within each layer and antiferromagnetic stacking of the layers. The ordering direction is in the plane of the layers [306, 307, 325], as exemplified in Fig. 4.4(a). The onset of magnetic order considerably lowers the symmetry: the corresponding magnetic space group is $P_S\bar{1}$, which contains only inversions, magnetic inversions, and magnetic translations [83, 306, 307, 325].

The dominant exchange interactions are not rotation invariant about the ordering direction, since they have an easy-plane anisotropy [306, 307]. Hence, there is no approximate spin-rotation symmetry, and we expect gapless lines to be generically stable because of the magnetic inversion symmetry h_{MI} present in $P_S\bar{1}$. Indeed, seemingly gapless lines have been reported in recent experiments [306, 307].

4.4.2.4 XXZ model of a stacked honeycomb quantum magnet

Let us now consider a simple spin model for $CoTiO_3$ whose linear spin-wave theory has been found to capture all but the fine details of the magnon spectrum, including the observed gapless lines [306, 307]. It consists of effective spin-one-half moments on the Co^{2+} ions, coupled by easy-plane XXZ interactions; see Appendix 4.B for details.

The effect of including additional symmetry-allowed SOC terms, which are not rotationally symmetric about the $\hat{z}$ axis, is to eliminate certain extraneous symmetries of the XXZ interactions. The strength of the various spin interactions in $CoTiO_3$ and other honeycomb magnets, including Kitaev, Gamma, and DM interactions, is still a subject of active research [306, 307, 326, 327]. Therefore, rather than predicting the aspect of the gap closures in the presence of all such subdominant SOC terms, we merely focus on the general effects of lowering the symmetry. For this purpose, we use the DM interaction to illustrate the general effects of lowering the XXZ model symmetries, while recognizing that this is not the dominant SOC term relevant to $CoTiO_3$. The four magnetic Co^{2+} ions per magnetic unit cell (identified in Fig. 4.3(a)) [307, 325] give rise to four magnon bands, which we label 1, 2, 3, and 4 in order of increasing energy.

Pure XXZ model With no additional interactions present, the XXZ model has more symmetry than required by the magnetic space group $P_S\bar{1}$; in particular, the ordering direction can be freely rotated about the stacking axis $\hat{z}$ at no energy cost [307]. Consequently, for a fixed in-plane order (like that shown in Fig. 4.4(a)), the model's spin space group (see Appendix 4.C) includes the unitary symmetry $g = \{\mathbb{1}; R(\pi\hat{z})|\boldsymbol{\tau}_g\}$, where the translation $\boldsymbol{\tau}_g$ connects like sublattices of the honeycomb in adjacent layers. The coefficient matrix $H_{\mathbf{k}}$ can hence be block-diagonalized into two sectors corresponding to the eigenvalues of g, and the band touchings from different sectors are generically surfaces (codimension one) [13]. Indeed,

[13] Equivalently, the symmetry g allows a Fourier transform in a unit cell smaller than the magnetic unit cell, essentially "unfolding" the band structure [306, 307] (see also Appendix 4.C).

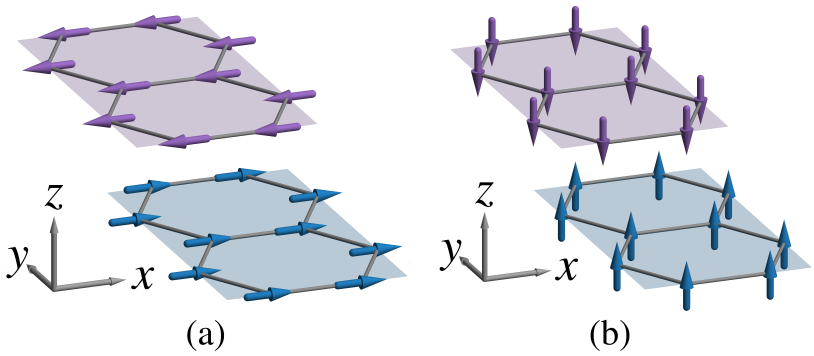

Figure 4.4: Magnetic orders in the stacked-honeycomb systems of Secs. 4.4.2.3 and 4.4.2.4. (a) When easy-plane interactions dominate, the order is in plane; the specific case of x-direction order, used in our numerical calculations, is shown. (b) When easy-axis interactions dominate, the order is parallel to the stacking direction $\hat{z}$.

with the parameters of Appendix 4.B, we find that gapless surfaces occur between bands 1 and 2 as well as between bands 3 and 4.

Another extraneous symmetry of the XXZ model is the effective magnetic inversion symmetry $h_{\mathrm{EMI}} = \{P; R(\pi\hat{z})|\boldsymbol{\tau}_h\}T$, distinct from the true magnetic inversion h_{MI} present in $P_S\bar{1}$. Indeed, h_{EMI} interchanges sites with the same ordering directions, while h_{MI} interchanges sites with opposite ordering directions. Both magnetic inversions work *within* the sectors that arise from the symmetry g, meaning either can stabilize magnon gapless lines, and both would have to be broken in order to destroy the gapless lines in the model, which occur between bands 2 and 3 (these are the gapless lines described in Refs. 306, 307). We emphasize, however, that h_{MI}, which is part of $P_S\bar{1}$, is model independent, presuming the magnetic space group has been accurately identified [307, 325].

Adding SOC terms The addition of the DM interaction breaks the symmetries g and h_{EMI} of the pure XXZ model (see Appendix 4.B for further details). The remaining magnetic inversion symmetry h_{MI} stabilizes gapless lines, which are shown in blue in Fig. 4.5 for the parameter set given in Appendix 4.B and with the specific x-direction order of Fig. 4.4(a). The gapless spirals already present in the pure XXZ model [306, 307] are qualitatively unchanged, and appear between bands 2 and 3 (Fig. 4.5(b)). This is expected, since here the DM interaction is a relatively small perturbation to the XXZ interaction, and the nodal lines are stable against small symmetry-preserving perturbations. On the other hand, the gapless lines between bands 1 and 2 (Fig. 4.5(a), blue lines) and 3 and 4 (Fig. 4.5(c), blue lines) are new and are the remnants of the gapless surfaces of the pure XXZ model, which have been reduced to lines by the DM interaction. We expect that including other symmetry-allowed subdominant interactions would significantly alter these gapless lines, though they would still appear as the remnants of the gapless surfaces as long as the subdominant interactions are small.

If the magnetic inversion symmetry h_{MI} were somehow broken, gapless lines would no

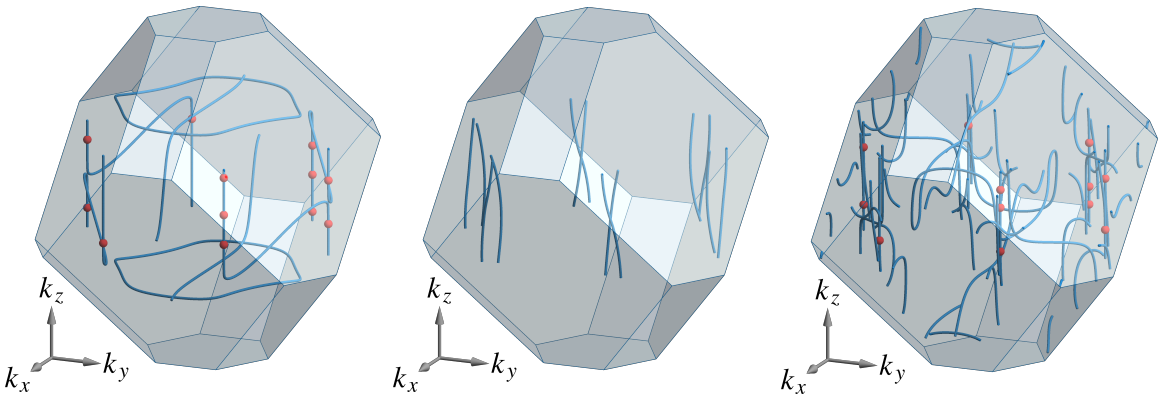

(a) Gap closings between bands 1 and 2. (b) Gap closings between bands 2 and 3. (c) Gap closings between bands 3 and 4.

Figure 4.5: Magnonic gap closings in a stacked honeycomb magnet modeled with an XXZ interaction together with a weak DM interaction, with parameter values given in Appendix 4.B. As argued in the text, the gap closings in the presence of magnetic inversion should generically be gapless lines, and indeed a plethora of gapless lines (shown in blue) are found. If magnetic inversion symmetry is broken (see main text and Appendix 4.B), the gap closings are Weyl points and are shown in red. Note that some of the gapless lines in (a) and (c) and all the lines in (b) reach the first-Brillouin-zone boundary and re-emerge at the opposite face.

longer be stable, and since no spin-rotation symmetry is present, the generically occurring band touching would become Weyl points. To demonstrate this, we introduce a small Zeeman field on one of the four atoms in the magnetic unit cell (see Appendix 4.B), hence explicitly breaking h_{MI}. (Incidentally, this perturbation also breaks inversion symmetry and the magnetic translation symmetry.) The remaining band touchings, all of which are Weyl points, are shown in red in Fig. 4.5: some of the gapless lines have been reduced to Weyl points, while others have fully disappeared.

Easy-axis XXZ model It is informative to contrast the easy-plane XXZ model discussed above with its easy-axis counterpart, in which the ordering direction is parallel to $\hat{z}$, with the order otherwise unchanged (see Fig. 4.4(b)). The magnetic space group associated with this order is $R_I\bar{3}$ [307], which also contains a model-independent magnetic inversion symmetry h_{MI}.

As in the easy-plane case, the easy-axis XXZ model gives rise to an additional, effective magnetic inversion symmetry h_{EMI}. Crucially, whereas the easy-plane case has no spin-rotation symmetry, the present model has spin-rotation symmetry about the $\hat{z}$ axis, meaning $H_{\mathbf{k}}$ can be block-diagonalized as in Eq. (4.18). Since h_{MI} interchanges the blocks $H_{\mathbf{k}}^{+}$ and $H_{\mathbf{k}}^{-}$, it causes them to have the same eigenvalues, making the bands everywhere at least doubly degenerate. Since h_{EMI} maps each block to itself, its effect is to generically give rise to gapless lines rather than gapless points.

The symmetries h_{MI} and h_{EMI} can be broken independently using different Zeeman fields on the four sublattices of the magnetic unit cell. The effects of breaking either or both of

these symmetries are presented in Table 4.1. The explicit form of the Hamiltonian and the parameters used in the numerics are presented in Appendix 4.B.

	h_{MI} unbroken	h_{MI} broken
h_{EMI} unbroken	• All bands are at least doubly degenerate because of h_{MI}. • Band touchings within each sector are generically *lines* because of h_{EMI}. • In numerics, gapless lines are observed between the two pairs of degenerate bands.	• The two sectors $H_{\mathbf{k}}^{+}$ and $H_{\mathbf{k}}^{-}$ are independent. Global double degeneracy is gone, and bands from different sectors generically cross on surfaces (codimension one). • Band touchings within each sector are generically *lines* because of h_{EMI}. • In numerics, gapless surfaces are observed between bands 2 and 3; gapless lines are observed between bands 1 and 2 and between bands 3 and 4.
h_{EMI} broken	• All bands are at least doubly degenerate because of h_{MI}. • Band touchings within each sector are generically *points*. • In numerics, *no* gapless lines are observed between the two pairs of degenerate bands.	• The two sectors $H_{\mathbf{k}}^{+}$ and $H_{\mathbf{k}}^{-}$ are independent. Global double degeneracy is gone, and bands from different sectors generically cross on surfaces (codimension one). • Band touchings within each sector are generically *points*. • In numerics, gapless surfaces were found between each pair of adjacent bands.

Table 4.1: The effects of the symmetries h_{MI} and h_{EMI} on the band touchings in the easy-axis stacked honeycomb XXZ model, which has spin-rotation symmetry about the $\hat{z}$ axis. See Sec. 4.4.2.4 for details and Appendix 4.B for parameter values.

* * *

The previous examples all pertain to band touchings at generic momenta, i.e., not at high-symmetry points of the Brillouin zone. Of course, as is commonly done in fermion systems [78, 302], these methods can also be applied specifically to high-symmetry lines or planes, which are left invariant by additional unitary symmetries [80]. Within these

manifolds, the additional symmetries can give rise to a block structure different from that at generic momenta.

We close the present section with the following remark: in Appendix 4.C, we show generally that unitary and antiunitary symmetries of the spin Hamiltonian that are compatible with the ground state have, respectively, Krein-unitary and Krein-antiunitary representations on the Krein-Hermitian single-particle magnon Hamiltonian. It is a deep result in quantum mechanics, known as Wigner's theorem, that the representations of physical symmetries in an ordinary Hilbert space can be either unitary or antiunitary [328]. The natural analogues of these operators in Krein spaces are Krein-unitary and Krein-antiunitary operators, respectively. However, the extension of Wigner's theorem to indefinite metric spaces [311] turns out to be richer than its Hilbert-space counterpart: in addition to Krein-unitary and Krein-antiunitary representations, two other possible types of representations arise, called Krein-pseudounitary and Krein-antipseudounitary, which have no analogue in ordinary Hilbert spaces. Whether such exotic symmetry representations arise in magnon or other bosonic BdG Hamiltonians and what physical consequences they may have are interesting questions left for future work.

4.5 Conclusion

In summary, after reviewing Krein-Hermitian Hamiltonians, particularly those arising as single-particle bosonic BdG Hamiltonians, we formulated a Krein-unitary SW transformation, paying special attention to the consequences of Krein stability theory and to the form of the effective reduced Hamiltonian. For simplicity, we assumed the Krein metric η is diagonal with entries ± 1. We found that if the unperturbed Hamiltonian K^0 is *within* a dynamically stable phase, then for sufficiently small perturbations, the effective Hamiltonian for a subspace of interest $\mathcal{P}_0$, given by $P_0 \tilde{K} P_0$, is dynamically stable and Krein Hermitian with respect to the metric $P_0 \eta P_0$. If the subspace of interest is composed only of positive-signature states, then the effective Hamiltonian is Hermitian. Also, if the (perturbed) Hamiltonian is purely real, then so is the effective Hamiltonian.

We argued that, in a translation-invariant Krein-Hermitian system, the SW transformation we formulated justifies the description of adjacent bands by reduced effective Hamiltonians, at least locally in momentum space. For a single-particle bosonic Hamiltonian $\tau^3 H_{\mathbf{k}}$ with $H_{\mathbf{k}_0} > 0$, a subset of contiguous positive-energy bands that is gapped from the rest of the spectrum near $\mathbf{k}_0$ can locally be described by a Hermitian reduced Hamiltonian. In particular, by considering two adjacent positive-energy bands, the generic codimension of band touchings is easily predicted, much as for Hermitian Hamiltonians. We then reviewed this line of reasoning in the context of magnon systems using examples from the literature, and emphasizing differences with electron systems.

In the linear spin-wave approximation, which we have adopted here, interaction between

the Holstein-Primakoff bosons are neglected and the eigenstates of the quadratic Hamiltonian are taken to be long-lived quasiparticles. This simplification works well for many magnetic materials [329], though it can fail even at zero temperature for systems with strong quantum fluctuations [329], [330]. Systems in which magnon interactions play an essential role are at the forefront of the field of topological magnons [330]. On the other hand, whereas electrons can be spinless only in an approximate sense, for magnons and other bosonic particles, space-time inversion truly squares to +1 regardless of additional material details [331].

Acknowledgements

This research was funded by the Natural Sciences and Engineering Research Council of Canada and the Canadian Institute for Advanced Research. G. M. thanks the *Fonds de recherche du Québec – Nature et technologies* for its support. Computations were partly performed on the Niagara supercomputer at the SciNet HPC Consortium [332, 333], part of Compute Ontario and the Digital Research Alliance of Canada. SciNet is funded by the Canada Foundation for Innovation; the Government of Ontario; Ontario Research Fund – Research Excellence; and the University of Toronto.

Appendix 4.A Details of perturbative SW transformation

This section provides more details on the perturbatively defined transformation presented in Sec. 4.3.2. The presentation follows that of Ref. 295, adapting it to Krein-Hermitian matrices.

We seek an effective Hamiltonian $\tilde{K}$ that is block diagonal in the subspace $\mathcal{P}_0$, meaning $\tilde{K}_\mathrm{o} = 0$, and that reproduces the spectrum of K order by order in the perturbation $\epsilon K'$ (see Eq. (4.14)). We assume that there exists a skew-Krein-unitary $W = -W^\sharp$ that block-diagonalizes the perturbed Hamiltonian K order by order in the perturbation $\epsilon K'$, and later confirm our assumption by establishing that explicit expressions for such a W can be found to all orders.

We further assume that W is block off-diagonal; i.e., $W_\mathrm{b} = 0$. Because of this, $[A_\mathrm{b}, W]$ is purely block off-diagonal and $[A_\mathrm{o}, W]$ is purely block diagonal for any A. Hence, the transformed Hamiltonian can be split into block-diagonal and block-off-diagonal parts:

$$\tilde{K}_\mathrm{b} = \sum_{l=0}^{+\infty} \frac{1}{(2l)!}[K_\mathrm{b}, W]^{(2l)} + \sum_{l=0}^{+\infty} \frac{1}{(2l+1)!}[K_\mathrm{o}, W]^{(2l+1)}, \tag{4.19a}$$

$$\tilde{K}_\mathrm{o} = \sum_{l=0}^{+\infty} \frac{1}{(2l)!}[K_\mathrm{o}, W]^{(2l)} + \sum_{l=0}^{+\infty} \frac{1}{(2l+1)!}[K_\mathrm{b}, W]^{(2l+1)}, \tag{4.19b}$$

where

$$[A,B]^{(l)} := [\ldots[[A,\underbrace{B],B]\ldots,B}_{l \text{ repetitions}}]. \tag{4.20}$$

We then further constrain the generating matrix W by demanding that $\tilde{K}_{\mathrm{o}} = 0$ order by order in the perturbation $\epsilon K'$, making the transformed Hamiltonian $\tilde{K} = \tilde{K}_{\mathrm{b}}$ purely block diagonal. Letting $W = \epsilon W^{(1)} + \epsilon^2 W^{(2)} + \ldots$, this requirement leads to the constraints of Eq. (4.15). As noted in the main text, these constraints are compatible with the assumption that W is skew-Krein-Hermitian to all orders.

Working in the eigenbasis of K^0, $K^0 t_i = E_i^0 t_i$, Eq. (4.15) can be solved order by order. For instance,

$$\begin{aligned} [K^0, W^{(1)}] &= -K'_{\mathrm{o}} \\ \Leftrightarrow \sum_c \left(K^0_{ac} W^{(1)}_{cb} - W^{(1)}_{ac} K^0_{cb}\right) &= -(K'_{\mathrm{o}})_{ab} \\ \Leftrightarrow \left(E^0_a - E^0_b\right) W^{(1)}_{ab} &= -(K'_{\mathrm{o}})_{ab}. \end{aligned} \tag{4.21a}$$

Letting m index states in $\mathcal{P}_0$ and l index states not in $\mathcal{P}_0$ (or vice versa), we may then write

$$W^{(1)}_{ml} = -\frac{K'_{ml}}{E^0_m - E^0_l}, \qquad W^{(1)}_{mm'} = W^{(1)}_{ll'} = 0. \tag{4.21b}$$

By the same token, one can find the expressions to all orders:

$$\begin{aligned} W^{(2)}_{ml} &= \frac{1}{E^0_m - E^0_l}\left(\sum_{m'} \frac{K'_{mm'} K'_{m'l}}{E^0_{m'} - E^0_l} - \sum_{l'} \frac{K'_{ml'} K'_{l'l}}{E^0_m - E^0_{l'}}\right) \\ &\vdots \end{aligned} \tag{4.22}$$

Using these expressions and that for $\tilde{K} = \tilde{K}_{\mathrm{b}}$, we find the effective Hamiltonian $P_0 \tilde{K} P_0 = P_0\big(\sum_{l=0}^{+\infty} \epsilon^l \tilde{K}^{(l)}\big) P_0$, whose matrix elements are $\tilde{K}_{mm'}$, order by order:

$$\tilde{K}^{(0)}_{mm'} = K^0_{mm'}, \tag{4.23a}$$

$$\tilde{K}^{(1)}_{mm'} = K'_{mm'}, \tag{4.23b}$$

$$\tilde{K}^{(2)}_{mm'} = \frac{1}{2}\sum_l K'_{ml} K'_{lm'} \left(\frac{1}{E^0_m - E^0_l} + \frac{1}{E^0_{m'} - E^0_l}\right), \tag{4.23c}$$

$$\vdots$$

The zeroth- and first-order expressions are manifestly Krein Hermitian with respect to $P_0 \eta P_0$; the higher orders, which involve mixing with states outside $\mathcal{P}_0$, are too, as can be seen using $K'_{ab} = \eta_{aa} K'^{\,*}_{ba} \eta_{bb}$ and the fact that η is diagonal with entries ± 1.

The formulae for $W^{(j)}$ and $\tilde{K}^{(j)}$ at all orders have the same form as those for a Hermitian

Hamiltonian, more of which are given in Refs. 295 and 294. The expansion is controlled as long as the perturbation is small compared to energy separations between states in $\mathcal{P}_0$ and states outside $\mathcal{P}_0$.

Appendix 4.B Details and parameter values for XXZ model

This appendix provides more details on the XXZ spin model and parameter values used in Sec. 4.4.2.4. As explained in the main text, it is based on models of $CoTiO_3$ wherein effective spin-one-half moments at each Co^{2+} ion (seen in Fig. 4.3) are coupled by XXZ interactions [306, 307]. In general, the Hamiltonian has the form

$$H_{\mathrm{XXZ}} = \sum_{i<j} \left(J_{ij} \left(S_i^x S_j^x + S_i^y S_j^y \right) + J_{ij}^{\perp} S_i^z S_j^z \right), \tag{4.24}$$

where i and j label spins and " $i < j$ " indicates that pairs of spins are not double counted. In the stacked honeycomb geometry under study, the $\hat{z}$ direction is taken to be the stacking direction (see Fig. 4.3). Hence, an XXZ interaction is of easy plane if $|J| > |J^{\perp}|$, and of easy axis if $|J| < |J^{\perp}|$; the magnetic ground-state order depends on the relative strength of the nonzero interactions and their coordination numbers.

Easy plane Our choice of which spins to couple with the interactions of Eq. (4.24) is loosely based on Refs. 306, 307, which model the magnon dispersion of $CoTiO_3$. An additional, weak coupling, J_9, is included to avoid accidental degeneracies along six lines in the Brillouin zone [14]. The couplings are as follows:

- If i and j are NN in-plane spins, $J_{ij} =: J_1 = -1$ and $J_{ij}^{\perp} =: J_1^{\perp} = 0.25\, J_1$ (see Ref. 306 for schematic representation);
- If i and j are next-nearest-neighbor (NNN) sites in adjacent layers, $J_{ij} =: J_2 = 0.5$ and $J_{ij}^{\perp} =: J_2^{\perp} = 0.25\, J_2$ (see Ref. 306);
- If i and j are NN sites in adjacent layers, $J_{ij} =: J_3 = 0.5$ and $J_{ij}^{\perp} =: J_3^{\perp} = 0.25\, J_3$ (see Ref. 306);
- If i and j are NN sites three layers apart, $J_{ij} =: J_9 = 0.02$ and $J_{ij}^{\perp} =: J_9^{\perp} = J_9$.

With these parameter values, the magnetic order is manifestly in plane, with ferromagnetic order within each layer and antiferromagnetically stacked layers. The ordering direction is chosen to be $\hat{x}$ (see Fig. 4.4(a)), and the Holstein-Primakoff transformation is carried out as shown in Appendix 4.C.

[14] See Supplementary Figure 4 of Ref. 307 for a depiction of these lines, which, as explained in the reference, project onto the corner K points of the 2D hexagonal Brillouin zone.

Easy-plane XXZ with DM As explained in Sec. 4.4.2.4, a weak DM interaction,

$$H_{\mathrm{DM}} = \sum_{i<j} \mathbf{D}_{ij} \cdot (\mathbf{S}_i \times \mathbf{S}_j)\,, \tag{4.25}$$

is added to the easy-plane XXZ model to break certain extraneous symmetries of the pure XXZ model.

In the space group $R\bar{3}$ of the stacked honeycomb $CoTiO_3$, the geometry of which we are using here, inversion centers forbid DM interactions on the intra-layer NN bonds. Hence, the simplest choice is to include it on the intra-layer NNN bonds; this leaves the magnetic order unchanged. The vector $\mathbf{D}_{ij}$ on one such bond is not constrained by symmetry; we choose it to be in the $\hat{x}$-$\hat{y}$ plane and perpendicular to the bond direction, pointing toward the center of each hexagonal plaquette, and with magnitude 0.25. The interactions on different bonds are constrained by the threefold rotation, inversion, and translation symmetries of $R\bar{3}$. The gapless lines of the associated linear spin-wave dispersion are represented in Fig. 4.5.

In order to break the magnetic inversion symmetry h_{MI} and destabilize the gapless lines, a Zeeman field $\mathbf{B}_1 = B_1\hat{x}$, with $B_1 = 0.0008$, is introduced on sublattice 1 in the magnetic unit cell (see Fig. 4.3), in the direction of the ground-state magnetic moment. This lifts the line degeneracies, leaving behind gapless points, as shown in Fig. 4.5.

Easy-axis XXZ In Sec. 4.4.2.4, we consider an easy-axis version of the model of Eq. (4.24), using the following parameters:

- If i and j are NN in-plane spins, $J_{ij} =: J_1 = -1$ and $J_{ij}^{\perp} =: J_1^{\perp} = 1.5\,J_1$;
- If i and j are NNN sites in adjacent layers, $J_{ij} =: J_2 = 0.5$ and $J_{ij}^{\perp} =: J_2^{\perp} = 1.5\,J_2$;
- If i and j are NN sites in adjacent layers, $J_{ij} =: J_3 = 0.5$ and $J_{ij}^{\perp} =: J_3^{\perp} = 1.5\,J_3$;
- If i and j are NN sites three layers apart, $J_{ij} =: J_9 = 0.02$ and $J_{ij}^{\perp} =: J_9^{\perp} = J_9$.

With these values, the magnetic order is clearly parallel to the stacking direction $\hat{z}$, with ferromagnetic order within each layer and antiferromagnetically stacked layers (Fig. 4.4(b)). The Holstein-Primakoff transformation is carried out as shown in Appendix 4.C.

In the results presented in the main text, Zeeman fields pointing along the moments are used to selectively break the symmetries h_{MI} and h_{EMI}. Labelling the four sublattices in the magnetic unit cell as shown in Fig. 4.3, the Zeeman fields are $\mathbf{B}_1 = B_1\hat{z}$, $\mathbf{B}_2 = B_2\hat{z}$, $\mathbf{B}_3 = -B_3\hat{z}$, and $\mathbf{B}_4 = -B_4\hat{z}$. Since h_{MI} constrains $B_1 = B_4$ and $B_2 = B_3$, and h_{EMI} constrains $B_1 = B_2$ and $B_3 = B_4$, the symmetries can be selectively broken in the following way:

- $B_1 = B_2 = 0.01$ and $B_3 = B_4 = 0$ to break h_{MI};
- $B_1 = B_3 = 0.01$ and $B_2 = B_4 = 0$ to break h_{EMI};
- $B_1 = B_3 = 0.01$ and $B_2 = B_4 = 0.03$ to break both h_{MI} and h_{EMI}.

Appendix 4.C Implementation of symmetries in magnon Hamiltonians

In this appendix, we provide an overview of how symmetries of a spin Hamiltonian translate to symmetries of the magnon Hamiltonian in a compatible ordered state. The spin Hamiltonians we consider describe localized moments in a crystal lattice and, accordingly, have the translational symmetry of the lattice.

We highlight the constraints that unitary and antiunitary symmetries place on the single-particle Bloch Hamiltonian (Eqs. (4.44) and (4.54)). We show that, in the right basis, magnetic inversion symmetry constrains the single-particle magnon Hamiltonian to be purely real.

4.C.1 Overview

The *spin space group* of a spin Hamiltonian together with a compatible classical ground state is the set of symmetries of the Hamiltonian which also leave the classical order invariant [83, 334–336]. Such symmetries have a well-defined implementation in the magnon Hamiltonian, which describes excitations above a specific classical ground state. Symmetries of the spin space group come in two types: those that include the operation of time reversal and those that do not [83, 279], which are represented, respectively, by Krein-antiunitary and Krein-unitary transformations of the single-particle magnon Hamiltonian [311], as shown below. Time reversal alone is never part of the spin space group.

Spin space groups are closely related to, though distinct from, *magnetic space groups*: a magnetic space group is the symmetry group of a crystal structure endowed with a magnetic order [83]. For example, since an effective spin Hamiltonian can have more symmetry than the physical system it models, the spin space group may contain symmetries not present in the magnetic space group. In particular, unlike the magnetic space group, the spin space group can have symmetries that act differently on spin and position space. We will denote such operations using a modified Seitz notation [83]: $g = \left\{Q_g; Q_g^{\mathrm{s}} \,|\boldsymbol{\tau}_g\right\}$, where the first entry denotes the O(3) operation acting in position space, the second entry denotes the O(3) operation acting on spin, and the third denotes the translation in position space. Given a spin labeled i, we refer to the site to which i is mapped by (the spatial part of) g as $g(i)$: $\mathbf{x}_{g(i)} = \{Q_g|\boldsymbol{\tau}_g\}\,\mathbf{x}_i = Q_g\mathbf{x}_i + \boldsymbol{\tau}_g$.

We will find that in the local frame, transformations in the spin space group are of the form

$$\tilde{\mathbf{S}}_i \to \tilde{\mathbf{S}}_i' = \left[\begin{array}{cc|c} * & * & 0 \\ * & * & 0 \\ \hline 0 & 0 & 1 \end{array}\right] \begin{bmatrix} \tilde{S}_j^x \\ \tilde{S}_j^y \\ \tilde{S}_j^z \end{bmatrix}. \tag{4.26}$$

Hence, these symmetry transformations mix together only the components transverse to the

local classical order.

4.C.2 Spin Hamiltonian

We begin with a spin Hamiltonian with a corresponding classical ground state. The order of the ground state may lower the symmetry of the system, giving rise to a *magnetic lattice* and a corresponding *magnetic unit cell*, which is potentially larger than the initial unit cell [83]. Spin interactions beyond bilinear order can also be included, and would not change our conclusions at the level of noninteracting bosons.

$$\hat{H} = \frac{1}{2}\sum_{ij} \mathbf{S}_i^\top M_{ij} \mathbf{S}_j - \sum_i \mathbf{B}_i^\top \mathbf{S}_i. \tag{4.27}$$

We may choose $M_{ij} = M_{ji}^\top$. Furthermore, the Hermiticity of $\hat{H}$ and the assumption of time-reversal symmetry (absent the Zeeman term) makes $M_{ij} = M_{ji}^\top$ real for all i and j.

Consider a classical ground state compatible with the spin Hamiltonian. To carry out the Holstein-Primakoff transformation, each spin is expressed in a local basis whose $\hat{\tilde{z}}$ direction (and quantization axis) is aligned with the classical ordering direction of that spin. Hence, we let

$$\mathbf{S}_i = R_i \tilde{\mathbf{S}}_i, \qquad \tilde{\mathbf{S}}_i = \begin{bmatrix} \tilde{S}_i^x & \tilde{S}_i^y & \tilde{S}_i^z \end{bmatrix}^\top, \tag{4.28}$$

where R_i is an appropriate SO(3) rotation matrix. There is, of course, freedom in the choice of R_i. The Hamiltonian becomes

$$\hat{H} = \frac{1}{2}\sum_{ij} \tilde{\mathbf{S}}_i^\top \tilde{M}_{ij} \tilde{\mathbf{S}}_j - \sum_i \tilde{\mathbf{B}}_i^\top \tilde{\mathbf{S}}_i, \tag{4.29a}$$

$$\begin{cases} \tilde{M}_{ij} \coloneqq R_i^\top M_{ij} R_j = \tilde{M}_{ji}^\top, \\ \tilde{\mathbf{B}}_i \coloneqq R_i^\top \mathbf{B}_i. \end{cases} \tag{4.29b}$$

The stability of the classical order implies that linear contributions (in $\tilde{S}_i^x$ and $\tilde{S}_i^y$) to the Hamiltonian vanish.

We now proceed to rewrite the spin operators in terms of Holstein-Primakoff bosons. Letting $\phi_i = \begin{bmatrix} b_i & b_i^\dagger \end{bmatrix}^\top$, in the linearized Holstein-Primakoff transformation, the spin operators become

$$\begin{cases} \tilde{S}_i^+ &= \sqrt{2S_i} b_i + \dots, \\ \tilde{S}_i^- &= \sqrt{2S_i} b_i^\dagger + \dots, \\ \tilde{S}_i^z &= S_i - b_i^\dagger b_i = S_i + \frac{1}{2} - \frac{1}{2}\phi_i^\dagger \phi_i, \end{cases} \tag{4.30}$$

where $\tilde{S}_i^\pm \coloneqq \tilde{S}_i^x \pm \mathrm{i}\tilde{S}_i^y$ are the raising and lowering operators in the local bases, and where S_i is the spin magnitude at site i, formally considered a large parameter controlling the expansion. This way of writing $\tilde{S}_i^z$ is key in ensuring it is invariant under symmetries.

Discarding terms beyond quadratic in boson operators, the linearized Hamiltonian takes the form

$$\hat{H} = E_{\mathrm{cl}} + \frac{1}{2}\sum_{ij} \phi_i^\dagger h_{ij} \phi_j + \mathcal{O}(\phi^3), \tag{4.31}$$

where E_{cl} is the classical energy and the h_{ij} are 2×2 coefficient matrices. Note that $h_{ji} = h_{ij}^\dagger$ as a consequence of $\tilde{M}_{ji} = \tilde{M}_{ij}^\top$. Furthermore, the particle-hole symmetry of h_{ij}, i.e., $h_{ij} = \tau^1 h_{ij}^* \tau^1$, stems from the reality of $\tilde{M}_{ij}$ and the symmetric way of writing $\tilde{S}_i^z$. This constraint leaves no redundancy in h_{ij}.

Quadratic boson Hamiltonian in Fourier space

The Fourier transformation is a paraunitary (and unitary) transformation that partially diagonalizes the Hamiltonian. Letting $i = (\mathbf{R}, \alpha)$, where $\mathbf{R}$ denotes the magnetic unit cell (of which there are N) and α denotes the magnetic sublattice (of which there are n),

$$\phi_{\mathbf{k}\alpha} \coloneqq \begin{bmatrix} b_{\mathbf{k}\alpha} \\ b_{-\mathbf{k}\alpha}^\dagger \end{bmatrix} = \frac{1}{\sqrt{N}} \sum_{\mathbf{R}} \mathrm{e}^{-\mathrm{i}\mathbf{k}\cdot\mathbf{x}_{\mathbf{R}\alpha}} \phi_{\mathbf{R}\alpha}, \tag{4.32a}$$

$$\phi_{\mathbf{R}\alpha} = \frac{1}{\sqrt{N}} \sum_{\mathbf{k}} \mathrm{e}^{\mathrm{i}\mathbf{k}\cdot\mathbf{x}_{\mathbf{R}\alpha}} \phi_{\mathbf{k}\alpha}. \tag{4.32b}$$

With this notation, the Hamiltonian becomes

$$\begin{aligned} \hat{H} &= E_{\mathrm{cl}} + \frac{1}{2}\sum_{ij} \phi_i^\dagger h_{ij} \phi_j \\ &= E_{\mathrm{cl}} + \frac{1}{2}\sum_{\mathbf{R}\mathbf{R}'} \sum_{\alpha\beta} \phi_{\mathbf{R}\alpha}^\dagger h_{\mathbf{R}\mathbf{R}';\alpha\beta} \phi_{\mathbf{R}'\beta}. \end{aligned} \tag{4.33}$$

Using the translational invariance of the magnetic lattice (and assuming the SO(3) matrices $R_i =: R_\alpha$ were chosen with the same translational invariance), we define $h_{\mathbf{R}-\mathbf{R}';\alpha\beta} \coloneqq h_{\mathbf{R}\mathbf{R}';\alpha\beta}$, as well as its Fourier transform

$$h_{\mathbf{k};\alpha\beta} \coloneqq \mathrm{e}^{-\mathrm{i}\mathbf{k}\cdot(\boldsymbol{\delta}_\alpha - \boldsymbol{\delta}_\beta)} \sum_{\mathbf{R}} \mathrm{e}^{-\mathrm{i}\mathbf{k}\cdot\mathbf{R}} h_{\mathbf{R};\alpha\beta}. \tag{4.34}$$

Note that $h_{ij} = h_{ji}^\dagger$ implies that $h_{\mathbf{k};\alpha\beta}^\dagger = h_{\mathbf{k};\beta\alpha}$, and that the particle-hole symmetry $h_{ij} = \tau^1 h_{ij}^* \tau^1$ manifests itself in momentum space as $\tau^1 h_{\mathbf{k};\alpha\beta}^* \tau^1 = h_{-\mathbf{k};\alpha\beta}$.

Finally, the magnon Hamiltonian becomes

$$\hat{H} = E_{\mathrm{cl}} + \frac{1}{2}\sum_{\mathbf{k}}\sum_{\alpha\beta}\phi^{\dagger}_{\mathbf{k}\alpha}h_{\mathbf{k};\alpha\beta}\phi_{\mathbf{k}\beta} \tag{4.35a}$$

$$= E_{\mathrm{cl}} + \frac{1}{2}\sum_{\mathbf{k}}\Phi^{\dagger}_{\mathbf{k}}H_{\mathbf{k}}\Phi_{\mathbf{k}}, \quad \Phi_{\mathbf{k}} := \begin{bmatrix}\phi_{\mathbf{k}A}\\ \phi_{\mathbf{k}B}\\ \vdots\end{bmatrix}, \tag{4.35b}$$

where we have introduced the spinor $\Phi_{\mathbf{k}}$ and the $2n \times 2n$ coefficient matrix $H_{\mathbf{k}}$, and where $\mathbf{k}$ is summed over momenta in the magnetic Brillouin zone [83]. The matrix $H_{\mathbf{k}}$ is Hermitian and (assuming the classical order is stable) positive semidefinite. Also, the PH symmetry now takes the form $\tau^1 H^*_{\mathbf{k}}\tau^1 = H_{-\mathbf{k}}$.

4.C.3 Unitary symmetries

Let g be a unitary symmetry of the spin space group, with unitary Hilbert-space implementation U_g. These are the operations of the spin space group that do not contain time reversal. In modified Seitz notation, we let $g = \left\{Q_g; Q^{\mathrm{s}}_g|\boldsymbol{\tau}_g\right\}$. Letting $\mathbf{S}'_i$ denote the transformed spin at site i,

$$\mathbf{S}'_i = U_g\mathbf{S}_iU^{\dagger}_g = (\det Q^{\mathrm{s}}_g)Q^{\mathrm{s}}_g\mathbf{S}_{g^{-1}i}. \tag{4.36}$$

Because spins are axial vectors, they transform with $(\det Q^{\mathrm{s}}_g)Q^{\mathrm{s}}_g$, which is always an SO(3) rotation matrix.

By definition of spin-space-group symmetries, the transformed spin $\mathbf{S}'_i$ has the same "classical" direction as $\mathbf{S}_i$; therefore, $\mathbf{S}'_i = R_i\tilde{\mathbf{S}}'_i$, like $\mathbf{S}_i = R_i\tilde{\mathbf{S}}_i$. This way, in the transformation in the local basis from $\tilde{\mathbf{S}}_i$ to $\tilde{\mathbf{S}}'_i$,

$$\tilde{\mathbf{S}}'_i = U_g\tilde{\mathbf{S}}_iU^{\dagger}_g = \tilde{Q}^i_g\tilde{\mathbf{S}}_{g^{-1}i}, \tag{4.37a}$$

$$\tilde{Q}^i_g := R^{\top}_i(\det Q^{\mathrm{s}}_g)Q^{\mathrm{s}}_gR_{g^{-1}i}, \tag{4.37b}$$

$\tilde{Q}^i_g$ is just a rotation about the local $\hat{\tilde{z}}$ axis.

Denoting the rotation angle at site i about the local $\hat{\tilde{z}}$ axis as θ^i_g, the ladder operators transform as $U_g\tilde{S}^{\pm}_iU^{\dagger}_g = \mathrm{e}^{\pm\mathrm{i}\theta^i_g}\tilde{S}^{\pm}_{g^{-1}i}$, while $U_g\tilde{S}^z_iU^{\dagger}_g = \tilde{S}^z_{g^{-1}i}$. The rotation angle θ^i_g is determined by g and the rotation matrices $\{R_i\}$. The bosons transform as

$$U_g\phi_iU^{\dagger}_g = u^i_g\phi_{g^{-1}i}, \tag{4.38a}$$

$$u^i_g = \begin{bmatrix}\mathrm{e}^{\mathrm{i}\theta^i_g} & \\ & \mathrm{e}^{-\mathrm{i}\theta^i_g}\end{bmatrix} = \tau^0\cos\theta^i_g + \mathrm{i}\tau^3\sin\theta^i_g. \tag{4.38b}$$

Note that in addition to being unitary, u^i_g is paraunitary (a unitary matrix that commutes with τ^3 is also paraunitary), so it gives valid boson operators. Furthermore, u^i_g is particle-

hole symmetric, $\tau^1 \left(u_g^i\right)^* \tau^1 = u_g^i$, so the transformed Hamiltonian will be particle-hole symmetric, as it must.

In Fourier space

Next, we consider the transformation in Fourier space. Although $\boldsymbol{\tau}_g$, the translational part of g, appears in the transformation for $\phi_{\mathbf{k}\alpha}$, it will not appear in the constraint on the Hamiltonian at the quadratic level. For notational convenience, let $(\mathbf{R}'\alpha') = g^{-1}(\mathbf{R}\alpha)$, meaning $\mathbf{x}_{\mathbf{R}'\alpha'} = \{Q_g|\boldsymbol{\tau}_g\}^{-1}\mathbf{x}_{\mathbf{R}\alpha}$.

We will use the fact that the rotation matrix $R_i =: R_\alpha$ (and hence $u_g^i =: u_g^\alpha$) does not depend on $\mathbf{R}$, but only on α, and also that the transformed sublattice index α' depends only on α (and not on $\mathbf{R}$). For this reason, we can think of the action of g (or g^{-1}) on the n sublattice indices α as a permutation.

$$\begin{aligned} U_g \phi_{\mathbf{k}\alpha} U_g^\dagger &= \frac{1}{\sqrt{N}} \sum_{\mathbf{R}} \mathrm{e}^{-\mathrm{i}\mathbf{k}\cdot\mathbf{x}_{\mathbf{R}\alpha}} \underbrace{U_g \phi_{\mathbf{R}\alpha} U_g^\dagger}_{u_g^\alpha \phi_{\mathbf{R}'\alpha'}} \\ &= \frac{u_g^\alpha}{\sqrt{N}} \sum_{\mathbf{R}} \mathrm{e}^{-\mathrm{i}\mathbf{k}\cdot\{Q_g|\boldsymbol{\tau}_g\}\mathbf{x}_{\mathbf{R}'\alpha'}} \phi_{\mathbf{R}'\alpha'} \\ &= \frac{u_g^\alpha}{\sqrt{N}} \sum_{\mathbf{R}} \mathrm{e}^{-\mathrm{i}\mathbf{k}\cdot(Q_g\mathbf{x}_{\mathbf{R}'\alpha'}+\boldsymbol{\tau}_g)} \phi_{\mathbf{R}'\alpha'}. \end{aligned} \tag{4.39}$$

We can sum over $\mathbf{R}'$ instead of $\mathbf{R}$ because the relation between $\mathbf{R}$ and $\mathbf{R}'$ is bijective:

$$\begin{aligned} U_g \phi_{\mathbf{k}\alpha} U_g^\dagger &= \mathrm{e}^{-\mathrm{i}\mathbf{k}\cdot\boldsymbol{\tau}_g} \frac{u_g^\alpha}{\sqrt{N}} \sum_{\mathbf{R}'} \mathrm{e}^{-\mathrm{i}\left(Q_g^\top \mathbf{k}\right)\cdot\mathbf{x}_{\mathbf{R}'\alpha'}} \phi_{\mathbf{R}'\alpha'} \\ &= \mathrm{e}^{-\mathrm{i}\mathbf{k}\cdot\boldsymbol{\tau}_g}\ u_g^\alpha\ \phi_{Q_g^\top \mathbf{k},\alpha'}. \end{aligned} \tag{4.40}$$

In terms of the $2n$-component spinor $\Phi_{\mathbf{k}}$,

$$\boxed{U_g \Phi_{\mathbf{k}} U_g^\dagger = \mathrm{e}^{-\mathrm{i}\mathbf{k}\cdot\boldsymbol{\tau}_g} V_g \Phi_{Q_g^\top \mathbf{k}},} \tag{4.41}$$

where V_g is a $2n \times 2n$ unitary, paraunitary, and particle-hole-symmetric (V_g, $\tau^1 \left(V_g\right)^* \tau^1 = V_g$) matrix:

$$V_g = C_g P_{g^{-1}} \otimes \tau^0 - \mathrm{i} S_g P_{g^{-1}} \otimes \tau^3. \tag{4.42}$$

In the above, $P_{g^{-1}}$ is the $n \times n$ permutation matrix for the permutation of sublattices $g^{-1}(\alpha)$, with components $P_{g^{-1}}^{\alpha\beta} = \delta^{\beta, g^{-1}(\alpha)}$, and C_g and S_g are $n \times n$ diagonal matrices with entries $\{\cos\theta_g^\alpha\}$ and $\{\sin\theta_g^\alpha\}$, respectively.

Finally, we find the transformed magnon Hamiltonian:

$$\begin{aligned} U_g \hat{H} U_g^\dagger &= E_{\text{cl}} + \frac{1}{2}\sum_{\mathbf{k}} \left(U_g \Phi_{\mathbf{k}}^\dagger U_g^\dagger\right) H_{\mathbf{k}} \left(U_g \Phi_{\mathbf{k}} U_g^\dagger\right) \\ &= E_{\text{cl}} + \frac{1}{2}\sum_{\mathbf{k}} \left(\Phi_{Q_g^\top \mathbf{k}}^\dagger V_g^\dagger\right) H_{\mathbf{k}} \left(V_g \Phi_{Q_g^\top \mathbf{k}}\right) \\ &= E_{\text{cl}} + \frac{1}{2}\sum_{\mathbf{k}} \Phi_{\mathbf{k}}^\dagger \; V_g^\dagger \; H_{Q_g \mathbf{k}} \; V_g \; \Phi_{\mathbf{k}}, \end{aligned} \tag{4.43}$$

so the constraint on $H_{\mathbf{k}}$ due to g is

$$\boxed{H_{\mathbf{k}} = V_g^\dagger \; H_{Q_g \mathbf{k}} \; V_g,} \tag{4.44}$$

or in terms of the single-particle magnon Hamiltonian $\tau^3 H_{\mathbf{k}}$,

$$\boxed{\tau^3 H_{\mathbf{k}} = V_g^\sharp \; \tau^3 H_{Q_g \mathbf{k}} \; V_g,} \tag{4.45}$$

making this a Krein-unitary transformation on the single-particle Hamiltonian.

For a unitary symmetry with $Q_g = \mathbb{1}$, the Nambu-Bloch Hamiltonian can be block-diagonalized at each $\mathbf{k}$ into sectors corresponding to the eigenvalues of V_g.

4.C.4 Antiunitary symmetries

Let h be an antiunitary symmetry in the spin space group. Such a transformation is made up of a spatial transformation (with unitary implementation U_h) along with time reversal. Let $\Theta_h = U_h T$ be the antiunitary operator that implements it in the Hilbert space. In modified Seitz notation, $h = \{Q_h; Q_h^{\text{s}} | \boldsymbol{\tau}_h\} T$. Since $\Theta_h^{-1} = T^{-1} U_h^\dagger$ and spin is odd under time reversal, we have

$$\begin{aligned} \mathbf{S}_i' &= \Theta_h \mathbf{S}_i \Theta_h^{-1} \\ &= U_h \underbrace{T \mathbf{S}_i T^{-1}}_{-\mathbf{S}_i} U_h^\dagger \\ &= -(\det Q_h^{\text{s}}) Q_h^{\text{s}} \mathbf{S}_{h^{-1} i}. \end{aligned} \tag{4.46}$$

Once again, $\mathbf{S}_i'$ has the same classical direction as $\mathbf{S}_i$, so $\mathbf{S}_i' = R_i \tilde{\mathbf{S}}_i'$, like $\mathbf{S}_i = R_i \tilde{\mathbf{S}}_i$; this is the key point that allows a well-defined implementation of h on the magnon Hamiltonian and enables us to write the transformation for $\tilde{\mathbf{S}}_i$:

$$\tilde{\mathbf{S}}_i' = \Theta_h \tilde{\mathbf{S}}_i \Theta_h^{-1} = \tilde{Q}_h^i \tilde{\mathbf{S}}_{h^{-1} i}, \tag{4.47a}$$

$$\tilde{Q}_h^i := -R_i^\top (\det Q_h^{\text{s}}) Q_h^{\text{s}} R_{h^{-1} i}. \tag{4.47b}$$

In this case, the transformation $\tilde{Q}_h^i$ is an improper rotation about the local $\hat{\tilde{z}}$ axis; i.e., an

$\mathcal{O}(3)$ matrix with determinant -1 that leaves the $\hat{\hat{z}}$ direction invariant.

Nevertheless, the ladder operators transform as $\Theta_h \tilde{S}_i^{\pm} \Theta_h^{-1} = \mathrm{e}^{\pm \mathrm{i}\theta_h^i} \tilde{S}_{h^{-1}i}^{\pm}$, while $\Theta_h \tilde{S}_i^z \Theta_h^{-1} = \tilde{S}_{h^{-1}i}^z$, where the parameter θ_h^i is determined by h and by the SO(3) matrices $\{R_i\}$. The bosons transform as

$$\begin{cases} \Theta_h \phi_i \Theta_h^{-1} & = u_h^i \phi_{h^{-1}i}, \\ \Theta_h \phi_i^\dagger \Theta_h^{-1} & = \phi_{h^{-1}i}^\dagger u_h^{i\,\dagger}, \end{cases} \tag{4.48a}$$

$$u_h^i = \begin{bmatrix} \mathrm{e}^{\mathrm{i}\theta_h^i} & \\ & \mathrm{e}^{-\mathrm{i}\theta_h^i} \end{bmatrix} = \tau^0 \cos\theta_h^i + \mathrm{i}\tau^3 \sin\theta_h^i. \tag{4.48b}$$

Like u_g^i, u_h^i is paraunitary, unitary, and particle-hole symmetric.

In Fourier space

Next, we consider the effect in Fourier space. Again, for notational convenience, we let $(\mathbf{R}'\alpha') = h^{-1}(\mathbf{R}\alpha)$, meaning $\mathbf{x}_{\mathbf{R}'\alpha'} = \{Q_h|\boldsymbol{\tau}_h\}^{-1}\mathbf{x}_{\mathbf{R}\alpha}$.

$$\begin{aligned} \Theta_h \phi_{\mathbf{k}\alpha} \Theta_h^{-1} &= \frac{1}{\sqrt{N}} \sum_{\mathbf{R}} \mathrm{e}^{\mathrm{i}\mathbf{k}\cdot\mathbf{x}_{\mathbf{R}\alpha}} \underbrace{\theta_h \phi_{\mathbf{R}\alpha} \theta_h^{-1}}_{u_h^\alpha \phi_{\mathbf{R}'\alpha'}} \\ &= \frac{u_h^\alpha}{\sqrt{N}} \sum_{\mathbf{R}} \mathrm{e}^{\mathrm{i}\mathbf{k}\cdot\{Q_h|\boldsymbol{\tau}_h\}\mathbf{x}_{\mathbf{R}'\alpha'}} \phi_{\mathbf{R}'\alpha'} \\ &= \frac{u_h^\alpha}{\sqrt{N}} \sum_{\mathbf{R}} \mathrm{e}^{\mathrm{i}\mathbf{k}\cdot(Q_h\mathbf{x}_{\mathbf{R}'\alpha'} + \boldsymbol{\tau}_h)} \phi_{\mathbf{R}'\alpha'} \\ &= \mathrm{e}^{\mathrm{i}\mathbf{k}\cdot\boldsymbol{\tau}_h} \frac{u_h^\alpha}{\sqrt{N}} \sum_{\mathbf{R}'} \mathrm{e}^{-\mathrm{i}\left(-Q_h^\top \mathbf{k}\right)\cdot\mathbf{x}_{\mathbf{R}'\alpha'}} \phi_{\mathbf{R}'\alpha'}, \end{aligned} \tag{4.49}$$

where in the last line, we have changed summation variable from $\mathbf{R}$ to $\mathbf{R}'$. Hence, we find

$$\Theta_h \phi_{\mathbf{k}\alpha} \Theta_h^{-1} = \mathrm{e}^{\mathrm{i}\mathbf{k}\cdot\boldsymbol{\tau}_h}\ u_h^\alpha\ \phi_{-Q_h^\top \mathbf{k},\alpha'}, \tag{4.50a}$$

$$\Theta_h \phi_{\mathbf{k}\alpha}^\dagger \Theta_h^{-1} = \mathrm{e}^{-\mathrm{i}\mathbf{k}\cdot\boldsymbol{\tau}_h}\ \phi_{-Q_h^\top \mathbf{k},\alpha'}^\dagger\ u_h^{\alpha\dagger}. \tag{4.50b}$$

In terms of the $2n$-component spinor $\Phi_{\mathbf{k}}$,

$$\boxed{\begin{aligned} \Theta_h \Phi_{\mathbf{k}} \Theta_h^{-1} &= \mathrm{e}^{\mathrm{i}\mathbf{k}\cdot\boldsymbol{\tau}_h}\ V_h\ \Phi_{-Q_h^\top \mathbf{k}}, && (4.51a) \\ \Theta_h \Phi_{\mathbf{k}}^\dagger \Theta_h^{-1} &= \mathrm{e}^{-\mathrm{i}\mathbf{k}\cdot\boldsymbol{\tau}_h}\ \Phi_{-Q_h^\top \mathbf{k}}^\dagger\ V_h^\dagger, && (4.51b) \end{aligned}}$$

where V_h is a $2n \times 2n$ unitary, paraunitary, and particle-hole-symmetric matrix:

$$V_h = C_h P_{h^{-1}} \otimes \tau^0 - \mathrm{i} S_h P_{h^{-1}} \otimes \tau^3, \tag{4.52}$$

where $P_{h^{-1}}$, C_h, and S_h are defined in analogy with the unitary case.

Finally, the transformed magnon Hamiltonian is

$$\begin{aligned}\Theta_h \hat{H} \Theta_h^{-1} &= E_{\mathrm{cl}} + \frac{1}{2}\sum_{\mathbf{k}} \left(\Theta_h \Phi_{\mathbf{k}}^\dagger \Theta_h^{-1}\right) H_{\mathbf{k}}^* \left(\Theta_h \Phi_{\mathbf{k}} \Theta_h^{-1}\right) \\ &= E_{\mathrm{cl}} + \frac{1}{2}\sum_{\mathbf{k}} \left(\Phi^\dagger_{-Q_h^\top \mathbf{k}} V_h^\dagger\right) H_{\mathbf{k}}^* \left(V_h \Phi_{-Q_g^\top \mathbf{k}}\right) \\ &= E_{\mathrm{cl}} + \frac{1}{2}\sum_{\mathbf{k}} \Phi_{\mathbf{k}}^\dagger \; V_h^\dagger \; H^*_{-Q_h \mathbf{k}} \; V_h \; \Phi_{\mathbf{k}},\end{aligned} \tag{4.53}$$

so the constraint on $H_{\mathbf{k}}$ due to h is

$$\boxed{H_{\mathbf{k}} = V_h^\dagger \; H^*_{-Q_h \mathbf{k}} \; V_h,} \tag{4.54}$$

or in terms of the single-particle magnon Hamiltonian $\tau^3 H_{\mathbf{k}}$,

$$\boxed{\tau^3 H_{\mathbf{k}} = V_h^\sharp \; \left(\tau^3 H_{-Q_h \mathbf{k}}\right)^* \; V_h,} \tag{4.55}$$

making this a *Krein-antiunitary* transformation on the single-particle Hamiltonian [311].

4.C.4.1 When is V_h symmetric?

Here, we identify necessary and sufficient conditions for $V_h = V_h^\top$ (or, equivalently, $V_h V_h^* = +1$).

First, since V_h is block diagonal in Nambu space, we can write it as a direct sum of its particle and hole sectors, $V_h = V_h^{\mathrm{p}} \oplus V_h^{\mathrm{h}}$; here, $(V_h^{\mathrm{p}})^{\alpha\beta} = \mathrm{e}^{-\mathrm{i}\theta_h^\alpha} \; \delta^{\beta, h^{-1}(\alpha)}$ and $V_h^{\mathrm{h}} = (V_h^{\mathrm{p}})^*$.

Necessary condition First, assume V_h is symmetric. Then,

$$\begin{aligned} &(V_h^{\mathrm{p}})^{\alpha\beta} \overset{!}{=} (V_h^{\mathrm{p}})^{\beta\alpha} \quad \forall\, \alpha, \beta \\ \Leftrightarrow \quad &\mathrm{e}^{-\mathrm{i}\theta_h^\alpha} \; \delta^{\beta, h^{-1}(\alpha)} \overset{!}{=} \mathrm{e}^{-\mathrm{i}\theta_h^\beta} \; \delta^{\alpha, h^{-1}(\beta)} \quad \forall\, \alpha, \beta. \end{aligned} \tag{4.56}$$

Since the equality of two numbers implies the equality of their absolute values, we have

$$\begin{aligned} \Rightarrow \quad &\left|\mathrm{e}^{-\mathrm{i}\theta_h^\alpha} \; \delta^{\beta, h^{-1}(\alpha)}\right| \overset{!}{=} \left|\mathrm{e}^{-\mathrm{i}\theta_h^\beta} \; \delta^{\alpha, h^{-1}(\beta)}\right| \quad \forall\, \alpha, \beta \\ \Leftrightarrow \quad &\delta^{\beta, h^{-1}(\alpha)} \overset{!}{=} \delta^{\alpha, h^{-1}(\beta)} \quad \forall\, \alpha, \beta \\ \Leftrightarrow \quad &\delta^{\beta, h^{-1}(\alpha)} \overset{!}{=} \delta^{\beta, h(\alpha)} \quad \forall\, \alpha, \beta \\ \Leftrightarrow \quad &h^{-1}(\alpha) \overset{!}{=} h(\alpha) \quad \forall\, \alpha \\ \Leftrightarrow \quad &h^2(\alpha) \overset{!}{=} \alpha \quad \forall\, \alpha. \end{aligned} \tag{4.57}$$

In other words, the permutation engendered on the sublattice indices by h must square to identity (called a *transposition*), i.e., it must be a permutation with only 1-cycles and 2-cycles.

Hence, the condition becomes

$$\left(\mathrm{e}^{-\mathrm{i}\theta_h^\alpha} - \mathrm{e}^{-\mathrm{i}\theta_h^\beta}\right)\delta^{\beta,h^{-1}(\alpha)} \overset{!}{=} 0 \qquad \forall\ \alpha,\beta. \tag{4.58}$$

- For $h^{-1}(\alpha) = \alpha$ (a 1-cycle), there is no constraint on $\mathrm{e}^{-\mathrm{i}\theta_h^\alpha}$.
- For $h^{-1}(\alpha) = \beta$ (and $h^{-1}(\beta) = \alpha$) (a 2-cycle), $\mathrm{e}^{-\mathrm{i}\theta_h^\alpha} = \mathrm{e}^{-\mathrm{i}\theta_h^\beta}$.

Hence, if V_h is symmetric, the permutation is a transposition (i.e., made up of 1-cycles and 2-cycles) and the phases $\mathrm{e}^{-\mathrm{i}\theta_h^\alpha}$ are the same within each cycle of the permutation.

Sufficient condition Assuming the permutation is a transposition and the phases $\mathrm{e}^{-\mathrm{i}\theta_h^\alpha}$ are the same within each cycle of the permutation, it is straightforward to see that V_h is symmetric.

4.C.5 Examples

4.C.5.1 Magnetic inversion symmetry

We consider magnetic inversion symmetry, i.e., $h = \{P|\boldsymbol{\tau}\}T$. In this case, $(\det R_h^{\mathrm{s}})R_h^{\mathrm{s}} = (\det P)P = \mathbb{1}$.

Consider a pair of sublattices α and α' related by h. We can always choose

$$\begin{cases} R_\alpha &= R(\eta_\alpha \hat{m}_\alpha), \\ R_{\alpha'} &= R((\eta_\alpha + \pi)\hat{m}_\alpha), \end{cases} \qquad \hat{m}_\alpha \perp \hat{z}, \tag{4.59}$$

where η_α and $\hat{m}_\alpha$ are an appropriate angle and unit vector, respectively. In the local frames, the transformation on the spins are

$$\tilde{Q}_h^\alpha = -R_\alpha^\top R_{\alpha'} = -R\left(\pi\hat{m}_\alpha\right), \tag{4.60a}$$

$$\tilde{Q}_h^{\alpha'} = -R_{\alpha'}^\top R_\alpha = -R\left(-\pi\hat{m}_\alpha\right) = -R\left(\pi\hat{m}_\alpha\right), \tag{4.60b}$$

where the last equality holds because SO(3) rotation matrices have period 2π.

The fact that $\tilde{Q}_h^\alpha = \tilde{Q}_h^{\alpha'}$ implies that $\theta_h^\alpha = \theta_h^{\alpha'}$. Hence, because the sublattice permutation is made up of 2-cycles and the phases θ_h^α are the same within each cycle, the matrix V_h is symmetric based on Appendix 4.C.4.1.

Hence, the constraint on the Hamiltonian is

$$H_{\mathbf{k}} = V_h^\dagger H_{\mathbf{k}}^* V_h, \qquad V_h = V_h^\top. \tag{4.61}$$

4.C.5.2 Time reversal with spin rotation

For coplanar spins, time reversal with spin rotation yields a time-reversal-like constraint on the magnon Hamiltonian. Specifically, if we consider spins in the y-z plane, $h = \{\mathbb{1}; R(\pi\hat{x})|0\}T$ and the rotation matrices can be chosen to be

$$R_\alpha = R(\eta_\alpha \hat{x}) = \begin{bmatrix} 1 & & \\ & \cos\eta_\alpha & -\sin\eta_\alpha \\ & \sin\eta_\alpha & \cos\eta_\alpha \end{bmatrix}. \tag{4.62}$$

With this choice, the local transformation on the spins is

$$\tilde{Q}_h^\alpha = -R(\eta_\alpha\hat{x})^\top R(\pi\hat{x}) R(\eta_\alpha \hat{x}) \tag{4.63a}$$

$$= \left[\begin{array}{c|c} -\tau^3 & \\ \hline & 1 \end{array}\right]. \tag{4.63b}$$

After transforming to the basis of ladder operators, with this specific choice of R_α, we find $\theta_h^\alpha = \pi$ for all α and

$$H_{\mathbf{k}} = H^*_{-\mathbf{k}}. \tag{4.64}$$

A different choice of $\{R_\alpha\}$ would have yielded different phases θ_h^α, and a more complicated matrix V_h.

4.C.5.3 Effective magnetic inversion symmetry

For coplanar spins with separate inversion and time-reversal+spin-rotation symmetries, one can have an effective magnetic inversion symmetry: $h = \{P; R_h^{\mathrm{s}}|\boldsymbol{\tau}\}T$, with any appropriate R_h^{s}.

For example, for spins in the y-z plane, $h = \{P; R(\pi\hat{x})|\boldsymbol{\tau}\}T$. Let α and α' denote a pair of sublattices related by P. These two sublattices have the same classical direction, so we can choose

$$R_\alpha = R_{\alpha'} = \begin{bmatrix} 1 & & \\ & \cos\eta_\alpha & -\sin\eta_\alpha \\ & \sin\eta_\alpha & \cos\eta_\alpha \end{bmatrix}. \tag{4.65}$$

This choice gives us the exact same result as in Appendix 4.C.5.2: $\theta_h^\alpha = \theta_h^{\alpha'} = \pi$; more generally, we will find $\theta_h^\alpha = \theta_h^{\alpha'}$. Therefore,

$$H_{\mathbf{k}} = V_h^\dagger H^*_{\mathbf{k}} V_h, \qquad V_h = V_h^\top \tag{4.66}$$

because the permutations are all 2-cycles with the same phases within each cycle.

4.C.5.4 Translation with spin rotation

Suppose that translation followed by spin rotation is an element of the spin space group; for example, $g = \{\mathbb{1}; R(\pi\hat{z})|\boldsymbol{\tau}\}$. Since this transformation has no spatial O(3) part, it acts locally in momentum space, and we get

$$H_{\mathbf{k}} = V_g^\dagger H_{\mathbf{k}} V_g, \qquad V_g \text{ unitary.} \tag{4.67}$$

But this is a unitary symmetry of the $H_{\mathbf{k}}$ *at a fixed momentum.* This means that $H_{\mathbf{k}}$ can be block-diagonalized, with the different blocks corresponding to different eigenvalues of V_g.

What does this additional structure correspond to, and why in this case does Fourier transforming leave remaining local unitary symmetries? Suppose g^2 is a primitive translation of the magnetic lattice. Then, one way of understanding this is to note that one can define modified translation operators (containing a global spin rotation by π about $\hat{z}$) whose eigenvalues span a Brillouin zone twice as large as the magnetic Brillouin zone. This is simply an alternate way of labeling the states, as it halves the bands and doubles the number of momenta.

4.C.5.5 Axial spin-rotation symmetry

Consider a global spin-rotation symmetry g about an axis; we can take it to be the $\hat{z}$ axis, in which case $g = \{\mathbb{1}; R(\theta\hat{z})|0\}$ for any θ. This implies the classical spin order is collinear, with spins pointing either in the $\hat{z}$ or $-\hat{z}$ directions.

It is easy to see that $\tilde{Q}_g^\alpha = R(\theta\hat{z})$ and $\theta_g^\alpha = \theta$ if the spin at sublattice α points in $+\hat{z}$ direction, whereas $\tilde{Q}_g^\alpha = R(-\theta\hat{z})$ and $\theta_g^\alpha = -\theta$ if the spin at sublattice α points in $-\hat{z}$ direction.

Hence, the associated matrix V_g is diagonal with eigenvalues of $\mathrm{e}^{\mathrm{i}\theta}$ and $\mathrm{e}^{-\mathrm{i}\theta}$. This implies that the coefficient matrix $H_{\mathbf{k}}$ is block diagonal, with the blocks corresponding to S_z-conserving sectors: one block contains annihilation operators for $+\hat{z}$ spins and creation operators for $-\hat{z}$ spins, and vice versa for the other block.

4.C.6 Magnetic inversion and reality condition

We show that in the appropriate basis, the constraint imposed by magnetic inversion symmetry on the Bloch Hamiltonian $H_{\mathbf{k}}$ is that it is purely real for each $\mathbf{k}$. This is expected for integer-spin excitations like magnons [312]; we nonetheless discuss how this arises for completeness.

Consider any (effective) magnetic inversion symmetry $h = \{P; Q^{\mathrm{s}}|\boldsymbol{\tau}\}T$, where Q^{s} is some O(3) operation and $\boldsymbol{\tau}$ is some spatial translation. We have seen that the constraint on $H_{\mathbf{k}}$ is local in momentum space, $H_{\mathbf{k}} = V_h^\dagger H_{\mathbf{k}}^* V_h$, with V_h symmetric. Since $V_h = V_h^{\mathrm{p}} \oplus V_h^{\mathrm{h}}$, this implies V_h^{p} and $V_h^{\mathrm{h}} = (V_h^{\mathrm{p}})^*$ are symmetric. The symmetric unitary matrix V_h^{p} can be

factorized as $V_h^{\mathrm{p}} = \ell^\top \ell$ using Autonne-Takagi decomposition, where ℓ is unitary. We then find $V_h = L^\top L$, where $L := \ell \oplus \ell^*$ is unitary, paraunitary, and particle-hole symmetric.

In the new basis defined by $\Phi_{\mathbf{k}} = L^\dagger \Phi'_{\mathbf{k}}$ the transformation $\Theta_h \Phi_{\mathbf{k}} \Theta_h^{-1} = \mathrm{e}^{\mathrm{i}\mathbf{k}\cdot\boldsymbol{\tau}} V_h \Phi_{\mathbf{k}}$ becomes

$$\begin{aligned} \Theta_h L^\dagger \Phi'_{\mathbf{k}} \Theta_h^{-1} &= \mathrm{e}^{\mathrm{i}\mathbf{k}\cdot\boldsymbol{\tau}} V_h L^\dagger \Phi'_{\mathbf{k}} \\ \Leftrightarrow \quad \Theta_h \Phi'_{\mathbf{k}} \Theta_h^{-1} &= \mathrm{e}^{\mathrm{i}\mathbf{k}\cdot\boldsymbol{\tau}} L^* V_h L^\dagger \Phi'_{\mathbf{k}}. \end{aligned} \tag{4.68}$$

Therefore,

$$V'_h = L^* V_h L^\dagger = L^* L^\top L L^\dagger = \mathbb{1}, \tag{4.69}$$

and the constraint due to magnetic inversion symmetry reads as $H'_{\mathbf{k}} = \left(H'_{\mathbf{k}}\right)^*$.

Hence, we have shown that there exists a ($\mathbf{k}$-independent) change of basis such that in that basis, the constraint due to magnetic inversion is simply that $H'_{\mathbf{k}}$ is purely real.

Chapter 5

Conclusion

In the present thesis, we have investigated certain novel properties of condensed-matter systems with Dirac-like quasiparticles, as well as some of the circumstances in which such physics arises. First, Chapter 1, the introductory chapter, provided some perspective and attempted to situate this work in its scientific and historical contexts. Special focus was placed on the overarching principles that organize the occurence of band touchings and Dirac-like physics in quantum systems: first, we discussed how the concept of decomposing a Hamiltonian into irreducible blocks based on its (unitary) symmetry group allows for its degeneracies or band touchings to be categorized into essential, type-(i) accidental, and type-(ii) accidental. We saw that these different kinds of band touchings are now understood to be protected by topological charges they carry, which can give rise to topological boundary states characteristic of SPT phases. We discussed a simple and general classification, denominated the "AZ+$\mathcal{P}$ classification" [76], that describes the (type-(ii) accidental) band touchings at general—i.e., not high-symmetry—momenta in electronic band structures, and the associated topological invariants. At high-symmetry momenta, where band touchings can be essential or type-(i) accidental, classification schemes are richer and more varied, and depend on the space-group symmetries.

We reviewed the Dirac and Weyl Hamiltonians as they arise in high-energy physics, and several notable condensed-matter systems in which they emerge as effective descriptions, placing each within the context described above. We devoted particular attention to the high-temperature cuprate superconductors as well as to graphene and the effects of strain thereon, since they play important roles in later parts of the thesis.

We also gave an overview of a family of linear magnetoelectric effects called the "Edelstein effects", or the "kinetic magnetoelectric effect", which play an important part in Chapter 3, paying special attention to the role of Weyl nodes as sources of magnetic moment in momentum space. Finally, we presented a primer on the basic mathematics of Krein-Hermitian Hamiltonians and Krein spaces (i.e., Hilbert spaces with an additional, indefinite inner product), which serve as a framework for the developments of Chapter 4.

5.1 Pseudo-magnetic fields of quasiparticles in nodal superconductors

Chapter 2 developed a theory of strain-induced pseudomagnetic fields and Landau levels in nodal superconductors, using the cuprates as an archetypal example. The pseudomagnetic fields arise from an inhomogeneous hopping amplitude, and from an inhomogeneous s-wave pairing gap on top of the cuprates' d-wave gap. Like in graphene and other materials in which similar effects have been predicted or observed, the Dirac-like description of the excitations is the crucial requirement for this physics. In addition to obtaining a low-energy theory of the Dirac nodes that allows for spatial modulation of parameters, we performed a numerical calculation with modulated parameters using a slab geometry, and found good agreement between the two.

In graphene and other non-superconducting systems whose low-energy descriptions are Dirac like, the deformation potential enters the low-energy Hamiltonian as a scalar potential, coupling minimally to the time derivative [91]. This scalar potential can make the Landau levels dispersive—hence broadening the associated peaks in the density of states and potentially impeding their detection—or even destroy the Landau levels altogether [207,337]. Instead, because of the nature of the Nambu formalism, a deformation potential would enter as a component of the pseudo-magnetic vector potential in a nodal superconductor. For this reason, strain-induced Landau levels are likely more robust in nodal superconductors than in Dirac or Weyl semimetals.

We proposed experimental realizations of strain-induced Landau levels in cuprate superconductors, and estimated that an achievable magnitude of strain could generate a first Landau level at roughly 1 meV, which would be resolvable with scanning-tunneling spectroscopy. Notably, these pseudomagnetic fields may provide a unique way to achieve a Landau-level spectrum of Bogoliubov quasiparticles, since ordinary magnetic fields do not couple to them the same way they do to electrons[1].

Several other closely related works have followed, identifying other superconducting systems in which pseudo-magnetic fields may arise or further studying the properties of these states.

Many of our results were reproduced in an article by Emilian M. Nica and Marcel Franz that was released shortly after ours [340], in which a similar system is considered. In that article, the authors point out that doping gradients, which can be described as a position-dependent chemical potential $\mu(\mathbf{r})$, also give rise to pseudo-magnetic fields in nodal superconductors—an important observation, since controlled doping gradients have been realized in cuprate samples [341]. Furthermore, they propose an additional means of

[1] Recently, it was predicted that a zeroth Landau level should exist in a Weyl in the mixed phase [338]. Such a Landau level is *not* due to strain or other inhomogeneities, but rather to the magnetic flux tubes traversing the material, and gives rise to a chiral magnetic effect in these systems [339]. The existence of Landau levels in such a state had been a long debated topic.

detecting the Landau quantization of the Bogoliubov quasiparticles: if a small supercurrent is applied, the energy of the quasiparticle excitations acquires a momentum-dependent shift, $E_{\mathbf{k}} = E^0_{\mathbf{k}} + \mathbf{v}_{\mathrm{s}} \cdot \mathbf{k}$, where $\mathbf{v}_{\mathrm{s}}$ is the superfluid velocity. Hence, as the supercurrent is varied, the density of states at the Fermi energy will exhibit quantum oscillations owing to the strain-induced Landau levels; these quantum oscillations should manifest themselves in transport properties, for instance. The authors also speculate that the system might exhibit a quantized thermal Hall conductance, in analogy with the quantum Hall states that emerge in two-dimensional systems under strong magnetic fields.

In Ref. 216, Tianyu Liu, Marcel Franz and Satoshi Fujimoto consider Weyl superconductors, a recently proposed class of 3D superconductors whose low-energy excitation spectrum hosts Weyl nodes, and predict that strain-induced pseudo-magnetic fields and associated Landau levels should arise in these materials as well. The authors show that their model should exhibit quantum oscillations in heat conductivity stemming from the strain-induced Landau levels in the excitation spectrum; indeed, unlike charge transport, heat transport by Bogoliubov quasiparticles is analogous to that by electrons. They conclude that such quantum oscillations should be observable in (yet-to-be-discovered) Weyl superconductors via quasiparticle spectroscopy and (longitudinal) thermal conductivity measurements.

In Ref. 342, the interplay of the pseudo-magnetic fields and the chiral anomaly in Weyl superconductors was studied. In Weyl semimetals, the so-called chiral anomaly, which stems from the Weyl nature of the low-energy excitations, gives rise to numerous exotic transport properties, like the anomalous Hall effect, the chiral magnetic effect, and negative magnetoresistivity [342]. These effects rely upon the application of an external magnetic field. The possibility of analogous effects in Weyl superconductors, however, are complicated by the fact that Bogoliubov quasiparticles, which have no definite charge, do not couple simply to a magnetic field. The authors of Ref. 342 describe two avenues for getting around this restriction and realizing negative magnetoresistance of thermal currents in Weyl superconductors: one is a fictitious magnetic field felt by the quasiparticles in the mixed, or Abrikosov, phase (see also Refs. 343–345), and the other is via strain-induced pseudo-magnetic fields.

In yet another article [346], it was predicted that a pseudo-magnetic field, such as that induced by strain, can stabilize a Fulde-Ferrell-Larkin-Ovchinnikov (FFLO) state in Weyl and Dirac superconductors.

In Ref. 347, Emilian M. Nica and Onur Erten consider possible instabilities of the strain-induced Landau level state of a (2D) d_{xy}-wave superconductor, and find that the zeroth Landau-level states have an instability toward ferromagnetism. They note that instabilities are unlikely to destroy superconductivity in the small-strain limit, implying that the bulk magnetic moment arising from the ferromagnetic order is screened via the Meissner effect.

Possible future directions include obtaining more quantitatively sound predictions for strain-induced Landau-level energies by performing a full mean-field theory to obtain the

spatially-varying parameters, refining the low-energy expansion, taking inspiration from results from graphene [141, 142], or further elaborating on the potential for inducing an inhomogeneous extended s-wave gap via the proximity effect.

5.2 Slightly gapped nodal lines as sources in the orbital Edelstein effect

Chapter 3 considered a tight-binding model of a metal featuring in its band structure nodal lines that are enforced by a non-symmorphic symmetry, and perpendicular to which electrons disperse linearly. We showed that, although the initial crystal class, being non gyrotropic, does not allow a linear magnetoelectric effect, the onset of charge ordering due to repulsive interactions between neighboring atoms can lower the symmetry and bring about a nonzero orbital Edelstein effect, while simultaneously gapping out the nodal lines.

We studied one such symmetry-broken phase in detail, and found that the nodal lines, once slightly gapped out by a mass proportional to the order parameter, act as sources of orbital magnetic moment $\mathbf{m}_{\mathbf{k}n}$ in momentum space, and seem to determine the magnetoelectric response tensor α^{orb}. We note here that despite the fact that, in the vicinity of a nodal line, the component of the orbital magnetic moment $\mathbf{m}_{\mathbf{k}n}$ parallel to the nodal line diverges as the parameter ν, proportional to the charge-density-wave order parameter and defined in Eq. (3.14), vanishes (see Eq. (3.20)), the response tensor α^{orb} remains continuous; specifically, the contribution from the divergent magnetic moment typically vanishes as $\alpha^{\text{orb}} \sim \nu \log \nu$ as $\nu \to 0$. We also applied a solenoid picture of currents circulating through the interatomic bonds in the spirit of Ref. 151, using it to understand the symmetry requirements for a nonzero α^{orb} from a simple, physical point of view.

Hence, we demonstrated that the Edelstein effect could serve as an indication of symmetry breaking in certain systems. In fact, during the writing of that manuscript, there appeared an article [273] proposing the onset of the orbital Edelstein effect as a means of detecting hidden quadrupolar order in certain diamond-structure compounds. Specifically, they consider cage compounds of the form $\text{Pr}T_2X_{20}$, some of which may exhibit spontaneous antiferro-quadrupole order. With the onset of such orders, the symmetry of the systems is lowered, and since the conduction electrons are coupled to the quadrupole moments, the Edelstein effect can emerge. Moreover, the anisotropy in the magnetoelectric response could constitute a way to discriminate between two different types of antiferro-quadrupole order that may arise. They consider two contributions to the Edelstein effect: one from the combined spin and atomic angular momentum of the conduction electrons, and the other from inter-site motion that gives rise to rotation of the electron wavepacket (the one we focused on). They also illustrate the magnetoelectric effect as stemming from the motion of solenoidal paths in the crystal; the onset of charge order gives rise to two sets of inequivalent solenoids and allows a net magnetization to arise. This picture is very much like the one we present in Chapter 3;

in fact, the space group in one of their symmetry-broken phases, $P\bar{4}2m$, is the same as our Phase I discussed in Sec. 3.4, though the parent phases and the symmetry-breaking orders differ.

Possible future directions include a search for similar models whose gapless lines, unlike the model of Chapter 3, are pinned by symmetry at a fixed energy, such that by tuning the Fermi energy, the entire Fermi surface can be made proximate to the gapless lines. In such a situation, the magnetoelectric response would be solely determined by the neighborhoods of the gapless lines, and an analytic understanding of their contribution to α^{orb} could be obtained, as was done with Weyl nodes in Ref. 151. One avenue for finding fixed-energy gapless lines in 3D, at least at general momenta, would be to look in AZ+$\mathcal{P}$ classes AIII, DIII, and CI (see Table 1.2); models in these classes would generically have gapless lines at zero energy because of chiral symmetry $\mathcal{S}$ or (modified) particle-hole symmetry $\mathfrak{C} = \mathcal{CP}$.

As we and others have remarked, distinguishing the orbital Edelstein effect from the spin Edelstein effect in experiment appears to be a difficult task, since both responses have the same symmetry properties. Moreover, when considering orbitals with angular momentum $l > 0$, the orbital magnetic moment has an "intra-atom" contribution from the atomic angular momentum (e.g., Refs. 348–351), distinct from the "inter-atom" contribution from wavepacket self-rotation discussed in Sec. 1.6.2 and Chapter 3 [151, 352–354]; both are regularly called the "orbital Edelstein effect". In first-principles calculations, the sum of both orbital effects is naturally calculated [354].

In addition to the developments described in Sec. 1.6.3, recent theoretical work has considered the possibility of the orbital Edelstein effect in topological insulators. In these states of matter, the bulk of the material is insulating, while the boundary is metallic, hosting topologically protected gapless states that can carry current. Ref. 354 reported that in topological insulators—specifically, Chern insulators and time-reversal-invariant $\mathbb{Z}^2$ topological insulators—with chiral crystal structures, driving a (surface) current in one direction can give rise to additional, "winding" surface currents in perpendicular directions, and a net magnetization. They conclude that the interatomic orbital Edelstein effect dominates compared to the spin and intra-atomic effects in a topological insulator, and is also much more pronounced in a topological insulator than in an ordinary metal, based on scaling arguments of surface currents vs. volume currents.

More broadly, several recent papers have reported an (intra-atom) orbital Edelstein effect much stronger than the spin Edelstein effect in specific systems [348, 355]. It appears these studies may not account for the possibility of the inter-atom orbital Edelstein effect, which is expected to arise concomitantly by symmetry. It would be interesting to compare the magnitude to the intra-atom and inter-atom effects in these systems.

Another potential question of interest for future studies concerns possible additional contributions to the orbital Edelstein effect. When calculated using linear response theory, the spin contribution to the response tensor α appearing in Eq. (1.111) includes other terms

contributing to the *spin* Edelstein effect [356–358], in addition to that of Eq. (1.112). For clean metals, the term of Eq. (1.112), which was the basis of the discussions of Sec. 1.6 and Chapter 3 and originates from the perturbation of the electronic distribution function, dominates the response because of its linear dependence on the relaxation time τ [356, 357]. The two additional terms, which arise from interband transitions and are, roughly speaking, proportional to τ^0 and τ^{-1}, respectively, can become important in disordered systems [356, 357] or in band insulators. The question of whether analogous interband contributions arise in the *orbital* Edelstein effect is unclear. As mentioned in the Sec. 1.6.2, many references, using various approaches, have found an additional contribution to the orbital magnetization coming from the electronic Berry curvature [165–168], though it has been questioned based on physical arguments [144, footnote 21]. This Berry phase contribution, which is independent of the relaxation time τ, may be analogous to the term proportional to τ^0 in the spin Edelstein effect, but to our knowledge, no works on the orbital Edelstein effect have uncovered a contribution proportional to τ^{-1} (see, e.g., Refs. 144, 160). It would be interesting to investigate if such a contribution arises—or why it does not arise—in the orbital Edelstein effect, especially in situations where the Fermi-surface contribution vanishes, like in the low-temperature regime of the model of Chapter 3.

5.3 Krein-unitary Schrieffer-Wolff transformation and band touchings in bosonic Bogoliubov–de Gennes Hamiltonians

Chapter 4 generalized the formalism of the perturbative Schrieffer-Wolff transformation to Krein-Hermitian Hamiltonians, a class of non-Hermitian Hamiltonians that are Hermitian with respect to an indefinite inner product, and that arise as the single-particle Hamiltonians of bosonic Bogoliubov–de Gennes systems, among other provenances. The transformation we formulated preserves the spectrum and is Krein-unitary, implying that the eigenstates of the resulting effective Hamiltonian are proper bosons, since they satisfy canonical commutation relations. The Schrieffer-Wolff transformation yields an effective reduced Hamiltonian for a subspace of interest, and our formalism shows that when the (full) Hamiltonian is Krein Hermitian, the effective reduced Hamiltonian is, in general, also Krein-Hermitian, but with respect to a different, smaller Krein metric. Under certain conditions, Krein-Hermitian Hamiltonians are diagonalizable with real eigenvalues, and we used Krein stability theory to assess in what circumstances perturbations preserve these properties.

We also showed that, for a Krein-positive-definite (defined in Sec. 1.7.2.2) Krein-Hermitian momentum-space Hamiltonian, a contiguous subset of positive-energy bands is locally described by an effective *Hermitian* Hamiltonian. Krein-positive-definite Krein-Hermitian Hamiltonians emerge, for example, in the single-particle description of thermodynamically stable bosonic Bogoliubov–de Gennes systems, such as those describing magnon excitations

about a magnetic ground state[2], and have the form

$$\tau^3 H_{\mathbf{k}}, \tag{5.1}$$

where $H_{\mathbf{k}}$ is a positive-definite Hermitian matrix, as explained in Sec. 4.2[3]. Their positive-energy eigenvalues give the energies of the bosonic eigenmodes: indeed, letting $T_{\mathbf{k}}$ be the diagonalizing transformation that appears in Eq. (4.5),

$$T_{\mathbf{k}}^{-1}(\tau^3 H_{\mathbf{k}})T_{\mathbf{k}} = \begin{bmatrix} \epsilon_{\mathbf{k},1} & & & & & \\ & \ddots & & & & \\ & & \epsilon_{\mathbf{k},n} & & & \\ & & & -\epsilon_{-\mathbf{k},1} & & \\ & & & & \ddots & \\ & & & & & -\epsilon_{-\mathbf{k},n} \end{bmatrix}, \tag{5.2}$$

where the bosonic mode energies $\epsilon_{\mathbf{k},\alpha} > 0$[4] appear in Eq. (4.4). Previously, effective few-band Hamiltonians for thermodynamically stable Krein-Hermitian systems had been calculated or postulated, but with little justification for the methods or for the form of the effective Hamiltonian [80, 277, 303, 313, 314]. Our work provides a more rigorous basis for the calculation of such effective Hamiltonians, as well as for their general form.

In *fermionic* systems (whether or not Bogoliubov–de Gennes), it is commonplace to postulate effective few-band Hamiltonians to understand certain properties of the systems; for example, this was done in Ref. 76 to study type-(ii) accidental band touchings and determine their generic codimension based on symmetry, the results of which are summarized in Table 1.2. Such a picture can be justified using the Schrieffer-Wolff transformation on the (Hermitian) many-band Bloch Hamiltonian, which yields a (Hermitian) few-band effective Hamiltonian, at least locally in momentum space.

Our Krein-unitary Schrieffer-Wolff transformation shows that a closely analogous picture holds in thermodynamically stable bosonic Bogoliubov–de Gennes systems, since the effective few-band Hamiltonians that (locally) describe contiguous positive-energy bands are *also* Hermitian. As explained in Sec. 4.4.1, this simple form of effective few-band Hamiltonians justifies codimension-counting approaches for type-(ii) accidental band touchings. In this way, we confirmed that band touchings of bosonic systems in AZ+$\mathcal{P}$ classes A and AI generically have codimension 3 and 2, respectively, like their fermionic counterparts (see Table 1.2). In other words, given the assumption of Krein-positive-definiteness, the usual

[2]Typically, the only exception is if $\mathbf{k} = 0$ harbors a Goldstone mode, in which case $\tau^3 H_{\mathbf{k}=0}$ is merely Krein positive *semi*definite.

[3]Note that physically, the presence of pairing terms in the quadratic boson Hamiltonian implies that quantum fluctuations alter the ground state, which is no longer simply the vacuum state of the original bosons [58, Eq. (26)]. Some symmetries may forbid such terms, but they are allowed in general.

[4]Again, in the presence of a Goldstone mode, one has $\epsilon_{\mathbf{k}=0,\alpha} = 0$ for some value(s) of α.

level-repulsion picture, which, as explained in Chapter 1, is closely tied to the notion of generic band-touching codimension, continues to hold.

This is a noteworthy result in that non-Hermitian matrices are not generally subjected to level repulsion; indeed, in some cases they even exhibit level *attraction* [359–361]. As a simple example, consider the matrix

$$K(t) = \begin{bmatrix} 2 & & & t \\ & 1 & t & \\ & -t & -1 & \\ -t & & & -2 \end{bmatrix}, \tag{5.3}$$

which is Krein Hermitian with respect to $\eta = \mathrm{diag}(1, 1, -1, -1)$ for each $t \in \mathbb{R}$. Its spectrum is $\{-\sqrt{4-t^2}, -\sqrt{1-t^2}, \sqrt{1-t^2}, \sqrt{4-t^2}\}$, and near the points $t = 1$ and $t = -1$ in parameter space, the middle eigenvalues exhibit *level attraction* rather than level repulsion, which is only possible because $K(t)$ is non-Hermitian (at least for $t \neq 0$). This behavior is not surprising, though, when we realize that $K(t)$ is Krein positive definite only on the open interval $t \in \,]-1, 1[\,$, and in that interval, the two positive-energy states can be described by an effective 2×2 Hermitian Hamiltonian, and our conclusions hold.

Furthermore, in Sec. 4.4, we used examples from recent literature to illustrate the complex combinations of Dirac-like band touchings that can arise in magnon systems because of the richness of the spin-space group symmetries that characterize them, and in Appendix 4.C, we provided a detailed account of how these symmetries are translated from the spin Hamiltonian to the magnon Hamiltonian. Specifically, we considered space-time-inversion-symmetric collinear antiferromagnets with and without spin-rotation symmetry as in Ref. 303 (an example of which is Cu_3TeO_6), inversion-symmetric Heisenberg ferromagnets as in Ref. 324, and an XXY spin model inspired by stacked-honeycomb magnets like $CoTiO_3$ [306, 307], but modified to heuristically illustrate the generic effects of additional spin-orbit coupling terms. This last example demonstrated how certain spin-space-group symmetries in weakly spin-orbit coupled systems allow both type-(i) and type-(ii) accidental band touchings anywhere in momentum space, as summarized in Table 4.1. We put special emphasis on how, at a qualitative level, the varied band-touching features in all these examples could be largely understood based solely on codimension-counting arguments and a careful consideration of their spin-space group symmetries. Though they were first introduced over half a century ago, the importance and utility of spin space groups seems to be underappreciated in the recent literature, and in fact, during the writing of this manuscript, there appeared another article [57] explaining the important role of spin-space-group symmetries in magnon band structures. The authors of that article go further, however, and detail the mechanics of the representation theory of these groups as applied to magnons.

It is worth commenting on the relevance of the present formalism to phonons, the bosonic excitations that describe the fluctuations of the ions in a crystal lattice about their

equilibrium positions. Elementary treatments of harmonic phonon dynamics are based on the ionic kinetic energies and a quadratic restoring potential [161, 362, 363]. In this case, the Hamiltonian takes the form

$$\begin{aligned} H_{\text{elementary}} &= \frac{1}{2}\sum_{\mathbf{k}}\sum_{\alpha,i} p_{\mathbf{k},\alpha,i} p^{\dagger}_{\mathbf{k},\alpha,i} + \frac{1}{2}\sum_{\mathbf{k}}\sum_{\alpha,\beta,i,j} u_{\mathbf{k},\alpha,i} D_{\alpha,\beta;i,j}(\mathbf{k}) u^{\dagger}_{\mathbf{k},\beta,j} \\ &= \sum_{\mathbf{k},n} \omega_{\mathbf{k}n}\left(a^{\dagger}_{\mathbf{k}n} a_{\mathbf{k}n} + \frac{1}{2}\right), \end{aligned} \tag{5.4}$$

where α and β are sublattice indices, i and j are Cartesian components, and n indexes the phonon branches. Here, the dynamical matrix $D_{\alpha,\beta;i,j}(\mathbf{k})$, which is essentially the Fourier transform of the ionic restoring force constants, is Hermitian, and yields the $\omega^2_{\mathbf{k}n}$ as its eigenvalues and the phonon polarizations as its eigenvectors. The system, then, is effectively Hermitian, and no Krein-Hermitian description is required. However, this can change in slightly more general situations, as pointed out in Ref. 186: for instance, when describing phonons of a system of ions in a magnetic field, an additional term appears in the Hamiltonian, which now takes the form [364–368]

$$H_{\text{mag}} \sim \frac{1}{2}pp^{\dagger} + \frac{1}{2}uDu^{\dagger} + uAp^{\dagger}. \tag{5.5}$$

Here, the third term on the right-hand side originates from the magnetic vector potential $\mathbf{A}(\mathbf{r})$ linearized at each ion's position. In this case, the effective single-particle Hamiltonian that gives the mode energies and the phonon polarizations is [364–368]

$$K_{\text{eff}} = -\mathrm{i}\begin{bmatrix} A & D \\ -\mathbb{1} & A \end{bmatrix}, \tag{5.6}$$

which is Krein Hermitian with respect to the Krein metric $\eta = \tau^2 \otimes \mathbb{1}$[5]. After switching to the basis in which the metric takes on the "canonical" diagonal form described in Sec. 1.7, the Schrieffer-Wolff of Chapter 4 is applicable to such phonon systems. Moreover, there appear to be no difficulties in working out the implementations of symmetry transformations on the Hamiltonian of Eq. (5.6) (as was done for magnons in Sec. 4.C), enabling an analysis of band touchings like those in magnon systems discussed in Chapter 4.

A possible future research direction is to attempt to derive a radius of convergence of our Krein-unitary perturbative Schrieffer-Wolff transformation, as has been done for the conventional Schrieffer-Wolff transformation [294]. In that case, the radius of convergence is specified in terms of $\|H'\|$, the operator norm of the perturbation. In the Krein-Hermitian case, it is not clear a priori whether this or some other metric is most appropriate to this

[5] It is also possible to write the single-particle Hamiltonians of *magnon* systems in a form that is Krein Hermitian with respect to $\tau^2 \otimes \mathbb{1}$ rather than $\tau^3 \otimes \mathbb{1}$—a comparison of the two formalisms is given in Ref. 279. Similarly, one should be able to rewrite the effective phonon Hamiltonian of Eq. (5.6) in a form where its Krein metric is $\tau^3 \otimes \mathbb{1}$, a process equivalent to expressing p and u in Eq. (5.5) in terms of ladder operators.

end. No matter the outcome, the quest for an answer will likely be fruitful and lead to exciting results.

Bibliography

[1] Geremia Massarelli, Gideon Wachtel, John Y. T. Wei, and Arun Paramekanti. Pseudo-Landau levels of Bogoliubov quasiparticles in strained nodal superconductors. *Phys. Rev. B*, 96:224516, Dec 2017.

[2] Geremia Massarelli, Bryce Wu, and Arun Paramekanti. Orbital Edelstein effect from density-wave order. *Phys. Rev. B*, 100:075136, Aug 2019.

[3] Arijit Haldar, Geremia Massarelli, and Arun Paramekanti. Higher-order topology and corner triplon excitations in two-dimensional quantum spin-dimer models. *Phys. Rev. B*, 104:184403, Nov 2021.

[4] Geremia Massarelli, Ilia Khait, and Arun Paramekanti. Krein-unitary Schrieffer-Wolff transformation and band touchings in bosonic Bogoliubov–de Gennes and other Krein-Hermitian Hamiltonians. *Phys. Rev. B*, 106:144434, Oct 2022.

[5] Oskar Vafek and Ashvin Vishwanath. Dirac fermions in solids: From high-T_c cuprates and graphene to topological insulators and Weyl semimetals. *Annual Review of Condensed Matter Physics*, 5(1):83–112, 2014.

[6] T. O. Wehling, A. M. Black-Schaffer, and A. V. Balatsky. Dirac materials. *Advances in Physics*, 63(1):1–76, 2014.

[7] S Banerjee, D S L Abergel, H Ågren, G Aeppli, and A V Balatsky. Interacting dirac materials. *Journal of Physics: Condensed Matter*, 32(40):405603, jul 2020.

[8] Patrik Fazekas. *Lecture Notes on Electron Correlation and Magnetism*, volume 5 of *Series in Modern Condensed Matter Physics*. World Scientific Publishing Co., Singapore, 1999.

[9] J. Fransson, A. M. Black-Schaffer, and A. V. Balatsky. Magnon dirac materials. *Phys. Rev. B*, 94:075401, Aug 2016.

[10] William G. Unruh and Ralf Schützhold, editors. *Quantum Analogues: From Phase Transitions to Black Holes and Cosmology*, volume 718 of *Lecture Notes in Physics*. Springer, Berlin, Heidelberg, 2007.

[11] B. Andrei Bernevig. It's been a Weyl coming. *Nature Physics*, 11(9):698–699, 2015.

[12] Grigory E Volovik. *The Universe in a Helium Droplet.* International Series of Monographs on Physics. Clarendon Press, Oxford, 2003.

[13] D. Vollhardt and P. Wölfle. Superfluid helium 3: Link between condensed matter physics and particle physics. *Acta Physica Polonica B*, 31(12):2837, 2000.

[14] Xie Chen, Zheng-Cheng Gu, and Xiao-Gang Wen. Local unitary transformation, long-range quantum entanglement, wave function renormalization, and topological order. *Phys. Rev. B*, 82:155138, Oct 2010.

[15] A. A. Burkov, M. D. Hook, and Leon Balents. Topological nodal semimetals. *Phys. Rev. B*, 84:235126, Dec 2011.

[16] Andreas W W Ludwig. Topological phases: classification of topological insulators and superconductors of non-interacting fermions, and beyond. *Physica Scripta*, T168:014001, dec 2016.

[17] D. J. Thouless, M. Kohmoto, M. P. Nightingale, and M. den Nijs. Quantized hall conductance in a two-dimensional periodic potential. *Phys. Rev. Lett.*, 49:405–408, Aug 1982.

[18] F. D. M. Haldane. Model for a quantum hall effect without landau levels: Condensed-matter realization of the "parity anomaly". *Phys. Rev. Lett.*, 61:2015–2018, Oct 1988.

[19] Chao-Xing Liu, Shou-Cheng Zhang, and Xiao-Liang Qi. The quantum anomalous hall effect: Theory and experiment. *Annual Review of Condensed Matter Physics*, 7(1):301–321, 2016.

[20] The Class for Physics of the Royal Swedish Academy of Sciences. Scientifc background on the Nobel Prize in Physics 2016: Topological phase transitions and topological phases of matter, October 2016. https://www.nobelprize.org/uploads/2018/06/advanced-physicsprize2016.pdf.

[21] Giuseppe De Nittis and Kiyonori Gomi. The cohomological nature of the Fu–Kane–Mele invariant. *Journal of Geometry and Physics*, 124:124–164, 2018.

[22] C. L. Kane and E. J. Mele. Z_2 topological order and the quantum spin Hall effect. *Phys. Rev. Lett.*, 95:146802, Sep 2005.

[23] Liang Fu, C. L. Kane, and E. J. Mele. Topological insulators in three dimensions. *Phys. Rev. Lett.*, 98:106803, Mar 2007.

[24] Liang Fu and C. L. Kane. Topological insulators with inversion symmetry. *Phys. Rev. B*, 76:045302, Jul 2007.

[25] J. von Neumann and E. P. Wigner. Über merkwürdige diskrete eigenwerte. *Physikalische Zeitschrift*, 30:465–467, 1929.

[26] Eugene Paul Wigner. *Gruppentheorie und ihre Anwendung auf die Quantenmechanik der Atomspektren.* Friedrich Vieweg und Sohn, Braunschweig, 1931.

[27] Hermann Weyl and Howard Percy Robertson. *The theory of groups and quantum mechanics.* Dutton, New York, N.Y., 1931.

[28] Frederick Seitz. On the reduction of space groups. *Annals of Mathematics*, 37(1):17–28, 1936.

[29] R. Winkler, L.Y. Wang, Y.H. Lin, and C.S. Chu. Robust level coincidences in the subband structure of quasi-2D systems. *Solid State Communications*, 152(23):2096–2099, 2012.

[30] Philip B. Allen and Warren E. Pickett. Accidental degeneracy in k-space, geometrical phase, and the perturbation of π by spin-orbit interactions. *Physica C: Superconductivity and its Applications*, 549:102–106, 2018.

[31] Volker Heine. *Group theory in quantum mechanics: an introduction to its present usage.* Pergamon Press Inc., Oxford, U.K., 1960.

[32] Conyers Herring. Accidental degeneracy in the energy bands of crystals. *Phys. Rev.*, 52:365–373, Aug 1937.

[33] M. V. Berry. Aspects of degeneracy. In G. Casati, editor, *Chaotic Behavior in Quantum Systems*, volume 120 of *NATO ASI Series (Series B: Physics)*, pages 123–140. Springer, Boston, MA, 1985.

[34] G. P. Mikitik and Yu. V. Sharlai. Manifestation of Berry's phase in metal physics. *Phys. Rev. Lett.*, 82:2147–2150, Mar 1999.

[35] Y. Quan, Z. P. Yin, and W. E. Pickett. Single nodal loop of accidental degeneracies in minimal symmetry: Triclinic $CaAs_3$. *Phys. Rev. Lett.*, 118:176402, Apr 2017.

[36] Chen Fang, Hongming Weng, Xi Dai, and Zhong Fang. Topological nodal line semimetals. *Chinese Physics B*, 25(11):117106, Nov 2016.

[37] Apoorv Tiwari and Tomáš Bzdušek. Non-Abelian topology of nodal-line rings in $\mathcal{PT}$-symmetric systems. *Phys. Rev. B*, 101:195130, May 2020.

[38] L. P. Bouckaert, R. Smoluchowski, and E. Wigner. Theory of Brillouin zones and symmetry properties of wave functions in crystals. *Phys. Rev.*, 50:58–67, Jul 1936.

[39] Conyers Herring. Character tables for two space groups. *Journal of the Franklin Institute*, 233(6):525–543, 1942.

[40] Andreas P. Schnyder. Lecture notes on: Accidental and symmetry-enforced band crossings in topological semimetals. In *Topological Matter School 2018, San Sebastian, Spain*, Aug 2018. https://www.fkf.mpg.de/6431357/topo_lecture_notes_schnyder_TMS18.pdf.

[41] Leon Balents. Viewpoint: Weyl electrons kiss. *Physics*, 4:36, 2011.

[42] M. Zahid Hasan. Discovery of Weyl fermions, topological Fermi arcs and topological nodal-line states of matter. *2Physics*, Feb 2016.

[43] Ashvin Vishwanath. Viewpoint: Where the Weyl things are. *Physics*, 8:84, 2015.

[44] Yundi Quan and Warren E Pickett. A maximally particle-hole asymmetric spectrum emanating from a semi-dirac point. *Journal of Physics: Condensed Matter*, 30(7):075501, Jan 2018.

[45] J. J. Sakurai and Jim Napolitano. *Modern Quantum Mechanics*. Pearson Education, Inc., publishing as Addison-Wesley, San Francisco, California, second edition, 2011.

[46] Andreas P. Schnyder, Shinsei Ryu, Akira Furusaki, and Andreas W. W. Ludwig. Classification of topological insulators and superconductors in three spatial dimensions. *Phys. Rev. B*, 78:195125, Nov 2008.

[47] Andreas P. Schnyder, Shinsei Ryu, Akira Furusaki, and Andreas W. W. Ludwig. Classification of topological insulators and superconductors. *AIP Conference Proceedings*, 1134(1):10–21, 2009.

[48] Alexei Kitaev. Periodic table for topological insulators and superconductors. *AIP Conference Proceedings*, 1134(1):22–30, 2009.

[49] Shinsei Ryu, Andreas P Schnyder, Akira Furusaki, and Andreas W W Ludwig. Topological insulators and superconductors: tenfold way and dimensional hierarchy. *New Journal of Physics*, 12(6):065010, jun 2010.

[50] Ching-Kai Chiu, Jeffrey C. Y. Teo, Andreas P. Schnyder, and Shinsei Ryu. Classification of topological quantum matter with symmetries. *Rev. Mod. Phys.*, 88:035005, Aug 2016.

[51] Xie Chen, Zheng-Cheng Gu, Zheng-Xin Liu, and Xiao-Gang Wen. Symmetry protected topological orders and the group cohomology of their symmetry group. *Phys. Rev. B*, 87:155114, Apr 2013.

[52] Ching-Kai Chiu, Hong Yao, and Shinsei Ryu. Classification of topological insulators and superconductors in the presence of reflection symmetry. *Phys. Rev. B*, 88:075142, Aug 2013.

[53] Takahiro Morimoto and Akira Furusaki. Topological classification with additional symmetries from Clifford algebras. *Phys. Rev. B*, 88:125129, Sep 2013.

[54] Ken Shiozaki and Masatoshi Sato. Topology of crystalline insulators and superconductors. *Phys. Rev. B*, 90:165114, Oct 2014.

[55] Barry Bradlyn, L. Elcoro, Jennifer Cano, M. G. Vergniory, Zhijun Wang, C. Felser, M. I. Aroyo, and B. Andrei Bernevig. Topological quantum chemistry. *Nature*, 547(7663):298–305, 2017.

[56] Luis Elcoro, Benjamin J. Wieder, Zhida Song, Yuanfeng Xu, Barry Bradlyn, and B. Andrei Bernevig. Magnetic topological quantum chemistry. *Nature Communications*, 12(1):5965, 2021.

[57] A. Corticelli, R. Moessner, and P. A. McClarty. Spin-space groups and magnon band topology. *Phys. Rev. B*, 105:064430, Feb 2022.

[58] Qiao-Ru Xu, Vincent P. Flynn, Abhijeet Alase, Emilio Cobanera, Lorenza Viola, and Gerardo Ortiz. Squaring the fermion: The threefold way and the fate of zero modes. *Phys. Rev. B*, 102:125127, Sep 2020.

[59] Su-Yang Xu, Nasser Alidoust, Guoqing Chang, Hong Lu, Bahadur Singh, Ilya Belopolski, Daniel S. Sanchez, Xiao Zhang, Guang Bian, Hao Zheng, Marious-Adrian Husanu, Yi Bian, Shin-Ming Huang, Chuang-Han Hsu, Tay-Rong Chang, Horng-Tay Jeng, Arun Bansil, Titus Neupert, Vladimir N. Strocov, Hsin Lin, Shuang Jia, and M. Zahid Hasan. Discovery of Lorentz-violating type II Weyl fermions in LaAlGe. *Science Advances*, 3(6):e1603266, 2017.

[60] Chen Fang, Yige Chen, Hae-Young Kee, and Liang Fu. Topological nodal line semimetals with and without spin-orbital coupling. *Phys. Rev. B*, 92:081201(R), Aug 2015.

[61] G. E. Volovik. Quantum phase transitions from topology in momentum space. In William G. Unruh and Ralf Schützhold, editors, *Quantum Analogues: From Phase Transitions to Black Holes and Cosmology*, volume 718 of *Lecture Notes in Physics*, pages 31–73. Springer, Berlin, Heidelberg, 2007.

[62] Petr Hořava. Stability of Fermi surfaces and K theory. *Phys. Rev. Lett.*, 95:016405, Jun 2005.

[63] Y. X. Zhao and Z. D. Wang. Topological classification and stability of Fermi surfaces. *Phys. Rev. Lett.*, 110:240404, Jun 2013.

[64] Y. X. Zhao and Z. D. Wang. Topological connection between the stability of Fermi surfaces and topological insulators and superconductors. *Phys. Rev. B*, 89:075111, Feb 2014.

[65] Shuichi Murakami. Phase transition between the quantum spin Hall and insulator phases in 3D: emergence of a topological gapless phase. *New Journal of Physics*, 9(9):356, sep 2007.

[66] Xiangang Wan, Ari M. Turner, Ashvin Vishwanath, and Sergey Y. Savrasov. Topological semimetal and fermi-arc surface states in the electronic structure of pyrochlore iridates. *Phys. Rev. B*, 83:205101, May 2011.

[67] A. A. Burkov and Leon Balents. Weyl semimetal in a topological insulator multilayer. *Phys. Rev. Lett.*, 107:127205, Sep 2011.

[68] Gang Xu, Hongming Weng, Zhijun Wang, Xi Dai, and Zhong Fang. Chern semimetal and the quantized anomalous hall effect in $hgcr_2se_4$. *Phys. Rev. Lett.*, 107:186806, Oct 2011.

[69] Tobias Meng and Leon Balents. Weyl superconductors. *Phys. Rev. B*, 86:054504, Aug 2012.

[70] Tobias Meng and Leon Balents. Erratum: Weyl superconductors [Phys. Rev. B 86, 054504 (2012)]. *Phys. Rev. B*, 96:019901, Jul 2017.

[71] Jay D. Sau and Sumanta Tewari. Topologically protected surface majorana arcs and bulk weyl fermions in ferromagnetic superconductors. *Phys. Rev. B*, 86:104509, Sep 2012.

[72] S. M. Young, S. Zaheer, J. C. Y. Teo, C. L. Kane, E. J. Mele, and A. M. Rappe. Dirac semimetal in three dimensions. *Phys. Rev. Lett.*, 108:140405, Apr 2012.

[73] Zhijun Wang, Yan Sun, Xing-Qiu Chen, Cesare Franchini, Gang Xu, Hongming Weng, Xi Dai, and Zhong Fang. Dirac semimetal and topological phase transitions in A_3bi ($a =$ Na, k, rb). *Phys. Rev. B*, 85:195320, May 2012.

[74] Zhijun Wang, Hongming Weng, Quansheng Wu, Xi Dai, and Zhong Fang. Three-dimensional dirac semimetal and quantum transport in cd_3as_2. *Phys. Rev. B*, 88:125427, Sep 2013.

[75] Shengyuan A. Yang, Hui Pan, and Fan Zhang. Dirac and weyl superconductors in three dimensions. *Phys. Rev. Lett.*, 113:046401, Jul 2014.

[76] Tomáš Bzdušek and Manfred Sigrist. Robust doubly charged nodal lines and nodal surfaces in centrosymmetric systems. *Phys. Rev. B*, 96:155105, Oct 2017.

[77] Guoqing Chang, Benjamin J. Wieder, Frank Schindler, Daniel S. Sanchez, Ilya Belopolski, Shin-Ming Huang, Bahadur Singh, Di Wu, Tay-Rong Chang, Titus Neupert, Su-Yang Xu, Hsin Lin, and M. Zahid Hasan. Topological quantum properties of chiral crystals. *Nature Materials*, 17(11):978–985, 2018.

[78] Steve M. Young and Charles L. Kane. Dirac semimetals in two dimensions. *Phys. Rev. Lett.*, 115:126803, Sep 2015.

[79] Shingo Kobayashi, Youichi Yanase, and Masatoshi Sato. Topologically stable gapless phases in nonsymmorphic superconductors. *Phys. Rev. B*, 94:134512, Oct 2016.

[80] Wonjune Choi, Tomonari Mizoguchi, and Yong Baek Kim. Nonsymmorphic-symmetry-protected topological magnons in three-dimensional Kitaev materials. *Phys. Rev. Lett.*, 123:227202, Nov 2019.

[81] Han Wu, Alannah M. Hallas, Xiaochan Cai, Jianwei Huang, Ji Seop Oh, Vaideesh Loganathan, Ashley Weiland, Gregory T. McCandless, Julia Y. Chan, Sung-Kwan Mo, Donghui Lu, Makoto Hashimoto, Jonathan Denlinger, Robert J. Birgeneau, Andriy H. Nevidomskyy, Gang Li, Emilia Morosan, and Ming Yi. Nonsymmorphic symmetry-protected band crossings in a square-net metal ptpb4. *npj Quantum Materials*, 7(1):31, 2022.

[82] Yundi Quan, Valentin Taufour, and Warren E. Pickett. Nonsymmorphic band sticking in a topological superconductor. *Phys. Rev. B*, 105:064517, Feb 2022.

[83] Christopher Bradley and Arthur Cracknell. *The mathematical theory of symmetry in solids: representation theory for point groups and space groups.* Oxford University Press, 2009.

[84] Jérôme Cayssol. Introduction to Dirac materials and topological insulators. *Comptes Rendus Physique*, 14(9):760–778, 2013.

[85] E. Sadurní, E. Rivera-Mociños, and A. Rosado. Discrete symmetry in graphene: the Dirac equation and beyond. *Revista mexicana de física*, 61:170–181, Jun 2015.

[86] Makoto Hashimoto, Inna M. Vishik, Rui-Hua He, Thomas P. Devereaux, and Zhi-Xun Shen. Energy gaps in high-transition-temperature cuprate superconductors. *Nature Physics*, 10(7):483–495, 2014.

[87] Henrik Bruus and Karsten Flensberg. *Many-Body Quantum Theory in Condensed Matter Physics: An Introduction.* Oxford University Press, Oxford, United Kingdom, 2004.

[88] Su-Yang Xu, Nasser Alidoust, Ilya Belopolski, Zhujun Yuan, Guang Bian, Tay-Rong Chang, Hao Zheng, Vladimir N. Strocov, Daniel S. Sanchez, Guoqing Chang, Chenglong Zhang, Daixiang Mou, Yun Wu, Lunan Huang, Chi-Cheng Lee, Shin-Ming Huang, BaoKai Wang, Arun Bansil, Horng-Tay Jeng, Titus Neupert, Adam Kaminski, Hsin Lin, Shuang Jia, and M. Zahid Hasan. Discovery of a Weyl fermion state with Fermi arcs in niobium arsenide. *Nature Physics*, 11(9):748–754, 2015.

[89] John S. Townsend. *A Modern Approach to Quantum Mechanics*. University Science Books, Mill Valley, California, second edition, 2012.

[90] Andrey K. Geim and Allan H. MacDonald. Graphene: Exporing carbon flatland. *Physics Today*, 60(8):35–41, Aug 2007.

[91] A. H. Castro Neto, F. Guinea, Nuno M. R. Peres, Kostya S. Novoselov, and Andre K. Geim. The electronic properties of graphene. *Reviews of Modern Physics*, 81(1):109, 2009.

[92] J. C. Slonczewski and P. R. Weiss. Band structure of graphite. *Phys. Rev.*, 109:272–279, Jan 1958.

[93] E. Kogan. Symmetry classification of energy bands in graphene and silicene. *Graphene*, 2(2):74–80, 2013.

[94] Aaron Bostwick, Taisuke Ohta, Thomas Seyller, Karsten Horn, and Eli Rotenberg. Quasiparticle dynamics in graphene. *Nature Physics*, 3(1):36–40, 2007.

[95] M. I. Katsnelson, K. S. Novoselov, and A. K. Geim. Chiral tunnelling and the klein paradox in graphene. *Nature Physics*, 2(9):620–625, 2006.

[96] Gerardo G Naumis, Salvador Barraza-Lopez, Maurice Oliva-Leyva, and Humberto Terrones. Electronic and optical properties of strained graphene and other strained 2d materials: a review. *Reports on Progress in Physics*, 80(9):096501, 2017.

[97] Douglas J. Scalapino, Steven R. White, and Shoucheng Zhang. Insulator, metal, or superconductor: The criteria. *Phys. Rev. B*, 47:7995–8007, Apr 1993.

[98] Eva Y Andrei, Guohong Li, and Xu Du. Electronic properties of graphene: a perspective from scanning tunneling microscopy and magnetotransport. *Reports on Progress in Physics*, 75(5):056501, Apr 2012.

[99] Haijun Zhang, Chao-Xing Liu, Xiao-Liang Qi, Xi Dai, Zhong Fang, and Shou-Cheng Zhang. Topological insulators in Bi_2Se_3, Bi_2Te_3 and Sb_2Te_3 with a single Dirac cone on the surface. *Nature Physics*, 5(6):438–442, 2009.

[100] D. Hsieh, Y. Xia, D. Qian, L. Wray, J. H. Dil, F. Meier, J. Osterwalder, L. Patthey, J. G. Checkelsky, N. P. Ong, A. V. Fedorov, H. Lin, A. Bansil, D. Grauer, Y. S. Hor, R. J. Cava, and M. Z. Hasan. A tunable topological insulator in the spin helical dirac transport regime. *Nature*, 460(7259):1101–1105, 2009.

[101] James F. Annett. Symmetry of the order parameter for high-temperature superconductivity. *Advances in Physics*, 39(2):83–126, 1990.

[102] Elbio Dagotto. Correlated electrons in high-temperature superconductors. *Rev. Mod. Phys.*, 66:763–840, Jul 1994.

[103] Tom Timusk and Bryan Statt. The pseudogap in high-temperature superconductors: an experimental survey. *Reports on Progress in Physics*, 62(1):61–122, Jan 1999.

[104] C. C. Tsuei and J. R. Kirtley. Pairing symmetry in cuprate superconductors. *Rev. Mod. Phys.*, 72:969–1016, Oct 2000.

[105] M. R. Norman, D. Pines, and C. Kallin. The pseudogap: friend or foe of high T_c? *Advances in Physics*, 54(8):715–733, 2005.

[106] Patrick A. Lee, Naoto Nagaosa, and Xiao-Gang Wen. Doping a mott insulator: Physics of high-temperature superconductivity. *Rev. Mod. Phys.*, 78:17–85, Jan 2006.

[107] Matthias Vojta. Lattice symmetry breaking in cuprate superconductors: stripes, nematics, and superconductivity. *Advances in Physics*, 58(6):699–820, 2009.

[108] Louis Taillefer. Scattering and pairing in cuprate superconductors. *Annual Review of Condensed Matter Physics*, 1(1):51–70, 2010.

[109] N. P. Armitage, P. Fournier, and R. L. Greene. Progress and perspectives on electron-doped cuprates. *Rev. Mod. Phys.*, 82:2421–2487, Sep 2010.

[110] B. Keimer, S. A. Kivelson, M. R. Norman, S. Uchida, and J. Zaanen. From quantum matter to high-temperature superconductivity in copper oxides. *Nature*, 518(7538):179–186, 2015.

[111] Eduardo Fradkin, Steven A. Kivelson, and John M. Tranquada. Colloquium: Theory of intertwined orders in high temperature superconductors. *Rev. Mod. Phys.*, 87:457–482, May 2015.

[112] Cyril Proust and Louis Taillefer. The remarkable underlying ground states of cuprate superconductors. *Annual Review of Condensed Matter Physics*, 10(1):409–429, 2019.

[113] J. M. Tranquada. Cuprate superconductors as viewed through a striped lens. *Advances in Physics*, 69(4):437–509, 2020.

[114] Tao Li. A short review of the recent progresses in the study of the cuprate superconductivity. *Chinese Physics B*, 30(10):100508, Oct 2021.

[115] Xingjiang Zhou, Wei-Sheng Lee, Masatoshi Imada, Nandini Trivedi, Philip Phillips, Hae-Young Kee, Päivi Törmä, and Mikhail Eremets. High-temperature superconductivity. *Nature Reviews Physics*, 3(7):462–465, 2021.

[116] Robert Laughlin. Hiawatha's valence bonding. *Annals of Improbable Research*, 10:8–20, May–Jun 2004.

[117] Andrew Zangwill. *A Mind Over Matter: Philip Anderson and the Physics of the Very Many.* Oxford University Press, Oxford, UK, first edition, 2021.

[118] J. G. Bednorz and K. A. Müller. Possible high T_c superconductivity in the Ba–La–Cu–O system. *Zeitschrift für Physik B Condensed Matter*, 64(2):189–193, 1986.

[119] P. W. Anderson, P. A. Lee, M. Randeria, T. M. Rice, N. Trivedi, and F. C. Zhang. The physics behind high-temperature superconducting cuprates: the 'plain vanilla' version of RVB. *Journal of Physics: Condensed Matter*, 16(24):R755, 2004.

[120] Subir Sachdev and Bernhard Keimer. Quantum criticality. *Physics Today*, 64(2):29–35, 2011.

[121] Arun Paramekanti. Strong coupling aspects of superconductivity. In *Boulder School 2014: Modern Aspects of Superconductivity*, Boulder, Colorado, 2014. https://boulderschool.yale.edu/sites/default/files/files/Paramekanti-Notes.pdf.

[122] M. Moretti Sala, V. Bisogni, C. Aruta, G. Balestrino, H. Berger, N. B. Brookes, G. M. de Luca, D. Di Castro, M. Grioni, M. Guarise, P. G. Medaglia, F. Miletto Granozio, M. Minola, P. Perna, M. Radovic, M. Salluzzo, T. Schmitt, K. J. Zhou, L. Braicovich, and G. Ghiringhelli. Energy and symmetry of dd excitations in undoped layered cuprates measured by Cu L_3 resonant inelastic x-ray scattering. *New Journal of Physics*, 13(4):043026, Apr 2011.

[123] F. C. Zhang and T. M. Rice. Effective Hamiltonian for the superconducting Cu oxides. *Phys. Rev. B*, 37:3759–3761, Mar 1988.

[124] B. Edegger, V. N. Muthukumar, and C. Gros. Gutzwiller–RVB theory of high-temperature superconductivity: Results from renormalized mean-field theory and variational Monte Carlo calculations. *Advances in Physics*, 56(6):927–1033, 2007.

[125] F. C. Zhang, C. Gros, T. M. Rice, and H. Shiba. A renormalised Hamiltonian approach to a resonant valence bond wavefunction. *Superconductor Science and Technology*, 1(1):36, 1988.

[126] Arun Paramekanti, Mohit Randeria, and Nandini Trivedi. Projected wave functions and high temperature superconductivity. *Phys. Rev. Lett.*, 87:217002, Nov 2001.

[127] Arun Paramekanti, Mohit Randeria, and Nandini Trivedi. High-T_c superconductors: A variational theory of the superconducting state. *Phys. Rev. B*, 70:054504, Aug 2004.

[128] Claudius Gros. Physics of projected wavefunctions. *Annals of Physics*, 189(1):53–88, 1989.

[129] I. M. Vishik, W. S. Lee, F. Schmitt, B. Moritz, T. Sasagawa, S. Uchida, K. Fujita, S. Ishida, C. Zhang, T. P. Devereaux, and Z. X. Shen. Doping-dependent nodal Fermi velocity of the high-temperature superconductor $Bi_2Sr_2CaCu_2O_{8+\delta}$ revealed using high-resolution angle-resolved photoemission spectroscopy. *Phys. Rev. Lett.*, 104:207002, May 2010.

[130] B. Andrei Bernevig and Taylor L. Hughes. *Topological Insulators and Topological Superconductors.* Princeton University Press, Princeton, New Jersey, 2013.

[131] Pavan Hosur and Xiaoliang Qi. Recent developments in transport phenomena in weyl semimetals. *Comptes Rendus Physique*, 14(9):857–870, 2013. Topological insulators / Isolants topologiques.

[132] Roni Ilan, Adolfo G. Grushin, and Dmitry I. Pikulin. Pseudo-electromagnetic fields in 3D topological semimetals. *Nature Reviews Physics*, 2(1):29–41, 2020.

[133] N. Levy, S. A. Burke, K. L. Meaker, M. Panlasigui, A. Zettl, F. Guinea, A. H. Castro Neto, and M. F. Crommie. Strain-induced pseudo–magnetic fields greater than 300 tesla in graphene nanobubbles. *Science*, 329(5991):544–547, 2010.

[134] Alexander J. Pearce, Eros Mariani, and Guido Burkard. Tight-binding approach to strain and curvature in monolayer transition-metal dichalcogenides. *Phys. Rev. B*, 94:155416, Oct 2016.

[135] Héctor Ochoa, Ricardo Zarzuela, and Yaroslav Tserkovnyak. Emergent gauge fields from curvature in single layers of transition-metal dichalcogenides. *Phys. Rev. Lett.*, 118:026801, Jan 2017.

[136] M.A. Zubkov. Emergent gravity and chiral anomaly in dirac semimetals in the presence of dislocations. *Annals of Physics*, 360:655–678, 2015.

[137] D. I. Pikulin, Anffany Chen, and M. Franz. Chiral anomaly from strain-induced gauge fields in dirac and weyl semimetals. *Phys. Rev. X*, 6:041021, Oct 2016.

[138] Adolfo G. Grushin, Jörn W. F. Venderbos, Ashvin Vishwanath, and Roni Ilan. Inhomogeneous weyl and dirac semimetals: Transport in axial magnetic fields and fermi arc surface states from pseudo-landau levels. *Phys. Rev. X*, 6:041046, Dec 2016.

[139] Alberto Cortijo, Yago Ferreirós, Karl Landsteiner, and María A. H. Vozmediano. Elastic gauge fields in Weyl semimetals. *Phys. Rev. Lett.*, 115:177202, Oct 2015.

[140] Alberto Cortijo and M. A. Zubkov. Emergent gravity in the cubic tight-binding model of weyl semimetal in the presence of elastic deformations. *Annals of Physics*, 366:45–56, 2016.

[141] Juan L. Mañes, Fernando de Juan, Mauricio Sturla, and María A. H. Vozmediano. Generalized effective hamiltonian for graphene under nonuniform strain. *Phys. Rev. B*, 88:155405, Oct 2013.

[142] Tianyu Liu and Hai-Zhou Lu. Analytic solution to pseudo-landau levels in strongly bent graphene nanoribbons. *Phys. Rev. Research*, 4:023137, May 2022.

[143] Hui Yan, Yi Sun, Lin He, Jia-Cai Nie, and Moses H. W. Chan. Observation of Landau-level-like quantization at 77 K along a strained-induced graphene ridge. *Phys. Rev. B*, 85:035422, Jan 2012.

[144] C. Şahin, J. Rou, J. Ma, and D. A. Pesin. Pancharatnam-Berry phase and kinetic magnetoelectric effect in trigonal tellurium. *Physical Review B*, 97(20):205206, 2018.

[145] Manfred Fiebig, Thomas Lottermoser, Dennis Meier, and Morgan Trassin. The evolution of multiferroics. *Nature Reviews Materials*, 1(8):16046, 2016.

[146] Manfred Fiebig. Revival of the magnetoelectric effect. *Journal of Physics D: Applied Physics*, 38(8):R123, 2005.

[147] Nicola A. Spaldin and Manfred Fiebig. The renaissance of magnetoelectric multiferroics. *Science*, 309(5733):391–392, 2005.

[148] Nicola A. Spaldin, Sang-Wook Cheong, and Ramamoorthy Ramesh. Multiferroics: Past, present, and future. *Physics Today*, 63(10):38–43, 2010.

[149] Chung Ming Leung, Jiefang Li, D. Viehland, and X Zhuang. A review on applications of magnetoelectric composites: From heterostructural uncooled magnetic sensors, energy harvesters to highly efficient power converters. *Journal of Physics D: Applied Physics*, 51(26):263002, 2018.

[150] John Frederick Nye. *Physical Properties of Crystals: Their Representation by Tensors and Matrices.* Oxford University Press, 1957.

[151] Taiki Yoda, Takehito Yokoyama, and Shuichi Murakami. Orbital Edelstein effect as a condensed-matter analog of solenoids. *Nano Letters*, 18(2):916–920, 2018.

[152] J. Rou, C. Şahin, J. Ma, and D. A. Pesin. Kinetic orbital moments and nonlocal transport in disordered metals with nontrivial band geometry. *Physical Review B*, 96(3):035120, 2017.

[153] Wen-Yu He and K. T. Law. Magnetoelectric effects in gyrotropic superconductors. *Phys. Rev. Research*, 2:012073, Mar 2020.

[154] A. G. Aronov and Y. B.. Lyanda-Geller. Nuclear electric resonance and orientation of carrier spins by an electric field. *JETP Lett.*, 50:431–434, 1989.

[155] V. M. Edelstein. Spin polarization of conduction electrons induced by electric current in two-dimensional asymmetric electron systems. *Solid State Communications*, 73(3):233–235, 1990.

[156] Jairo Sinova, Sergio O. Valenzuela, J. Wunderlich, C. H. Back, and T. Jungwirth. Spin Hall effects. *Reviews of Modern Physics*, 87(4):1213, 2015.

[157] Aurelien Manchon, Hyun Cheol Koo, Junsaku Nitta, S. M. Frolov, and R. A. Duine. New perspectives for Rashba spin–orbit coupling. *Nature Materials*, 14(9):871, 2015.

[158] Vanessa Sih, R. C. Myers, Y. K. Kato, W. H. Lau, A. C. Gossard, and D. D. Awschalom. Spatial imaging of the spin Hall effect and current-induced polarization in two-dimensional electron gases. *Nature Physics*, 1(1):31, 2005.

[159] Satoshi Fujimoto. Magnetoelectric effects in heavy-fermion superconductors without inversion symmetry. *Phys. Rev. B*, 72:024515, Jul 2005.

[160] Shudan Zhong, Joel E. Moore, and Ivo Souza. Gyrotropic magnetic effect and the magnetic moment on the Fermi surface. *Physical Review Letters*, 116(7):077201, 2016.

[161] Neil W. Ashcroft and N. David Mermin. *Solid State Physics*. Holt, Rinehart and Winston, 1976.

[162] Taiki Yoda, Takehito Yokoyama, and Shuichi Murakami. Current-induced orbital and spin magnetizations in crystals with helical structure. *Scientific Reports*, 5:12024, 2015.

[163] Ganesh Sundaram and Qian Niu. Wave-packet dynamics in slowly perturbed crystals: Gradient corrections and Berry-phase effects. *Phys. Rev. B*, 59:14915–14925, Jun 1999.

[164] Ming-Che Chang and Qian Niu. Berry phase, hyperorbits, and the hofstadter spectrum: Semiclassical dynamics in magnetic Bloch bands. *Phys. Rev. B*, 53:7010–7023, Mar 1996.

[165] Di Xiao, Junren Shi, and Qian Niu. Berry phase correction to electron density of states in solids. *Phys. Rev. Lett.*, 95:137204, Sep 2005.

[166] Di Xiao, Yugui Yao, Zhong Fang, and Qian Niu. Berry-phase effect in anomalous thermoelectric transport. *Phys. Rev. Lett.*, 97:026603, Jul 2006.

[167] Junren Shi, G. Vignale, Di Xiao, and Qian Niu. Quantum theory of orbital magnetization and its generalization to interacting systems. *Phys. Rev. Lett.*, 99:197202, Nov 2007.

[168] Raffaele Resta. Electrical polarization and orbital magnetization: the modern theories. *Journal of Physics: Condensed Matter*, 22(12):123201, 2010.

[169] Tetsuya Furukawa, Yuri Shimokawa, Kaya Kobayashi, and Tetsuaki Itou. Observation of current-induced bulk magnetization in elemental tellurium. *Nature Communications*, 8(1):954, 2017.

[170] S. D. Ganichev, E. L. Ivchenko, V. V. Bel'kov, S. A. Tarasenko, M. Sollinger, D. Weiss, W. Wegscheider, and W. Prettl. Spin-galvanic effect. *Nature*, 417(6885):153–156, 2002.

[171] Y. Shiomi, K. Nomura, Y. Kajiwara, K. Eto, M. Novak, Kouji Segawa, Yoichi Ando, and E. Saitoh. Spin-electricity conversion induced by spin injection into topological insulators. *Phys. Rev. Lett.*, 113:196601, Nov 2014.

[172] C. H. Li, O. M. J. van 't Erve, J. T. Robinson, Y. Liu, L. Li, and B. T. Jonker. Electrical detection of charge-current-induced spin polarization due to spin-momentum locking in Bi_2Se_3. *Nature Nanotechnology*, 9(3):218–224, 2014.

[173] Yuichiro Ando, Takahiro Hamasaki, Takayuki Kurokawa, Kouki Ichiba, Fan Yang, Mario Novak, Satoshi Sasaki, Kouji Segawa, Yoichi Ando, and Masashi Shiraishi. Electrical detection of the spin polarization due to charge flow in the surface state of the topological insulator $Bi_{1.5}Sb_{0.5}Te_{1.7}Se_{1.3}$. *Nano Letters*, 14(11):6226–6230, 11 2014.

[174] Jifa Tian, Ireneusz Miotkowski, Seokmin Hong, and Yong P. Chen. Electrical injection and detection of spin-polarized currents in topological insulator Bi_2Te_2Se. *Scientific Reports*, 5(1):14293, 2015.

[175] J.-C. Rojas-Sánchez, S. Oyarzún, Y. Fu, A. Marty, C. Vergnaud, S. Gambarelli, L. Vila, M. Jamet, Y. Ohtsubo, A. Taleb-Ibrahimi, P. Le Fèvre, F. Bertran, N. Reyren, J.-M. George, and A. Fert. Spin to charge conversion at room temperature by spin pumping into a new type of topological insulator: α-Sn films. *Phys. Rev. Lett.*, 116:096602, Mar 2016.

[176] K. Kondou, R. Yoshimi, A. Tsukazaki, Y. Fukuma, J. Matsuno, K. S. Takahashi, M. Kawasaki, Y. Tokura, and Y. Otani. Fermi-level-dependent charge-to-spin current conversion by Dirac surface states of topological insulators. *Nature Physics*, 12(11):1027–1031, 2016.

[177] Qi Song, Jian Mi, Dan Zhao, Tang Su, Wei Yuan, Wenyu Xing, Yangyang Chen, Tianyu Wang, Tao Wu, Xian Hui Chen, X. C. Xie, Chi Zhang, Jing Shi, and Wei Han. Spin injection and inverse edelstein effect in the surface states of topological kondo insulator SmB_6. *Nature Communications*, 7(1):13485, 2016.

[178] Victor M. Edelstein. Magnetoelectric effect in polar superconductors. *Phys. Rev. Lett.*, 75:2004–2007, Sep 1995.

[179] S. K. Yip. Two-dimensional superconductivity with strong spin-orbit interaction. *Phys. Rev. B*, 65:144508, Mar 2002.

[180] Victor M. Edelstein. Triplet superconductivity and magnetoelectric effect near the s-wave-superconductor–normal-metal interface caused by local breaking of mirror symmetry. *Phys. Rev. B*, 67:020505, Jan 2003.

[181] Victor M. Edelstein. Magnetoelectric effect in dirty superconductors with broken mirror symmetry. *Phys. Rev. B*, 72:172501, Nov 2005.

[182] Teemu Ojanen. Magnetoelectric effects in superconducting nanowires with Rashba spin-orbit coupling. *Phys. Rev. Lett.*, 109:226804, Nov 2012.

[183] François Konschelle, Ilya V. Tokatly, and F. Sebastián Bergeret. Theory of the spin-galvanic effect and the anomalous phase shift φ_0 in superconductors and Josephson junctions with intrinsic spin-orbit coupling. *Phys. Rev. B*, 92:125443, Sep 2015.

[184] Morten Amundsen and Jacob Linder. Supercurrent vortex pinball via a triplet Cooper pair inverse Edelstein effect. *Phys. Rev. B*, 96:064508, Aug 2017.

[185] Wen-Yu He and K. T. Law. Superconducting orbital magnetoelectric effect and its evolution across the superconductor-normal metal phase transition. *Phys. Rev. Research*, 3:L032012, Jul 2021.

[186] Max Lein and Koji Sato. Krein-Schrödinger formalism of bosonic Bogoliubov–de Gennes and certain classical systems and their topological classification. *Phys. Rev. B*, 100:075414, Aug 2019.

[187] Vincent P Flynn, Emilio Cobanera, and Lorenza Viola. Deconstructing effective non-Hermitian dynamics in quadratic bosonic Hamiltonians. *New Journal of Physics*, 22(8):083004, aug 2020.

[188] Vincent P. Flynn, Emilio Cobanera, and Lorenza Viola. Restoring number conservation in quadratic bosonic Hamiltonians with dualities. *EPL (Europhysics Letters)*, 131(4):40006, Semptember 2020.

[189] Yuki Kawaguchi and Masahito Ueda. Spinor Bose-Einstein condensates. *Physics Reports*, 520(5):253–381, 2012.

[190] Lloyd N. Trefethen and Mark Embree. *Spectra and Pseudospectra: The Behavior of Nonnormal Matrices and Operators.* Princeton University Press, 41 William Street, Princeton, New Jersey 08540, 2005.

[191] G. W. Stewart and J. Sun. Matrix perturbation theory. In Werner Reinboldt and Daniel Siewiorek, editors, *Computer Science and Scientific Computing.* Academic Press, inc., Boston, 1990.

[192] B. Amorim, A. Cortijo, F. de Juan, A. G. Grushin, F. Guinea, A. Gutiérrez-Rubio, H. Ochoa, V. Parente, R. Roldán, P. San-Jose, J. Schiefele, M. Sturla, and M. A. H. Vozmediano. Novel effects of strains in graphene and other two dimensional materials. *Physics Reports*, 617:1 – 54, 2016.

[193] F. Guinea, M. I. Katsnelson, and A. K. Geim. Energy gaps and a zero-field quantum hall effect in graphene by strain engineering. *Nat Phys*, 6(1):30–33, 01 2010.

[194] María A. H. Vozmediano, M. I. Katsnelson, and Francisco Guinea. Gauge fields in graphene. *Physics Reports*, 496(4):109–148, 2010.

[195] Kenjiro K. Gomes, Warren Mar, Wonhee Ko, Francisco Guinea, and Hari C. Manoharan. Designer Dirac fermions and topological phases in molecular graphene. *Nature*, 483(7389):306–310, 03 2012.

[196] Ilija Zeljkovic, Daniel Walkup, Badih A. Assaf, Kane L. Scipioni, R. Sankar, Fangcheng Chou, and Vidya Madhavan. Strain engineering Dirac surface states in heteroepitaxial topological crystalline insulator thin films. *Nat. Nano.*, 10(10):849–853, 10 2015.

[197] Jian Liu, D. Kriegner, L. Horak, D. Puggioni, C. Rayan Serrao, R. Chen, D. Yi, C. Frontera, V. Holy, A. Vishwanath, J. M. Rondinelli, X. Marti, and R. Ramesh. Strain-induced nonsymmorphic symmetry breaking and removal of Dirac semimetallic nodal line in an orthoperovskite iridate. *Phys. Rev. B*, 93:085118, Feb 2016.

[198] Masayuki Ochi, Ryotaro Arita, Nandini Trivedi, and Satoshi Okamoto. Strain-induced topological transition in $SrRu_2O_6$ and $CaOs_2O_6$. *Phys. Rev. B*, 93:195149, May 2016.

[199] Liyan Zhu, Shan-Shan Wang, Shan Guan, Ying Liu, Tingting Zhang, Guibin Chen, and Shengyuan A. Yang. Blue phosphorene oxide: Strain-tunable quantum phase transitions and novel 2D emergent fermions. *Nano Letters*, 16(10):6548–6554, 2016. PMID: 27648670.

[200] C. Rayan Serrao, Jian Liu, J. T. Heron, G. Singh-Bhalla, A. Yadav, S. J. Suresha, R. J. Paull, D. Yi, J.-H. Chu, M. Trassin, A. Vishwanath, E. Arenholz, C. Frontera, J. Železný, T. Jungwirth, X. Marti, and R. Ramesh. Epitaxy-distorted spin-orbit Mott insulator in Sr_2IrO_4 thin films. *Phys. Rev. B*, 87:085121, Feb 2013.

[201] A. Lupascu, J. P. Clancy, H. Gretarsson, Zixin Nie, J. Nichols, J. Terzic, G. Cao, S. S. A. Seo, Z. Islam, M. H. Upton, Jungho Kim, D. Casa, T. Gog, A. H. Said, Vamshi M. Katukuri, H. Stoll, L. Hozoi, J. van den Brink, and Young-June Kim. Tuning magnetic coupling in Sr_2IrO_4 thin films with epitaxial strain. *Phys. Rev. Lett.*, 112:147201, Apr 2014.

[202] K. J. Choi, M. Biegalski, Y. L. Li, A. Sharan, J. Schubert, R. Uecker, P. Reiche, Y. B. Chen, X. Q. Pan, V. Gopalan, L.-Q. Chen, D. G. Schlom, and C. B. Eom. Enhancement of ferroelectricity in strained $BaTiO_3$ thin films. *Science*, 306(5698):1005–1009, 2004.

[203] Clifford W. Hicks, Daniel O. Brodsky, Edward A. Yelland, Alexandra S. Gibbs, Jan A. N. Bruin, Mark E. Barber, Stephen D. Edkins, Keigo Nishimura, Shingo Yonezawa, Yoshiteru Maeno, et al. Strong increase of T_c of Sr_2RuO_4 under both tensile and compressive strain. *Science*, 344(6181):283–285, 2014.

[204] Hsueh-Hui Kuo, Jiun-Haw Chu, Johanna C. Palmstrom, Steven A. Kivelson, and Ian R. Fisher. Ubiquitous signatures of nematic quantum criticality in optimally doped Fe-based superconductors. *Science*, 352(6288):958–962, 2016.

[205] Scott C. Riggs, M. C. Shapiro, Akash V. Maharaj, S. Raghu, E. D. Bauer, R. E. Baumbach, P. Giraldo-Gallo, Mark Wartenbe, and I. R. Fisher. Evidence for a nematic component to the hidden-order parameter in URu_2Si_2 from differential elastoresistance measurements. *Nat. Comm.*, 6:6425 EP –, 03 2015.

[206] Eun-Ah Kim and A. H. Castro Neto. Graphene as an electronic membrane. *EPL (Europhysics Letters)*, 84(5):57007, 2008.

[207] Vinu Lukose, R. Shankar, and G. Baskaran. Novel electric field effects on landau levels in graphene. *Phys. Rev. Lett.*, 98:116802, Mar 2007.

[208] Alejandro A. Pacheco Sanjuan, Zhengfei Wang, Hamed Pour Imani, Mihajlo Vanević, and Salvador Barraza-Lopez. Graphene's morphology and electronic properties from discrete differential geometry. *Phys. Rev. B*, 89:121403, Mar 2014.

[209] E. V. Castro, M. A. Cazalilla, and M. A. H. Vozmediano. Raise and collapse of strain-induced pseudo-Landau levels in graphene. *ArXiv e-prints*, October 2016.

[210] L. Covaci and F. M. Peeters. Superconducting proximity effect in graphene under inhomogeneous strain. *Phys. Rev. B*, 84:241401, Dec 2011.

[211] K. G. S. H. Gunawardana and Bruno Uchoa. Andreev reflection in edge states of time-reversal-invariant Landau levels. *Phys. Rev. B*, 91:241402, Jun 2015.

[212] Pouyan Ghaemi, Jérôme Cayssol, D. N. Sheng, and Ashvin Vishwanath. Fractional topological phases and broken time-reversal symmetry in strained graphene. *Phys. Rev. Lett.*, 108:266801, Jun 2012.

[213] Bruno Uchoa and Yafis Barlas. Superconducting states in pseudo-Landau-levels of strained graphene. *Phys. Rev. Lett.*, 111:046604, Jul 2013.

[214] Alberto Cortijo, Dmitri Kharzeev, Karl Landsteiner, and Maria A. H. Vozmediano. Strain-induced chiral magnetic effect in Weyl semimetals. *Phys. Rev. B*, 94:241405, Dec 2016.

[215] P. Rinkel, P. L. S. Lopes, and I. Garate. Signatures of the chiral anomaly in phonon dynamics. *ArXiv e-prints*, oct 2016.

[216] Tianyu Liu, D. I. Pikulin, and M. Franz. Quantum oscillations without magnetic field. *Physical Review B*, 95(4):041201, 2017.

[217] Stephan Rachel, Lars Fritz, and Matthias Vojta. Landau levels of majorana fermions in a spin liquid. *Phys. Rev. Lett.*, 116:167201, Apr 2016.

[218] Jean Dalibard, Fabrice Gerbier, Gediminas Juzeliūnas, and Patrik Öhberg. Colloquium: Artificial gauge potentials for neutral atoms. *Rev. Mod. Phys.*, 83:1523–1543, Nov 2011.

[219] Binbin Tian, Manuel Endres, and David Pekker. Landau levels in strained optical lattices. *Phys. Rev. Lett.*, 115:236803, Dec 2015.

[220] Eun-Ah Kim, Michael J. Lawler, Paul Oreto, Subir Sachdev, Eduardo Fradkin, and Steven A. Kivelson. Theory of the nodal nematic quantum phase transition in superconductors. *Phys. Rev. B*, 77:184514, May 2008.

[221] Pierre Gilles De Gennes. *Superconductivity of metals and alloys.* Addison-Wesley, Boston, 1989.

[222] Satoshi Kashiwaya and Yukio Tanaka. Tunnelling effects on surface bound states in unconventional superconductors. *Reports on Progress in Physics*, 63(10):1641, 2000.

[223] T. L.öfwander, V. S. Shumeiko, and G. Wendin. Andreev bound states in high-T_c superconducting junctions. *Superconductor Science and Technology*, 14(5):R53, 2001.

[224] Guy Deutscher. Andreev–Saint-James reflections: A probe of cuprate superconductors. *Rev. Mod. Phys.*, 77:109–135, Mar 2005.

[225] Matthew W. Hooker. Properties of PZT-based piezoelectric ceramics between −150 and 250 °C. 1998.

[226] S. Trolier-McKinstry and P. Muralt. Thin film piezoelectrics for MEMS. *Journal of Electroceramics*, 12(1):7–17, Jan 2004.

[227] Gabriel Kotliar and Jialin Liu. Superexchange mechanism and d-wave superconductivity. *Phys. Rev. B*, 38:5142–5145, Sep 1988.

[228] M. C. Aronson, S. B. Dierker, B. S. Dennis, S.-W. Cheong, and Z. Fisk. Pressure dependence of the superexchange interaction in antiferromagnetic La_2CuO_4. *Phys. Rev. B*, 44:4657–4660, Sep 1991.

[229] J. A. Bonetti, D. S. Caplan, D. J. Van Harlingen, and M. B. Weissman. Electronic transport in underdoped $YBa_2Cu_3O_{7-\delta}$ nanowires: Evidence for fluctuating domain structures. *Phys. Rev. Lett.*, 93:087002, Aug 2004.

[230] V. Hinkov, D. Haug, B. Fauqué, P. Bourges, Y. Sidis, A. Ivanov, C. Bernhard, C. T. Lin, and B. Keimer. Electronic liquid crystal state in the high-temperature superconductor $YBa_2Cu_3O_{6.45}$. *Science*, 319(5863):597–600, 2008.

[231] R. Daou, J. Chang, David LeBoeuf, Olivier Cyr-Choiniere, Francis Laliberte, Nicolas Doiron-Leyraud, B. J. Ramshaw, Ruixing Liang, D. A. Bonn, W. N. Hardy, and Louis Taillefer. Broken rotational symmetry in the pseudogap phase of a high-T_c superconductor. *Nature*, 463(7280):519–522, 01 2010.

[232] M. J. Lawler, K. Fujita, Jhinhwan Lee, A. R. Schmidt, Y. Kohsaka, Chung Koo Kim, H. Eisaki, S. Uchida, J. C. Davis, J. P. Sethna, and Eun-Ah Kim. Intra-unit-cell electronic nematicity of the high-T_c copper-oxide pseudogap states. *Nature*, 466(7304):347–351, 07 2010.

[233] Y. Sato, S. Kasahara, H. Murayama, Y. Kasahara, E.-G. Moon, T. Nishizaki, T. Loew, J. Porras, B. Keimer, T. Shibauchi, and Y. Matsuda. Thermodynamic evidence for nematic phase transition at the onset of pseudogap in $YBa_2Cu_3O_y$. *ArXiv e-prints*, jun 2017.

[234] S. Okamoto, D. Sénéchal, M. Civelli, and A.-M. S. Tremblay. Dynamical electronic nematicity from Mott physics. *Phys. Rev. B*, 82:180511, Nov 2010.

[235] A. V. Mallik, U. K. Yadav, A. Medhi, H. R. Krishnamurthy, and V. B. Shenoy. Crucial role of Internal Collective Modes in Underdoped Cuprates. *ArXiv e-prints*, March 2016.

[236] W. Eerenstein, N. D. Mathur, and J. F. Scott. Multiferroic and magnetoelectric materials. *Nature*, 442:759–765, 2006.

[237] Ramaroorthy Ramesh and Nicola A. Spaldin. Multiferroics: Progress and prospects in thin films. *Nature materials*, 6(1):21, 2007.

[238] Sang-Wook Cheong and Maxim Mostovoy. Multiferroics: a magnetic twist for ferroelectricity. *Nature Materials*, 6(1):13, 2007.

[239] G. Lawes and G. Srinivasan. Introduction to magnetoelectric coupling and multiferroic films. *Journal of Physics D: Applied Physics*, 44(24):243001, 2011.

[240] L. E. Fuentes-Cobas, J. A. Matutes-Aquino, M. E. Botello-Zubiate, A. González-Vázquez, M. E. Fuentes-Montero, and D. Chateigner. Chapter 3 - advances in magnetoelectric materials and their application. In K. H. J. Buschow, editor, *Handbook of Magnetic Materials*, volume 24, pages 237–322. Elsevier, 2015.

[241] Zhaoqiang Chu, MohammadJavad PourhosseiniAsl, and Shuxiang Dong. Review of multi-layered magnetoelectric composite materials and devices applications. *Journal of Physics D: Applied Physics*, 51(24):243001, 2018.

[242] M. Zahid Hasan and Charles L. Kane. Colloquium: Topological insulators. *Reviews of Modern Physics*, 82(4):3045, 2010.

[243] Xiao-Liang Qi and Shou-Cheng Zhang. Topological insulators and superconductors. *Reviews of Modern Physics*, 83(4):1057, 2011.

[244] Adolfo G. Grushin and Fernando de Juan. Finite-frequency magnetoelectric response of three-dimensional topological insulators. *Physical Review B*, 86:075126, 2012.

[245] D. A. Pesin and A. H. MacDonald. Topological magnetoelectric effect decay. *Physical Review Letters*, 111(1):016801, 2013.

[246] D. Schmeltzer and Avadh Saxena. Magnetoelectric effect induced by electron–electron interaction in three dimensional topological insulators. *Physics Letters A*, 377(25-27):1631–1636, 2013.

[247] A. G. Mal'Shukov, Hans Skarsvåg, and Arne Brataas. Nonlinear magneto-optical and magnetoelectric phenomena in topological insulator heterostructures. *Physical Review B*, 88(24):245122, 2013.

[248] Dashdeleg Baasanjav, O. A. Tretiakov, and Kentaro Nomura. Magnetoelectric effect in topological insulator films beyond the linear response regime. *Physical Review B*, 90(4):045149, 2014.

[249] Takahiro Morimoto, Akira Furusaki, and Naoto Nagaosa. Topological magnetoelectric effects in thin films of topological insulators. *Physical Review B*, 92(8):085113, 2015.

[250] Di Xiao, Jue Jiang, Jae-Ho Shin, Wenbo Wang, Fei Wang, Yi-Fan Zhao, Chaoxing Liu, Weida Wu, Moses H. W. Chan, Nitin Samarth, and Cui-Zu Chang. Realization of the axion insulator state in quantum anomalous Hall sandwich heterostructures. *Physical Review Letters*, 120(5):056801, 2018.

[251] Yoshinori Tokura, Kenji Yasuda, and Atsushi Tsukazaki. Magnetic topological insulators. *Nature Reviews Physics*, 1(2):126–143, 2019.

[252] L. S. Levitov, Yu V. Nazarov, and G. M. Eliashberg. Magnetoelectric effects in conductors with mirror isomer symmetry. *Sov. Phys. JETP*, 61(1):133–137, 1985.

[253] Sergey D. Ganichev, Maxim Trushin, and John Schliemann. Spin polarisation by current. In Evgeny Y. Tsymbal and Igor Zutic, editors, *Handbook of Spin Transport and Magnetism*, pages 504–513. Chapman and Hall/CRC, 2 edition, 2016.

[254] Y. K. Kato, R. C. Myers, A. C. Gossard, and D. D. Awschalom. Current-induced spin polarization in strained semiconductors. *Physical Review Letters*, 93(17):176601, 2004.

[255] A. Yu Silov, P. A. Blajnov, J. H. Wolter, R. Hey, K. H. Ploog, and N. S. Averkiev. Current-induced spin polarization at a single heterojunction. *Applied Physics Letters*, 85(24):5929–5931, 2004.

[256] Y. K. Kato, R. C. Myers, A. C. Gossard, and D. D. Awschalom. Electrical initialization and manipulation of electron spins in an L-shaped strained n-InGaAs channel. *Applied Physics Letters*, 87(2):022503, 2005.

[257] N. P. Stern, S. Ghosh, G. Xiang, M. Zhu, N. Samarth, and D. D. Awschalom. Current-induced polarization and the spin Hall effect at room temperature. *Physical Review Letters*, 97(12):126603, 2006.

[258] C. L. Yang, H. T. He, Lu Ding, L. J. Cui, Y. P. Zeng, J. N. Wang, and W. K. Ge. Spectral dependence of spin photocurrent and current-induced spin polarization in an InGaAs/InAlAs two-dimensional electron gas. *Phys. Rev. Lett.*, 96:186605, May 2006.

[259] H. J. Zhang, S. Yamamoto, Y. Fukaya, M. Maekawa, H. Li, A. Kawasuso, T. Seki, E. Saitoh, and K. Takanashi. Current-induced spin polarization on metal surfaces probed by spin-polarized positron beam. *Scientific Reports*, 4:4844, 2014.

[260] V. A. Shalygin, A. N. Sofronov, L. E. Vorob'ev, and I. I. Farbshtein. Current-induced spin polarization of holes in tellurium. *Physics of the Solid State*, 54(12):2362–2373, 2012.

[261] Stepan S. Tsirkin, Pablo Aguado Puente, and Ivo Souza. Gyrotropic effects in trigonal tellurium studied from first principles. *Physical Review B*, 97:035158, 2018.

[262] Felix Flicker, Fernando de Juan, Barry Bradlyn, Takahiro Morimoto, Maia G. Vergniory, and Adolfo G. Grushin. Chiral optical response of multifold fermions. *Physical Review B*, 98:155145, 2018.

[263] Chengwang Niu, Jan-Philipp Hanke, Patrick M. Buhl, Hongbin Zhang, Lukasz Plucinski, Daniel Wortmann, Stefan Blügel, Gustav Bihlmayer, and Yuriy Mokrousov. Mixed topological semimetals and orbital magnetism in two-dimensional spin-orbit ferromagnets. *arXiv e-prints*, page arXiv:1805.02549, May 2018.

[264] Li-kun Shi and Justin C. W. Song. Symmetry, spin-texture, and tunable quantum geometry in a WTe_2 monolayer. *Physical Review B*, 99(3):035403, 2019.

[265] Ana Silva, Jans Henke, and Jasper van Wezel. Elemental chalcogens as a minimal model for combined charge and orbital order. *Physical Review B*, 97(4):045151, 2018.

[266] Martin Gradhand and Jasper van Wezel. Optical gyrotropy and the nonlocal Hall effect in chiral charge-ordered $TiSe_2$. *Physical Review B*, 92(4):041111, 2015.

[267] J. Orenstein and Joel E. Moore. Berry phase mechanism for optical gyrotropy in stripe-ordered cuprates. *Physical Review B*, 87(16):165110, 2013.

[268] T. Thonhauser. Theory of orbital magnetization in solids. *International Journal of Modern Physics B*, 25(11):1429–1458, 2011.

[269] David Vanderbilt. *Berry Phases in Electronic Structure Theory: Electric Polarization, Orbital Magnetization and Topological Insulators.* Cambridge University Press, 2018.

[270] Raffaele Resta. Electrical polarization and orbital magnetization: The position operator tamed. *Handbook of Materials Modeling: Methods: Theory and Modeling*, pages 1–31, 2018.

[271] Di Xiao, Ming-Che Chang, and Qian Niu. Berry phase effects on electronic properties. *Reviews of Modern Physics*, 82(3):1959, 2010.

[272] L. D. Landau and E. M. Lifshitz. *Electrodynamics of Continuous Media*, volume 8 of *Course of Theoretical Physics.* Pergamon Press, 1960.

[273] Takayuki Ishitobi and Kazumasa Hattori. Magnetoelectric effects and charge-imbalanced solenoids: Antiferro quadrupole orders in a diamond structure. *Journal of the Physical Society of Japan*, 88(6):063708, 2019.

[274] Fabio Bagarello, Jean-Pierre Gazeau, Franciszek Hugon Szafraniec, and Miloslav Znojil, editors. *Non-Selfadjoint Operators in Quantum Physics.* John Wiley & Sons, Ltd, 2015.

[275] J.H.P. Colpa. Diagonalization of the quadratic boson hamiltonian. *Physica A: Statistical Mechanics and its Applications*, 93(3):327–353, 1978.

[276] Jean-Paul Blaizot and Georges Ripka. *Quantum theory of finite systems.* MIT Press, Cambridge, MA, 1986.

[277] S. Shivam, R. Coldea, R. Moessner, and P. McClarty. Neutron Scattering Signatures of Magnon Weyl Points. *arXiv e-prints*, page arXiv:1712.08535, December 2017.

[278] P. A. McClarty, X.-Y. Dong, M. Gohlke, J. G. Rau, F. Pollmann, R. Moessner, and K. Penc. Topological magnons in Kitaev magnets at high fields. *Phys. Rev. B*, 98:060404(R), Aug 2018.

[279] Fuyan Lu and Yuan-Ming Lu. Magnon band topology in spin-orbital coupled magnets: classification and application to α-$RuCl_3$. *arXiv e-prints*, page arXiv:1807.05232, July 2018.

[280] Zongping Gong, Yuto Ashida, Kohei Kawabata, Kazuaki Takasan, Sho Higashikawa, and Masahito Ueda. Topological phases of Non-Hermitian systems. *Phys. Rev. X*, 8:031079, Sep 2018.

[281] Kohei Kawabata, Ken Shiozaki, Masahito Ueda, and Masatoshi Sato. Symmetry and topology in non-Hermitian physics. *Phys. Rev. X*, 9:041015, Oct 2019.

[282] Paul A. McClarty and Jeffrey G. Rau. Non-Hermitian topology of spontaneous magnon decay. *Phys. Rev. B*, 100:100405(R), Sep 2019.

[283] P. Sathish Kumar, Igor F. Herbut, and R. Ganesh. Dirac Hamiltonians for bosonic spectra. *Phys. Rev. Research*, 2:033035, Jul 2020.

[284] Carl M Bender, Stefan Boettcher, and Peter N Meisinger. PT-symmetric quantum mechanics. *Journal of Mathematical Physics*, 40(5):2201–2229, 1999.

[285] Carl M Bender. Making sense of non-Hermitian Hamiltonians. *Reports on Progress in Physics*, 70(6):947–1018, may 2007.

[286] Ali Mostafazadeh. Pseudo-Hermiticity versus PT symmetry: The necessary condition for the reality of the spectrum of a non-Hermitian Hamiltonian. *Journal of Mathematical Physics*, 43(1):205–214, 2002.

[287] Ali Mostafazadeh. Pseudo-Hermiticity versus PT symmetry. ii. a complete characterization of non-Hermitian Hamiltonians with a real spectrum. *Journal of Mathematical Physics*, 43(5):2814–2816, 2002.

[288] Ali Mostafazadeh. Pseudo-Hermiticity versus PT symmetry iii: Equivalence of pseudo-Hermiticity and the presence of antilinear symmetries. *Journal of Mathematical Physics*, 43(8):3944–3951, 2002.

[289] Ali Mostafazadeh. Krein-space formulation of $\mathcal{PT}$ symmetry, $\mathcal{CPT}$-inner products, and pseudo-Hermiticity. *Czechoslovak Journal of Physics*, 56(9):919–933, 2006.

[290] Toshiaki Tanaka. PT-symmetric quantum theory defined in a Krein space. *Journal of Physics A: Mathematical and General*, 39(22):L369–L376, may 2006.

[291] Toshiaki Tanaka. General aspects of PT-symmetric and P-self-adjoint quantum theory in a Krein space. *Journal of Physics A: Mathematical and General*, 39(45):14175–14203, oct 2006.

[292] Sergio Albeverio and Sergii Kuzhel. *PT-Symmetric Operators in Quantum Mechanics: Krein Spaces Methods*, chapter 6, pages 293–344. John Wiley & Sons, Ltd, 2015.

[293] Ramy El-Ganainy, Konstantinos G Makris, Mercedeh Khajavikhan, Ziad H Musslimani, Stefan Rotter, and Demetrios N Christodoulides. Non-Hermitian physics and PT symmetry. *Nature Physics*, 14(1):11–19, 2018.

[294] Sergey Bravyi, David P. DiVincenzo, and Daniel Loss. Schrieffer–wolff transformation for quantum many-body systems. *Annals of Physics*, 326(10):2793–2826, 2011.

[295] Roland Winkler. Quasi-degenerate perturbation theory. In *Spin–Orbit Coupling Effects in Two-Dimensional Electron and Hole Systems*, pages 201–206. Springer, Berlin, Heidelberg, 2003.

[296] E. M. Kessler. Generalized Schrieffer-Wolff formalism for dissipative systems. *Phys. Rev. A*, 86:012126, Jul 2012.

[297] E. M. Kessler, G. Giedke, A. Imamoglu, S. F. Yelin, M. D. Lukin, and J. I. Cirac. Dissipative phase transition in a central spin system. *Phys. Rev. A*, 86:012116, Jul 2012.

[298] Ryuichi Shindou, Jun-ichiro Ohe, Ryo Matsumoto, Shuichi Murakami, and Eiji Saitoh. Chiral spin-wave edge modes in dipolar magnetic thin films. *Phys. Rev. B*, 87:174402, May 2013.

[299] Ryuichi Shindou and Jun-ichiro Ohe. Magnetostatic wave analog of integer quantum hall state in patterned magnetic films. *Phys. Rev. B*, 89:054412, Feb 2014.

[300] Zixian Zhou, Liang-Liang Wan, and Zhi-Fang Xu. Topological classification of excitations in quadratic bosonic systems. *J. Phys. A: Math. Theor.*, 53(42):425203, oct 2020.

[301] Liang-Liang Wan, Zixian Zhou, and Zhi-Fang Xu. Squeezing-induced topological gap opening on bosonic bogoliubov excitations. *Phys. Rev. A*, 103:013308, Jan 2021.

[302] Apoorv Tiwari and Tomá š Bzdušek. Non-abelian topology of nodal-line rings in $\mathcal{PT}$-symmetric systems. *Phys. Rev. B*, 101:195130, May 2020.

[303] Kangkang Li, Chenyuan Li, Jiangping Hu, Yuan Li, and Chen Fang. Dirac and nodal line magnons in three-dimensional antiferromagnets. *Phys. Rev. Lett.*, 119:247202, Dec 2017.

[304] Weiliang Yao, Chenyuan Li, Lichen Wang, Shangjie Xue, Yang Dan, Kazuki Iida, Kazuya Kamazawa, Kangkang Li, Chen Fang, and Yuan Li. Topological spin excitations in a three-dimensional antiferromagnet. *Nature Physics*, 14(10):1011–1015, Oct 2018.

[305] Song Bao, Jinghui Wang, Wei Wang, Zhengwei Cai, Shichao Li, Zhen Ma, Di Wang, Kejing Ran, Zhao-Yang Dong, D. L. Abernathy, Shun-Li Yu, Xiangang Wan, Jian-Xin Li, and Jinsheng Wen. Discovery of coexisting dirac and triply degenerate magnons in a three-dimensional antiferromagnet. *Nature Communications*, 9(1):2591, Jul 2018.

[306] Bo Yuan, Ilia Khait, Guo-Jiun Shu, F. C. Chou, M. B. Stone, J. P. Clancy, Arun Paramekanti, and Young-June Kim. Dirac magnons in a honeycomb lattice quantum XY magnet cotio_3. *Phys. Rev. X*, 10:011062, Mar 2020.

[307] M. Elliot, P. A. McClarty, D. Prabhakaran, R. D. Johnson, H. C. Walker, P. Manuel, and R. Coldea. Order-by-disorder from bond-dependent exchange and intensity signature of nodal quasiparticles in a honeycomb cobaltate. *Nature Communications*, 12(1):3936, Jun 2021.

[308] Ming-Wen Xiao. Theory of transformation for the diagonalization of quadratic Hamiltonians. *arXiv e-prints*, page arXiv:0908.0787, August 2009.

[309] Vittorio Peano and Hermann Schulz-Baldes. Topological edge states for disordered bosonic systems. *Journal of Mathematical Physics*, 59(3):031901, 2018.

[310] Hermann Schulz-Baldes and Carlos Villegas-Blas. Signatures for J-Hermitians and J-unitaries on Krein spaces with real structures. *Mathematische Nachrichten*, 290(11-12):1840–1858, 2017.

[311] L. Bracci, G. Morchio, and F. Strocchi. Wigner's theorem on symmetries in indefinite metric spaces. *Communications in Mathematical Physics*, 41(3):289–299, 1975.

[312] J. J. Sakurai. *Modern Quantum Mechanics.* Addison-Wesley, Reading, Massachusetts, 1994.

[313] Ryuichi Shindou, Ryo Matsumoto, Shuichi Murakami, and Jun-ichiro Ohe. Topological chiral magnonic edge mode in a magnonic crystal. *Phys. Rev. B*, 87:174427, May 2013.

[314] Hiroki Kondo, Yutaka Akagi, and Hosho Katsura. Three-dimensional topological magnon systems. *Phys. Rev. B*, 100:144401, Oct 2019.

[315] Andor Kormányos, Viktor Zólyomi, Neil D. Drummond, Péter Rakyta, Guido Burkard, and Vladimir I. Fal'ko. Monolayer MoS_2: Trigonal warping, the Γ valley, and spin-orbit coupling effects. *Phys. Rev. B*, 88:045416, Jul 2013.

[316] Andor Kormányos, Viktor Zólyomi, Neil D. Drummond, and Guido Burkard. Spin-orbit coupling, quantum dots, and qubits in monolayer transition metal dichalcogenides. *Phys. Rev. X*, 4:011034, Mar 2014.

[317] Andor Kormányos, Guido Burkard, Martin Gmitra, Jaroslav Fabian, Viktor Zólyomi, Neil D Drummond, and Vladimir Fal'ko. $\mathbf{k} \cdot \mathbf{p}$ theory for two-dimensional transition metal dichalcogenide semiconductors. *2D Materials*, 2(2):022001, apr 2015.

[318] Andor Kormányos, Guido Burkard, Martin Gmitra, Jaroslav Fabian, Viktor Zólyomi, Neil D Drummond, and Vladimir Fal'ko. Corrigendum: $\mathbf{k}\cdot\mathbf{p}$ theory for two-dimensional transition metal dichalcogenide semiconductors (2015 2D Mater. 2 022001). *2D Materials*, 2(4):049501, nov 2015.

[319] Khadijeh Beiranvand, Abdolmohammad Ghalambor Dezfuli, and Mohammad Sabaeian. A two-band spinful k.p Hamiltonian of monolayer MoS2 from a nine-band model based on group theory. *Superlattices and Microstructures*, 120:812–823, 2018.

[320] Junyeong Ahn, Dongwook Kim, Youngkuk Kim, and Bohm-Jung Yang. Band topology and linking structure of nodal line semimetals with Z_2 monopole charges. *Phys. Rev. Lett.*, 121:106403, Sep 2018.

[321] W. B. Rui, Y. X. Zhao, and Andreas P. Schnyder. Topological transport in dirac nodal-line semimetals. *Phys. Rev. B*, 97:161113(R), Apr 2018.

[322] Si Li, Ying Liu, Botao Fu, Zhi-Ming Yu, Shengyuan A. Yang, and Yugui Yao. Almost ideal nodal-loop semimetal in monoclinic $CuTeO_3$ material. *Phys. Rev. B*, 97:245148, Jun 2018.

[323] Y. X. Zhao and Y. Lu. PT-symmetric real dirac fermions and semimetals. *Phys. Rev. Lett.*, 118:056401, Feb 2017.

[324] Alexander Mook, Jürgen Henk, and Ingrid Mertig. Magnon nodal-line semimetals and drumhead surface states in anisotropic pyrochlore ferromagnets. *Phys. Rev. B*, 95:014418, Jan 2017.

[325] R. E. Newnham, J. H. Fang, and R. P. Santoro. Crystal structure and magnetic properties of $CoTiO_3$. *Acta Crystallographica*, 17(3):240–242, Mar 1964.

[326] Huimei Liu, Jiří Chaloupka, and Giniyat Khaliullin. Kitaev spin liquid in $3d$ transition metal compounds. *Phys. Rev. Lett.*, 125:047201, Jul 2020.

[327] Shreya Das, Sreekar Voleti, Tanusri Saha-Dasgupta, and Arun Paramekanti. XY magnetism, Kitaev exchange, and long-range frustration in the $J_{\text{eff}} = \frac{1}{2}$ honeycomb cobaltates. *Phys. Rev. B*, 104:134425, Oct 2021.

[328] Eugene Wigner. *Group Theory and its Application to the Quantum Mechanics of Atomic Spectra.* Academic Press Inc., New York, 1959.

[329] M. E. Zhitomirsky and A. L. Chernyshev. Colloquium: Spontaneous magnon decays. *Rev. Mod. Phys.*, 85:219–242, Jan 2013.

[330] Alexander Mook, Kirill Plekhanov, Jelena Klinovaja, and Daniel Loss. Interaction-stabilized topological magnon insulator in ferromagnets. *Phys. Rev. X*, 11:021061, Jun 2021.

[331] T. T. Zhang, H. Miao, Q. Wang, J. Q. Lin, Y. Cao, G. Fabbris, A. H. Said, X. Liu, H. C. Lei, Z. Fang, H. M. Weng, and M. P. M. Dean. Phononic helical nodal lines with $\mathcal{PT}$ protection in MoB_2. *Phys. Rev. Lett.*, 123:245302, Dec 2019.

[332] Marcelo Ponce, Ramses van Zon, Scott Northrup, Daniel Gruner, Joseph Chen, Fatih Ertinaz, Alexey Fedoseev, Leslie Groer, Fei Mao, Bruno C. Mundim, Mike Nolta, Jaime Pinto, Marco Saldarriaga, Vladimir Slavnic, Erik Spence, Ching-Hsing Yu, and W. Richard Peltier. Deploying a top-100 supercomputer for large parallel workloads: The Niagara supercomputer. In *Proceedings of the Practice and Experience in Advanced Research Computing on Rise of the Machines (Learning)*, PEARC '19, New York, NY, USA, 2019. Association for Computing Machinery.

[333] Chris Loken, Daniel Gruner, Leslie Groer, Richard Peltier, Neil Bunn, Michael Craig, Teresa Henriques, Jillian Dempsey, Ching-Hsing Yu, Joseph Chen, L Jonathan Dursi, Jason Chong, Scott Northrup, Jaime Pinto, Neil Knecht, and Ramses Van Zon. SciNet: Lessons learned from building a power-efficient top-20 system and data centre. *Journal of Physics: Conference Series*, 256:012026, nov 2010.

[334] W. Brinkman and R. J. Elliott. Space group theory for spin waves. *Journal of Applied Physics*, 37(3):1457–1459, 1966.

[335] W. F. Brinkman, Roger James Elliott, and Rudolf Ernst Peierls. Theory of spin-space groups. *Proceedings of the Royal Society of London. Series A. Mathematical and Physical Sciences*, 294(1438):343–358, 1966.

[336] William Brinkman. Magnetic symmetry and spin waves. *Journal of Applied Physics*, 38(3):939–943, 1967.

[337] Eduardo V. Castro, Miguel A. Cazalilla, and María A. H. Vozmediano. Raise and collapse of pseudo landau levels in graphene. *Phys. Rev. B*, 96:241405, Dec 2017.

[338] M. J. Pacholski, C. W. J. Beenakker, and İ. Adagideli. Topologically protected Landau level in the vortex lattice of a Weyl superconductor. *Phys. Rev. Lett.*, 121:037701, Jul 2018.

[339] M. J. Pacholski, C. W. J. Beenakker, and İ. Adagideli. Universal chiral magnetic effect in the vortex lattice of a Weyl superconductor. *Annals of Physics*, 417:168103, 2020. Eliashberg theory at 60: Strong-coupling superconductivity and beyond.

[340] Emilian M. Nica and Marcel Franz. Landau levels from neutral Bogoliubov particles in two-dimensional nodal superconductors under strain and doping gradients. *Phys. Rev. B*, 97:024520, Jan 2018.

[341] B. J. Taylor, C. A. McElroy, I. K. Lum, A. M. Leese de Escobar, M. C. de Andrade, T. J. Wong, E. Y. Cho, and M. B. Maple. Correlation of structural, magnetic, and electronic transitions of a novel charge-gradient $\mathrm{yba_2cu_3o}_{\nabla x}$ film. *Phys. Rev. B*, 91:144511, Apr 2015.

[342] Takuro Kobayashi, Taiki Matsushita, Takeshi Mizushima, Atsushi Tsuruta, and Satoshi Fujimoto. Negative thermal magnetoresistivity as a signature of a chiral anomaly in Weyl superconductors. *Phys. Rev. Lett.*, 121:207002, Nov 2018.

[343] A. S. Alexandrov. Theory of quantum magneto-oscillations in underdoped cuprate superconductors. *Journal of Physics: Condensed Matter*, 20(19):192202, Apr 2008.

[344] Sumilan Banerjee, Shizhong Zhang, and Mohit Randeria. Theory of quantum oscillations in the vortex-liquid state of high-T_c superconductors. *Nature Communications*, 4(1):1700, 2013.

[345] R. Corcoran, P. Meeson, Y. Onuki, P.-A. Probst, M. Springford, K. Takita, H. Harima, G. Y. Guo, and B. L. Gyorffy. Quantum oscillations in the mixed state of the type II superconductor 2H-$\mathrm{NbSe_2}$. *Journal of Physics: Condensed Matter*, 6(24):4479, Jun 1994.

[346] Taiki Matsushita, Tianyu Liu, Takeshi Mizushima, and Satoshi Fujimoto. Charge/spin supercurrent and the Fulde-Ferrell state induced by crystal deformation in Weyl/Dirac superconductors. *Phys. Rev. B*, 97:134519, Apr 2018.

[347] Emilian M. Nica and Onur Erten. Interacting topological bound states and Majorana fermions in strained nodal superconductors. *Phys. Rev. B*, 100:174510, Nov 2019.

[348] Leandro Salemi, Marco Berritta, Ashis K. Nandy, and Peter M. Oppeneer. Orbitally dominated Rashba-Edelstein effect in noncentrosymmetric antiferromagnets. *Nature Communications*, 10(1):5381, 2019.

[349] Annika Johansson, Börge Göbel, Jürgen Henk, Manuel Bibes, and Ingrid Mertig. Spin and orbital Edelstein effects in a two-dimensional electron gas: Theory and application to $\mathrm{SrTiO_3}$ interfaces. *Phys. Rev. Research*, 3:013275, Mar 2021.

[350] Haowei Xu, Jian Zhou, Hua Wang, and Ju Li. Light-induced static magnetization: Nonlinear Edelstein effect. *Phys. Rev. B*, 103:205417, May 2021.

[351] Tarik P. Cysne, Filipe S. M. Guimarães, Luis M. Canonico, Tatiana G. Rappoport, and R. B. Muniz. Orbital magnetoelectric effect in zigzag nanoribbons of p-band systems. *Phys. Rev. B*, 104:165403, Oct 2021.

[352] Dongwook Go, Jan-Philipp Hanke, Patrick M. Buhl, Frank Freimuth, Gustav Bihlmayer, Hyun-Woo Lee, Yuriy Mokrousov, and Stefan Blügel. Toward surface orbitronics: giant orbital magnetism from the orbital rashba effect at the surface of sp-metals. *Scientific Reports*, 7(1):46742, 2017.

[353] Daisuke Hara, M. S. Bahramy, and Shuichi Murakami. Current-induced orbital magnetization in systems without inversion symmetry. *Phys. Rev. B*, 102:184404, Nov 2020.

[354] Ken Osumi, Tiantian Zhang, and Shuichi Murakami. Kinetic magnetoelectric effect in topological insulators. *Communications Physics*, 4(1):211, 2021.

[355] Luca Chirolli, Maria Teresa Mercaldo, Claudio Guarcello, Francesco Giazotto, and Mario Cuoco. Colossal orbital Edelstein effect in noncentrosymmetric superconductors. *Phys. Rev. Lett.*, 128:217703, May 2022.

[356] Ion Garate and A. H. MacDonald. Influence of a transport current on magnetic anisotropy in gyrotropic ferromagnets. *Phys. Rev. B*, 80:134403, Oct 2009.

[357] Hang Li, H. Gao, Liviu P. Zârbo, K. Výborný, Xuhui Wang, Ion Garate, Fatih Doğan, A. Čejchan, Jairo Sinova, T. Jungwirth, and Aurélien Manchon. Intraband and interband spin-orbit torques in noncentrosymmetric ferromagnets. *Phys. Rev. B*, 91:134402, Apr 2015.

[358] Jorge Ramírez-Ruiz, Samuel Boutin, and Ion Garate. NMR in an electric field: A bulk probe of the hidden spin and orbital polarizations. *Phys. Rev. B*, 96:235201, Dec 2017.

[359] Terrence Tao. When are eigenvalues stable? In *What's new: Updates on my research and expository papers, discussion of open problems, and other maths-related topics*, Oct 2008. https://terrytao.wordpress.com/2008/10/28/when-are-eigenvalues-stable/.

[360] Ramis Movassagh. Eigenvalue attraction. *Journal of Statistical Physics*, 162(3):615–643, 2016.

[361] N. R. Bernier, L. D. Tóth, A. K. Feofanov, and T. J. Kippenberg. Level attraction in a microwave optomechanical circuit. *Phys. Rev. A*, 98:023841, Aug 2018.

[362] A. A. Maradudin and S. H. Vosko. Symmetry properties of the normal vibrations of a crystal. *Rev. Mod. Phys.*, 40:1–37, Jan 1968.

[363] A. A. Maradudin, E. W. Montroll, and G. H. Weiss. *Theory of lattice dynamics in the harmonic approximation.* Academic Press Inc., New York, 1963.

[364] A. Holz. Phonons in a strong static magnetic field. *Il Nuovo Cimento B (1971-1996)*, 9(1):83–95, 1972.

[365] Jian-Sheng Wang and Lifa Zhang. Phonon Hall thermal conductivity from the Green-Kubo formula. *Phys. Rev. B*, 80:012301, Jul 2009.

[366] Lifa Zhang, Jie Ren, Jian-Sheng Wang, and Baowen Li. Topological nature of the phonon Hall effect. *Phys. Rev. Lett.*, 105:225901, Nov 2010.

[367] Tao Qin, Jianhui Zhou, and Junren Shi. Berry curvature and the phonon hall effect. *Phys. Rev. B*, 86:104305, Sep 2012.

[368] Roman Süsstrunk and Sebastian D. Huber. Classification of topological phonons in linear mechanical metamaterials. *Proceedings of the National Academy of Sciences*, 113(33):E4767–E4775, 2016.